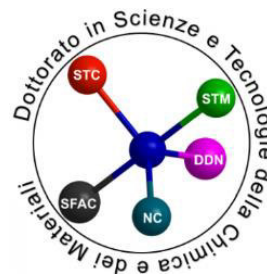




ISTITUTO ITALIANO  
DI TECNOLOGIA



# **CARBON NANO-ONIONS FOR BIOMEDICAL APPLICATIONS**



**A thesis submitted to the University of Genoa  
for the degree of Doctor of Philosophy**

**By  
Viviana Maffeis**

**March 2018**

**University of Genoa**

# Contents

Declaration.....	i
Acknowledgements.....	ii
Abstract.....	iii
Abbreviations.....	iv
<b>1. Introduction.....</b>	<b>1</b>
1.1 Carbon Nano Materials .....	1
1.1.1 Fullerene .....	1
1.1.2 Nanodiamond.....	2
1.1.3 Carbon Dot.....	2
1.1.4 Graphene .....	3
1.1.5 Carbon nanotube .....	3
1.1.6 Carbon nanohorn .....	3
1.2 Surface Functionalization .....	4
1.2.1 Covalent Surface Functionalization .....	4
1.2.2 Noncovalent Surface Functionalization .....	4
1.3 Carbon nano-onion.....	5
1.4 Synthetic pathways for CNO preparation .....	6
1.4.1 Annealing of nanodiamonds .....	7
1.4.2 Arcing Graphite Underwater .....	8
1.4.3 Pulse Laser Ablation .....	10
1.4.4 Radio-frequency plasma-enhanced Chemical Vapor Deposition (CVD).....	11
1.4.5 Other synthetic methods for CNOs fabrication .....	13
1.3 Properties and characterization of CNO.....	15
1.3.1 Raman Spectroscopy .....	15
1.3.2 Thermochemistry .....	17
1.3.3 Textural properties and porosity .....	17
1.3.4 Electronic properties of carbon nano-onions .....	19
1.3.5 Electrochemistry .....	21
1.4 CNOs – Toxicological aspects.....	23
1.5 Nanotechnology in biomedicine.....	27
1.5.1 Size and Shape.....	28
1.5.2 Surface Properties .....	28
1.5.3 Surface Charges .....	29
1.5.4 PEGylation .....	29
1.5.5 Polysaccharides.....	29
1.5.6 Conjugation with Targeting Ligands .....	30
1.5.7 Drug Loading .....	31
1.6 Conclusion .....	31
1.7 References .....	34

<b>2. CNO for biomedical imaging</b> .....	<b>39</b>
2.1 Introduction .....	39
2.2 Experimental.....	40
2.2.1 Highly surface functionalized carbon nano-onions for bright light bioimaging .....	40
2.2.2 Synthesis of p-CNO, benz-CNO and ox-CNO .....	40
2.2.3 Synthesis of fluo-CNO .....	42
2.3 Results and discussion .....	42
2.3.1 Thermo Gravimetric Analysis (TGA).....	42
2.3.2 Fourier-transform infrared spectroscopy (FTIR) .....	43
2.3.3 Raman Spectroscopy .....	44
2.3.4 Fluorescence Spetroscopy .....	44
2.3.5 Dinamic Light Scattering (DLS) and $\zeta$ -potential measurements.....	45
2.3.6 Cell studies .....	46
2.3.7 Toxicity.....	47
2.3.8 Cellular Uptake .....	48
2.4 Conclusion .....	48
2.5 Efficient covalent ligation methodology of Isoquinolines onto Carbon Nano-onions (CNOs) .....	50
2.5.1 Introduction .....	50
2.5.2 Experimental.....	52
2.5.2.1 Deprotection of Blue Emissive Isoquinolines.....	52
2.5.2.2 Characterization of Isoquinoline 1.1 .....	53
2.5.2.3 Characterization of Isoquinoline 2.1 .....	54
2.5.2.4 Characterization of Isoquinoline 3.1 .....	54
2.5.2.5 Synthesis of 1-CNO .....	55
2.5.2.6 Synthesis of 2-CNO .....	55
2.5.2.7 Synthesis of 3-CNO .....	55
2.5.3 Results and Discussion .....	56
2.5.3.1 Blue Emissive Isoquinolines-CNOs Characterization .....	56
2.5.4 Conclusion .....	58
2.6 References .....	59
<b>3. CNO as vaccine carrier</b> .....	<b>60</b>
3.1 Introduction .....	60
3.1.1 Nanovaccinology.....	61
3.2 Experimental.....	62
3.2.1 Covalent Immobilization of Glycopeptides and Proteins onto Carbon Nano-onions (CNOs) ....	62
3.2.2 Synthesis of Benzyl- N-acetyl L-cysteine.....	63
3.2.3 Synthesis of functionalized fluorescein .....	64
3.2.4 Synthesis of fluorescein-functionalized glycopeptide .....	65
3.2.5 Synthesis of Maleimido-PEG conjugate .....	66

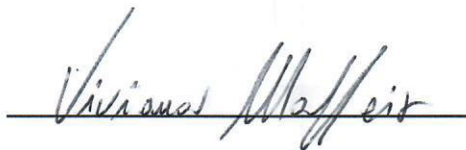
3.2.6 Reduction of organic disulfide bonds with TCEP .....	67
3.2.7 Mal-CNO synthesis .....	68
3.2.8 Gly-CNO synthesis .....	69
3.2.9 BSA-CNO synthesis .....	70
3.3 Results and Discussion .....	71
3.3.1 Absorption and Emission Spectroscopy .....	71
3.3.2 Absorption studies of the fluorescent glycopeptide .....	72
3.3.3 Emission studies of the fluorescent glycopeptide .....	73
3.3.4 (FT-IR) .....	74
3.3.5 Confocal Microscopy .....	74
3.3.6 Glycopeptide-CNO conjugate characterization .....	75
3.3.7 BSA-CNO conjugate characterization .....	77
3.3.8 Absorption and Emission Spectroscopy .....	79
3.3.9 Absorption and emission studies of Gly-CNO .....	80
3.3.10 Absorption and emission studies of BSA-CNO .....	81
3.3.11 Cell Studies: Toxicity .....	82
3.3.12 Cell Studies: Cellular Uptake .....	83
3.4 Conclusion .....	84
3.5 References .....	85
<b>4. CNO for photodynamic therapy.....</b>	<b>87</b>
4.1 Introduction .....	87
4.1.1 Carbon Nanomaterials for Photodynamic Therapy .....	88
4.1.2 Inhibited phototoxicity of a carbon nano-onion immobilized diiodo-BODIPY photosensitizer ....	89
4.2 Experimental.....	90
4.2.1 Synthesis of the pyrene-diiodoBODIPY dye.....	90
4.2.2 Synthesis of 4-(prop-2-ynoxy)benzaldehyde .....	92
4.2.3 Synthesis of 1,3,5,7-Tetramethyl-8-(4-Propargyloxyphenyl)-4,4-difloroboradiaza-s-indacene ..	92
4.2.4 Synthesis of 2,6-Diiodo-1,3,5,7-tetramethyl-8-(4-Propargyloxyphenyl)-4,4-difloroboradiaza-s-indacene .....	93
4.2.5 Synthesis of 1-(azidomethyl)pyrene .....	93
4.2.6 Synthesis of photosensitizer 3 .....	94
4.2.7 Synthesis of 3/CNO Nano-hybrid.....	95
4.2.8 Synthesis of 3/benz-CNO Nano-hybrid .....	96
4.3 Results and discussion.....	96
4.3.1 Absorption and Emission spectroscopy of pyrene-diiodoBODIPY dye .....	96
4.3.2 Absorption and Emission spectroscopy of 3/CNO and 3/benz-CNO .....	96
4.3.3 Biological Studies of Nano-hybrid 3/CNO.....	97
4.3.4 Biological Studies of Nano-hybrid 3/benz-CNO.....	100
4.3.5 Photobleaching studies .....	101
4.3.6 Photobleaching studies for 3/CNO .....	103

4.3.7 Photobleaching studies for 3/benz-CNO .....	104
4.4 Conclusion .....	105
4.5 References .....	106
<b>5. CNOs for Photocatalysis .....</b>	<b>108</b>
5.1 Introduction .....	108
5.2 Experimental .....	109
5.2.1 General Procedure for Radical Thiol-Ene Reaction .....	109
5.2.2 Synthesis of compound 1 .....	109
5.2.3 Synthesis of compound 2 .....	110
5.2.4 Synthesis of compound 3 .....	110
5.2.5 Synthesis of compound 4 .....	111
5.2.6 Synthesis of compound 5 .....	111
5.2.7 Synthesis of compound 6 .....	112
5.3 Results and discussion .....	112
5.3.1 Bismuth Oxide and Tungsten Oxide Photocatalytic Initiation of Radical Thiol-Ene Reaction .....	112
5.3.2 Nanomaterials screened for the thiol-ene ligation reaction .....	113
5.3.3 Carbon NM-MO composites investigation .....	114
5.3.4 Carbon NM-MO composites characterization .....	116
5.3.5 Carbon NM-MO composites screened for the thiolene-ligation under visible light .....	117
5.3.6 Scope Expantion .....	118
5.3.7 Mechanism .....	123
5.4 Conclusion .....	123
5.5 References .....	124
<b>6. Materials and Methods .....</b>	<b>126</b>
6.1 Materials .....	126
6.2 Instrumentation .....	126
6.2.1 Thermogravymetric analysis (TGA) .....	126
6.2.2 Attenuated total reflectance Fourier transformed infrared (ATR FTIR) spectroscopy .....	126
6.2.3 Raman spectroscopy .....	126
6.2.4 Absorption and fluorescence spectroscopy .....	126
6.2.5 Fluorescence quantum yields .....	127
6.2.6 Dynamic light scattering (DLS) and zeta-potential measurements .....	127
6.2.7 Transmission electron microscopy (TEM) .....	127
6.2.8 High-resolution mass spectrometry (HRMS) .....	127
6.2.9 Nuclear Magnetic Resonance Spectroscopy (NMR) .....	127
6.2.10 Confocal microscopy .....	128
6.3 Biological methods .....	128
6.3.1 Cell Culture .....	128
6.3.2 Sample preparation for cell study .....	128

6.3.3 Cell viability .....	128
6.3.4 Cellular imaging .....	128
6.4 References .....	129
<b>7. Conclusion and Outlook .....</b>	<b>130</b>

### DECLARATION

This thesis is being submitted for the degree of Doctor of Philosophy in the University of Genoa, Italy and has not been submitted before for any degree or examination in this or any other University. Except where acknowledgement is given, all work described is original and carried out by the author alone. Permission is granted so that the Library may lend or copy this thesis upon request. This permission covers only single copies, made for study purposes, subject to normal conditions of acknowledgement.

A handwritten signature in cursive script, reading "Viviana Maffei", is written over a horizontal line.

Viviana Maffei

## **Acknowledgements**

I am deeply grateful to my supervisor, Prof. Silvia Giordani, for her training, advice and introduction to the wonders of carbon nanomaterials chemistry, especially for her guidance and invaluable assistance in making this research possible.

A special thank also to the members of the Giordani group (former and present), for their discussion and help and for keeping the lab exciting and interesting, in particular to Prof. Marco Frasconi e Dr. Juergen Bartelmess for the fruitful scientific discussions and precious support; to Dr. Stefania Lettieri and Dr. Marta D'Amora for their advice and for dedicating their time in proof reading my thesis. Thanks to Adalberto and Francesca for having shared knowledge and made this experience unique. A particular thank also to Prof. Eoin M. Scanlan for hosting me in his lab at Trinity College Dublin, for his collaboration and support.

I would like to acknowledge the Istituto Italiano di Tecnologia for financial support. The NACH, NAPH and D3 departments for access to instrumentation. I would also like to thank my tutor at the University of Genoa, Prof. Renata Riva for the feedback and opportunities given.

Last, and certainly not least, I would like to thank my parents, Adele and Giuseppe, and my beloved sister Aurora. Their support, encouragement, and advice allowed me to stay focused, throughout this journey.



## Abstract

The biomedical applications of carbon nanomaterials are under intensive investigation for the development of next-generation therapeutics. Although much focus has been placed on carbon nanotubes (CNTs) and graphene, other carbon nanomaterials including carbon nanohorns (CNHs), nanodiamonds (NDs) and fullerenes have emerged as suitable candidates for biomedical applications. Among these multi-shell fullerenes, also known as carbon nano-onions (CNOs), are the less studied carbon nanomaterials in biomedicine. The unique properties of carbon nano-onions, such as high surface area-to-volume ratio, thermal conductivity, electrical conductance, mechanical stiffness and ease of chemical functionalization render them fascinating materials for diverse applications including drug-delivery, diagnostics, biological imaging and tissue engineering. Carbon nanomaterials are emerging as smart nanostructures for biomedicine due to the possibility to incorporate multiple functionalities and moieties internally or externally. They can be modified at a precise physicochemical level to optimize targeting in the complex *in vivo* environment and also engineered for fluorescence detection, magnetic resonance imaging and ablation of tumor cells. Herein, robust and versatile synthetic strategies for the modification of carbon nano-onions (CNOs) are reported. The development of novel CNO conjugates represent a promising platform for the realization of novel technology scaffold for molecular imaging, photodynamic therapy and molecular transporter of fully synthetic carbohydrate-based vaccines for immunotherapy due to the large specific surface area and unique optical and electrochemical properties of CNOs. Through the methodologies described, these smart nano-materials can envisage the realization of multi stimuli-responsive and dynamic architectures capable of changing their physicochemical behavior upon encountering specific micro-environmental signals becoming relevant for diagnosis, imaging and therapies of specific disease applications.

## List of Abbreviation

A-CNOs	carbon nano-onions obtained by arching
ADCs	antibody–drug conjugates
AFM	atomic-force microscopy
APCs	antigen-presenting cells
B-CNO	boron-doped carbon nano-onion
BET	Brunauer-Emmett-Teller static nitrogen adsorption technique
BODIPY	borondipyrromethene
BSA	bovine serum albumin
C <sub>60</sub>	buckminsterfullerene
Cdots	carbon dots
CLEM	correlative light electron microscopy
CNF	carbon fibers
CNH	carbon nanohorns
CNM	carbon nanomaterials
CNM-MO	carbon nanomaterial/metal oxide
CNO	carbon nano-onions
CNOs	carbon nano-onions
CNT	carbon nanotubes
CVD	chemical vapor deposition
DLS	dynamic light scattering
DMF	dimethylformamide
DMSO	dimethyl sulfoxide
EDX	energy-dispersive X-ray spectroscopy
EELS	electron energy loss spectroscopy
ELNES	energy-loss near-edge structure
FA	folic acid
FITC	fluorescein isothiocyanate

FT-IR	fourier transform infrared spectroscopy
GO	graphene oxide
GQDs	graphene quantum dots
HOPG	highly oriented pyrolytic graphite
HREM	high-resolution electron microscope
HR-MAS	high-resolution magic-angle spinning NMR spectroscopy
HRTEM	high-resolution transmission electron microscopy
MRI	magnetic resonance imaging
MWCNT	multi-wall carbon nanotubes
N-CNO	carbon nano-onions obtained by thermal annealing
ND	nanodiamonds
NMR	nuclear magnetic resonance spectroscopy
PBS	phosphate buffered saline
PDT	photodynamic therapy
PEG	polyethylene glycol
RGO	reduced graphene oxide
ROS	reactive oxygen species
SEM	scanning electron microscope
STM	scanning tunneling microscopy
SWCNT	single wall carbon nanotubes
TEM	transmission electron microscopy
TGA	thermo-gravimetric analysis
THF	tetrahydrofuran
UDD	ultra- disperse diamonds
XPS	X-ray photoelectron spectroscopy
XRD	X-ray diffraction spectroscopy

# 1. Introduction

## 1.1 Carbon Nano Materials

In the past decade nanomaterials have begun to emerge as valuable opportunities in biomedical research and clinical applications.<sup>1</sup> This has become possible by coupling their inherent properties<sup>2,3</sup> with the established knowledge of molecular and biomolecular recognition. In particular, carbon nanomaterials (CNMs) are among the most broadly discussed, researched and applied synthetic nanomaterials.<sup>4,5,6</sup> This is due to their diverse intrinsic electronic, magnetic and optical properties, chemical versatility and ease of manipulation, biocompatibility as well as their performance as a chemically robust platform. Carbon nanomaterials typically range from 1 nm to 100 nm in size, which is comparable to the sizes of proteins (1–100 nm) and DNA (2–3 nm in width) in biological environments, and the sizes of natural biological barriers *in vivo* including ion channels (a few nanometers) and the glomerular filtration barrier (5–10 nm).<sup>7</sup> The favorable sizes of carbon nanomaterials have made them ideal nanocapsules and nanocarriers to load and deliver drugs and genes to specific targets *in vivo*. Moreover, the optical properties unique to some carbon nanomaterials have also attracted a lot of interest for a variety of biological and medical applications including biosensing, imaging, and therapy. R&D in different areas of nanomedicine is expected to revolutionize the disease diagnosis and treatment approaches in the near future. Nanosized contrast agents are anticipated to lead way to advancements in understanding biological processes at the molecular level. Nanomedical approaches to drug delivery focuses on developing nanoscale particles or molecules to improve the bioavailability of a drug. Special attention has been given to bioassay applications such as biosensors, biomedical devices, and biofuel cells using nanomaterials. Nanotechnology on a chip is a new paradigm for total chemical analysis systems. Nanorobotics and nanomanipulation technologies will eventually allow moving and manipulating nanoscale materials and assemble them into nanosystems such as nanoscale robotics.

CNMs exhibit huge diversity in structure, existing in many forms such as, diamond, graphene, amorphous carbon, C<sub>60</sub> and carbon nanotubes (CNTs). These materials can be classified according to the number of dimensions in zero-dimensional (0-D) nanoparticles such as fullerenes, carbon nano-onions and nanodiamonds one-dimensional (1-D) nanotubes, two-dimensional (2-D) layered materials such as graphene (Figure 1).

### 1.1.1 Fullerene

The discovery of C<sub>60</sub> fullerene by Smalley, Kroto, Curl et al. in 1985 can be considered as the starting point of the CNM revolution.<sup>4</sup> The nanometer size of the C<sub>60</sub> molecules can impart various unconventional capabilities to afford stealth nanoparticles for imaging and drug/gene delivery. First of all, the hollow cavity of the C<sub>60</sub> sphere can be used to load certain metal ions such as Gd<sup>3+</sup> or <sup>99m</sup>Tc, resulting in contrast agents for magnetic resonance imaging (MRI) as well as nuclear medicine.<sup>8,9</sup> Furthermore, it is found that the hydrophobic surface of the C<sub>60</sub> molecules binds strongly to oligodeoxynucleotide<sup>10</sup> leading to efficient gene delivery vehicles that can pass through both the cell membrane and the nuclear membrane to improve the efficacy of gene therapy.<sup>11</sup>

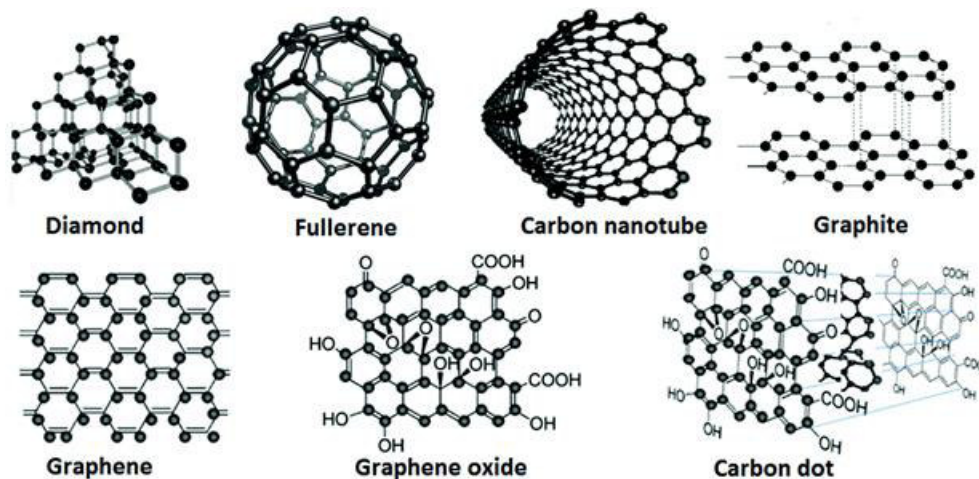


Figure 1. The world of synthetic carbon allotropes.

### 1.1.2 Nanodiamond

Another type of CNM in this size regime are carbon nanodiamonds (NDs), which combine the characteristics of diamond; optical transparency, chemical stability and biological compatibility, with the attractive nanomaterial's properties such as small size, large surface area and high adsorption capacity.<sup>12</sup> One important additional feature of NDs is their low toxicity.<sup>13</sup> NDs are primarily made through the controlled detonation of explosives to yield core-shell particles with diameters of 4–5 nm. The synthesis of fluorescent NDs is also possible through the introduction of nitrogen vacancies (N-V centres), which are typically introduced by electron irradiation (2 MeV) of 100 nm NDs followed by annealing (900 °C) in vacuum.<sup>14</sup> In addition, ultrasmall (1.6 nm) fluorescent NDs of roughly 400 carbon atoms and containing Si vacancies have been also reported. For bioimaging and therapy purposes, nanodiamond has several advantages. Firstly, nanodiamond is a highly photostable fluorophore that is almost nonphotobleachable, allowing for long-time imaging without concerns of signal decay.<sup>15</sup> Secondly, the fluorescence quantum efficiency is surprisingly high, usually ranging from 0.7 to 1, significantly higher than molecular fluorophores with similar emission wavelengths.<sup>16</sup> Thirdly, nanodiamond has been reported to be highly biocompatible and non-toxic to biological tissues and organisms.<sup>15</sup> Moreover, the abundant dangling bonds on the surface of nanodiamonds allow for easy surface functionalization via both covalent and noncovalent means without affecting the intrinsic optical properties of the N-V centers in the core, rendering them employed as fluorescent labels for *in vitro* imaging of subcellular structures and certain biomarkers,<sup>17,18</sup> *in vivo* whole animal imaging,<sup>19,20</sup> drug and gene delivery,<sup>21,22</sup> and tissue engineering.<sup>23,24</sup>

### 1.1.3 Carbon Dot

The most recent addition to the 0-D family of CNMs are carbon dots (Cdots), also referred to as graphene quantum dots (GQDs). The earliest reported syntheses of Cdots was by the laser ablation of a carbon target<sup>25</sup> and from candle soot.<sup>26</sup> Today, Cdots can be prepared by pyrolysis,<sup>27</sup> hydrothermal and electrochemical treatments,<sup>28</sup> and microwave synthesis of a wide variety of carbon sources such as biomass

and waste materials.<sup>29,30</sup> These methods provide access to Cdots whose luminescence spans the visible spectrum.<sup>31,32</sup>

#### **1.1.4 Graphene**

Graphene comprises a single, layer of  $sp^2$  carbon and as such can be considered the molecular parent of the  $sp^2$  CNMs. Graphene's ability to absorb light of all wavelengths coupled to its excellent electron transport properties has generated enormous interest. Typically, graphene is prepared by mechanical and liquid phase exfoliation of graphite,<sup>33,34</sup> recently large scale preparation of graphene using surfactants has been reported.<sup>35</sup> In addition to pristine graphene several surface treated forms such as photoluminescent graphene oxide (GO) and reduced graphene oxide (RGO) have also been used for biosensing applications, tumor imaging and drug/gene delivery.<sup>36,37</sup>

#### **1.1.5 Carbon nanotube**

Carbon nanotubes, are tubular structures of rolled-up sheets of graphene comprising single-wall (SWCNTs) and multi-wall (MWCNTs) species. SWCNTs exhibit metallic, semi-metallic and semiconducting, properties which may be exploited for several applications.<sup>38</sup> These properties depend on the nature of the rolled graphene sheet, which dictates the chirality of the species. The general synthesis of CNTs employs chemical vapour deposition of carbon in the presence of a transition metal catalyst.

#### **1.1.6 Carbon nanohorn**

Closely related to SWCNTs are single-walled carbon nanohorns (CNHs). These are conical structures with diameters of 2–5 nm and lengths of 40–50 nm which typically assemble into dahlia-flower like or bud-like aggregates with a diameter of about 100 nm. CNHs possess good porosity and high surface area which can be exploited for biomedical applications.<sup>39</sup> Importantly, CNHs can be produced in high yield in the absence of metal catalyst by either  $CO_2$  laser ablation of pure graphite or pulsed arc discharge of carbon rods.

The purity of synthesized CNMs is an essential consideration for any possible biological and medical application. Impurities may interfere with the detection of analytes and a polydisperse sample influences both the optical properties and the ability to form ordered assemblies. Of the CNMs, fullerene derivatives are the only members that can be synthesized with precisely known composition. For example, CNTs must be rigorously purified to remove the transition metal catalyst species.<sup>40,41</sup> Furthermore, *in vivo* applications require the removal of carbonaceous fragments which can act as reactive oxygen species. The size dependent optical properties of CNMs also necessitates the use of separation procedures to obtain monodisperse samples.<sup>42</sup> Techniques for the separation of chiral CNTs include ultracentrifugation<sup>43</sup> and gel permeation chromatography.<sup>44</sup> Centrifugation techniques have also been used for the length separation of CNTs<sup>45</sup> and the size-selective purification of dispersed graphene flakes.<sup>46</sup> In addition, Cdots have been separated from non-luminescent materials using C-18 HPLC.

## 1.2 Surface Functionalization

In order to employ for various nanomedicinal applications, nanomaterials should be subjected to suitable surface modifications. The aim of such surface modification strategies is to enhance the solubility and stability of nanosized materials in aqueous media as well as to impart them with biological properties and functionalities. As a brief note, CNMs are typically covalently functionalized through chemical reactions directly with the carbon atoms in the  $sp^2$  carbon shell, and a library of standard chemical reactions have been developed for carbon nanomaterials chemistry. They can be either covalently or non-covalently functionalized to impart water solubility, depending on the need for specific biological applications. Carbon dots are by nature rich in  $-OH$  and  $-COOH$  functional groups, which can easily form hydrogen bonds with water molecules and thus endow carbon dots with good solubility in aqueous environment; nonetheless, it is still desired to further functionalize them with PEG or other functional groups to increase biocompatibility. Nanodiamond, on the other hand, is similar to fullerenes, carbon nanotubes and graphene because of their poor solubility in aqueous solvents which render them prone to aggregation due to hydrophobic interactions. However, this can be addressed through surface functionalization by covalent<sup>47,48</sup> or non-covalent methods.<sup>49,50</sup> In the following chapters, I will illustrate covalent and non-covalent surface treatments for CNO functionalization.

### 1.2.1 Covalent Surface Functionalization

Most carbon nanomaterials are insoluble in water due to their hydrophobic surfaces made of  $sp^2$  carbon atoms. Covalent surface functionalization introduces heteroatoms (mostly O and N) and functional groups to the pristine carbon nanostructures and thus increases water solubility. The functional groups also provide handles for further conjugation with other functional molecules to improve biocompatibility and impart certain functions to the original carbon nanomaterials. In the case of  $sp^2$  carbon species covalent functionalization results in the permanent disruption of the  $\pi$ -electronic network which can influence the optical properties of the material. This can be avoided through the use of noncovalent methods which largely rely on  $\pi$ - $\pi$  stacking interactions between the CNM surface and molecules such as pyrenes and porphyrins and can be used to modulate the CNM optical properties.

### 1.2.2 Noncovalent Surface Functionalization

Non-covalent surface functionalization works by supramolecular interactions between the pristine carbon nanomaterial and the coating molecule/polymer, which impart minimum structural damage and disturbance to the intrinsic properties of the functionalized carbon nanomaterials. The supramolecular interactions employed for non-covalent surface functionalization include  $\pi$ - $\pi$  stacking and hydrophobic interactions. Strong non-covalent binding of pyrene moieties to the sidewalls of SWCNTs due to  $\pi$ - $\pi$  stacking is useful for functionalization of nanotubes for biological applications. The  $\pi$ -stacking chemistry has been widely utilized in the past decade for functionalization of not only nanotubes, but also various forms of graphene and carbon materials.<sup>51,52</sup> Besides non bioactive molecules, polymeric biomolecules such DNA and proteins have also be employed for solubilization of SWCNTs. Single-stranded DNA (ssDNA) was used to assist the dispersion and suspension of SWCNTs in water by helically wrapping to the surface of the nanotube, as first reported by Zheng et al.<sup>53</sup> It was suggested that strong  $\pi$ - $\pi$  stacking between nanotube surface and the

aromatic bases of ssDNA is responsible for the formation of hybrid between nanotube and DNA, which is elegant since DNA is a molecule of central importance in biology and the carbon nanotube represents an artificial 1D carbon nanocrystal.<sup>53</sup>

### **1.3 Carbon nano-onion**

Although carbon nano-onions were discovered before fullerenes and nanotubes, they stayed for a long time in the shadow of more popular and better investigated nanocarbons. Carbon nano-onions, which are the main materials investigated in my Ph.D. project, consist of spherical closed carbon shells and owe their name to the concentric layered structure resembling that of an onion. During my Ph. D. course, the physico-chemical properties of CNOs have been studied and novel technology platforms based on carbon nano-onions for bioimaging, synthetic nano-vaccine carriers and photo-dynamic therapy applications have been developed. CNOs have been shown to be ideal for the future rational design of carbon nanomaterial based medical technologies because of their unique 0-D structure, small (5 nm) diameter, good biocompatibility and efficient cell-uptake compared to 1-D nanotubes and 2-D graphene. The exclusive properties of the material, such as high surface area-to-volume ratio, thermal conductivity, electrical conductance, mechanical stiffness and ease of chemical functionalization render CNOs fascinating materials for diverse applications including drug-delivery, diagnostics, biological imaging and tissue engineering. The high biocompatibility and the efficient cellular uptake of these nanomaterials together with their high fluorescence reveal great promises for the development of new architectures for targeted imaging nanotherapeutics and antigen delivery devices. Furthermore, CNO can envisage the realization of multi stimuli-responsive and dynamic materials capable of changing their physicochemical behavior upon encountering specific micro-environmental signals becoming relevant for diagnosis, imaging and therapies of specific disease applications.



## 1.4 Synthetic pathways for CNO preparation

Since the discovery of the fullerene  $C_{60}$  in 1985 by Curl, Kroto and Smalley using laser desorption experiments<sup>4</sup>, several allotropes of carbon were discovered in the following years. This includes carbon nano-onions, also known as multi-shell fullerenes which were discovered in 1992 by Ugarte utilizing intense electron-beam irradiation<sup>54</sup>. Toward this, carbon soot particles were irradiated in a 300-kV high-resolution electron microscope (HREM) using an electron dose 10-20 times higher than under normal operating conditions (the usual dose was  $10\text{-}20 \text{ A cm}^{-2}$ ). It is worth to highlight that electron-beam heating did not lead to the same result as thermal heating, because of the contribution of the excitation process. Strong irradiation heats the sample by energy absorption and ruptures bonds through electron excitations. Furthermore, high-energy particles can transfer momentum to the nuclei, displacing atoms to interstitial lattice sites. The formation mechanism of these multiple-shell spheres rely on the graphitic structure stimulated by irradiation. By increasing irradiation, there is a gradual reorganization of the initial material into quasi-spherical particles composed of concentric graphitic shells and consequently the separation of the graphitic spheres as single units (Figure 2). These multilayered particles exhibit a diameter of about 5nm and the distance between the carbon layers was determined to be about 0.34 nm, which approximately corresponds to the distance between two graphitic planes<sup>54</sup> (Figure 3).

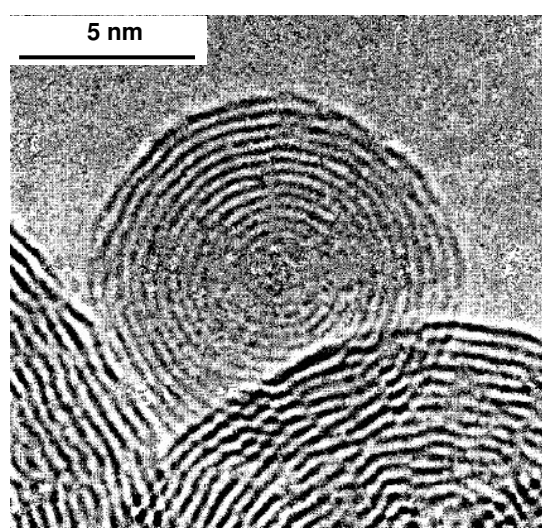


Figure 2. HRTEM image of a quasi-spherical onion-like graphitic particles generated by electron irradiation. (dark lines represent graphitic shells, and the distance between layers is 0.34 nm). Reprinted with permission from reference<sup>54</sup>. Copyright 1995 Elsevier.

However, this synthetic procedure is a low yield process. After the discovery of carbon onions, many efforts have been focused on synthetic pathways to obtain these concentric spherical shell structures with higher yield and to understand the formation mechanism of such materials. Over the last years, different methods of synthesis have been developed including high-temperature nanodiamonds annealing, arc discharge, laser ablation, chemical vapor deposition and their physical properties have been widely investigated.

### 1.4.1 Annealing of nanodiamonds

A detailed analysis of the effects of the annealing temperature on carbon nano-onions has been reported by Kuznetsov et al. in 1999<sup>5</sup>. Annealing of nanodiamonds with a  $sp^3$  diamond framework and a diameter of typically 2-5 nm was performed in a tube furnace using vacuum at high temperature. It has been proven by many researchers that upon heating to high temperatures (at least 900°C), a transformation of the diamond phase to a graphitic phase begins because enough kinetic energy is required to keep on breaking C-C bonds in the diamond core<sup>55</sup>. Indeed, a structural rearrangement of the particles including the elimination of dangling bonds at the nanodiamond surface and the closure of graphite sheets results in the decrease of the surface energy, which is supposed to be the driving force to form closed graphite shells continuously.<sup>56</sup> According to this, when the temperature is lower than 900°C, CNOs cannot be effectively generated. The amorphous carbon and the nanodiamond crystals coexist. Moreover, the non-carbonaceous material traces are still present in the sample. Thermal desorption data indicates that hydrogen – the last non-carbon contaminant - desorbs from the nanodiamond surface at approximately 850°C. At temperatures between 900°C and 1100°C, the CNOs are formed but still a small amount of nanodiamonds can be detected within the core of the particles. Only above 1400°C, nanodiamonds are completely transformed into CNOs<sup>56</sup>. The main product obtained by this synthetic method is a perfectly spherical multi-layered structure with 6 to 7 graphitic shells. It is worth to mention that the formation process of CNOs under annealing conditions includes a sequence of essential steps. The core step involves the formation of graphite fragments. The graphitization initiated by a significant thermal displacement of a single carbon atom at temperatures close to the Debye temperature initiates at the external surface of the nanodiamond particles and progresses towards its crystal bulk. Therefore, graphite fragments with different numbers of carbon atoms exfoliate from the external surface of any diamond plane and surround the nanodiamond particles – see Figure 3. Secondly, the connection and curvature of graphite sheets between diamond planes and especially the closure of graphite layers play a key role. The graphite fragments increased with increasing annealing temperature and gradually connected up into curved graphitic sheets close to diameters of  $C_{60}$  and higher fullerenes. Basically, in the case of high-temperature-treated or electron-irradiated amorphous carbon particles, the multiple-shell spheres were formed based on irradiation-stimulated graphitization.

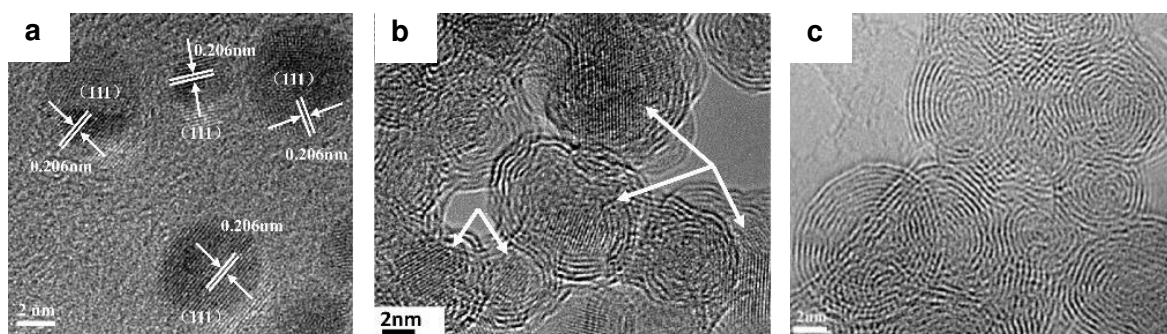


Figure 3. (a) HRTEM of abundant nanodiamonds. Marked lattice spacing is measured to be 0.206 nm, which coincides with the  $d$  value of the (111) lattice plane of diamond with cubic structure. (b) Spherical particle consisting of onion shells with a diamond core (pointed by the white arrows). (c) Spherical carbon onion with external graphitic layers and closed quasi-spherical internal shells. Reprinted with permission from reference <sup>56</sup>. Copyright (2014) American Chemical Society.

### 1.4.2 Arcing Graphite Underwater

In 2001 Sano and co-workers described a non-vacuum method to synthesize large-scale carbon nano-onions by an arc discharge between two graphite electrodes submerged in deionized water<sup>57, 58</sup>. In this method, two electrodes of high purity were electrically arced under water by applying a bias potential of 16-17 V between them and maintain a constant current of 30 A. Carbon nano-onions obtained thereby exhibit diameters of 25-30nm and 10-15 shells around a core found to be consistent with that of the C<sub>60</sub> molecule – see Figure 4. Therefore, carbon nano-onions with a hollow core surrounded by multilayered sp<sup>2</sup> carbon shells prepared from arcing graphite underwater are considerably larger than carbon nano onions obtained from nanodiamonds<sup>59</sup>. The nano-onions were obtained in the form of floating powder on the water surface, while the rest of the product, containing a mixture of graphitic nanotubes and nanoparticles was found to be at the bottom of the water tank. This process gives a material of high purity through a natural segregation from the other carbon structures. Although it may be presumed that the density of carbon nano-onions is less than that of water, this is not the case. It was found that the particles were floating on water despite of their density (1.64 g/cm<sup>3</sup>) being higher than that of water. Therefore, the floating carbon onions on the water surface are presumed to be due to the formation mechanism based on the formation of large van der Waals crystals.

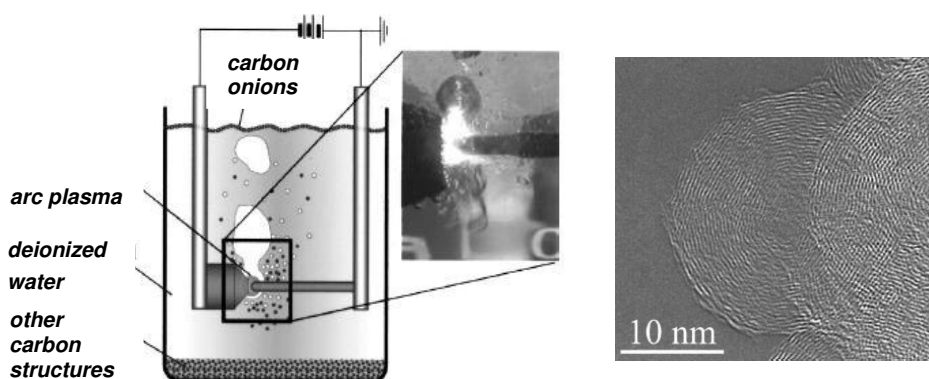
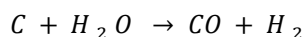


Figure 4. Scheme of the apparatus used for the arc discharge synthesis of CNOs in water and the HRTEM image of the resulting product collected as the floating powder on the top of the water surface. Reprinted with permission from reference<sup>57</sup>. Copyright (2002), AIP Publishing LLC.

Basically, subsequent to the formation of onions, they cluster into larger van der Waals crystals<sup>59</sup>. These clusters readily float to the top of the water surface remaining separated at the surface of the water even after vigorous dispersion through ultrasonication. In this arc-in-water system, onions are naturally agglomerated and float, being separated from the other large products that settle on the bottom of the beaker.

Sano and co-workers proposed that during an arching underwater process a plasma zone between electrodes exists and the temperature between them can reach up to 4000K (the sublimation temperature of carbon) and that a gas bubble due to the vaporization of the surrounding liquid is generated<sup>59</sup>. The main gas

components are CO and H<sub>2</sub> produced by the reaction of C atomic vapor and H<sub>2</sub>O at the gas-liquid interface as



The formation mechanism of carbon nano-onions in that case involves the graphitization of a liquid carbon drop. The sharp temperature gradient from the hot plasma region to the gas-water interface is fundamental to cause a rapid solidification of the vaporized carbon. The temperature at the hot plasma is estimated to be approximately 4000 K (the melting and boiling points of graphite are 3823 K and 4203K, respectively), while the temperature at the gas-water interface is the boiling point of water, 373 K. Remarkably, at high temperature, carbon from graphite electrode vaporizes and condenses when in contact with the surrounding cold aqueous environment. The generated temperature gradients induce an important range of conditions for the formation of graphitic nanoparticles; this fact leads to wide size and shape distributions (Figure 5). For the condition of arc-discharge, the elimination of the energetic dangling bonds during the cooling of quasi-liquid carbon is suggested to be the driving force to induce curvature and closure leading to the formation of CNOs.

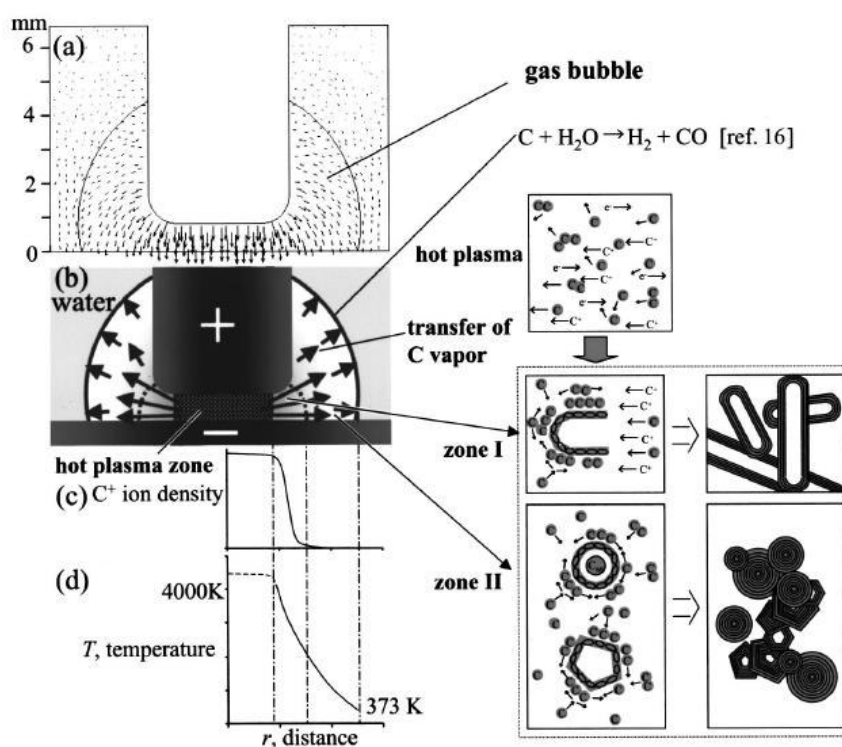


Figure 5. Representation of the formation mechanism of onions by arc discharge in water. The formation of elongated nanoparticles in zone (I) and in zone (II) is also shown schematically. Reprinted with permission from reference<sup>57</sup>. Copyright (2002), AIP Publishing LLC.

### 1.4.3 Pulse Laser Ablation

The recent developments of laser technologies offer unique opportunities for carbon nanostructures fabrication. The conditions for carbon nano-union formation, using a laser vaporization technique in a laser ablation chamber, were investigated by Dorobantu et al<sup>60</sup>. They reported a laser-assisted technique for the synthesis of high-quality CNOs by ablating pure graphite targets. This synthetic process requires a specialized equipment. Basically, the laser ablation chamber consists of a quartz tube mounted inside a tube furnace. It is important to keep the temperature of the furnace constant at 900°C during the entire experiment and the quartz tube is O-ring sealed to ensure pressure control from 10<sup>-3</sup> Torr up to atmospheric pressure. The essential parameters applied for obtaining CNOs was a laser wavelength of 248 nm, 25 ns pulse length and 10 Hz repetition rate. In addition, the pressure inside the reactor was fixed at 7 Torr, while the argon flow was kept at about 300 L/h. The plume resulting from the laser irradiation of the graphite target was 20-30 mm long and the ablation products condensed on a water-cooled cold finger (Figure 6).

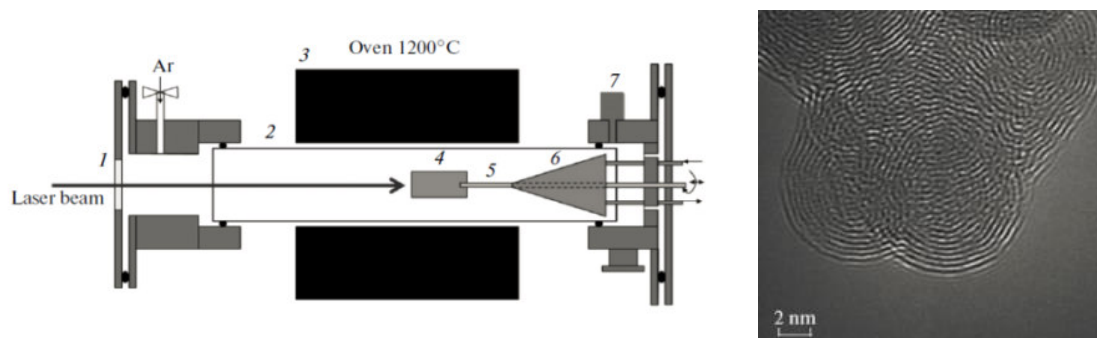


Figure 6. Scheme of the laser ablation chamber apparatus. Chamber schematics: 1-quartz laser window; 2-quartz tube; 3-electrical oven; 4-target; 5-graphite transfer rod; 6-cold finger; 7-vacuum gauge. Reprinted with permission from reference<sup>60</sup>. Copyright © 2014, Allerton Press, Inc.

HRTEM analysis of the collected deposits indicate that the diameter of the observed CNOs, formed by 10-20 shells with a hollow core (less than 5 nm), are typically in the range of 10 to 25 nm. The graphitic interlayer distance was estimated to be 0.35 nm and the interatomic distance in between the carbon atoms was found to be 0.24 nm as evidenced by the insets in Figure 7. In addition, no amorphous carbon was detected inside the concentric shell structure, thus it has to be underlined that pure carbon nano-unions have been obtained.

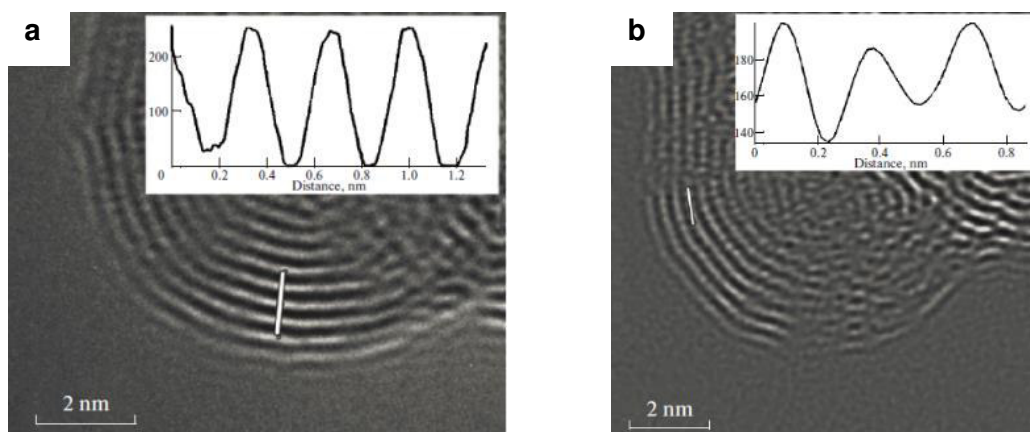


Figure 7. HRTEM images of the graphitic interlayer distance (a) and the interatomic distance (b) of CNOs. The results of the measurements are presented in the inset. Reprinted with permission from reference<sup>60</sup>. Copyright © 2014, Allerton Press, Inc.

#### 1.4.4 Radio-frequency plasma-enhanced Chemical Vapor Deposition (CVD)

After the discovery of carbon nano-onions, Chen and co-workers reported the synthesis of CNOs by radio-frequency plasma-enhanced chemical vapor deposition (CVD)<sup>61</sup>. This method allows for the synthesis of large quantities of carbon nano-onions by the deposition of methane over the surface of a Cobalt catalyst. The radio-frequency plasma-enhanced CVD process is somehow similar to the classical pyrolytic CVD process used for the growth of carbon fibers or carbon nanotubes, but the key difference is focused on the gas decomposition principle. Although, the pyrolytic CVD techniques use conventional Fe, Co, Ni and their alloys as catalysts, up to now, these methods have not produced any carbon onions. This method might not be suitable for the formation of pentagonal carbon rings, which are indispensable for curvature of the graphite sheet. In the case of radio-frequency plasma-enhanced CVD, initially the hydrocarbon is adsorbed at the surfaces of the catalytic particles and in the meantime, the process of glow discharge leads to CH<sub>4</sub> decomposition, resulting in the formation of carbon rings, which tend to nucleate on the surfaces of the catalyst. Furthermore, in the presence of atomic hydrogen in the plasma, free carbon valences on the ends of carbon layers can be stabilized by the formation of C-H bonds. Notably, the formation mechanism of CNOs described in this paragraph is absolutely different from the others discussed so far. The low temperatures required in the radio-frequency plasma-enhanced CVD underline the fact that CNOs can be fabricated without the help of high energy levels. Furthermore, the formation of many cages in successive stages from the core to the surface is essential to carbon nano-onion formation. The nucleus is a dome formed by one part of a C<sub>60</sub> molecule and only the growth of this dome by addition of hexagons and pentagons leads to the formation of a first cage. This first cage is the substrate on which further layers may nucleate and grow into a second, third, etc. spherical cage as shown in Figure 8. With the increase of cage surface area, the new secondary surface may involve pentagons, hexagons and heptagons which deposit with various degrees of epitaxial coherence, resulting in formation of wavy carbon sheets. The product

obtained by this method is pure and can be easily separated from the catalytic particles. In addition, the average size of these carbon nano-onions ranges from a few to several tens of nanometers<sup>61</sup>.

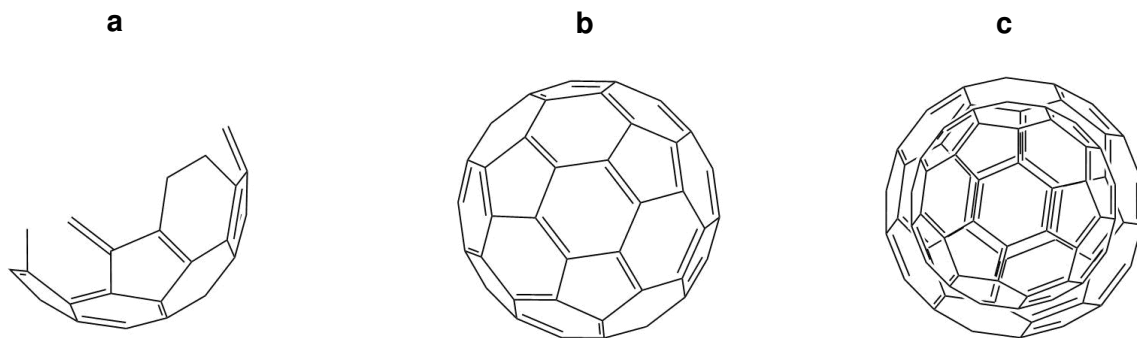


Figure 8. Scheme of the formation mechanism of onions by radio-frequency plasma-enhanced chemical vapor deposition. The formation of onions is based on the formation of many cages in successive stages from the core to the surface. (a) the nucleus is a dome formed by one cap of a  $C_{60}$  molecule; (b) the nucleus grows into a cage by the addition of hexagons and pentagons; (c) a second cage is nucleated on the first cage as substrate.<sup>61</sup>

It is important to underline that the core of carbon nano-onions fabricated by CVD can be either filled with metal, or remain completely empty. In the method described above, the catalyst is not encapsulated by carbon layers because the rings tend to nucleate on the surfaces of the catalyst. This is in agreement with the formation mechanism previously reported. However, modifications of this method lead to a different formation mechanism that results in the encapsulation of the catalyst in the shells. Li and co-workers have reported a novel method for the synthesis of CNOs via catalytic decomposition of methane over a Nickel catalyst supported on aluminum at  $600^{\circ}\text{C}$ <sup>62</sup>. The carbon nano-onions obtained consist of several concentric carbon layers with sizes ranging from 5 to 50 nm covering a nickel particle. When the nickel particle has a quasi-spherical structure, the graphite layers roll around the spherical particle and form a similar spherical carbon onion-like structure. When the nickel particle is a polyhedron the result is a polyhedral carbon onion-like construct (Figure 9). According to this, the growth of CNOs suggests a different formation mechanism where the CNOs form directly from the gas phase and the Ni particles act as catalyst inducing curvature in graphite layers, remaining trapped in the carbon shells.

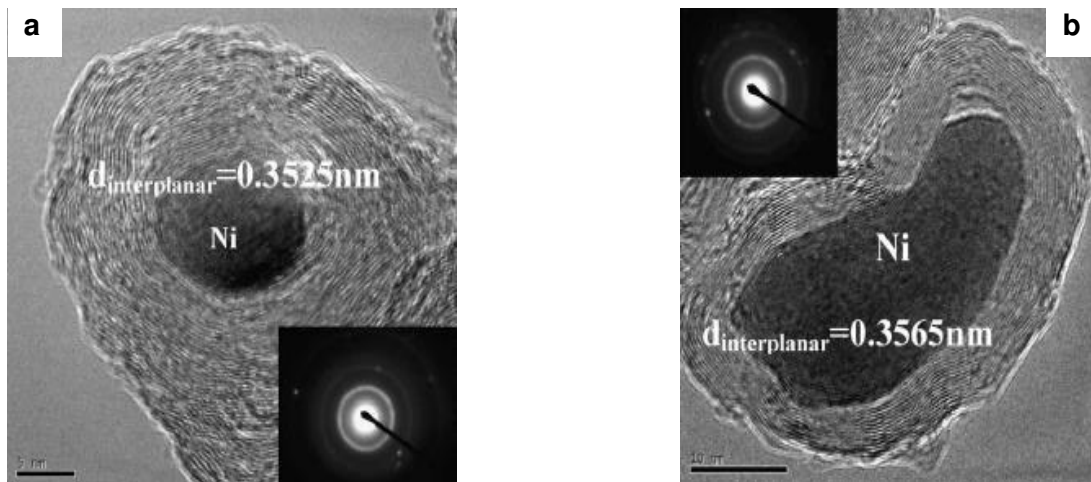
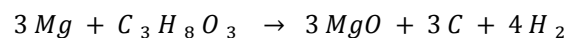


Figure 9. HRTEM images of onions synthesized by chemical vapor deposition using a Ni/Al catalyst. The images show that the shape of the carbon onions depends on the shape of the nickel particles. (a) quasi-spherical nickel particle leads to quasi-spherical carbon onions; (b) polyhedron nickel particle results in polyhedral carbon onions. Reprinted with permission from reference <sup>62</sup>.

#### 1.4.5 Other synthetic methods for CNOs fabrication

Other methods for the synthesis of carbon nano onions include catalytic synthesis using counterflow diffusion flames<sup>63</sup>, heavy shocking of polycrystalline silicon carbide powder, and assembly of aromatic molecules such as polymers<sup>64</sup>. These methods lead to carbon nano-onions with diameters around 60-80 nm. In 2005, Liu and co-workers reported the synthesis of CNOs via thermal reduction of glycerin with magnesium<sup>65</sup>. In this method, glycerin and magnesium were heated at 650°C during 12 hours resulting in the formation of carbon nano-onions with diameters ranging from 60 to 90 nm. The reaction can be expressed as the following equation:



Temperature plays an important role in the reaction, in fact under different other temperature conditions no CNOs have been observed.

Another research hotspot in the last years has been the fabrications of doped carbon materials with excellent physicochemical properties by using annealing treatment, CVD deposition and plasma etching. Chemical doping in carbon materials using heteroatoms (e.g. N, S, O and P) is a useful technique to modulate the intrinsic electronic characteristic, surface and local chemical features of the materials. In contrast to graphene, carbon nanotubes (CNTs) and carbon fibers (CNFs), carbon nano-onions (CNOs) have specific p and  $\pi$  electronic structures due to their high curvature. According to this, Lin and colleagues reported a systematic study on the preparation of boron-doped CNOs via a high temperature thermal treatment (1500-2400°C) starting from nanodiamonds in a graphite furnace<sup>66</sup> – see Figure 10.



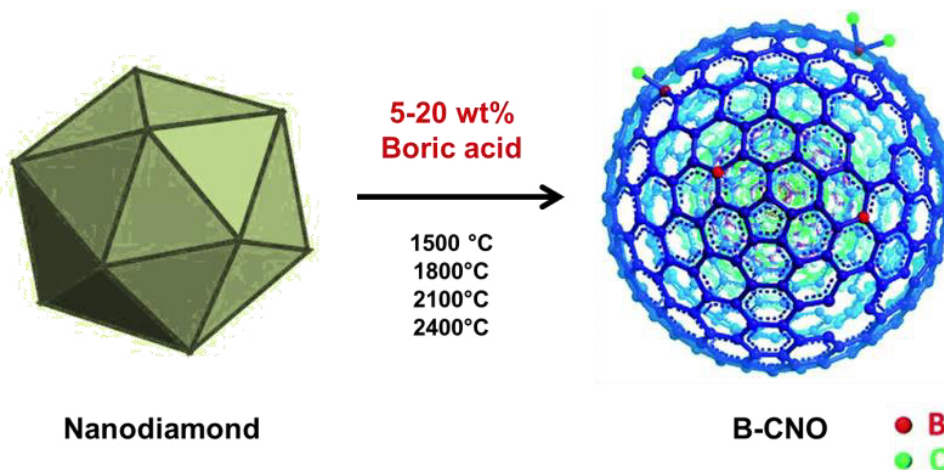


Figure 10. Schematic illustration for the fabrication of various Boron-doped carbon nano-onion samples (B-CNO) from ultra-disperse diamonds (UDD). Adapted from reference [66] with permission from The Royal Society of Chemistry.

The boron atom can be incorporated into carbon matrix because it has a comparable atomic size and three valence electrons for binding with carbon atoms. The formed B-C bond is longer than C-C bond (ca. 0.5%), leading to chemical disorder of the graphite layers, and to a p-type (or hole) doped carbon material. The results indicate that the incorporation of boron in CNOs can effectively change their electronic structure and properties. These novel boron doped CNO materials exhibit a higher catalytic activity than pristine CNOs for the oxygen reduction reaction (ORR), a very important pathway in energy conversion, corrosion and biosensing.

Among all the methods published in literature for the synthesis of CNOs, annealing of nanodiamonds and arc discharge under water of graphite electrodes offer reasonable amounts of pure CNOs although their sizes differ considerably. Current research has therefore been directed towards the selective synthesis of small CNOs with regular size. It is noteworthy that fullerene reactivity is partially dictated by the degree of surface strain: the higher the curvature, the greater the reactivity. Accordingly, small CNOs show an enhanced reactivity rather than large CNOs. This was demonstrated by Echegoyen et al. who studied the differences between carbon nano-onions obtained from annealing of nanodiamonds characterized by a smaller radii and consequently higher curvature and arcing graphite under water<sup>67</sup>. The different behaviour of these CNOs is described in the next paragraph.

## 1.3 Properties and characterization of CNO

Various methods for the synthesis of carbon nano-onions have been reported as described in the previous paragraph. Interestingly, the physicochemical properties of CNOs strictly depend on their synthetic pathways and different synthetic methods lead to CNOs of different size, shape and curvature, which are responsible for differences in the CNO's reactivity. The structure of the CNOs, the number of graphene layers and the distance between them, as well as the presence of defects, determine the physicochemical properties. Moreover, the structural and electrochemical characteristics of the nanostructures are important for their consequent functionalization and further application. As already stated in the previous chapter, since Ugarte increased the current in the electron microscopy for the first time and observed CNOs, two main preparative methods have been described in the literature. Kuznetov et al.<sup>5</sup> reported the production of pure CNOs in high yields by annealing carbon nanodiamond particles at temperatures above 1200°C and more recently, Sano et al.<sup>57</sup> described a method of producing CNOs that involves arching between two graphite electrodes under water. Remarkably, the carbon nano-onions obtained by both methodologies are rather different. The annealing of the ultradispersed nanodiamond particles (5 nm in average diameter) under vacuum produces mainly small CNOs with 6-8 shells and diameters of about 5nm. On the other hand, the arching of graphite under water leads to the formation of large CNOs with diameters in the range of 15-25 nm, what corresponds to 20-30 shells. Moreover, although the CNOs from both samples show interlayer distances of 0.34 nm, which corresponds to the distance between graphene sheets, it has been reported that CNOs obtained from nanodiamonds contain more defects than the CNOs obtained from arching<sup>68</sup>. According to this, a different behavior of the carbon nano-onions in terms of reactivity and subsequent functionalization is notable. In the following chapter, the analysis of the physical properties of CNOs with techniques such as NMR, Raman, TGA, EELS, and powder X-ray diffraction will be depicted. Briefly, thermogravimetric analyses of CNOs reveals a high thermal stability in air, even higher than that of C<sub>60</sub>. Electron energy loss spectroscopy (EELS) studies suggests the presence of  $\pi$  electrons. High-resolution magic-angle spinning (HR-MAS) solid-state NMR spectroscopy clearly show one peak positioned at 110 or 120 ppm. Such peaks are characteristic of sp<sup>2</sup> bonds and are usually observed for CNOs and graphite, respectively and are attributed to sp<sup>2</sup> carbon. The difference in the peak position may be related to the curvature of the onion shells causing changes in the angle of the carbon-carbon bonds<sup>68</sup>. The presence of a large number of sp<sup>2</sup>-hybridized carbon atoms, as observed in the NMR spectra, should render them susceptible to addition reactions. Furthermore, the Raman spectroscopic studies indicate that the CNOs obtained by thermal annealing (N-CNOs) have a larger number of surface defects than the CNOs obtained by arching (A-CNOs). Therefore, the earlier are expected to be more susceptible to reactions occurring at the defect sites on the surface than the latter. The N-CNOs with a higher degree of disorder along with the higher curvature of the surface are more reactive than the A-CNOs, even though the N-CNOs are thermodynamically more stable.

### 1.3.1 Raman Spectroscopy

Raman spectroscopy is a useful technique for exploring the structural properties and the behavior of various forms of carbon. In the case of carbon nano-onions, two broad peaks at about 1350 and 1580 cm<sup>-1</sup> can be detected on the spectrum<sup>55</sup>. The first Raman features, centered at 1350 cm<sup>-1</sup>, are attributed to the D band, which indicates the vibration of carbon atoms with dangling bonds. It is correlated with the disorder induced

in the structure due to the presence of  $sp^3$  carbons. The second observed Raman features at around  $1580\text{ cm}^{-1}$  are associated with the G band, which is attributed to the CNO's  $sp^2$  carbon network. This is the only band present in the Raman spectrum of single crystals of graphite. In addition, the intensity of the G band is related to the disorder within the carbon  $sp^2$  sheets. The intensity ratio of D to G band ( $I_D/I_G$ ) indicates the degree of the crystalline perfection. For instance, the absence of the D peak in highly oriented pyrolytic graphite (HOPG) implies perfect graphene planes. Thus, a very weak D peak and a strong G peak from carbon nano-onions indicate that only slight imperfections are present in the graphene planes of the onions.

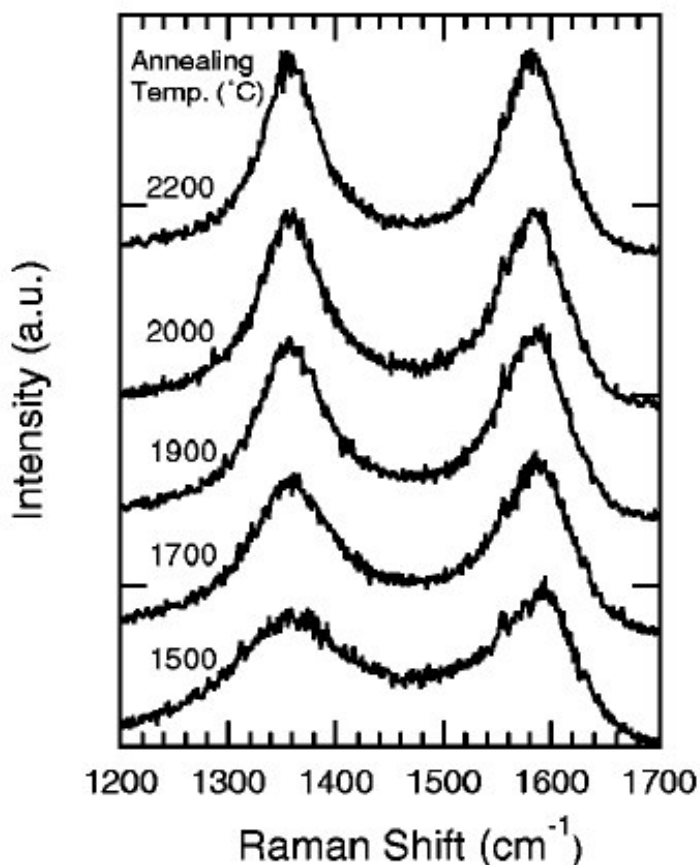


Figure 11. Raman spectra of CNOs obtained from annealing of nanodiamonds increasing the temperature from 1500 to 2200°C. Reprinted with permission from reference [55]. Copyright (2001), AIP Publishing LLC.

The band at about  $1580\text{ cm}^{-1}$  corresponds to the  $E_{2g}$  mode in the graphite structure of carbon (G band). It can be observed that the  $I_D/I_G$  decreases with increasing annealing temperatures (Figure 11). Furthermore, depending on the different properties of the CNOs, the Raman spectra of the CNOs obtained from annealing and from arching are slightly different, although both sources exhibit D and G bands. The D band appears at around  $1313\text{ cm}^{-1}$  and the G band at  $1581\text{ cm}^{-1}$  for the A-CNOs, while the corresponding bands appear at  $1307$  and  $1593\text{ cm}^{-1}$  for N-CNOs respectively. Moreover, the observed Raman features in the range of  $2500\text{--}3200\text{ cm}^{-1}$  are attributed to  $sp^3$  and  $sp$  carbon networks. Interestingly, the D/G ratio is 0.8 and 1.4 for A-CNOs and N-CNOs, respectively. This indicates that the outermost graphene sheet in the small N-CNOs contains

more defects than in the large A-CNOs. This is also confirmed from the full width at half maximum of the G band, which is broader for the N-CNOs than for the A-CNOs. Raman and TGA studies indicate that the structure of the N-CNOs is more defective and more thermodynamically stable than the structure of the A-CNOs. This is an example of defects leading to stability, presumably for entropic reasons<sup>69</sup>. Remarkably, the functionalization on the surface of the nanostructures correlates with the composition and the structure of the material. After oxidation, the Raman spectra of CNOs obtained from annealing of nanodiamonds shows a significant increase of the D/G ratio indicating an increase in the number of surface defects. In contrast, the oxidation on CNOs obtained from arching graphite under water, which are larger in diameter require more aggressive conditions such as the treatment with a 1:1 mixture of HNO<sub>3</sub> and H<sub>2</sub>SO<sub>4</sub> to increase the surface defects.

### 1.3.2 Thermochemistry

The formation of CNOs from nanodiamonds at high temperatures is related to the transformation of the (111) diamond planes to the (001) graphite planes. Accordingly, X-ray powder diffraction spectra confirms that the interlayer spacing of 0.21 nm, consistent with the *d* value of the (111) lattice plane of diamond with a cubic structure becomes of 0.34 nm close to the (001) planes of graphite after the annealing process<sup>68</sup>. Interestingly, the layers are formed when bending and closure of the graphitic sheets takes place by the formation of pentagons in the carbon network. The thermodynamic driving force of the transformation of nanodiamond to CNOs was attributed to a decrease of the surface energy due to the elimination of the surface dangling bonds in nanodiamond during heat treatment. However, the change in local carbon geometry from sp<sup>3</sup> to sp<sup>2</sup>, and other factors may also contribute. Costa and co-workers investigated the enthalpies of formation of CNOs at 25°C by high-temperature oxidation calorimetry<sup>69</sup>. It was found that CNOs are more stable than their fullerene counterparts. Furthermore, the stability of CNOs increases with surface area and functional groups. CNOs with oxygen containing functional groups can be considered partially oxidized, and therefore release less heat during complete oxidation to CO<sub>2</sub> and H<sub>2</sub>O. Therefore, such CNOs have a higher stability when being compared to CNOs free of functional groups. Additionally, not only the different synthetic pathways correlate with a difference in thermal stability, but also the cooling process after the formation of CNOs seems to play an important role. In air, N-CNOs show remarkably higher stability with a decomposition temperature around 700°C. In contrast, the larger A-CNOs show lower thermal stability and undergo decomposition at 500°C. The enhanced stability of the N-CNOs may be attributed to the fact that they were heated for 1 h (1650°C) and then subsequently cooled very slowly. The slow cooling process may allow for structural reorganization to a thermodynamically more stable structure. In contrast, the A-CNOs were rapidly cooled as they were produced in the surrounding solvent medium (water)<sup>68</sup>.

### 1.3.3 Textural properties and porosity

Although the original annealing procedure described by Kuznetsov et al. involved heating the nanodiamond particles under high vacuum<sup>69</sup>, recently Echegoyen and co-workers noticed that pure samples of onions with very high yield could also be obtained by using a slightly positive pressure of helium. Additionally, after annealing in an inert atmosphere, a second annealing was performed at 450°C in an air atmosphere to remove amorphous carbon after formation of the CNOs. The resulting CNOs are spherical-shell structures with six to eight graphitic layers and diameters of a few nanometers. These CNOs are very similar to the

CNOs obtained by the standard procedure proposed by Kuznetov, but the new procedure does not require the use of high-vacuum systems. To study the influence of the synthetic conditions on the resulting carbon nano-onion structure, modifications in the atmosphere and temperature conditions were performed. Basically, nanodiamonds were annealed at 1650 or 1750°C for 1 h under a He atmosphere and then the resulting CNOs were annealed at 450 or 750°C under an atmosphere of N<sub>2</sub>, CO<sub>2</sub> or air. In agreement with gas adsorption measurements, it was proven that annealing under different atmosphere altered the CNOs textural properties. The Brunauer-Emmett-Teller (BET) static nitrogen adsorption technique is a powerful tool to measure and analyze micro and mesoporus structures, the pore volumes as well as the specific surface area of nanostructures. Basically, annealing of CNOs at 1750°C and further additional annealing in air atmosphere led to more micropores and the total micropore area significantly increased (Table 1). Thus, during thermal annealing, the sp<sup>3</sup>-to-sp<sup>2</sup> conversion results in a decrease in density and an increase in pore volume and specific surface areas that occurs along with a loss of surface functional groups and volatile impurities.

**Table 1. Textural parameters of CNOs according to the N<sub>2</sub> adsorption/desorption isotherms**

Sample	$S_{\text{BET}}^{[a]}$ [m <sup>2</sup> g <sup>-1</sup> ]	Micropore Area [m <sup>2</sup> g <sup>-1</sup> ] <sup>[b]</sup>	Pore volume $V_p$ [cm <sup>3</sup> g <sup>-1</sup> ] <sup>[c]</sup>	Pore size [nm]
CNOs(1650)-N <sub>2</sub>	385	37.9	1.04	10.78
CNOs(1750)-N <sub>2</sub>	442	107.2	1.56	11.10
CNOs(1650)-AIR	488	116.3	1.56	12.79
CNOs(1750)-AIR	581	418.5	1.86	12.79
CNOs(1750)-CO <sub>2</sub>	399	20.3	1.19	11.96

[a]  $S_{\text{BET}}$ : BET specific surface area. [b] Based on the t-Plot method. [c] Single-point adsorption, total pore volume of the pores.

Table 1. Textural parameters of CNOs prepared under different atmosphere and temperature conditions according to the N<sub>2</sub> adsorption/desorption isotherms.<sup>70</sup>

### 1.3.4 Electronic properties of carbon nano-ions

A powerful tool for studying the electronic state of materials and nanostructures is the Electron energy-loss spectroscopy (EELS). Especially, the energy-loss near-edge structure (ELNES) in the core-loss spectrum is directly correlated to the density of the unoccupied conduction band states. The shape of the ELNES thus contains useful information about the nearest neighbor environment of atoms in covalent bonding. Chhowalla and co-workers studied the dielectric characteristics of carbon ions and polycrystalline graphite by measuring the low loss features in the electron energy loss spectra (EELS)<sup>71</sup>. The low loss EELS spectra for graphite and carbon ions are shown in Figure 12. The broad peaks at higher energies represent the plasmon energy from collective excitation of both  $\sigma$  and  $\pi$  valence electrons. However, the more important result is the position of the low energy peaks that arise from the collective plasmon excitation of the  $\pi$  electrons. The  $\pi$  plasmon for the carbon ions is centered at 5.7 eV ( $4.6 \mu\text{m}^{-1}$ ) compared to 6.6 eV for graphite. The origin of the absorption feature at  $4.6 \mu\text{m}^{-1}$  in carbon ions can be attributed to the collective excitations of  $\pi$  plasmons. Samples annealed in air show a constant absorption peak at  $4.6 \mu\text{m}^{-1}$  with a variable width ranging from  $1.2$ - $1.6 \mu\text{m}^{-1}$ . The substantial decrease in the widths for samples annealed for longer time is attributed to the elimination of amorphous carbon.

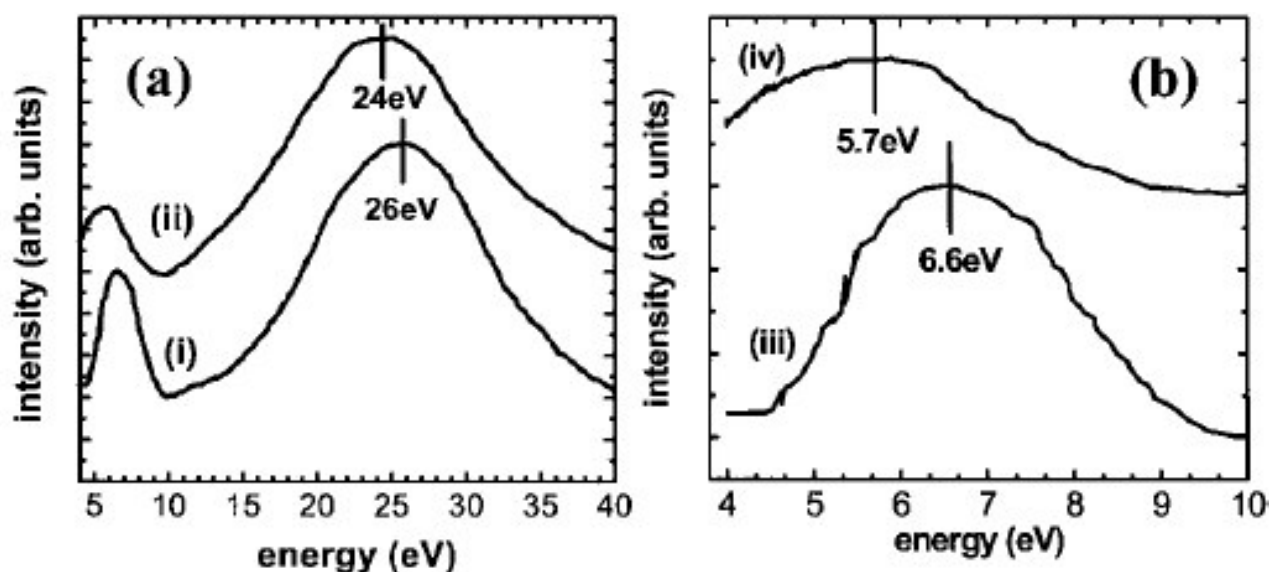


Figure 12. (a) Low loss region of EELS for (i) polycrystalline graphite and (ii) carbon ions. (b) Enlarged  $\pi$ -plasmon energy region. The  $\pi$ -plasmon of (iii) graphite is centered at 6.6 eV while the maximum of the (iv) carbon ion  $\pi$ -plasmon is located at 5.7 eV. Reprinted with permission from reference [71]. Copyright (2003), American Physical Society.

Tomita and co-workers studied the structure and the electronic properties of carbon onions depending on the annealing temperature<sup>72</sup>. HRTEM observation demonstrated that diamond nanoparticles are transformed into spherical carbon onions by the annealing at 1700°C, and finally into polyhedral onions above 1900°C.

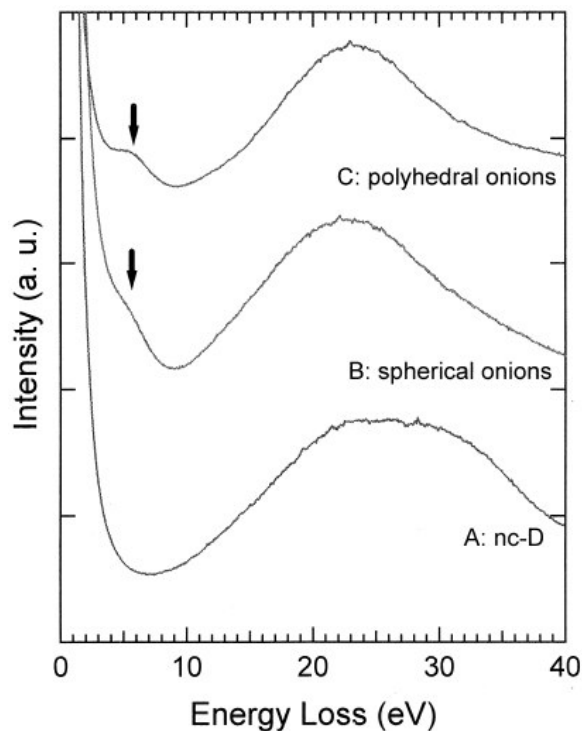


Figure 13. EELS spectra in low-loss region of 5 nm nanocrystalline diamonds (spectrum A), spherical carbon onions (spectrum B) and polyhedral carbon onions (spectrum C). Reprinted with permission from reference [72]. Copyright © 1999 Elsevier Science B.V. All rights reserved.

EELS studies suggested that the spherical onion consists of small domains of graphitic  $sp^2$  sheets with dangling bond defects in the peripheries suggesting the presence of  $\pi$  electrons. Interestingly, in spherical onions,  $\pi$  electrons are localized in the small domains and do not act as conduction electrons. On the other hand, in polyhedral onions, the further graphitization decreases the number of dangling bonds and leads to the delocalization of  $\pi$  electrons that act now as conduction electrons. Therefore, the core-loss spectrum results revealed that a number of  $sp^3$  bonds are contained in spherical carbon onions. It is plausible, that during the junction of (001) graphite planes with each other, a number of  $sp^3$  bonds remain in the spherical onion as interlayer bridges which link the (001) graphite planes. De Vita et al. theoretically performed the first-principles molecular dynamics simulations of a microscopic surface-induced diamond-to-graphite transition. Their simulation implied that, at an advanced state of the transition, there is an intermediate disordered state, where  $sp^3$  and  $sp^2$  bonds coexist;  $sp^3$  bonds are located at the periphery of graphitic  $sp^2$  sheets. In the transformation process from the diamond nanoparticle to the polyhedral onion, the spherical onion is an intermediate state as shown in Figure 13. Electron energy-loss spectroscopy (EELS) study indeed pointed out that the spherical onion contains a number of  $sp^3$  bonds in the structure<sup>72</sup>.  $Sp^3$  bonds at

the peripheries of graphitic  $sp^2$  sheets are seen to act as defects and may induce dangling bonds in the onions. That leads to imperfectly closed graphitic shells with a number of defects such as dangling bonds. Moreover, graphitization proceeds with increasing annealing temperature, and spherical onions are transformed into polyhedral ones. Tomita and co-workers suggested that the  $\pi$  electrons in spherical onions are localized in small domains of  $sp^2$  graphitic sheets and do not act as conduction electrons. On the contrary, polyhedral onions have ordered graphitic structure, and thus  $\pi$  electrons in them act as conduction electrons. Thus, spherical onions consists of small domains of the graphitic  $sp^2$  sheets with dangling bond defects in the peripheries.  $\pi$  electrons in spherical onions are thus localized in the small domains and do not act as conduction electrons. In the polyhedral onions, the graphitization proceeds further, resulting in the decrease in the number of dangling bonds and the localization of  $\pi$  electrons. As a result of the decrease in the number of defects,  $\pi$  electrons in polyhedral onions are delocalized and  $\pi$  electrons act as conduction electrons<sup>55</sup>.

### 1.3.5 Electrochemistry

It is well known that the electrochemical behavior of carbon nanostructures, especially their capacitance, is strictly dependent on the nature of the CNO surface.<sup>73</sup> The localized surface electrons, which are due to surface structural or chemical defects as well as the existence of localized  $\pi$  electrons on the interfacial graphite layers play an important role. Electrochemical studies indicate pseudorectangular cathodic and anodic profiles, that are typical for double-layer. No changes of the current were observed after prolonged potential cycling between -100 and + 500 mV (vs. Ag/AgCl). Therefore, the high degree of reversibility indicates that there are no chemical processes or other changes occurring between charge and discharge cycles. The rectangular cyclic voltammograms shapes observed for all the samples over a wide range of voltage scan rates (5, 10, 20, 50, 75 and 100 mVs<sup>-1</sup>) indicate a fast charge transport within the electrodes and electrical double layer capacitance (Figure 14). The voltammogram's shape remained almost undistorted upon increase of the scan rate, indicating excellent wetting and easy transport of ions within the films. Furthermore, the effect of the sweep rate on the CNOs' voltammograms was also studied.<sup>73</sup> These results indicate that the charge-discharge processes of the electrical double layer are highly reversible and kinetically facile. The difference between the observed capacitive current behavior for the different CNO samples is likely the result of more porous structures and more defects on the surface of the samples prepared under air and CO<sub>2</sub> atmospheres. Analysis of the specific capacitances demonstrated that the second modification slightly changes the electrochemical properties of the CNO films. Basically, it was found that annealing under air improved the penetration of the supporting electrolyte into the films and thus improved the electrochemical properties.<sup>73</sup>

Moreover, Echegoyen, Plonska-Brzezinska and co-workers studied the voltammetric behavior of CNOs functionalized with carboxylic groups<sup>74</sup>. It was reported that the functionalization of CNOs with carboxylic groups leads to a less porous and more uniform nanostructures in comparison to layers of unmodified material. Consequently, a difference in capacitance of functionalized and non-modified nano-onions can be detected. A lot of attention has been paid to the capacitive properties of thin films of carbon nanostructures due to their porous structures and large surface areas. These materials exhibit properties of typical double-layer capacitors, in which energy storage arises mainly from the separation of electronic and ionic charges at the interface between the electrode material and the electrolyte in solution. Thus, the chemistry of the



functional groups on the carbon nanostructures and the number of defects strongly affect the capacitive properties of the films. Moreover, the electronic properties on the CNO surface with carboxylic groups are responsible for a slower charge transfer process at negative potentials. Indeed, oxidized CNOs are electrochemically active at negative potentials due to carboxylic group reduction<sup>74</sup>.

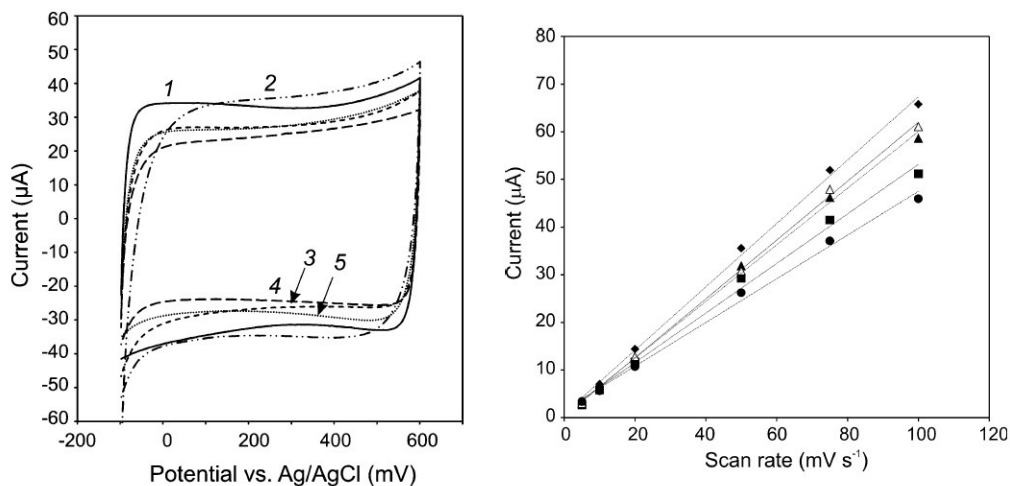


Figure 14. (A) Cyclic voltammograms of (1) CNOs(1650)-AIR, (2) CNOs(1750)-AIR, (3) CNOs(1650)-N2, (4) CNOs(1750)-N2, (5) CNOs(1650)-N2 in 0.1 mol L<sup>-1</sup> NaCl. The sweep rate is 5 mV s<sup>-1</sup>. (B) Dependence of the capacitive current on the sweep rate. Reprinted with permission from reference[75].

## 1.4 CNOs – Toxicological aspects

In the last few years, our group intensively explored the toxicological aspects of CNOs for biological applications. Giordani's results shown that a carefully designed functionalization strategy is crucial to modulate the inflammatory response. The size of the nanostructure also seems to play a key role. Most studies concerned with inflammatory properties of carbon nanotubes were carried out using raw non-functionalized nanotubes. However, this raw materials are generally impure and contain amounts of carbonaceous impurities, metal catalyst residues and microbial contaminants that are highly probable responsible of a variety of deleterious effects previously attributed to CNTs such as granulomatous inflammation, release of cytosolic enzymes and pulmonary fibrosis. In 2013, Giordani et al. reported a comprehensive *in vitro* and *in vivo* analysis of the inflammatory potential induced by purified and functionalized CNOs. Pristine carbon nano-onions (p-CNOs) were synthesized by thermal annealing of d-NDs followed by air annealing to ensure high-purity. Successively, they were functionalized, as confirmed by Raman and FT-IR spectroscopies, following the one-pot Tour reaction previously reported<sup>76,77</sup> and then coupled with a fluoresceinamine by amide reaction in order to allow for the *In vitro* visualization. To evaluate the ability of macrophages (Macs) to internalize SWCNTs and CNOs, immortalized bone-marrow derived mouse macrophages (iBMM) and mouse bone-marrow-derived dendritic cells (BMDCs) were incubated in the presence of the fluorescein-labeled nanoparticles. The results showed the internalization of carbon nanoparticles (NPs). We also studied the ability of p-CNOs to induce activation and maturation of dendritic cells (DCs); the results showed no distinguishable effect on the expression of the different cell surface markers tested, no induced secretion of the inflammatory cytokines along with a negligible alteration of the secretion of the inflammatory cytokines. They further demonstrated the ability of these NPs to promote the release of the inflammatory cytokines IL-1  $\beta$  by BMDCs in the presence of TLR ligands and to induce the activation of the NLRP3 inflammasome. CNOs exhibited a weaker inflammatory potential compared to SWCNTs, both *in vitro* and *in vivo*. CNOs were taken up by antigen-presenting cells to a greater extent and were more efficiently targeted to draining lymph nodes. They also investigated the impact of the chemical functionalization on the inflammatory properties, showing that the functionalization significantly reduces the release of IL-1  $\beta$  both *in vitro* and *in vivo*<sup>78</sup>. With the aim of developing an efficient nanoprobe suitable for both imaging and targeting, the Giordani group reported the multiple covalent functionalization of CNOs with fluorescein and folic acid to simultaneously image and target cancer cells.<sup>79</sup> Nanomaterials decorated with folic acid showed high specificity due to the ability to bind the receptors highly overexpressed by cancer cells. p-CNOs were modified by diazonium chemistry to yield benz-CNOs bearing carboxylic acid groups and to produce silyl-CNOs, which display alkyne functionalities on the surface. After the deprotection of the silyl group from the phenylacetylene, multi-functionalized CNOs (benz-alkyne/CNOs), which contain benzoic acid and phenylacetylene groups, were produced. The success of the double step functionalization procedure was confirmed by XPS, Raman spectroscopy as well as by FT-IR spectroscopy. The preparation of the CNOs bearing both targeting and imaging agents was accomplished by two consecutive synthetic procedures from benzalkyne/CNO derivatives. The folic acid derivative (FA-PEG) was introduced by the condensation reaction of a primary amine with the benzoic acid unit on the CNOs to produce FA-CNOs and then the attachment of fluorescein derivative (FITC-PEG) was accomplished by a copper catalysed azide-alkyne Huisgen cycloaddition (CuAAC) onto the alkyne functionalities, producing the dual functionalized FA-FITC/CNOs derivatives.

To investigate the possible effects induced by the different CNOs conjugates, HeLa (epithelial cervix adenocarcinoma) and KB cells (human epidermoid carcinoma cells), were incubated with different concentrations of benz-CNOs, FA-FITC/CNOs and FITC-CNOs derivatives; low cytotoxicity was exerted in both cell lines. The localization of FA-FITC/CNOs and FITC-CNOs in HeLa and KB cells, were studied by confocal microscopy. No apoptotic effect was observed in HeLa cells, after incubation with FA-FITC/CNOs for 24 h. The fluorescent nanoparticles were efficiently internalized and localized into lysosomal compartments, as demonstrated from the intense yellow co-localization signals. For comparison, FITCCNOs conjugates were also internalized by HeLa cells, but to a lower extend. In order to understand the mechanism for the cellular internalization of CNOs, correlative light electron microscopy (CLEM) analyses were performed in HeLa cells, confirming an endocytosis pathway for the uptake. TEM analysis of the subcellular regions revealed the presence of large aggregates inside late-endosome/lysosome vesicles (Figure 15). Confocal images of KB cells confirmed the internalization of FA-FITC/CNOs and the localization in vesicles; furthermore, the presence of free folic acid in solution results in minimal internalization of the FA-FITC/CNOs as a consequence of the competition for the folate receptors on the cell membranes. These evidences suggested an uptake based on a folate mediated endocytosis pathway. In comparison, KB cells incubated with FITC-CNOs showed a low green signal, which became more intense after a prolonged exposition. This evidence was also observed for the HeLa cells, suggesting a non-specific adsorption of FITC-CNOs on the cell membrane after long time of incubation.<sup>79</sup>

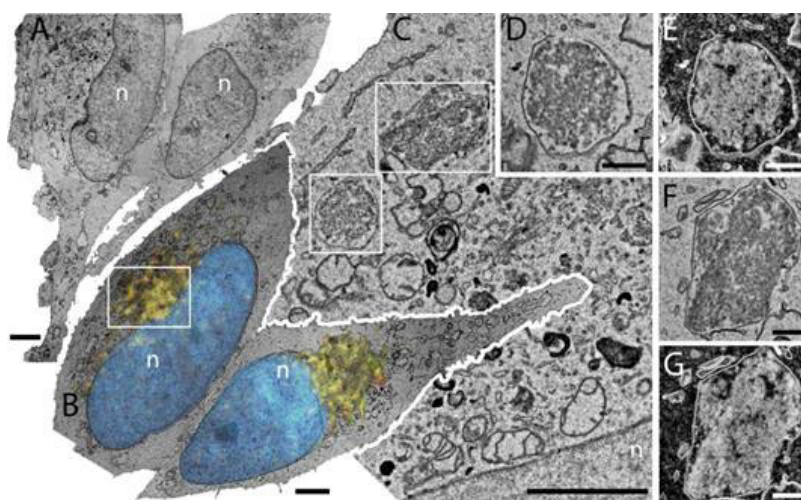


Figure 15. Correlative light electron microscopy analysis of HeLa cells doped with  $10 \mu\text{g mL}^{-1}$  of FA-FITC/CNOs for 12 h at  $37 \text{ }^\circ\text{C}$ . A) Low magnification TEM reconstruction of two cells doped with FA-FITC/CNOs. B) Superimposed fluorescence and TEM reconstruction of the same cells shown in A (imaged in a different section). The co-localization of FA-FITC/CNOs (green fluorescence) within lysosomes stained with Lysotracker (red) results in yellow fluorescence. C) Higher magnification TEM image of the boxed area in B. Note, the two endosomes containing FA-FITC/CNOs. D–G) Higher magnification images of the boxed areas from C imaged, respectively, in defocused TEM (D, F) and in high angular annular dark field (HAADF) scanning TEM (E, G). The nuclei are labeled with “n”. Scale bars: A, B) 4  $\mu\text{m}$ , C) 2.5  $\mu\text{m}$ , D–G) 0.5  $\mu\text{m}$ . Reprinted with permission from [79]. Copyright 2015 John Wiley and Sons. (For interpretation of the references to colour in this figure legend, the reader is referred to the web version of this article.)

They also investigated the capabilities of boron dipyrromethene (BODIPY) functionalized CNOs as imaging agent in human breast cancer cells (MCF-7).<sup>80</sup> After the incubation with benz- and BODIPY-CNOs at different concentration, cellular viability tests were performed and no cytotoxic effects were observed up to 72 h. Furthermore, confocal microscopy showed that BODIPY-CNOs were efficiently internalized by the cells and located predominantly in the lysosomes, as confirmed by the yellow co-localization signals (Figure 16)

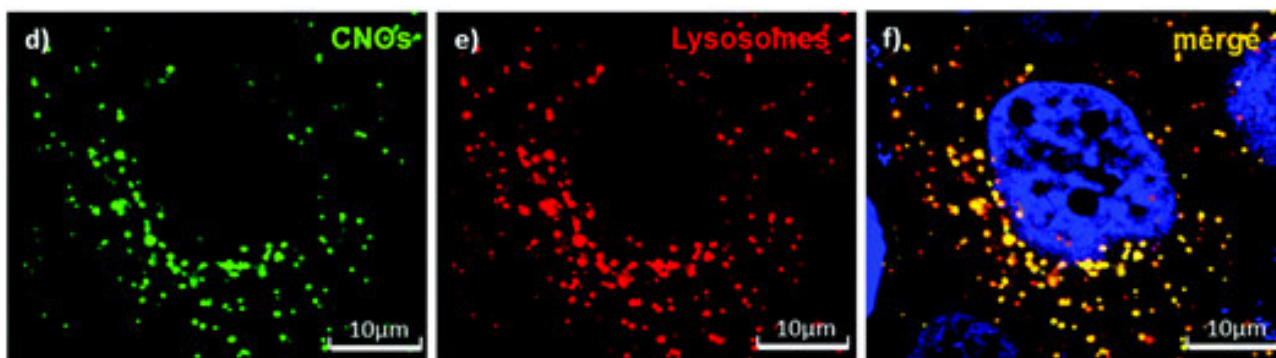


Figure 16. BODIPY functionalized CNOs (BODIPY-CNOs): structure (A) and confocal images of MCF-7 cells incubated for 48 h with 10 lg/mL BODIPY-CNOs (B). Adapted with permission from [80]. Copyright 2014 The Royal Society of Chemistry.

Once the *In vitro* studies on different cell lines was evaluated, long term effects on more complex vertebrate systems were consequently assessed. In 2015 the ecotoxicological effects of CNOs were investigated by using the fresh-water polyp *Hydra vulgaris* as model organism<sup>81</sup>. The eco-toxicological effects of pristine and functionalized CNOs on the morphology, reproductive and regenerative capabilities of freshwater polyp *Hydra vulgaris* were investigated. p-CNOs were decorated with different functionalities, including benzoic acid (benz-CNO), pyridine (py-CNO) and methylpyridinium (py<sup>+</sup>-CNO). *In vivo* uptake and biodistribution studies were conducted after exposing *Hydra vulgaris* to both pristine and modified CNOs at different concentrations. All CNO types were efficiently internalized, with aggregates visible in the body, head and tentacles of animals as small dark spots (Figure 17); furthermore, by dissociating treated animals into single cell suspensions, CNO nanoparticles were found to be located within the cytoplasm. Finally, more interestingly, no behavioral or morphological alterations were observed. The long-term effects on the regenerative and reproductive capabilities of polyps treated with CNOs were estimated. No significant difference in the regenerative potential and the growth rates of treated and polyps were observed in comparison to the controls, suggesting that CNOs did not affect the regeneration efficiency along with the absence of toxic effects over a long time scale. Finally, the effects of CNO exposure on apoptosis were studied after macerating CNO-treated *Hydra* into a single-cell suspension; moreover, the nuclear morphology was monitored by fluorescence microscopy. All CNOs showed no significant adverse effects, except for a slightly increase of the apoptosis rate of *Hydra* cells treated with benz-CNOs<sup>81</sup>.

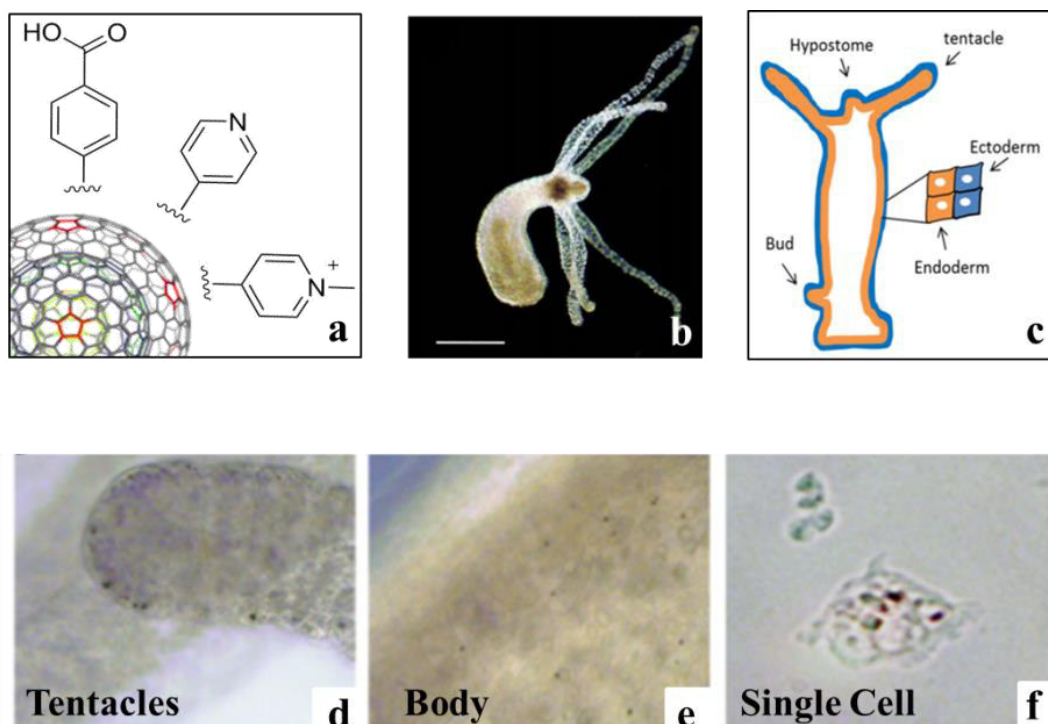


Figure 17. Toxicological studies of CNOs on the development and the reproductive capability of *Hydra vulgaris* polyp. (a) Chemical functionalization of CNOs with benzoic acid, pyridine and pyridinium moieties; (b,c) Structural anatomy of *Hydra vulgaris*. Scale bar, 500  $\mu\text{m}$ . *In vivo* uptake and biodistribution of CNOs in tentacles (d) and body columns (e). Representative single cells obtained by polyps treated with pyridine-CNOs (f) Adapted with permission from [81].

Recently, the Giordani group reported the first study on the biological impact of CNOs on vertebrates<sup>82</sup>, investigating the possible toxic effects induced by functionalized CNOs on zebrafish (*Danio Rerio*) during the development. Zebrafish embryos and larvae were exposed at different concentrations of benz-CNOs and BODIPY-CNOs, and several toxicological aspects were investigated. Their results showed that CNOs derivatives did not affect the survival and hatching rates of treated zebrafish embryo/larvae up to  $10 \mu\text{g mL}^{-1}$ , whereas a significant difference compared with the negative control ( $p < 0.01$ ) was observed at higher concentration ( $50$  and  $100 \mu\text{g mL}^{-1}$ ); however, according to the OECD methodology, CNOs conjugates are evaluated as a nontoxic nanomaterial. The heart beat rate and frequency of movements in zebrafish larvae at 72 hpf were found to be comparable with that of the control group. Moreover, CNOs did not exert significant adverse effects on the zebrafish organogenesis. In contrast with the results reported for zebrafish treated with other CNMs<sup>83, 84</sup>, CNOs showed a good biocompatibility in this small vertebrate. The *in vivo* biodistribution of BODIPY-CNOs inside the zebrafish larvae was studied by means of inverted selective plane illumination microscopy (iSPIM) (Figure 18). The results showed a homogeneous distribution of the CNOs in the whole zebrafish larvae body<sup>82</sup>.

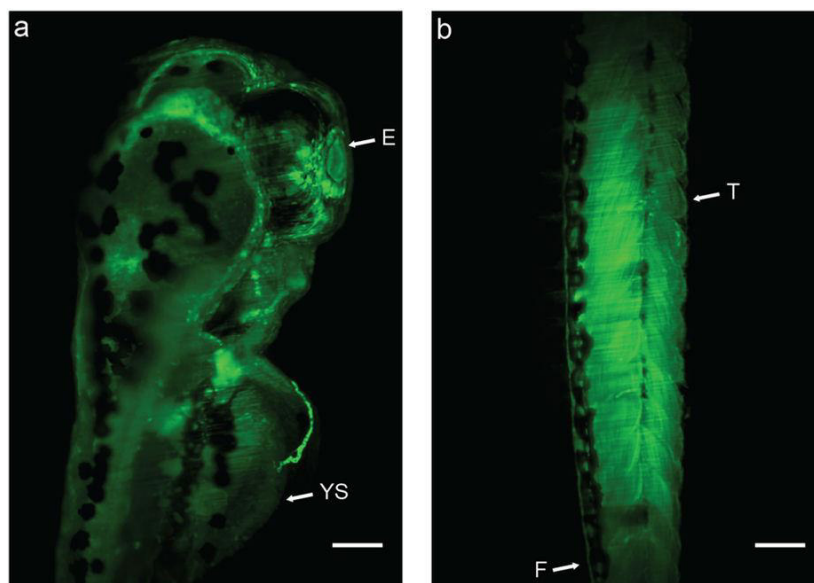


Figure 18. Maximum intensity projections of the superior part (a) and tail (b) of treated larvae ( $100 \mu\text{g mL}^{-1}$  of BODIPY-CNOs. Exposure time: 200 ms, step size:  $0.7 \mu\text{m}$ . Scale bars,  $100 \mu\text{m}$ . E, eye; YS, yolk sac; T, tail; F, finfold. Reprinted with permission from [82].

The published results let us believe that especially highly surface functionalized, small diameter CNOs are promising materials for biological and medicinal applications based on a high biocompatibility. The surface modification with different functional groups and the further conjugation with other functional molecules such as fluorophores, revealed an enhancement of water solubility and biocompatibility along with an enhanced cell penetration capability. Furthermore, *in vitro* and *in vivo* experiments demonstrated particular and promising features such as low cytotoxicity and weak inflammatory potential, confirming the ability of CNOs as imaging and targeting agents. The effects on living systems and, especially, on the human health are of utmost importance in the perspective of biological and biomedical applications and many efforts have yet to be done for a real use of a CNO-based platform in nanomedicine. However, the highly promising properties showed until now are expected to open novel avenues for the development of safe, non-toxic and effective nanomedicine technologies where CNOs could act as shuttle for the delivery of biomedically relevant drugs.

## 1.5 Nanotechnology in biomedicine

Nanotechnology has demonstrated great potential to improve cancer treatments by affecting the ways in which cancer is diagnosed, prevented, and treated.<sup>85,86,87,88</sup> In particular, targeted drug delivery using nanoscale carriers holds great promise to substantially improve therapeutic indices (the ratio between the toxic dose and the therapeutic dose of a drug) of incorporated drug molecules; in fact, a number of them are currently under advanced-stage clinical trials or are being used in clinical settings.<sup>89</sup> However, the physicochemical properties of the nanoparticles (chemical compositions, sizes, shapes, structures, morphologies, and surface properties) need to be finely tuned to develop an effective NP system and to

understand the interactions that occur between the nanomaterials and biological systems at each stage of the drug delivery process (Figure 19).

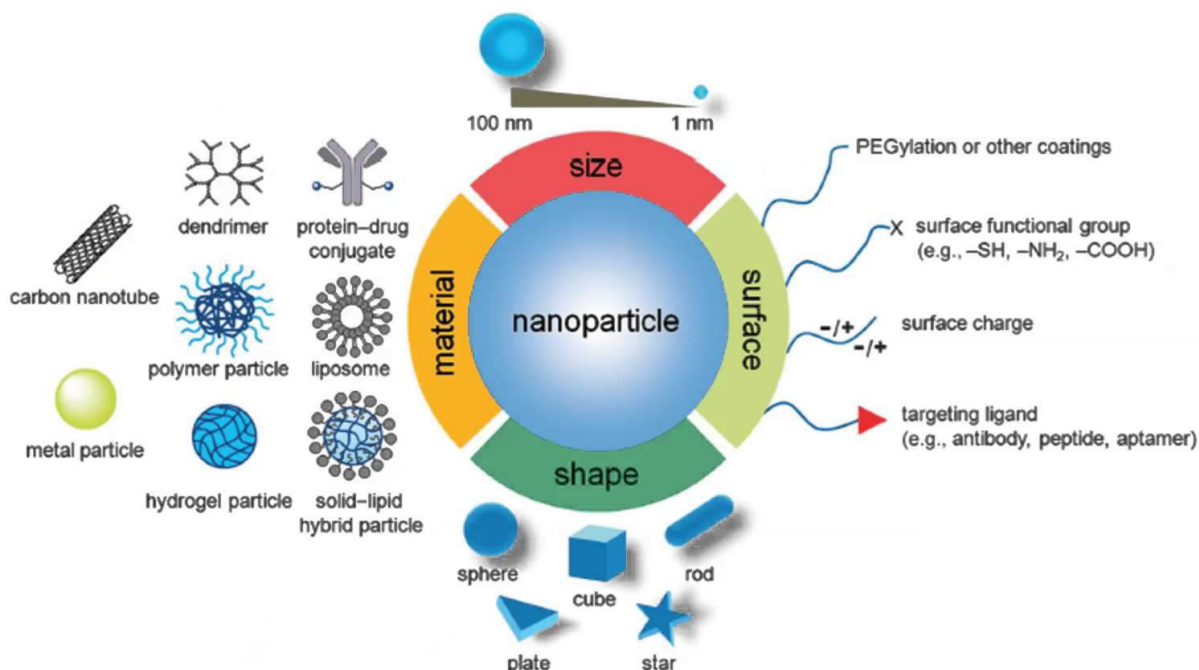


Figure 19. A summary of nanoparticles that have been explored as carriers for drug delivery in cancer therapy, together with illustrations of biophysicochemical properties. Reprinted with permission from [89].

### 1.5.1 Size and Shape

The size and shape, as well as the uniformity, are two important parameters of a drug-delivery system based on nanoparticles, as they determine the *in vivo* distribution, toxicity, and targeting ability.<sup>90</sup> Additionally, they can influence drug loading, drug release, and *in vitro* and *in vivo* stability. For example, smaller particles have a greater risk of aggregation during storage and incubation *in vitro*, but typically have a longer circulation half-life *in vivo*. The degradation of polymer nanoparticles can be strongly affected by their size as a result of water availability and removal of degradation products. Many studies have demonstrated that nanoparticles have a number of advantages over their micrometer-sized counterparts with sizes in the range of 0.1–100 nm for drug-delivery applications.<sup>91</sup> Generally, nanoparticles have relatively higher intracellular uptake and broader availability to a range of biological targets owing to their small sizes and increased mobility.

### 1.5.2 Surface Properties

In addition to both size and shape, the surface characteristics of nanoparticles represent another critical parameter in determining their drug-loading efficiency and release profile, circulation half-life, tumor targeting, and clearance from the body. Ideally, the nanoparticles should have a hydrophilic surface to resist the adsorption of plasma proteins and thus escape the uptake by macrophages.<sup>92</sup> This can be achieved in two ways: coating the surface of nanoparticles with a hydrophilic polymer such as PEG, or directly fabricating nanoparticles from block copolymers containing both hydrophilic and hydrophobic segments. Studies by Elsabahy and Wooley suggested that the surface chemistry of nanoparticles can greatly impact their toxicity,

immunogenicity, and biodistribution; excess positive charges tend to result in rapid opsonization and clearance.<sup>93</sup>

### **1.5.3 Surface Charges**

The zeta potential of a nanoparticle is commonly used to characterize its surface charge. This variable reflects the electrostatic potential of a particle and is influenced by the composition of the particle as well as the medium in which the nanoparticle is suspended. Nanoparticles with a zeta potential above 30 mV (either positive or negative) have been shown to be stable in suspensions, as repulsion forces originating from the surface charges can prevent the particles from aggregation. Additionally, the inner surface of blood vessels and the surfaces of cells contain various types of negatively charged species, which repel negatively charged nanoparticles. When the surface charge of nanoparticles becomes higher (either positive or negative), they will become more easily scavenged by macrophages, resulting in greater clearance by the MPS. Therefore, control over the surface charge can help minimize the nonspecific interactions between nanoparticles and the MPS, preventing the loss of nanoparticles in undesired locations.<sup>94</sup> Complete exclusion of nonspecific interactions, however, is currently unattainable.

### **1.5.4 PEGylation**

In order to increase the tumor targeting efficiency, it is necessary to prolong the circulation of nanoparticles in the bloodstream by minimizing opsonization. The most commonly used approach to achieve this goal is to coat the surface of nanoparticles with a hydrophilic brush made of PEG chains.<sup>90</sup> Studies have shown that the conformation of PEG on the nanoparticles surface is of the utmost importance in repelling opsonins. While PEG coatings with a brush-like configuration reduce phagocytosis and complement activation, those in a mushroom-like configuration are potent complement activators to induce phagocytosis.<sup>92</sup> Since the initial use of PEG in extending the circulation half-life of a protein,<sup>95</sup> PEGylation has been widely adopted to protect nanoparticles such as liposomes,<sup>96</sup> polymer nanoparticles and micelles<sup>97</sup> from premature clearance during circulation. The PEG chains form a hydrated shell that allows the nanoparticle to evade opsonization and subsequent phagocytosis.<sup>98</sup> However, this protective shell can interfere with the interactions between a nanoparticle and the target cell.<sup>99</sup> For example, PEGylated liposomal doxorubicin showed a prolonged plasma half-life, which is believed to correlate with better therapeutic efficacy. However, the formulation resulted in lower tumor accumulation than the same liposomes with no PEG coating, indicating a counterproductive effect of PEGylation.<sup>100</sup>

### **1.5.5 Polysaccharides**

As a major class of natural polymers, polysaccharides have been widely used in drug delivery and tissue engineering because of their good biocompatibility, availability, and easy modification.<sup>101</sup> As a result of their capability to avoid the complement system and opsonization, some polysaccharides, such as dextran and heparin, have also been recognized as stealth-coating materials. Some studies have shown that the polysaccharides, such as chitosan and hyaluronic acid, even display certain ligand activities of their own. Nanoparticles coated with these polysaccharides show more efficient cellular uptake than other nanoparticles because of specific interactions with various receptors on the surface of target cells.<sup>102</sup>



Therefore, polysaccharides have gained increasing interest in the development of nanomedicine as an effective surface modification strategy. Nanoparticles incorporating polysaccharides can be prepared using many different methods, which have been extensively reviewed.<sup>103</sup> Polysaccharides can be applied as surface coatings on nanoparticles through electrostatic interactions or directly incorporated into the nanoparticles during synthesis. Alternatively, hydrophilic polysaccharides can be grafted to hydrophobic molecules, such as cholesterol, and then used to form nanoparticles through self-assembly, which can also encapsulate hydrophobic drugs in the core. Furthermore, nanoparticles can be prepared through conjugation of polysaccharides to synthetic polymers.

### 1.5.6 Conjugation with Targeting Ligands

Many techniques and tools are currently available to armor nanoparticles for active targeting of cancerous cells. Traditionally, monoclonal antibodies have been used to target epitopes on the surface of cells, but the extensive screening of peptide and aptamer libraries has greatly expanded the repertoire of ligands available for targeted delivery.<sup>85</sup> The currently used targeting ligands include antibodies, antibody fragments, peptides (e.g., RGD for  $\alpha_v\beta_3$  integrin), aptamers (e.g., those for prostate-specific membrane antigen and VEGF), oligosaccharides, and even small molecules (folate and SV-119), as long as they can specifically recognize and bind to an overexpressed target on the cell surface. Here we only provide a brief discussion on these ligands:

1) Monoclonal antibodies (MAbs) are macromolecules widely used as targeting ligands because of their immediate availability and their high affinity and specificity for molecular targets. These ligands usually possess a molecular weight of approximately 150 kDa and exhibit high binding affinities. To date, MAbs have been conjugated to essentially all different types of nanoparticles, such as SPIONs,<sup>103</sup> QDs,<sup>104</sup> liposome,<sup>105</sup> and Au nanocages,<sup>106</sup> to give them site-specific targeting ability. However, the bulky size and redundant constant region may cause some major issues in the use of MAbs as targeting ligands because of their immunogenicity and size increase (i.e., the overall size of nanoparticles will dramatically increase). The use of antibody fragments, affibodies, and peptides may help overcome this shortcoming.

2) Single-chain variable fragments (scFv) are fusion proteins of the variable regions of the heavy and light chains of an antibody (VH and VL) connected with a short linker peptide of 10–25 amino acids. The molecular weight of an scFv is about 27 kDa. By engineering the MAbs to cut down the redundant parts of the scFv, the size and immunogenicity of the original antibody can be largely reduced.

3) Affibodies are small, stable Z-domain scaffolds consisting of 58 amino acids and derived from the IgG binding domain of staphylococcal protein A. The binding pocket is composed of 13 amino acids and is able to bind to a variety of targets, depending on the randomization of the amino acids. In contrast with IgGs, the small size (6–15 kDa) of affibodies enables penetration into tumor tissue. Affibodies possess a high receptor affinity, which mimics the active portion of the Fab region of the corresponding antibody. Their short plasma half-life makes them good candidates as tumor imaging probes, but less ideal for tumor targeting, where long circulation half-life is required.<sup>107</sup>

4) Peptides represent a viable targeting moiety with several advantageous characteristics, including low molecular weight (ca. 1 kDa), tissue penetration capability, lack of immunogenicity, ease of production, and relative flexibility in chemical conjugation processes.<sup>107</sup> Various peptides that can recognize cancer-specific epitopes overexpressed on tumor cells and vasculature have been used as targeting moieties for drugs and

drug carriers. For example, RGD peptides showed a high affinity in binding toward integrin, which are typically overexpressed by the endothelium during tumor angiogenesis. By conjugating RGD to the surface of SPIONs, the nanoparticles showed superior targeting affinity and specificity.<sup>108</sup> One possible disadvantage is that peptides sometimes exhibit a lower binding affinity to receptors as compared to MAbs, but this can be compensated by increasing the coverage density of peptides.

5) Aptamers are short, single-stranded, synthetic nucleic acid oligomers, DNA or RNA, that can form complex three-dimensional structures with a capability to bind to surface markers with high affinity and specificity.<sup>109</sup> Advantages of aptamers include availability, ease of chemical synthesis, low molecular weight, and lack of immunogenicity. Many publications have reported the conjugation of aptamers to polymer nanoparticles as targeting ligands.<sup>109</sup>

6) Endogenous ligands, such as folic acid, epidermal growth factor (EGF), and transferrin, are attractive for tumor targeting because they can bind to their respective receptors with low immunogenicity and high affinity. Several protocols have been reported to conjugate folic acid, EGF,<sup>110</sup> and transferrin<sup>111</sup> to various types of nanoparticles. In summary, the choice of a targeting ligand revolves around numerous considerations, including availability, easiness of production, diversity, affinity and protocols for conjugation and immunogenicity.

### 1.5.7 Drug Loading

Theoretically, a successful drug-delivery system based on nanoparticles should have a high drug-loading capacity to minimize the quantity of materials needed for administration. Loading of drug molecules into the nanoparticles can be achieved in different ways such as chemical surface functionalization, incorporation at the time of nanoparticle formation or absorption (as well as adsorption) of the drug after the formation of nanoparticles by incubating them with a highly concentrated drug solution. The efficiency of drug loading onto a nanoparticle is determined by the properties of both the drug molecules and the carrier material. The properties of the material include its molecular weight, polymer composition, drug-polymer interaction, and the functional groups (e.g., carboxy or ester) at both ends of each polymer chain.<sup>112</sup> A macromolecule or protein has the greatest loading efficiency when the drug loading is performed at or near its isoelectric point, which gives it the minimum solubility and maximum absorption. For small molecules, the use of electrostatic interactions between the drug and matrix material is an effective way to increase the drug-loading efficiency.<sup>113</sup>

## 1.6 Conclusion

A number of such delivery systems have been approved for cancer therapy in the clinics, with many more currently under clinical trials or preclinical evaluations (see Table 2 for a list). Nanoparticle-based therapeutics are poised to significantly improve the treatment outcomes for oncological diseases, promising to reshape the landscape of the pharmaceutical industry.<sup>114</sup>

Table 2. Delivery systems approved for cancer therapy in clinics.

Trade name	Formulation	Drug	Company	Application	Phase of development
<b>Abraxane</b>	albumin-bound nanoparticle	paclitaxel	Abraxis Bioscience, Inc.	metastatic breast cancer <sup>115</sup>	approved
<b>Caelyx</b>	PEGylated liposome	doxorubicin	Schering-Plough	metastatic breast and ovarian cancer, Kaposi sarcoma <sup>116</sup>	approved
<b>DaunoXome</b>	liposome	daunorubicin	Galen Ltd	Kaposi sarcoma <sup>117</sup>	approved
<b>DepoCyt</b>	liposome	cytarabine	Pacira Pharmaceuticals, Inc.	lymphoma <sup>118</sup>	approved
<b>Doxil Kaposi</b>	liposome	doxorubicin	Sequus Pharmaceuticals, Inc.	sarcoma <sup>119</sup>	approved
<b>Genexol-PM</b>	polymeric micellar nanoparticle	paclitaxel	Samyang Biopharmaceuticals	breast cancer <sup>120</sup>	approved
<b>Marqibo</b>	liposome	vincristine sulfate	Talon Therapeutics, Inc.	lymphoblastic leukemia <sup>121</sup>	approved
<b>Myocet</b>	liposome	doxorubicin	Zeneus Pharma Ltd	metastatic breast cancer <sup>122</sup>	approved
<b>Oncaspar</b>	PEGylated asparaginase	Enzon Pharmaceuticals, Inc.	Enzon Pharmaceuticals, Inc.	acute lymphoblastic leukemia <sup>123</sup>	approved
<b>Zinostatin</b>	stimalamer poly(styrene-co-maleic acid)-conjugated neocarzinostatin	neocarzinostatin	Astellas Pharma, Inc.	hepatocellular carcinoma <sup>124</sup>	approved
<b>CYT-6091</b>	gold nanoparticle	tumor necrosis factor alpha	Cytimmune Sciences, Inc.	pancreatic cancer, melanoma, soft tissue sarcoma, ovarian, and breast cancer <sup>125</sup>	phase I/II
<b>Docetaxel-PNP</b>	polymeric nanoparticle	docetaxel	Samyang Biopharmaceuticals	advanced solid malignancies <sup>126</sup>	phase I
<b>TKM-080301</b>	lipid nanoparticle	siRNA	National Institutes of Health Clinical Center	liver cancer <sup>127</sup>	phase I

The use of nanoprobes as imaging agents is a very promising new development for obtaining detailed images of living systems. The combination of drug delivery features with imaging techniques allows the researchers to follow the distribution of the drug inside the organism and gives further hints for the optimization of disease treatment.

## 1.7 References

- (1) Alivisatos, P. *Nat. Biotechnology* **2004**, 22 (1), 47–52.
- (2) Kelly, K. L.; Coronado, E.; Zhao, L. L.; Schatz, G. C. *J. Phys. Chem. B* **2003**, 107, 668–677.
- (3) Saha, K.; Agasti, S. S.; Kim, C.; Li, X.; Rotello, V. M. *Chem. Rev.* **2011**, 112, 2739–2779.
- (4) Kroto, H. W.; Heath, J. R.; O'Brien, S. C.; Curl, R. F.; Smalley, R. E. *Nature* **1985**, 318 (14), 162–163.
- (5) Kuznetsov, V. L.; Zilberberg, I. L.; Butenko, Y. V.; Chuvilin, A. L.; Segall, B. *J. Appl. Phys.* **1999**, 86 (2), 863–870.
- (6) S. Iijima, *Nature*, **1991**, 354, 56–58.
- (7) Ruggiero, A.; Villa, C. H.; Bander, E.; Rey, D. A.; Bergkvist, M.; Batt, C. A.; Manova-todorova, K.; Deen, W. M.; Scheinberg, D. A.; Mcdevitt, M. R. *Proc. Natl. Acad. Sci. U.S.A.* 2010, 107, 12369–12374.
- (8) Kato, H.; Kanazawa, Y.; Okumura, M.; Taninaka, A.; Yokawa, T.; Shinohara, H. *J. Am. Chem. Soc.* **2003**, 125, 4391–4397
- (9) Karam, L. R.; Mitch, M. G.; Coursey, B. M. *Appl. Radiat. Isot.* **1997**, 48, 771–776.
- (10) Boutorine, A. S.; Tokuyama, H.; Takasugi, M.; Isobe, H.; Nakamura, E.; Helene, C. *Angew. Chem., Int. Ed.* **1994**, 33, 2462–2465.
- (11) Isobe, H.; Nakanishi, W.; Tomita, N.; Jinno, S.; Okayama, H.; Nakamura, E. *Mol. Pharmaceutics* **2006**, 3, 124–134.
- (12) Mochalin, V. N.; Shenderova, O.; Ho, D.; Gogotsi, Y. *Nat. Nanotechnol.*, **2012**, 7, 11–23.
- (13) Schrand, A. M.; Huang, H.; Carlson, C.; Schlager, J. J.; Omacr Sawa, E.; Hussain, S. M.; and Dai, L.; *J. Phys. Chem. B*, **2007**, 111, 2–7.
- (14) Schirhagl, R.; Chang, K.; Loretz, M.; Degen, C. L. . *Annu. Rev. Phys. Chem.*, **2014**, 65, 83–105.
- (15) Yu, S.; Kang, M.; Chang, H.; Chen, K.; Yu, Y. *J. Am. Chem. Soc.* 2005, 127, 17604–17605.
- (16) Gaebel, T.; Popa, I.; Gruber, A.; Domhan, M.; Jelezko, F. *New J. Phys.* **2004**, 6, 98.
- (17) Chang, Y.; Lee, H.; Chen, K.; Chang, C.; Tsai, D.; Fu, C.; Lim, T.; Tzeng, Y.; Fang, C.; Han, C.; Chang, H.; Fann, W. *Nat. Nanotechnol.*, **2008**, 3, 284–288.
- (18) Zhang, X.; Lam, R.; Xu, X.; Chow, E. K.; Kim, H. *Adv. Mater.* **2011**, 23, 4770–4775.
- (19) Mohan, N.; Chen, C.; Hsieh, H.; Wu, Y. *Nano Lett.* **2010**, 10, 3692–3699.
- (20) Vijayanthimala, V.; Cheng, P.; Yeh, S.; Liu, K.; Hsiao, C.; Chao, J.; Chang, H. *Biomaterials* **2012**, 33 (31), 7794–7802.
- (21) Zhang, X.; Chen, M.; Lam, R.; Xu, K. X.; Osawa, E.; Ho, D. *ACS Nano* **2009**, 3, 2609–2616.
- (22) Alhaddad, A.; Adam, M.; Botsoa, J.; Dantelle, G.; Perruchas, S.; Gacoin, T.; Mansuy, C.; Lavielle, S. *Small* **2011**, 7, 3087–3095.
- (23) Thalhammer, A.; Edgington, R. J.; Cingolani, L. A.; Schoepfer, R.; Jackman, R. B. *Biomaterials* **2010**, 31 (8), 2097–2104.
- (24) Zhang, Q.; Mochalin, V. N.; Neitzel, I.; Knoke, I. Y.; Han, J.; Klug, C. A.; Zhou, J. G.; Lelkes, P. I.; Gogotsi, Y. *Biomaterials* **2011**, 32 (1), 87–94.
- (25) Sun, Y.; Zhou, B.; Lin, Y.; *J. Am. Chem. Soc.*, **2006**, 128, 7756–7757.
- (26) Liu, H.; Ye, T.; and Mao, C. *Angew. Chem., Int. Ed.*, **2007**, 46, 6473–6475. H. Liu, T. Ye and C. Mao
- (27) Zhu, L.; Yin, Y.; Wang, C.; Chen, S. *Mater. Chem. C*, **2013**, 1, 4925–4932.

- (28) Gao, X.; Ding, C.; Zhu, A.; Tian, Y. *Anal. Chem.*, **2014**, 86, 7071–7078.
- (29) Wei, W.; Xu, C.; Ren, J.; Qu, X. *Chem. Commun.*, **2012**, 48, 1284–1286.
- (30) Lin, Z.; Xue, W.; Chen, H.; Lin, J. *Anal. Chem.*, **2011**, 83, 8245–8251.
- (31) Baker, S. N.; Baker, G. A. *Angew. Chem., Int. Ed.*, **2010**, 49, 6726–6744.
- (32) Liu, J.; Teng, M.; Zhang, X.; Wang, K.; Li, C.; Zheng, Y.; You, X. *Org. Electron.* **2012**, 13 (10), 2177–2184.
- (33) Allen, M. J.; Tung, V. C.; Kaner, R. B. *Chem. Rev.*, **2010**, 110, 132–145.
- (34) Coleman, J. N. *Acc. Chem. Res.*, **2013**, 46, 14–22.
- (35) K. R. Paton, E. Varrla, C. Backes, R. J. Smith, U. Khan, A. O'Neill, C. Boland, M. Lotya, O. M. Istrate, P. King, T. Higgins, S. Barwich, P. May, P. Puczkarski, I. Ahmed, M. Moebius, H. Pettersson, E. Long, J. Coelho, S. E. O'Brien, E. K. McGuire, B. M. Sanchez, G. S. Duesberg, N. McEvoy, T. J. Pennycook, C. Downing, A. Crossley, V. Nicolosi and J. N. Coleman, *Nat. Mater.*, **2014**, 13, 624–630.
- (36) Paul, A.; Hasan, A.; Kindi, H. Al; Gaharwar, A. K.; Rao, V. T. S.; Nikkhah, M.; Shin, S. R.; Krafft, D.; Dokmeci, M. R.; Shum-Tim, D.; Khademhosseini, A. *ACS Nano* **2014**, 8 (8), 8050–8062.
- (37) Yang, K.; Feng, L.; Shi, X.; Liu, Z. *Chem Soc Rev* **2013**, 42 (2), 530–547.
- (38) Kauffman, D. R.; Star, A. *Angew. Chem., Int. Ed.*, **2008**, 47, 6550–6570.
- (39) Yang, B. C.; Noguchi, H.; Murata, K.; Yudasaka, M.; Hashimoto, A.; Iijima, S.; Kaneko, K. *Adv. Mater.*, **2005**, 17, 866–870.
- (40) Dai, H. *Acc. Chem. Res.*, **2002**, 35, 1035–1044.
- (41) Hu, H.; Zhao, B.; Itkis, M. E.; Haddon, R. C. *J. Phys. Chem. B*, **2003**, 107, 13838–13842.
- (42) Hersam, M. C. *Nat. Nanotechnol.*, **2008**, 3, 387–394.
- (43) Ghosh, S.; Bachilo, S. M.; Weisman, R. B. *Nat. Nanotechnol.*, **2010**, 5, 443–450.
- (44) Engel, M.; Moore, K. E.; Alam, A.; Dehm, S.; Krupke, R.; Flavel, B. S. *ACS Nano*, **2014**, 8, 9324–9331.
- (45) Fagan, J. A.; Becker, M. L.; Chun, J.; Nie, P.; Bauer, B. J.; Simpson, J. R.; Hight-walker, A.; Hobbie, E. K. *Langmuir*, **2008**, 24, 13880–13889.
- (46) Khan, U.; Porwal, H.; Neill, A. O.; Nawaz, K.; May, P.; Coleman, J. N. *Carbon*, **2012**, 50, 470–475.
- (47) Dyke, C. A.; Tour, J. M. *J. Phys. Chem. A*, **2004**, 108, 11151–11159.
- (48) Georgakilas, V.; Kordatos, K.; Prato, M.; Guldi, D. M.; Holzinger, M.; Hirsch, A.; Farmaceutiche, S.; Uni, V.; Europa, P. *J. Am. Chem. Soc.*, **2002**, 124, 760–761.
- (49) Hirsch, A. *Angew. Chem., Int. Ed.*, **2002**, 41, 1853–1859.
- (50) Pantarotto, D.; Singh, R.; McCarthy, D.; Erhardt, M.; Briand, J. P.; Prato, M.; Kostarelos, K.; Bianco, A. *Angew. Chemie - Int. Ed.* **2004**, 43 (39), 5242–5246.
- (51) Chen, R. J.; Zhang, Y.; Wang, D.; Dai, H. *J. Am. Chem. Soc.* **2001**, 123, 3838–3839
- (52) Lou, X.; Pagnouille, C.; Detrembleur, C.; Bailly, C. *Chem. Mater.* **2004**, 16, 4005–4011
- (53) Zheng, M.; Jagota, A.; Semke, E. D.; Diner, B. A.; Mclean, R. S.; Lustig, S. R.; Richardson, R. E.; Tassi, N. G. *Nat. Materials* **2003**, 2 338–342.
- (54) Ugarte, D. *Carbon N. Y.* **1995**, 33 (7), 989–993.
- (55) Tomita, S.; Sakurai, T.; Ohta, H.; Fujii, M.; Hayashi, S. *J. Chem. Phys.* **2001**, 114 (2001), 7477–7482.
- (56) Zou, Q.; Wang, M. Z.; Li, Y. G.; Lv, B.; Zhao, Y. C. *J. Exp. Nanosci.* **2010**, 5 (6), 473–487.
- (57) Sano, N.; Wang, H.; Alexandrou, I.; Chhowalla, M.; Teo, K. B. K.; Amaratunga, G. A. J.; Iijima, K. *J.*

*Appl. Phys.* **2002**, *92* (5), 2783–2788.

- (58) Alexandrou, I.; Wang, H.; Sano, N.; Amaratunga, G. A. J. *J. Chem. Phys.* **2004**, *120* (2), 1055–1058.
- (59) Guo, J.; Wang, X.; Yao, Y.; Yang, X.; Liu, X.; Xu, B. *Mater. Chem. Phys.* **2007**, *105* (2–3), 175–178.
- (60) Dorobantu, D.; Bota, P. M.; Boerasu, I.; Bojin, D.; Enachescu, M. *Surf. Eng. Appl. Electrochem.* **2014**, *50* (5), 390–394.
- (61) Chen, X. H.; Deng, F. M.; J.X., W.; Yang, H. S.; Wu, G. T.; Zhang, X. B.; Peng, J. C.; Li, W. Z. *Chem. Phys. Lett.* **2001**, *336*, 201–204.
- (62) He, C.; Zhao, N.; Du, X.; Shi, C.; Ding, J. *Scr. Mater.* **2006**, *54*, 689–693.
- (63) Hou, S. S.; Chung, D. H.; Lin, T. H. *Carbon N. Y.* **2009**, *47* (4), 938–947.
- (64) Yan, Y.; Yang, H.; Zhang, F.; Tu, B.; Zhao, D. *Carbon* **2007**, *45*, 2209–2216.
- (65) Du, J.; Liu, Z.; Li, Z.; Han, B.; Sun, Z.; Huang, Y. *Mater. Chem. Phys.* **2005**, *93*, 178–180.
- (66) Lin, Y.; Zhu, Y.; Zhang, B.; Kim, Y. A.; Endo, M.; Su, D. S. *J Mater Chem A* **2015**, *3*, 21805–21814.
- (67) Echegoyen, L.; Ortiz, A.; Chaur, M. N.; Palkar, A. J. *Chem. Nanocarbons* **2010**, 463–483.
- (68) Palkar, A.; Melin, F.; Cardona, C. M.; Elliott, B.; Naskar, A. K.; Edie, D. D.; Kumbhar, A.; Echegoyen, L. *Chem. - An Asian J.* **2007**, *2* (5), 625–633.
- (69) Costa, G. C. C.; Mcdonough, J. K.; Gogotsi, Y.; Navrotsky, A. *Carbon N. Y.* **2013**, *69*, 490–494.
- (70) Palkar, A.; Melin, F.; Cardona, C. M.; Elliott, B.; Naskar, A. K.; Edie, D. D.; Kumbhar, A.; Echegoyen, L. *Chem. - An Asian J.* **2007**, *2* (5), 625–633.
- (71) Chhowalla, M.; Wang, H.; Sano, N.; Teo, K. B. K.; Lee, S. B.; Amaratunga, G. a J. *Phys. Rev. Lett.* **2003**, *90* (15), 155504.
- (72) Tomita, S.; Fujii, M.; Hayashi, S.; Yamamoto, K. *Chem. Phys. Lett.* **1999**, *305*, 225–229.
- (73) Zeiger, M.; Jäckel, N.; Aslan, M.; Weingarth, D.; Presser, V. *Carbon N Y* **2015** *84*, 584–598.
- (74) Plonska-Brzezinska, M. E.; Breczko, J.; Palys, B.; Echegoyen, L. *Chemphyschem* **2013**, *14* (1), 116–124.
- (75) Mykhailiv, O.; Lapinski, A.; Molina-ontoria, A.; Regulska, E. *ChemPhysChem* **2015**, *16*, 2182 – 2191
- (76) Flavin, K.; Lawrence, K.; Bartelmess, J.; Tasiar, M.; Navio, C.; Bittencourt, C.; Shea, D. F. O.; Guldi, D. M.; Giordani, S. *ACS Nano* **2011**, *5*, 1198–1206.
- (77) Flavin, K.; Chaur, M. N.; Echegoyen, L.; Giordani, S. *Org. Lett.* **2010**, *12*, 14268–14269.
- (78) Yang, M.; Flavin, K.; Kopf, I.; Radics, G.; Hearnden, C. H. A.; McManus, G. J.; Moran, B.; Villalta-Cerdas, A.; Echegoyen, L. A.; Giordani, S.; Lavelle, E. C. *Small* **2013**, *9* (24), 4194–4206.
- (79) Frasconi, M.; Marotta, R.; Markey, L.; Flavin, K.; Spampinato, V.; Ceccone, G.; Echegoyen, L.; Scanlan, E. M.; Giordani, S. *Chemistry* **2015**, *21* (52), 19071–19080.
- (80) Bartelmess, J.; De Luca, E.; Signorelli, A.; Baldrighi, M.; Becce, M.; Brescia, R.; Nardone, V.; Parisini, E.; Echegoyen, L.; Pompa, P. P.; Giordani, S. *Nanoscale* **2014**, *6* (22), 13761–13769.
- (81) Marchesano, V.; Ambrosone, A.; Bartelmess, J.; Strisciante, F.; Tino, A.; Echegoyen, L.; Tortiglione, C.; Giordani, S. *Nanomaterials* **2015**, *5* (3), 1331–1350.
- (82) D'Amora, M.; Rodio, M.; Bartelmess, J.; Sancataldo, G.; Brescia, R.; Cella Zanicchi, F.; Diaspro, A.; Giordani, S. *Sci. Rep.* **2016**, *6*, 33923.
- (83) Usenko, C. Y.; Harper, S. L.; Tanguay, R. L. *Carbon N Y* **2007**, *45*, 1891–1898.
- (84) Wang, A. Z.; Langer, R.; Farokhzad, O. C.; *Annu. Rev. Med.* **2012**, *63*, 185 – 198.

- (85) Peer, D.; Karp, J. M.; Hong, S.; Farokhzad, O. C.; Margalit, R.; Langer, R. *Nat. Nanotechnol.* **2007**, *2*, 751 – 760.
- (86) Mura, S.; Couvreur, P. *Adv. Drug Deliv. Rev.* **2012**, *64* (13), 1394–1416.
- (87) Zamboni, W. C.; Torchilin, V.; Patri, A. K. *Clin Cancer Res* **2012**, *18*, 3229–3241.
- (88) Chauhan, V. P.; Jain, R. K. *Nat. Publ. Gr.* **2013**, *12* (11), 958–962.
- (89) Meel, R. Van Der; Vehmeijer, L. J. C.; Kok, R. J.; Storm, G.; Gaal, E. V. B. Van. *Adv. Drug Deliv. Rev.* **2013**.
- (90) N. Kamaly, Z. Xiao, P. M. Valencia, A. F. Radovic- Moreno, O. C. Farokhzad, *Chem. Soc. Rev.* **2012**, *41*, 2971 –3010.
- (91) Panyam, J.; Labhasetwar, V. *Adv. Drug Delivery Rev* **2003**, *55*, 329–347.
- (92) Shi, X.; Bussche, A. Von; Hurt, R. H.; Kane, A. B.; Gao, H. *Nat. Nanotechnology* **2011**, *6*, 714-718.
- (93) M. Elsabahy, K. L. Wooley, *Chem. Soc. Rev.* **2012**, *41*, 2545 –2561.
- (94) Jang, J.; Jeong, S.; Seo, J.; Kim, M.; Sim, E.; Oh, Y.; Nam, S.; Park, B.; Cheon, J. *J. Am. Chem. Soc* **2011**, *133*, 7636–7639.
- (95) Abuchowski, A.; Mccoy, J. R.; Palczuk, N. C.; Es, T. V. A. N.; Davis, F. F. *J. Biol. Chem.* **1976**, *252* (11), 3582–3586.
- (96) Klibanov, A. L.; Maruyama, K.; Torchilin, V. P.; Huang, L. *FEBS Lett.* **1990**, *268*, 235 – 237.
- (97) Lee, S.; Yun, M.; Jeong, S. W.; In, C.; Kim, J.; Seo, M.; Pai, C.; Kim, S. *J. Control. Release* **2011**, *155* (2), 262–271.
- (98) Xie, H. G.; Zheng, J. N.; Li, X. X.; Liu, X. D.; Zhu, J.; Wang, F.; Xie, W. Y.; Ma, X. J. *Langmuir* **2010**, *26*, 17156 – 17164.
- (99) Du, H.; Chandaroy, P.; Hui, S. W. *Biochim. Biophys. Acta Biomembr.* **1997**, *1326*, 236 – 248.
- (100) Cui, J.; Li, C.; Guo, W.; Li, Y.; Wang, C.; Zhang, L.; Zhang, L.; Hao, Y.; Wang, Y. *J. Controlled Release* **2007**, *118*, 204 – 215.
- (101) Liu, Z.; Jiao, Y.; Wang, Y.; Zhou, C.; Zhang, Z. *Adv. Drug Deliv. Rev.* **2008**, *60* (15), 1650–1662.
- (102) Yuan, Z.; Zhang, Z.; Zhu, D.; Sun, X.; Gong, T.; Liu, J.; Luan, C. *Mol. Pharmaceutics* **2009**, *6*, 305 – 314.
- (103) Mahmoudi, M.; Sant, S.; Wang, B.; Laurent, S.; Sen, T. *Adv. Drug Deliv. Rev.* **2011**, *63* (1–2), 24–46.
- (104) Tada, H.; Higuchi, H.; Wanatabe, T. M.; Tada, H.; Higuchi, H.; Wanatabe, T. M.; Ohuchi, N. *Cancer Res.* **2007**, *67*, 1138 – 1144.
- (105) Park, J. W.; Hong, K.; Kirpotin, D. B.; Colbern, G.; Shalaby, R.; Baselga, J.; Shao, Y.; Nielsen, U. B.; Marks, J. D.; Moore, D.; Papahadjopoulos, D.; Benz, C. C. *Clin. Cancer Res.* **2002**, *8*, 1172 – 1181.
- (106) Arosio, D.; Manzoni, L.; Araldi, E. M. V; Scolastico, C. *Bioconjugate Chem.* **2011**, 664–672.
- (107) Tai, W.; Mahato, R.; Cheng, K. *J. Control. Release* **2010**, *146* (3), 264–275.
- (108) Zhang, C.; Jugold, M.; Woenne, E. C.; Lammers, T.; Morgenstern, B.; Mueller, M. M.; Zentgraf, H.; Bock, M.; Eisenhut, M.; Semmler, W.; Kiessling, F. *Cancer Res.* **2007**, *67*, 1555 – 1562.
- (109) Orava, E. W.; Cicmil, N.; Gariépy, J. *BBA - Biomembr.* **2010**, *1798* (12), 2190–2200.
- (110) Lidke, D. S.; Nagy, P.; Heintzmann, R.; Arndt-jovin, D. J.; Post, J. N.; Grecco, H. E.; Jares-erijman, E. A.; Jovin, T. M. *Nat. Biotechnol.* **2004**, *22*, 198 – 203.
- (111) Qian, Z. M.; Li, H.; Sun, H.; Ho, K. *Pharmacol. Rev.* **2002**, *54*, 561 – 587.
- (112) Govender, T.; Riley, T.; Ehtezazi, T.; Garnett, M. C.; Stolnik, S.; Illum, L.; Davis, S. S. *Int. J. Pharm.*



2000, 199, 95–110

- (113) Y. Chen, V. J. Mohanraj, J. E. Parkin, *Lett. Pept. Sci.* **2003**, 10, 621 – 629.
- (114) A. Z. Wang, R. Langer, O. C. Farokhzad, *Annu. Rev. Med.* **2012**, 63, 185 – 198.
- (115) Montero, A. J.; Adams, B.; Diaz-, C. M., Gluck, S. *Expert Rev. Clin. Pharmacol.* **2011**, 4, 329 – 334.
- (116) Brien, M. E. R. O.; Wigler, N.; Inbar, M.; Rosso, R.; Grischke, E.; Santoro, A.; Catane, R. *Ann. Oncol.* **2004**, 15, 440 – 449.
- (117) Petre, C. E. *Int. J. Nanomed.* **2007**, 2, 277 – 288
- (118) Angst, M. S.; Drover, D. R. *Clin. Pharmacokinet.* **2006**, 45, 1153 – 1176.
- (119) Barenholz, Y. C. *J. Control. Release* **2012**, 160 (2), 117–134.
- (120) Oerlemans, C.; Bult, W.; Bos, M.; Storm, G.; Nijsen, J. F. W.; Hennink, W. E. *Pharm. Res.* **2010**, 27, 2569 – 2589.
- (121) Silverman, J. A.; Deitcher, S. R. *Cancer Chemother. Pharmacol.* **2013**, 71, 555 – 564.
- (122) Lao, J.; Madani, J.; Puértolas, T.; Álvarez, M.; Hernández, A.; Pazo-cid, R.; Artal, Á.; Torres, A. A. *Drug Delivery* **2013**, 456409.
- (123) P. A. Dinndorf, J. Gootenberg, M. H. Cohen, P. Keegan, R. Pazdur, *Oncologist* **2007**, 12, 991 – 998.
- (124) Okusaka, S. Okada, H. Ueno, M. Ikeda, R. Iwata, H. Furukawa, K. Takayasu, N. Moriyama, T. Sato, K. Sato, *Oncology* **2002**, 62, 228 – 233
- (125) Libutti, S. K.; Paciotti, G. F.; Byrnes, A. A.; Alexander, H. R.; Gannon, W. E.; Walker, M.; Seidel, G. D.; Yuldasheva, N.; Tamarkin, L. *Clin. Cancer Res.* **2010**, 16, 6139 – 6149.
- (126) K. H. Jung, K. P. Kim, D. H. Yoon, Y. S. Hong, C. M. Choi, J. H. Ahn, D. H. Lee, J. L. Lee, M. H. Ryu, B. Y. Ryoo, H. M. Chang, T. W. Kim, S. B. Kim, S.W. Kim, C. Suh, Y. K. Kang, J. Lee, K. S. Bae, Y. M. Kim, *J. Clin. Oncol.* **2012**, 30-34.
- (127) Shen, H.; Sun, T.; Ferrari, M. *Cancer Gene Ther.* **2012**, 19, 367 –373.

## 2. CNO for biomedical imaging

### 2.1 Introduction

The recognition and labelling of biologically and environmentally important species has emerged as a significant goal in the field of biomedicine in recent years.<sup>1,2,3</sup> Fluorogenic methods in conjunction with suitable probes are preferable approaches for the measurement of analytes because fluorimetry is rapidly performed, is nondestructive, is highly sensitive, is suitable for high-throughput screening applications, and can afford real information on the localization and quantity of the targets of interest. To date, various fluorophores with different excitation and emission wavelengths have been employed, such as coumarin, pyrene, 1,8-naphthalimide, xanthenes, squaraine, cyanine, boron dipyrromethene difluoride (BODIPY), nitrobenzofurazan.<sup>4</sup> Among the fluorophores developed, xanthenes, including rhodamines and fluoresceins, are highly favorable because of their excellent photophysical properties, such as high extinction coefficients, excellent quantum yields, great photostability in water, and relatively long emission wavelengths. As a typical xanthene dye, fluorescein was first synthesized by von Bayer in 1871 with resorcinol and phthalic anhydride via Friedel-Crafts acylation/cyclodehydration. Some of the advantageous features of the fluorescein fluorophores are good water solubility, visible excitation and emission (an absorption maximum at 494 nm and emission maximum of 521 nm in water), and maximum brightness at physiological pH.<sup>5</sup> However, fluorescein derivatives are nonfluorescent when they exist in the lactone form. On the other hand the ring opened form can induce color changes and fluorescence enhancements. Interests in designing and synthesizing new fluorescein derivatives are still enormous to meet needs in the recognition and sensing of biologically and environmentally important chemical species in biology. In literature, fluorescein based sensors as nontoxic fluorescent dyes are reported to be extensively used as fluorescent indicators and tags, pH probes of intercellular fluids, protein sensors and ions detectors in cell biology and neurology.<sup>1</sup> Because of the good physicochemical properties of the fluorescein we used it in order to develop a fluorescent labelled CNOs in order to study the cytotoxicity and the localization of the CNO within cells. The investigation of novel nano-platforms capable of carrying therapeutic agents and with recognition capabilities for specific targeting and optical outputs for imaging is of major interest in the treatment of cancer<sup>6</sup> and of other types of infections, such as HIV.<sup>7</sup> As discussed in the previous chapter, CNOs have great promise for use as effective biomarkers for cell imaging due to their excellent properties such as low cytotoxicity, high photostability, absence of quenching, and photobleaching in cells if functionalized properly. However, reports discussing fluorescence labelled CNOs as materials for biological imaging are rare. In the first year of my PhD, a highly fluorescent imaging probe based on carbon nano-onions (CNOs) for biological imaging have been developed and characterized. Different strategies for CNOs functionalization have been investigated and a versatile and robust strategy for the preparation of highly surface modified CNOs for biomedical imaging was deeply explored. The results reveal a critical correlation between the surface functionalization and the dispersion of the modified CNOs in physiological conditions. In addition, because the development of imaging probes based on carbon nanomaterials for biomedical studies requires the understanding of their biological response as well as the efficient and safety exposition of the nanomaterial to the cell compartment where is designed to operate, the biocompatibility and the cytotoxicity were systematically investigated in HeLa Cells.

## 2.2 Experimental

### 2.2.1 Highly surface functionalized carbon nano-onions for bright light bioimaging

One of the major drawbacks for the potential applications of CNMs is their poor solubility in common solvents. In order to improve the solubility of these nanomaterials in different solvents, surface modification of CNMs with different functional groups has been developed by either covalent or noncovalent synthetic methods, as already discussed in chapter 1. A well-established procedure for the surface grafting of CNOs is the radical addition based on the in situ generated diazonium salts. However, other surface chemistries should be investigated because they could result favorable for specific applications. In the first instance, two different synthetic strategies for the surface functionalization of CNOs were compared: the Tour reaction and the oxidation of the surface with nitric acid. If with the Tour reaction, benzoic acid functionalities were introduced by reacting p-CNOs with 4-aminobenzoic acid and sodium nitrite in an acidified DMF/water mixture (Figure 1), with the oxidation, carboxylic acid functionalities were introduced by heating p-CNOs under reflux in 3 N HNO<sub>3</sub> for 48 h (Figure 2). The number of functionalities introduced by oxidation were significantly higher. The high degree of surface functionalization of the ox-CNOs in comparison to previously reported chemical modification of CNOs, such as the grafting of the CNO surface with benzoic acid groups by radical addition procedure, was observed by TGA performed in air. The thermal decomposition of the benzoic acid groups was revealed, followed by the decomposition of the CNOs core. The comparison of the TGA weight loss curves (Figure 1) of p-CNO with that of benz-CNO reveals a decrease in the decomposition temperature from 655 °C to 648 °C. The coverage of benzoic acid groups on the surface of the benz-CNO was calculated from the TGA weight loss at 450 °C and around 50 benzoic functionalities per CNO were estimated. In comparison, the modification of the CNOs by the chemical oxidation procedure shows a decrease in the decomposition temperature from 655 °C to 626 °C yielding to 210 carboxylic functionalities per CNO (Figure 2). Moreover, the higher surface coverage of carboxylic acid groups also results in an enhancement of the dispersibility of CNOs in water.

### 2.2.2 Synthesis of p-CNO, benz-CNO and ox-CNO

The synthesis of p-CNOs (6–8 shells) was performed by annealing nanodiamond powder (Molto, 5 nm average particle size) under a positive pressure of helium at 1650 °C in a tubular furnace. In order to obtain benz-CNO, NaNO<sub>2</sub> (1.47 g, 21.3 mmol) was dissolved in 20 mL deionized water and cooled to 0 °C. This solution was added at once to a solution of 4-aminobenzoic acid (2.88 g, 21.0 mmol) in 30 mL DMF at 0 °C. Conc. HCl (200 µL) was added and the mixture was stirred for 30 min at 0 °C. p-CNOs (31 mg) were dispersed in 20 mL DMF by ultrasonication for 20 min and the dispersion was added to the reaction mixture, which was stirred at 0 °C for 4 h and at RT for additional 3 days. Following this, the CNOs were separated from the reaction mixture by centrifugation (30 min, 2100g) and purified by subsequent re-dispersion – centrifugation steps in water, DMF, and methanol. After drying at 60 °C overnight, 25 mg of benz-CNOs were recovered (Figure 1). The oxidation was performed directly on the sp<sup>2</sup> carbon present on the p-CNOs surface, leading to the creation of hybridized sp<sup>3</sup> carbon atoms. 40 mg of pristine CNOs were dispersed in 30 mL of a solution of nitric acid (3M) and stirred under reflux for 48 h. After cooling to room temperature, the CNOs were filtered off on a nylon filter membrane (pore size 0.2 µm) and washed with water, methanol and acetone. 38 mg of ox-CNO were recovered as black powder after drying overnight at RT (Figure 2).

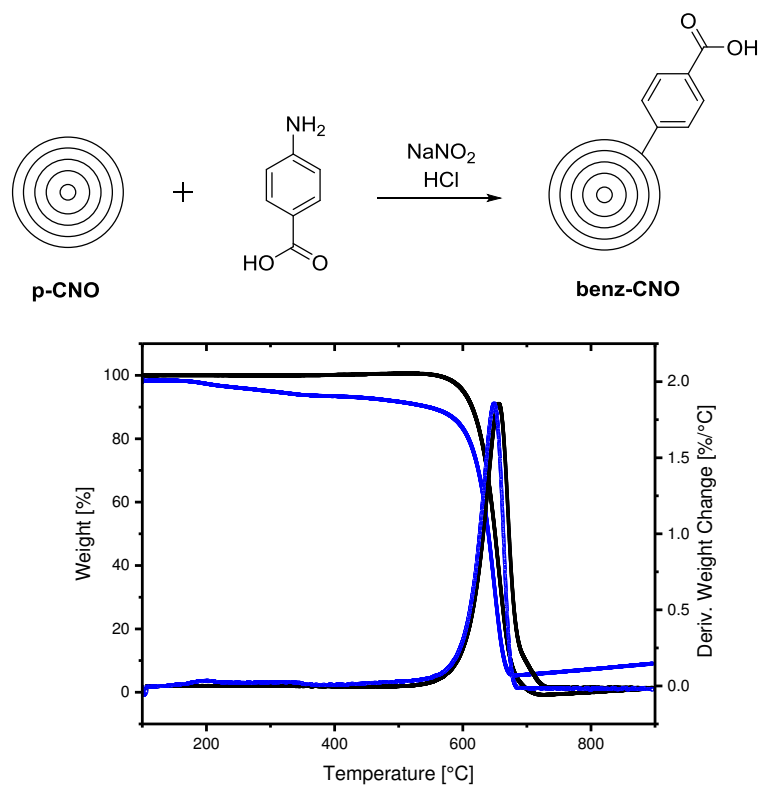


Figure 1. Synthetic procedure for the covalent functionalization of benz-CNO. Thermogravimetric analysis of p-CNO (black) and benz-CNO (blue) and the corresponding weight loss derivatives are reported.

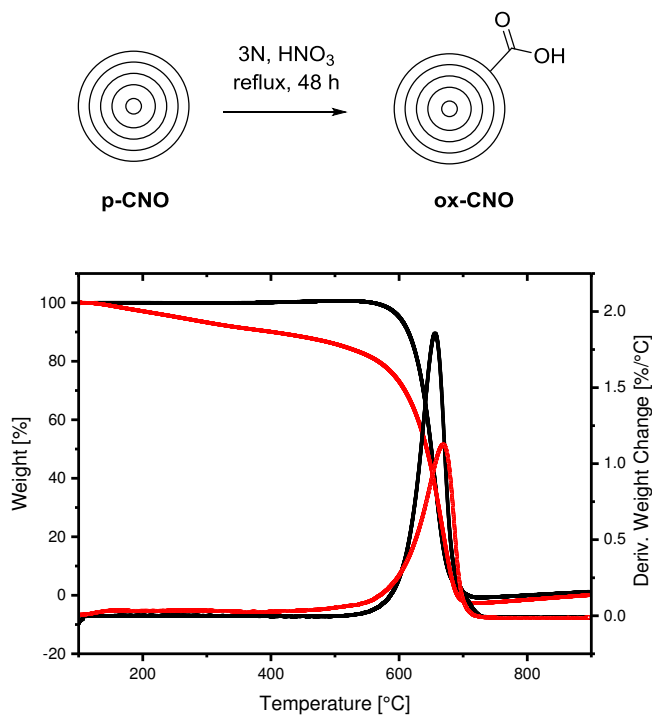
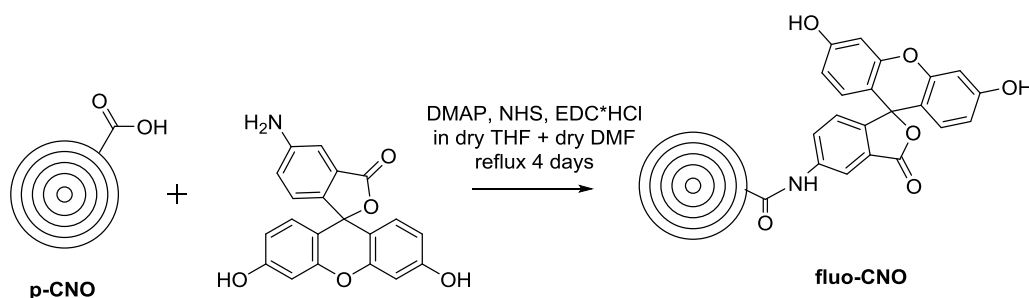


Figure 2. Synthetic procedure for the covalent functionalization of ox-CNO. Thermogravimetric analysis of p-CNO (black) and ox-CNO (red) and the corresponding weight loss derivatives are reported.

### 2.2.3 Synthesis of fluo-CNO

Once obtained a highly surface functionalized CNOs decorated with carboxylic acid groups, these functionalities were derivatized by amide coupling with fluoresceinamine in order to obtain an efficient imaging agent. A dispersion of ox-CNO (15 mg) was prepared by ultrasonication (20 min at 37 kHz) in a mixture (30 mL) of dry THF and DMF (2:1). The mixture was deoxygenated under N<sub>2</sub> and 50 mg (0.41 mmol) of DMAP, 50 mg (0.43 mmol) of NHS and 80 mg (0.42 mmol) of EDC-HCl were added. The reaction mixture was briefly sonicated and after the addition of 40 mg (0.12 mmol) of fluoresceinamine (isomer I) heated under reflux for 4 days under N<sub>2</sub>. After cooling to RT, the CNOs were redispersed in DMF, filtered off (nylon membrane, pore size 0.2 μm) and washed with THF and acetone. 12 mg of fluo-CNO were recovered as black powder after drying under air for one day.



Scheme 1. Synthetic procedure for preparation of fluorescein decorated CNOs.

After reaction, the fluo-CNOs were isolated and washed with plenty of THF and acetone in order to completely remove the fluorescein physically adsorbed on the surface of the fluo-CNOs. The successful surface modification of the p-CNO with carboxylic acid groups to yield ox-CNO and the coupling with fluorescein to obtain fluo-CNO, was characterized by a variety of techniques, including thermogravimetric analysis (TGA), Fourier transform infrared (FTIR), Raman, absorption and fluorescence spectroscopies, dynamic light scattering (DLS) and Zeta potential measurements.

## 2.3 Results and discussion

### 2.3.1 Thermo Gravimetric Analysis (TGA)

TGA performed in air reveals a decrease in the decomposition temperature from 655 °C to 617 °C for p-CNO and ox-CNO respectively (Figure 3). The coverage of carboxylic acid groups on the surface of the ox-CNO was calculated from the TGA weight loss at 450 °C and around 210 carboxylic functionalities per CNO were estimated. The attachment of fluoresceinamine on the ox-CNO to yield fluo-CNO results in a further decrease of the decomposition temperature to 578 °C, as resulted from the TGA curve. The number of fluorescein molecules per CNO was calculated from the weight loss at 450 °C of the fluo-CNO and are approx. 28 units per unit. The higher surface coverage of carboxylic acid groups as already mention, along with the presence of the fluorophore, results in an enhancement of the capability of the CNO constructs to be dispersible in water.

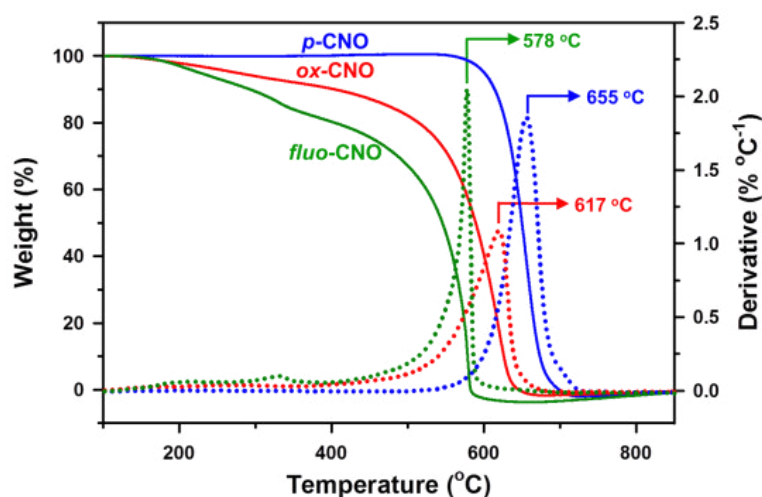


Figure 3. Thermogravimetric analysis and the corresponding weight loss derivatives of p-CNO (blue), ox-CNO (red) and fluo-CNO (green). All experiments were run in air with a temperature rate of 10 °C min<sup>-1</sup>.

### 2.3.2 Fourier-transform infrared spectroscopy (FTIR)

The chemical modification of p-CNO was confirmed by solid-state ATR FT-IR spectroscopy which displays the characteristic stretching and vibration bands of the carboxylic acid groups in the case of ox-CNO and the fluorescein functionalities for the fluo-CNOs. The FTIR spectrum of ox-CNO shows a peak at around 1680 cm<sup>-1</sup> corresponding to the stretching vibrations of C=O (Figure 4). A significant change of the FTIR spectra was observed after coupling of fluorescein amine on the surface modified CNO, and new bands corresponding to the vibrations of the fluorescein moiety are seen in the spectrum of fluo-CNO.

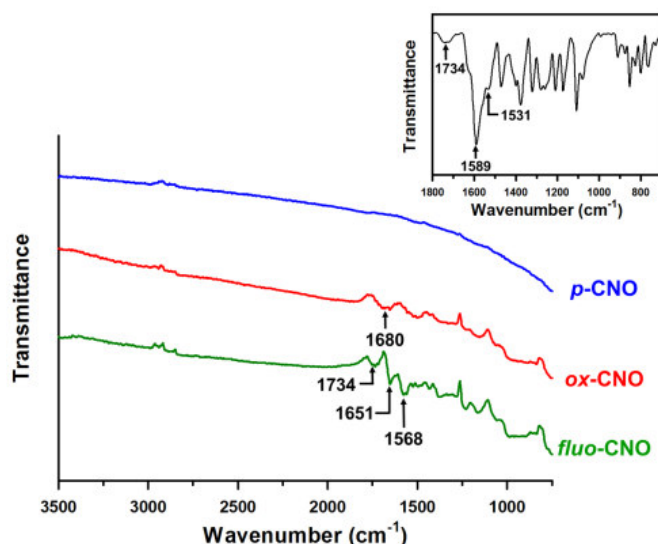


Figure 4. ATR-FTIR spectra of p-CNO (blue), ox-CNO (red) and fluo-CNO (green). Inset: ATR-FTIR spectra of fluoresceinamine. Each ATR-FTIR spectrum was accumulated from 256 scans with normal resolution using germanium crystals.

### 2.3.3 Raman Spectroscopy

Raman spectra of p-CNO, ox-CNO and fluo-CNO are shown in Figure 5. ox-CNO display a little lowering of the D-band ( $1320\text{ cm}^{-1}$ ) compared to the G-band ( $1580\text{ cm}^{-1}$ ), suggesting purification of the pristine CNOs from carbonaceous material upon nitric acid treatment. As expected the amidation of the carboxyl moiety leading to fluo-CNO did not alter significantly the ratio between the D and G bands.

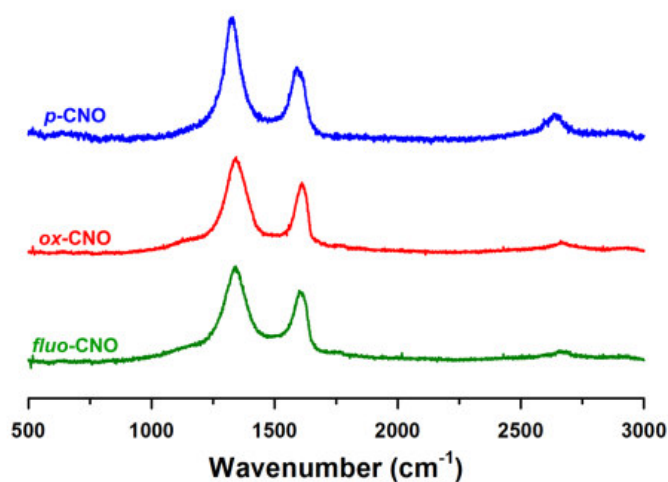


Figure 5. Raman spectra of p-CNO (blue), ox-CNO (red) and fluo-CNO (green). The Raman spectra were normalized for the G-band at  $1580\text{ cm}^{-1}$ .

### 2.3.4 Fluorescence Spectroscopy

The emission properties of the fluorescein labeled CNOs were tested under different conditions. Upon photoexcitation at 490 nm of a dispersion of fluo-CNO in DMSO, an intense emission band was observed with a maximum at 544 nm (Figure 6). The fluorescence spectra of dispersions of fluo-CNO in phosphate buffer and cell culture medium give rise to an emission centered at around 518 nm, which is slightly shifted in comparison to the emission of free fluorescein in PBS ( $\lambda_{em} = 513\text{ nm}$ ). The difference in the wavelength of maximum emission between free fluorescein and fluo-CNO implies a different environment surrounding the fluorophores anchored on the surface of the CNOs. Another aspect relates to the photostability of the fluorescein anchored on the fluo-CNO. We found that a dispersion of fluo-CNO in phosphate buffer retains the photophysical properties upon two weeks storage at  $4\text{ }^{\circ}\text{C}$ .

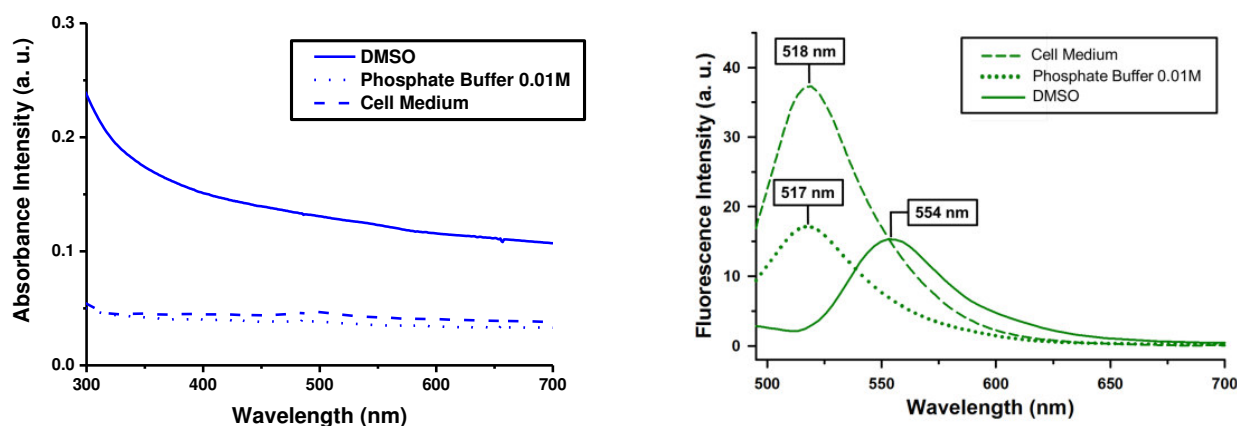


Figure 6. Absorption and Emission spectra ( $\lambda_{exc} = 490 \text{ nm}$ ) of fluo-CNO dispersed in DMSO (solid line), phosphate buffer 0.01 M (dotted line) and cell culture medium (dashed line). The fluo-CNO samples were dispersed at concentration of  $10 \mu\text{g mL}^{-1}$ . The fluorescence spectra of the cell culture medium was subtracted to the spectra of fluo-CNO.

### 2.3.5 Dynamic Light Scattering (DLS) and $\zeta$ -potential measurements

In order to examine the behavior of the CNOs under physiological conditions DLS and zeta-potential measurements were performed not only in DMSO but also in phosphate buffer 0.01 M and cell culture medium (DMEM with 10% FBS, 2% Penstrep and 1% glutamine). The dispersion of ox-CNO or fluo-CNO was carried out at an initial concentration of  $500 \mu\text{g/mL}$  by sonication of the sample for 30 min in DMSO, phosphate buffer 0.01M (pH 7.4) and cell medium, followed by dilution of the samples to achieve final concentrations of 50, 20, 10, 5 and  $1 \mu\text{g/mL}$ . Although previously reported benz-CNOs displayed a significant tendency to agglomerate with time, ox-CNO reveal an effective hydrodynamic diameter in DMSO and in phosphate buffer of  $115 \pm 1 \text{ nm}$  and  $105 \pm 1 \text{ nm}$  respectively at a final concentration of  $10 \mu\text{g/mL}$ . These values of diameters does not change significantly with the time as well as the concentration of ox-CNO, suggesting the low tendency of these dispersions to form large agglomerates even at relatively high concentrations. Under similar conditions hydrodynamic diameters of  $171 \pm 8 \text{ nm}$  and  $179 \pm 33 \text{ nm}$  were measured for the fluo-CNO dispersed in DMSO and in phosphate buffer. The dispersion of the particles in cell medium has a dramatic effect on the behaviour of the ox-CNO with an average hydrodynamic diameter of  $828 \pm 110 \text{ nm}$ . An average diameter of  $225 \pm 36 \text{ nm}$  was measured for a dispersion of fluo-CNO in cell medium. The huge difference described is probably due to the protein corona mechanism which is often present with nanoparticles tested in physiological condition. The concept of the nanoparticle–protein corona of course is important in shaping the surface properties, charges, resistance to aggregation and hydrodynamic size of nanoparticles and requires further investigations.

Z-potential measurements of ox-CNO and fluo-CNO samples were performed in phosphate buffer 0.01M at pH 7.4 and Cell Medium. Under these conditions the zeta-potentials for the ox-CNO was  $-41 \pm 1 \text{ mV}$ , independently on the CNO concentrations used. A change in the zeta-potential was observed after functionalization of the CNOs with fluorescein, indicating that the carboxy functionalities have a significant effect on the charging capacity of each particle. For comparison, the zeta-potential of a dispersion of p-CNO



in phosphate buffer 0.01 M was  $-18 \pm 2$  mV. The dispersion of ox-CNO and fluo-CNO samples in cell medium resulted respectively in a decrease of the zeta-potential values to  $-23 \pm 1$  mV and  $-20 \pm 2$  mV (Table 1).

Table 1. Effective hydrodynamic diameter obtained from dynamic light scattering (DLS) measurements and Zeta-potential of ox-CNO and fluo-CNO.

Sample	Effective Hydrodynamic Diameter (nm)			Zeta-Potential (mV)	
	DMSO	PBS 0.01M	Cell Medium	PBS 0.01M	Cell Medium
<i>ox-CNO</i>	115 ± 1	105 ± 1	828 ± 110	-41 ± 1	-23 ± 1
<i>fluo-CNO</i>	171 ± 8	179 ± 33	225 ± 36	-38 ± 1	-20 ± 2

The results clearly show that CNOs might encounter biological interfaces after suspension in a tissue culture or biological medium. In a given medium, the most important nanoparticle characteristics that determine the surface properties are the material's chemical composition, surface functionalization, shape and angle of curvature, porosity, hydrophobicity or hydrophilicity. Other quantifiable properties, such as effective surface charge (zeta potential), particle aggregation, state of dispersion, stability/biodegradability are determined by the characteristics of the suspending media, including the ionic strength, pH, temperature and the presence of large organic molecules (for example proteins). The interface between carbon nanomaterials and biological systems for sure comprises a dynamic series of interactions between nanomaterial surfaces and biological surfaces but the biophysicochemical interactions and the relationships between structure and activity determined by nanomaterial in cells (membrane surfaces, endosomal compartments, organelles and cytoplasm) require a deeper understanding.

### 2.3.6 Cell studies

Because the cytocompatibility of functionalized nanomaterials is a fundamental consideration when investigating their use as bioimaging agents, Dr. Marco Frasconi, Senior Post Doc in NACM group at iit, tested these probes based on fluorescently functionalized CNOs in HeLa cells for in-vitro imaging. The cytotoxicity of ox-CNO and fluo-CNO samples dispersed in cell medium was tested at different concentrations (1, 2, 5 and 10  $\mu\text{g mL}^{-1}$ ) in HeLa cells (Figure 7 and 8). The obtained percentage viability at different administration time did not result in significant cytotoxicity of the differently functionalized CNOs. The viability of the HeLa cells treated with ox-CNO and fluo-CNO was found to be higher than 80% for an incubation time of 24 h at 37 °C at all concentration of CNOs tested. Confocal live cell imaging was performed in order to explore the ability of the fluorescein labelled CNOs to be internalized by cells and to localize their presence in cellular compartments. HeLa cells grown in subconfluent monolayer on a glass slide were treated with a dispersion of fluo-CNO in DMEM at concentrations of 1, 5 and 10  $\mu\text{g mL}^{-1}$ . After 24 h of incubation at 37 °C, the cells were carefully rinsed with fresh media to remove the excess of CNOs and treated with Hoechst 33342, for live nuclear staining.

### 2.3.7 Toxicity

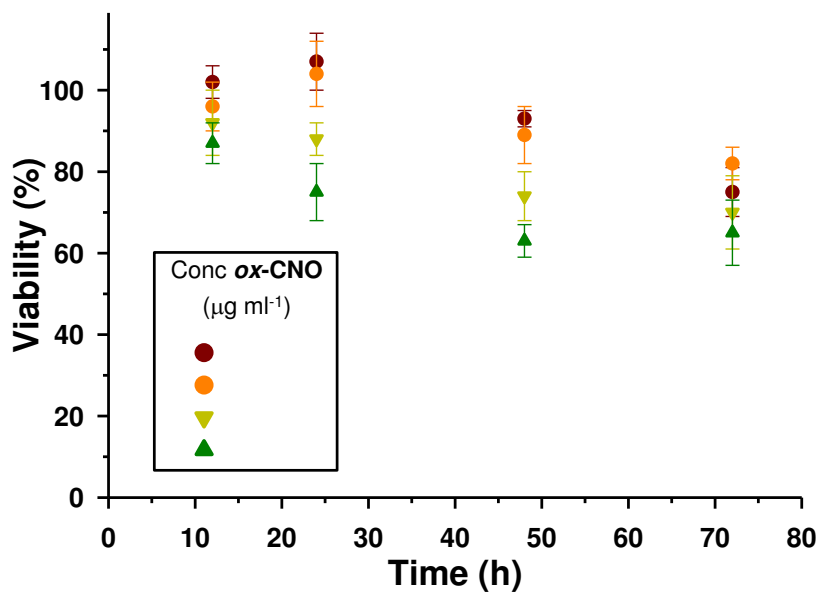


Figure 7. Cellular viability of HeLa cells after exposure to 1, 2, 5 and 10 µg mL<sup>-1</sup> ox-CNO. The viability was evaluated for the samples of CNOs against a non-treated control.

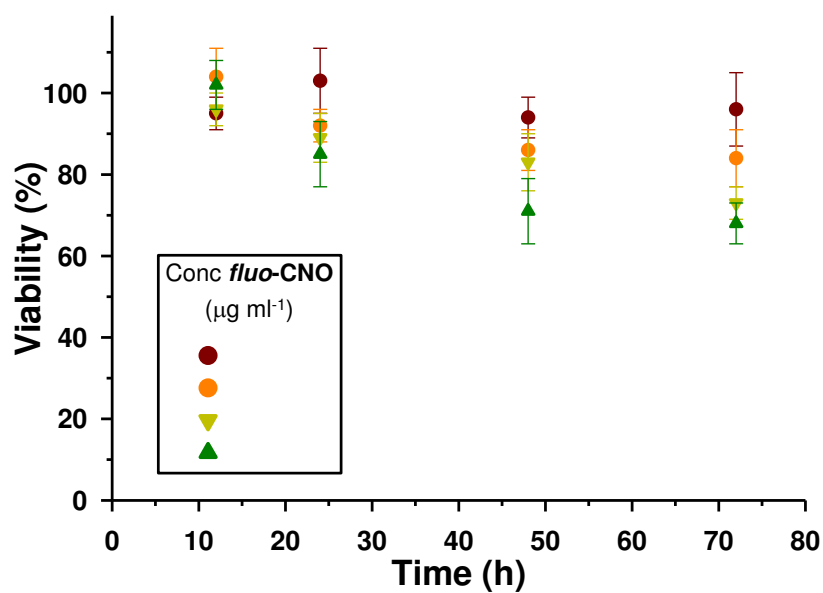


Figure 8. Cellular viability of HeLa cells after exposure to 1, 2, 5 and 10 µg mL<sup>-1</sup> fluo-CNO. The viability was evaluated for the samples of CNOs against a non-treated control.

### 2.3.8 Cellular Uptake

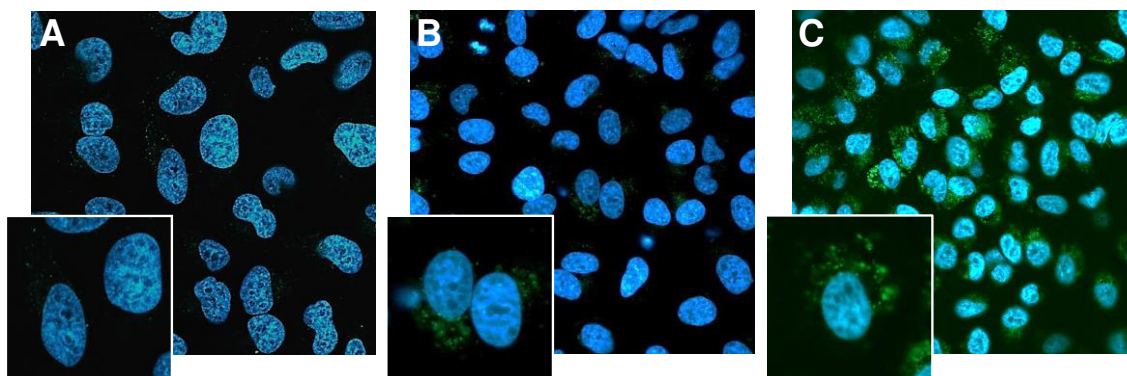


Figure 9. Confocal image of HeLa cells after incubation for 24 h with 1 (A), 5 (B), 10 (C)  $\mu\text{g mL}^{-1}$  of fluo-CNO. Nuclei were stained with Hoechst 33342 (blue).

The cellular uptake characteristics of the fluo-CNO in the concentration range investigated are shown in Figure 9. The green fluorescence signal detected in the cells clearly indicates that fluo-CNOs were internalized by cells. Cells treated with 1  $\mu\text{g mL}^{-1}$  fluo-CNO display a point-like distribution of the fluorescence signal in the perinuclear region (Figure 9 A). In agreement with previous studies on the cellular uptake of CNOs functionalized with fluorophores, the localization of the fluo-CNO in living cells within the cytoplasmic compartment is likely due to intravesicle storage of the CNOs as a consequence of the cell internalization of fluo-CNO by an endocytosis pathway. For higher concentrations of fluo-CNO, 5 and 10  $\mu\text{g mL}^{-1}$  (Figures 9 B and C), the cells display a widely spread green emission from the fluorescein coupled onto the CNOs, indicating an efficient cellular internalization of the fluo-CNO. The high biocompatibility and minimal systemic toxicity of these fluorescent CNOs along with an efficient cellular uptake in the perinuclear region as demonstrated by using confocal live cell imaging encourage the use of these fluorescent nanomaterials in biomedical applications and the further investigation of these materials as biosensors for cancer cells.

## 2.4 Conclusion

A fluorescent probe based on carbon nano-onions (CNOs) for biological imaging has been synthesized and fully characterized. We have demonstrated a versatile strategy for the preparation of highly surface modified CNOs by oxidation of the defects on the CNOs surface and a chemical functionalization of the carboxyl groups by amide coupling with fluoresceinamine. The modification of CNOs by chemical oxidation of the defects on the outer shell of these carbon nanoparticles results in an extensive surface functionalization with carboxyl groups that translate in excellent dispersability in water and high emission properties. These are key features in the field of biomedical applications. Moreover, we have systematically investigated the importance of surface functionalization in physiological conditions. The high biocompatibility and minimal systemic toxicity of these fluorescent CNOs along with an efficient cellular uptake, make these functionalized CNOs suitable candidates as fluorescent probes for bioimaging studies and hold promise as multifunctional

nanomaterial for theranostic applications. In summary, in comparison to the previously reported chemical modification of CNOs through the well-known Tour reaction which introduced benzoic acid groups by radical addition on CNO surface, the new functionalization based on oxidation provide better emission properties and dispersability in physiological condition due to the excellent loading achieved. The results reveal also a high biocompatibility and minimal cytotoxicity along with an efficient cellular uptake which render this carbon nano-material a good candidate for in vivo optical imaging. According to that, the second stage of my research project has been focused on introducing targeting ligands to CNOs. Attachment of sugar moieties to carbon nanomaterials is a very attractive technique not only because of improvements in water solubility but also because play an important role in many cell-cell interactions. Therefore, CNOs conjugated with specific targeting peptides might facilitate the delivery of functional CNOs to site of interest within cells. Moreover, through the optimization of chemical modifications with small molecules and biomolecules, these highly surface functionalized CNOs are expected to emerge as ideal platform for the preparation of sophisticated multi-functional smart materials capable of imaging, recognition, targeting, and drug delivery, a work currently in the focus of my research activities.

## 2.5 Efficient covalent ligation methodology of Isoquinolines onto Carbon Nano-onions (CNOs)

### 2.5.1 Introduction

The emission of fluorescence labelled CNMs is largely dependent on the chemical and photophysical nature of the implemented fluorophores. In addition, the linkage between the fluorophores and CNMs can play an important role, since it influences largely the interaction between the building blocks. In most cases, the emission intensity of a fluorophore bound to a CNMs lower than that of the free dye in solution. In the corresponding section of this review article, several examples will be presented where this effect is observed. Typically, the remaining fluorescence signal is intense enough for cellular imaging. The reduced fluorescence intensity can be led back to a high intrinsic absorption of the CNMs, especially when taking into account that most CNMs show plasmonic absorption over the whole spectral range. On the other hand, the quenching of the fluorophores photo-excited states by the CNM is observed. This can be due to different kinds of electronic interactions, involving energy or electron transfer events from the photo-excited chromophore to the CNM or vice versa. Amongst many examples in the literature, typical CNM based systems showing photo-induced electron transfer consist of CNTs in combination with phthalocyanines,<sup>8,9</sup> porphyrins,<sup>10</sup> and also boron azadipyromethenes.<sup>11</sup> Many of these CNT–dye-conjugates were successfully probed in antenna systems for solar cell application. For imaging, this fluorescence quenching is obviously a large drawback, which was overcome by developing synthetic strategies to electronically separate the fluorophore from the CNM. This can be accomplished, for example, by the introduction of molecular spacers, biomolecules or coatings between the fluorophore and the CNM.

We study this feature in collaboration with Prof. Riva's group. They have synthesized a library of furo[2,3-c]isoquinolines bearing a linker of different length and an amino group Boc protected (See Figure 10). Various examples illustrating this concept will be discussed in the next paragraph of this chapter.

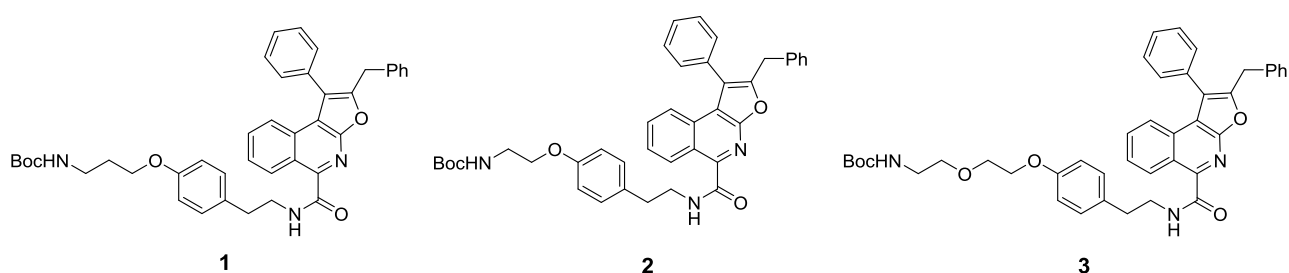


Figure 10. Library of Isochinolines employed for the conjugation with ox-CNOs.

In 2000, Cushman et al.<sup>12</sup> synthesized and evaluated a series of indenoisoquinolines as topoisomerase I (top1) inhibitors and as cytotoxic agents in human cancer cell cultures. The synthesis relied on the condensation of substituted Schiff bases with homophthalic anhydrides to produce cis-3-aryl-4-carboxyisoquinolones that were cyclized to indenoisoquinolines in the presence of thionyl chloride. Both top1 inhibitory activity and cytotoxicity has been found maximized in a single compound (See Figure 11), which have been proved to be a very potent top1 inhibitor.

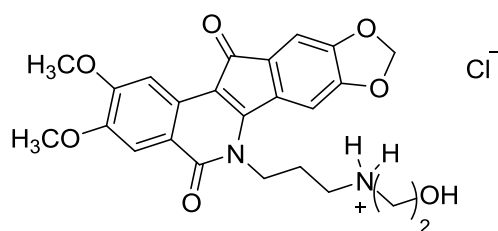


Figure 11. Indeno[1,2-c]isoquinoline hydrochloride: cytotoxic topoisomerase I inhibitor.

Structurally related indenoisoquinolines would hopefully lead to novel anticancer agents that act through top1 inhibition. In 2015, Carta et al.<sup>13</sup> reported the synthesis of a small library of 3-ethylpyrrolo[3,2-f]quinoline derivatives to identify a novel class of dyes for use in biological studies. According to the spectroscopic analyses performed to evaluate the fluorimetric parameters of quantum yield and brightness, 7-methyl- and 6,7-dimethylpyrroloquinolin(9)one derivatives were found to be the best blue luminescent dyes for biological applications. To enhance the luminescence profiles and to obtain probes that could be conjugated to functional groups of supramolecular drug delivery systems, these compounds were further modified at position 3 to obtain 3-heptanoic acid and 3-aminohexylpyrroloquinolin(9)one methylated derivatives. The most brilliant 6,7-dimethyl-3-aminohexylpyrroloquinolinone hydrochloride was conjugated to pullulan, a biocompatible polysaccharide used to produce colloidal systems for drug delivery. Comparative studies showed that this compound can be properly exploited as a blue fluorescent label in biological investigations, namely cell trafficking and pharmacokinetics/biodistribution studies. These molecules possess higher fluorescence efficiency than commercial dyes in biological media, making them suitable alternatives to commercially available products in current use.

Recently, Prof. Riva's group have developed an efficient synthesis of a rather unexplored heterotricyclic scaffold of furo[2,3-*c*]isoquinolines through a two-step procedure from simple or readily available starting materials (Figure 12).<sup>14</sup>

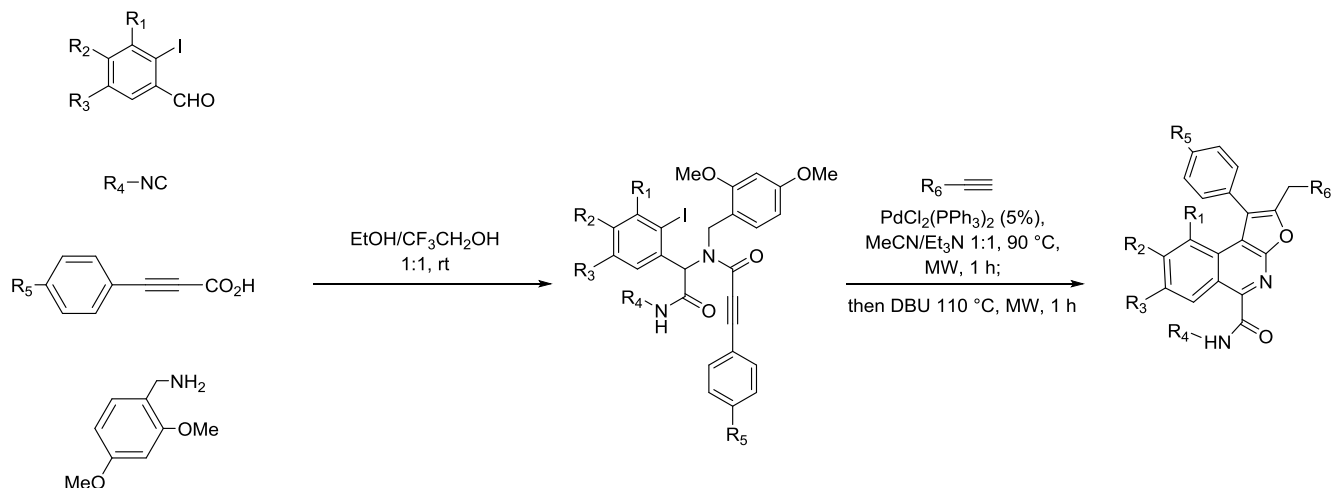


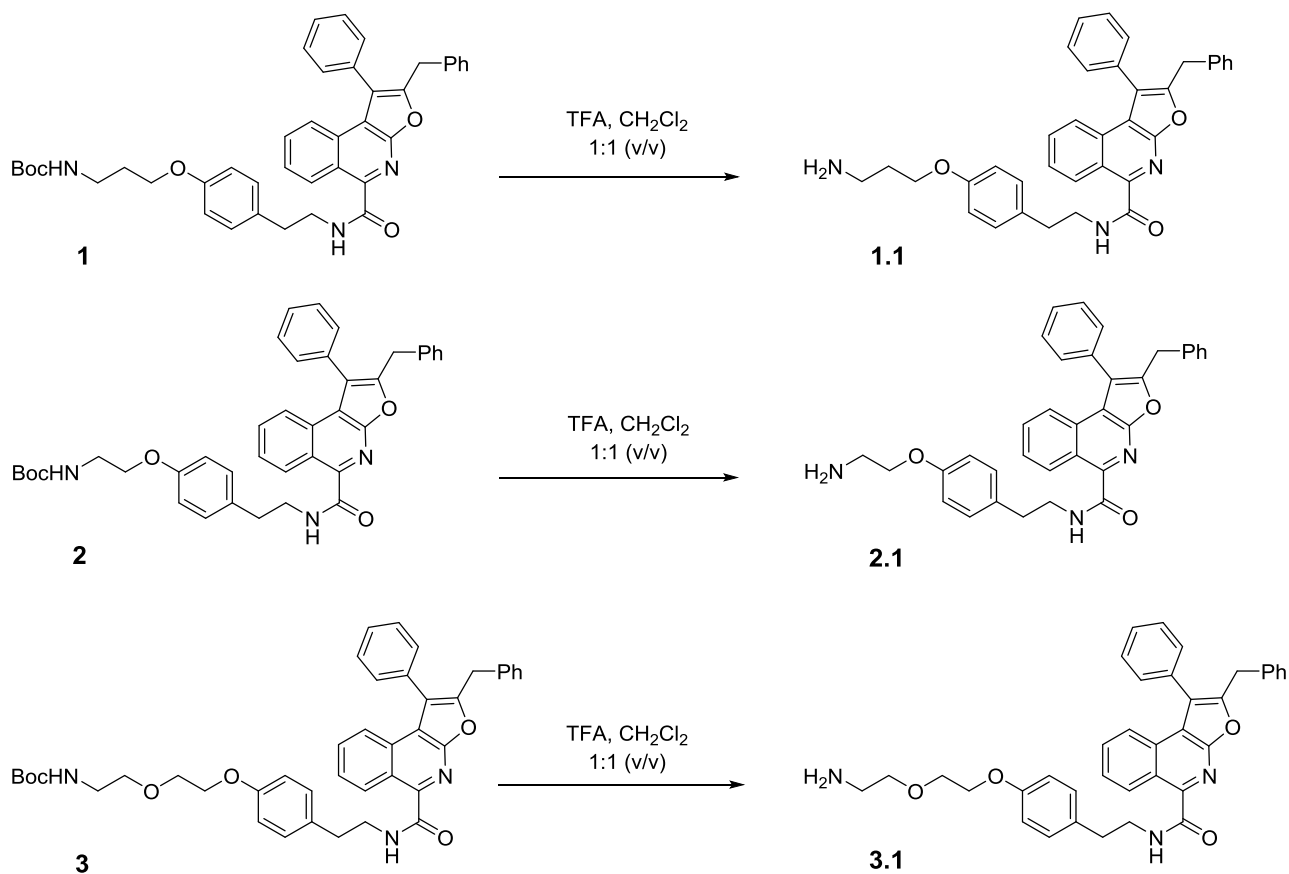
Figure 12. Synthesis of furo[2,3-*c*]isoquinolines by two-step procedure. Reprinted with permission of reference [14].

This approach is characterized by an Ugi multicomponent reaction furnishing the substrate for a Pd-catalyzed insertion-alkynylation-cycloisomerization cascade to provide the final compounds in moderate to high yield. All the furo[2,3-*c*]isoquinolines synthesized with this method display pronounced blue luminescence in solution or in the solid state. Furthermore, the photophysical characterization by absorption and emission spectroscopy reveals that the emission wavelength, Stokes shift, and fluorescence intensity is largely dependent on the donor substitution pattern on the isoquinoline part of the tricyclic core and also to a minor extent by the 4-aryl substituent on the furomoiety. Studies to explore the functionalization and modulate the photophysical properties of this novel tricyclic luminophore system are currently underway.

## 2.5.2 Experimental

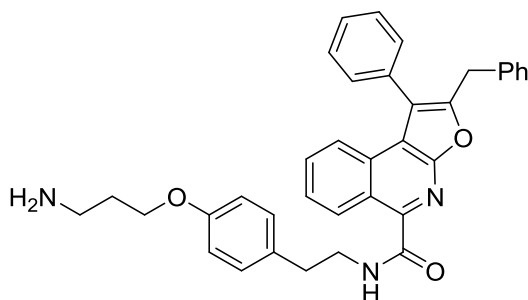
### 2.5.2.1 Deprotection of Blue Emissive Isoquinolines

In collaboration with Prof. Riva's group (UniGe), a highly reproducible ligation methodology for covalent modification of CNOs with blue emissive isoquinolines<sup>14,15</sup> has been developed. Following the Boc deprotection with TFA in CH<sub>2</sub>Cl<sub>2</sub> 1:1 (v/v) affording the isoquinoline with the deprotected linker containing a free amine (Scheme 2), the coupling between the fluorophore and the carboxylic acid groups on the surface of the CNOs to furnish the target isoquinoline-CNO was investigated.



Scheme 2. Boc deprotection of three isoquinolines bearing linker differing in length.

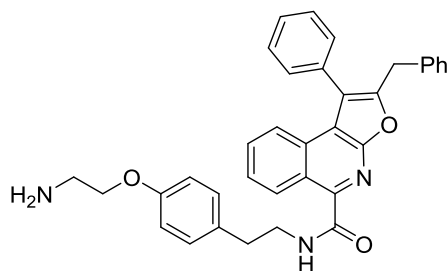
### 2.5.2.2 Characterization of Isoquinoline 1.1



<sup>1</sup>H NMR (600 MHz, CDCl<sub>3</sub>) δ 9.53 (d, J = 8.5 Hz, 1H), 8.21 (t, J = 5.7 Hz, 1H), 7.77 (d, J = 8.4 Hz, 2H), 7.60 – 7.47 (m, 8H), 7.31 – 7.28 (m, 3H), 7.26 – 7.21 (m, 3H), 7.16 (d, J = 7.2 Hz, 2H), 6.80 (s, 2H), 4.11 (s, 2H), 4.05 (s, 2H), 3.71 (d, J = 6.4 Hz, 2H), 3.26 (s, 2H), 2.91 (t, J = 7.1 Hz, 2H), 2.15 (s, 2H). <sup>13</sup>C NMR (151 MHz, CDCl<sub>3</sub>) δ 166.74 (s), 156.79 (s), 154.93 (s), 154.62 (s), 142.49 (s), 137.33 (s), 133.18 (s), 132.38 (s), 132.21 (s), 130.54 (s), 130.35 (s), 130.10 (s), 129.24 (s), 128.82 (dd, J = 23.0, 14.6 Hz), 127.06 (s), 126.64 (s), 125.19 (s), 122.81 (s), 119.79 (s), 116.78 (s), 114.89 (s), 77.45 (s), 77.24 (s), 77.03 (s), 66.46 (s), 41.62 (s), 39.32 (s), 35.19 (s), 33.01 (s), 29.93 (s), 26.89 (s), 1.35 – 0.91 (m). HRMS (APCI+) m/z calcd for C<sub>36</sub>H<sub>34</sub>N<sub>3</sub>O<sub>3</sub> [M + H]<sup>+</sup> 556.261863, found 556.259468.

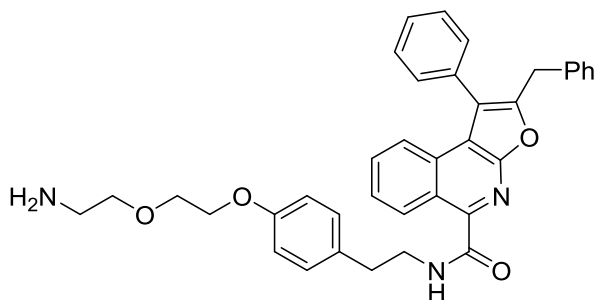


### 2.5.2.3 Characterization of Isoquinoline 2.1



<sup>1</sup>H NMR (600 MHz, CDCl<sub>3</sub>) δ 9.54 (d, J = 6.1 Hz, 1H), 8.16 (s, 1H), 7.75 (d, J = 8.2 Hz, 1H), 7.60 – 7.44 (m, 6H), 7.33 – 7.26 (m, 3H), 7.26 – 7.19 (m, 3H), 7.13 (d, J = 25.3 Hz, 2H), 6.79 (s, 2H), 4.19 – 4.01 (m, 4H), 3.76 – 3.61 (m, 2H), 3.30 (s, 2H), 2.87 (s, 2H). <sup>13</sup>C NMR (151 MHz, CDCl<sub>3</sub>) δ 166.33 (s), 156.17 (s), 154.61 (s), 154.43 (s), 142.42 (s), 137.16 (s), 132.95 (s), 132.41 (s), 132.22 (s), 130.34 (s), 130.02 (d, J = 18.0 Hz), 129.01 (s), 128.86 – 128.58 (m), 128.44 (s), 126.84 (s), 126.38 (s), 124.99 (s), 122.53 (s), 119.57 (s), 116.45 (s), 114.73 (s), 77.24 (s), 77.03 (s), 76.82 (s), 63.63 (s), 41.30 (s), 35.06 (s), 32.79 (s), 29.72 (s), 14.17 (d, J = 9.4 Hz). HRMS (APCI+) m/z calcd for C<sub>35</sub>H<sub>32</sub>N<sub>3</sub>O<sub>3</sub>[M + H]<sup>+</sup> 542.244610, found 542.243818.

### 2.5.2.4 Characterization of Isoquinoline 3.1



<sup>1</sup>H NMR (600 MHz, CDCl<sub>3</sub>) δ 9.52 (s, 1H), 8.22 (s, 1H), 7.78 (d, J = 7.9 Hz, 2H), 7.63 – 7.45 (m, 6H), 7.34 – 7.11 (m, 8H), 6.84 (s, 2H), 4.13 (s, 4H), 3.62 (d, J = 135.5 Hz, 6H), 3.18 (s, 2H), 2.92 (s, 2H). <sup>13</sup>C NMR (151 MHz, CDCl<sub>3</sub>) δ 157.08 (s), 154.65 (s), 154.41 (s), 142.59 (s), 137.14 (s), 132.99 (s), 132.17 (s), 131.87 (s), 130.33 (s), 130.19 (s), 129.95 (s), 129.04 (s), 128.69 (d, J = 13.6 Hz), 128.49 (s), 126.86 (s), 126.43 (s), 124.99 (s), 122.58 (s), 119.62 (s), 116.52 (s), 115.05 (s), 77.25 (s), 77.04 (s), 76.83 (s), 70.12 (s), 67.31 (s), 66.59 (s), 41.34 (s), 34.93 (s), 32.81 (s), 29.72 (s), 1.04 (s). HRMS (APCI+) m/z calcd for C<sub>37</sub>H<sub>36</sub>N<sub>3</sub>O<sub>4</sub> [M + H]<sup>+</sup> 586.272722, found 586.270033.

The coupling of blue emissive isoquinolines onto CNOs have been obtained by using a reaction involving the amide bond formation between the amino groups of the isoquinolines and the carboxylic acids groups on the surface of the CNOs. The modification of CNOs by chemical oxidation of the defects on the outer shell of these carbon nanoparticles results in an extensive surface functionalization with carboxyl groups. The functionalized CNOs display high emission properties due to the presence of high surface coverage of carboxylic acid groups and the good functionalization provided.

#### **2.5.2.5 Synthesis of 1-CNO**

A dispersion of ox-CNO (10 mg) was prepared by ultrasonication (20 min at 37 kHz) in a mixture (30 mL) of dry THF and DMF (2:1). The mixture was deoxygenated under N<sub>2</sub> and 20 mg (0.20 mmol) of DMAP, 20 mg (0.21 mmol) of N-Hydroxysulfosuccinimide (sulfo-NHS) and 35 mg (0.22 mmol) of EDC-HCl were added. The reaction mixture was briefly sonicated and after the addition of 20 mg of isoquinoline 1.1 heated under reflux for 4 days under N<sub>2</sub>. After cooling to RT, the CNOs were redispersed in DMF, filtered off on a nylon membrane (pore size 0.2 μm) and washed with THF, DMSO and acetone in order to completely remove the isoquinoline physically adsorbed on the surface of the CNOs. The resulting material was re-dispersed in DMSO, filtered again and centrifuged to wash out any non-covalently bound species. 12 mg of 1-CNO were recovered as black powder after drying under air for one day (Scheme 3).

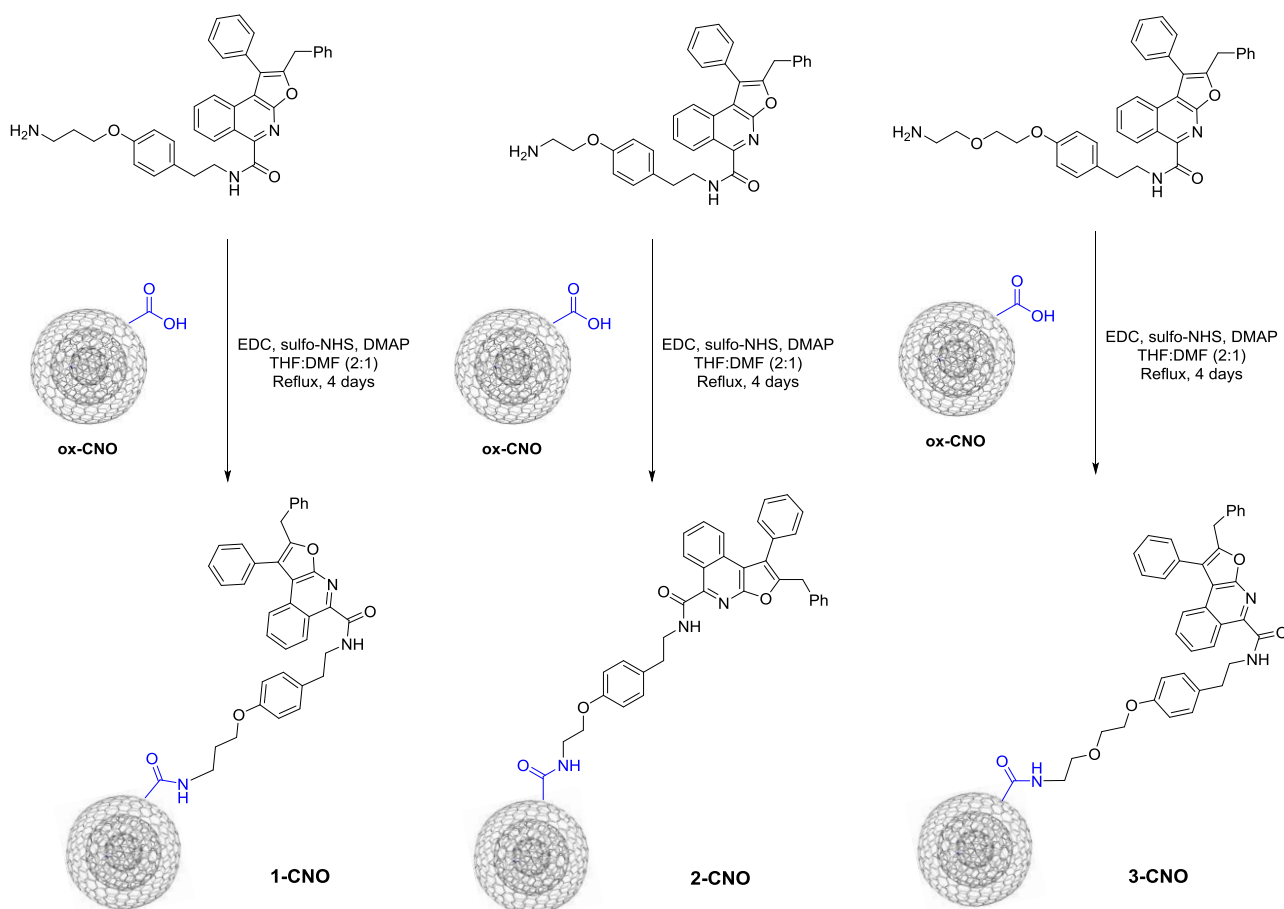
#### **2.5.2.6 Synthesis of 2-CNO**

A dispersion of ox-CNO (15 mg) was prepared by ultrasonication (20 min at 37 kHz) in a mixture (30 mL) of dry THF and DMF (2:1). The mixture was deoxygenated under N<sub>2</sub> and 20 mg (0.20 mmol) of DMAP, 20 mg (0.21 mmol) of N-Hydroxysulfosuccinimide (sulfo-NHS) and 35 mg (0.22 mmol) of EDC-HCl were added. The reaction mixture was briefly sonicated and after the addition of 20 mg of isoquinoline 2.1 heated under reflux for 4 days under N<sub>2</sub>. After cooling to RT, the CNOs were redispersed in DMF, filtered off on a nylon membrane (pore size 0.2 μm) and washed with THF, DMSO and acetone in order to completely remove the isoquinoline physically adsorbed on the surface of the CNOs. The resulting material was re-dispersed in DMSO, filtered again and centrifuged to wash out any non-covalently bound species. 14 mg of 2-CNO were recovered as black powder after drying under air for one day (Scheme 3).

#### **2.5.2.7 Synthesis of 3-CNO**

A dispersion of ox-CNO (15 mg) was prepared by ultrasonication (20 min at 37 kHz) in a mixture (30 mL) of dry THF and DMF (2:1). The mixture was deoxygenated under N<sub>2</sub> and 20 mg (0.20 mmol) of DMAP, 20 mg (0.21 mmol) of N-Hydroxysulfosuccinimide (sulfo-NHS) and 35 mg (0.22 mmol) of EDC-HCl were added. The reaction mixture was briefly sonicated and after the addition of 20 mg of isoquinoline 3.1 heated under reflux for 4 days under N<sub>2</sub>. After cooling to RT, the CNOs were redispersed in DMF, filtered off on a nylon membrane (pore size 0.2 μm) and washed with THF, DMSO and acetone in order to completely remove the isoquinoline physically adsorbed on the surface of the CNOs. The resulting material was re-dispersed in DMSO, filtered again and centrifuged to wash out any non-covalently bound species. 12 mg of 3-CNO were recovered as black powder after drying under air for one day (Scheme 3).

The successful surface modification of the p-CNO with carboxylic acid groups to yield ox-CNO and the coupling with isoquinolines to obtain blue emissive CNOs, was confirmed by absorption and emission studies, thermogravimetric analysis and dynamic light scattering measurements.



Scheme 3. Synthetic procedure for preparation of isoquinolines decorated ox-CNOs.

## 2.5.3 Results and Discussion

### 2.5.3.1 Blue Emissive Isoquinolines-CNOs Characterization

The high degree of surface functionalization of 1-CNO, 2-CNO and 3-CNO in comparison to the ox-CNO, was observed by TGA analysis. TGA performed in air shows thermal decomposition of surface organics at 401 °C, 380 °C and 392 °C for 1-CNO, 2-CNO and 3-CNO respectively followed by the decomposition of the CNO core at around 551 °C (Figure 14, top section). In order to calculate the average number of functional groups per onion, it has been assumed based on TEM observations, that CNOs contain, on average, six shells and that the core is a  $C_{60}$  fullerene. The number of carbon atoms in each shell is estimated as:  $60 \times n^2$ , where  $n$  is the number of shells that we are considering. The outer 6<sup>th</sup> shell contains 2160 carbon atoms and the total number of carbon atoms in the onion is 5460. Therefore, the average mass of onions is  $5460 \times 12 = 65520 \text{ g mol}^{-1}$ . Calculating the mass of the functional groups attached to the CNO is possible to estimate the number of functionalities per onion. According to that, 79, 63 and 123 functionalities have been estimated for 1-CNO, 2-CNO and 3-CNO respectively.

The emission properties of the isoquinoline labelled CNOs were tested in DMSO. Upon photoexcitation at 350 nm of a dispersion of 1-CNO, 2-CNO and 3-CNO in DMSO, an intense emission band was observed with a maximum at 400 nm, 408 nm and 398 nm for 1-CNO, 2-CNO and 3-CNO respectively (Figure 14, bottom section). The concentration of isoquinoline 1 in a  $10 \mu\text{g mL}^{-1}$  dispersion of 1-CNO in DMSO was determined to be about  $1.13 \times 10^{-6}$  M by absorption (Figure 14, middle section). A concentration of  $4.65 \times 10^{-5}$  M and  $6.83 \times 10^{-7}$  M was estimated for 2-CNO and 3-CNO respectively (Figure 14, middle section). The isoquinolines loading onto carbon-nanoonion is in comparison with the functionalization previously carried on with green and red emitting dyes.<sup>16, 17</sup> Moreover, from the fluorescence spectra, it is notable a quenching of 20% for 1-CNO, 15% for 2-CNO and 20% for 3-CNO in comparison with the free blue emissive dye at the same absorption supporting the value obtained with the UV-spectroscopy.

The size of the clusters formed were investigated by dynamic light scattering (DLS) in DMSO at a concentration of  $10 \mu\text{g mL}^{-1}$ . DLS is driven by collisions with the solvent molecules present, which are in constant movement due to their thermal energy. According to that, this measurement depends on the size of the particle core, the surface structures, particle concentration, and the type of ions in the medium. After 20 min sonication ox-CNO revealed an effective hydrodynamic diameter in DMSO of  $277 \pm 1$  nm. On the other hand 1-CNO, 2-CNO and 3-CNO revealed a hydrodynamic diameter in DMSO of  $390 \pm 1$  nm,  $546 \pm 5$  nm and  $332 \pm 2$  nm respectively, suggesting a good surface functionalization along with a better dispersion in solution and a lower size for particles bearing an extra oxygen in the linker (Figure 13).

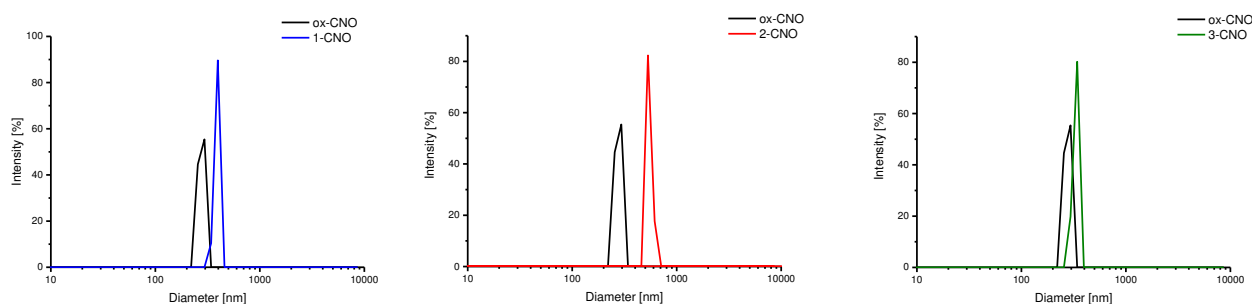


Figure 13. Effective hydrodynamic diameter obtained from dynamic light scattering (DLS) measurements of 1-CNO, 2-CNO and 3-CNO in DMSO at a concentration of  $10 \mu\text{g mL}^{-1}$ .

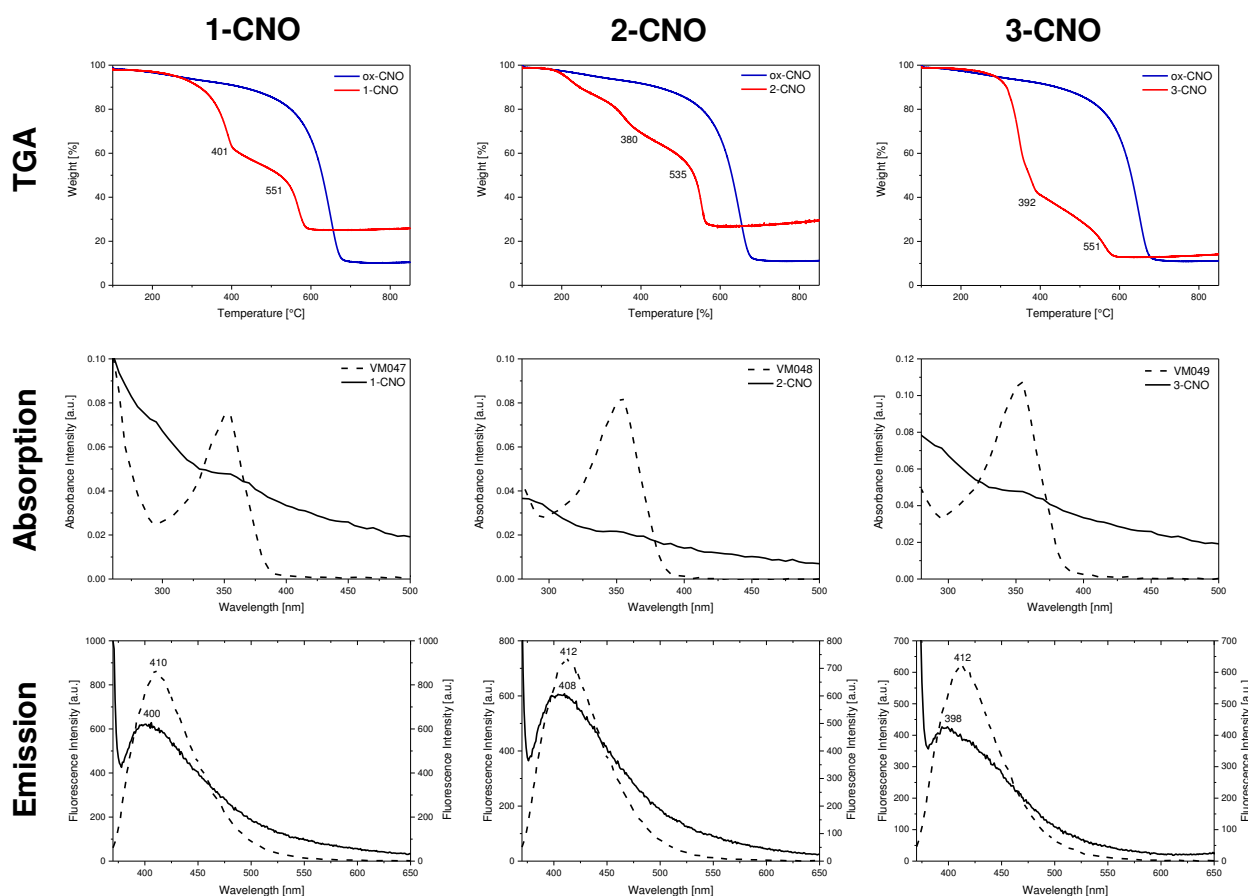


Figure 14. Characterization of the functionalized 1-CNO, 2-CNO and 3-CNO. (Top section) Thermogravimetric analysis of ox-CNO (blue), and 1-CNO, 2-CNO and 3-CNO (red). All experiments were run in air with a temperature rate of  $10\text{ }^{\circ}\text{Cmin}^{-1}$ . (Middle section) Absorption spectra of 1-CNO, 2-CNO and 3-CNO (solid line) and free isoquinoline 1, 2 and 3 (dotted line) in DMSO at a concentration of  $10\text{ }\mu\text{g mL}^{-1}$ . (Bottom section) Emission spectra ( $\lambda_{\text{exc}} = 350\text{ nm}$ ) of 1-CNO, 2-CNO and 3-CNO (solid line) and free isoquinoline 1, 2 and 3 (dotted line) in DMSO at a concentration of  $10\text{ }\mu\text{g mL}^{-1}$ .

## 2.5.4 Conclusion

In summary, we have demonstrated a versatile strategy for the preparation of highly surface modified CNOs by oxidation of the defects on the surface of CNOs and chemical functionalization of the carboxyl groups by amide coupling with isoquinolines which were never reacted before with CNOs. The intrinsic electronic, magnetic and optical properties of CNOs along with their high surface-to-volume ratio, chemical versatility and ease of manipulation, as well as their performance as a chemically robust platform render these functionalized CNOs valuable candidate for blue high emissive materials. Unfortunately, due to their low solubility in biological medium, they result unsuitable for biological applications. Despite that, the substitution pattern on the core of the isoquinoline with high polar functional groups such as sulfonamides, amines or carboxylic acid groups, often used in drugs to improve their solubility, could improve significantly their physico-chemical properties. This is a work currently in the focus of my group's research.

## 2.5.5 References

- (1) Kim, H. N.; Guo, Z.; Zhu, W.; Tian, H. *Chem. Soc. Rev.* **2011**, 40, 79-93.
- (2) Xu, Z.; Kim, S. K.; Yoon, J. *Chem. Soc. Rev.* **2010**, 39, 1457-1466.
- (3) Silva, A. P. De; Gunaratne, H. Q. N.; Gunnlaugsson, T.; Huxley, A. J. M.; Mccoy, C. P.; Rademacher, J. T.; Rice, T. E. *Chem. Rev.* **1997**, 97, 1515.
- (4) Duke, R. M.; Veale, E. B.; Pfeffer, F. M.; Kruger, P. E.; Gunnlaugsson, T. *Chem. Soc. Rev.* **2010**, 39, 3936.
- (5) Gonçalves, M.; Sameiro, T.; *Chem. Rev.* **2009**, 109, 190-212.
- (6) Zhang, J.; Yang, P. L.; Gray, N. S. *Nat. Rev. Cancer* **2009**, 9, 28-39.
- (7) Gunaseelan, S.; Gunaseelan, K.; Deshmukh, M.; Zhang, X.; Sinko, P. J. *Adv. Drug Deliv. Rev.* **2010**, 62 (4-5), 518-531.
- (8) Bartelmess, J.; Ballesteros, B.; Torre, G. De; Kiessling, D.; Campidelli, S.; Prato, M.; Guldi, D. M. *J. Am. Chem. Soc.*, **2010**, 132, 16202-16211.
- (9) Bottari, G.; Torre, G. De; Guldi, D. M. *Chem. Rev.*, **2010**, 110, 6768-6816.
- (10) Hasobe, T.; Fukuzumi, S.; Kamat, P. V. *J. Am. Chem. Soc.*, **2005**, 127, 11884-11885.
- (11) Flavin, K.; Lawrence, K.; Bartelmess, J.; Tasiar, M.; Navio, C.; Bittencourt, C.; Shea, D. F. O.; Guldi, D. M.; Giordani, S. *ACS Nano*, **2011**, 5, 1198-1206.
- (12) Cushman, M.; Jayaraman, M.; Vroman, J. A.; Fukunaga, A. K.; Fox, B. M.; Kohlhagen, G.; Strumberg, D.; Pommier, Y. *J. Med. Chem.* **2000**, 43, 3688-3698.
- (13) Carta, D.; Balasso, A.; Caliceti, P.; M. G. Ferlin *ChemMedChem* **2015**, 10, 1846 - 1862.
- (14) Moni, L.; Gers-Panther, C.F.; Anselmo, M.; Müller, T. J. J.; Riva R. *Chem. Eur. J.* **2016**, 22, 2020-2031
- (15) Moni, L.; Denißen, M.; Valentini, G.; Muller, T. J. J.; Riva, R.; *Chem. Eur. J.* **2015**, 21, 753 - 762.
- (16) Frasconi, M.; Maffei, V.; Bartelmess, J.; Echegoyen, L.; Giordani, S. *Methods Appl. Fluoresc.* **2015**, 3 (4), 44005.
- (17) Giordani, S.; Bartelmess, J.; Frasconi, M.; Biondi, I.; Cheung, S.; Grossi, M.; Wu, D.; Echegoyen, L.; O'Shea, D. F. *J. Mater. Chem. B* **2014**, 2 (42), 7459-7463.

### 3. CNO as vaccine carrier

#### 3.1 Introduction

The modification of nanomaterials with biologically active substrates such as glycopeptides, glycoproteins and antibodies offers a fascinating platform technology for developing targeted nanotherapeutics and vaccine candidates. In the second step, the development of a general synthetic strategy for CNO modification using cysteine as a ligation site for peptide and protein conjugation has been investigated (Figure 1). The 'proof of concept' has been demonstrated using a model synthetic glycopeptide substrate (prepared in collaboration with Prof. Scanlan) and reproduced using the native bovine serum albumin protein (BSA).

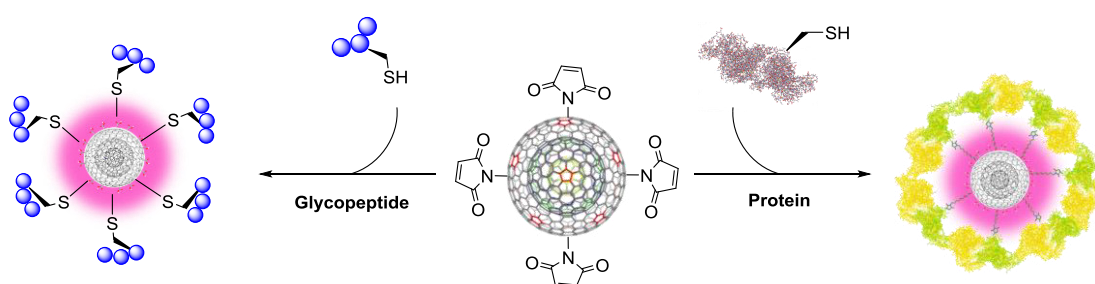


Figure 1. Schematic representation of the bioconjugations investigated.

In order to visualize the CNOs *in vitro* and to monitor the localization pattern of the glycopeptide modified CNOs, a fluorescently labelled glycopeptide for the preliminary studies was synthesized. Given the numerous biological applications associated with synthetic glycopeptides, the ability to transfer these compounds into the cells using nano-platforms offers fascinating prospects for the development of these compounds as nano-therapeutics. Therefore, the application of maleimide functionalised CNOs as general carrier substrates for cysteine containing glycopeptides and proteins might offer an extremely innovative platform technology. As a medical nanoplatform, the design of multifunctional carbon nanomaterials for targeted bioimaging and drug delivery, in which carbon nano-onions may act as a carrier has been developed to strengthen the delivery of functional onions to sites of clinical interest.

### 3.1.1 Nanovaccinology

Vaccines have a tremendous global impact on human health, from the near-eradication of several contagious diseases to the annual prevention of recurrent epidemics in a variety of vulnerable populations. However, most vaccines in use today were developed using techniques pioneered more than 100 years ago and do not reflect the full potential of the field. With the introduction of emerging biotechnologies such as genetic engineering, rapid advances have been made in the design, synthesis, and application of modern vaccines against a myriad of preventable diseases. Recently, nanotechnology has been applied to address the clear biomimicry challenge inherent to the next generation of more potent and sophisticated adjuvants. Although early adjuvants, such as aluminum hydroxide, have been successful in stimulating the immune response, the advent of nanoscale antigen delivery platforms has catalyzed the transition from these simple immunoactive chemical agents to adjuvants that can engage and direct immune responses more akin to the methods employed by pathogens themselves.<sup>1,2,3,4,5,6,7</sup> Vaccine adjuvants are an essential component of vaccine design, helping to generate immunity to pathogen antigens in the absence of infection. Recent advances in nanoscale engineering have created a new class of particulate bionanotechnology that uses biomimicry to better integrate adjuvant and antigen. These pathogen-like particles, or PLPs, can come from a variety of sources, ranging from fully synthetic platforms to biologically derived, self-assembling systems. By employing molecularly engineered targeting and stimulation of key immune cells, recent studies utilizing PLPs as vaccine delivery platforms have shown great promise against high-impact, unsolved vaccine targets ranging from bacterial and viral pathogens to cancer and addiction.<sup>3,8</sup>

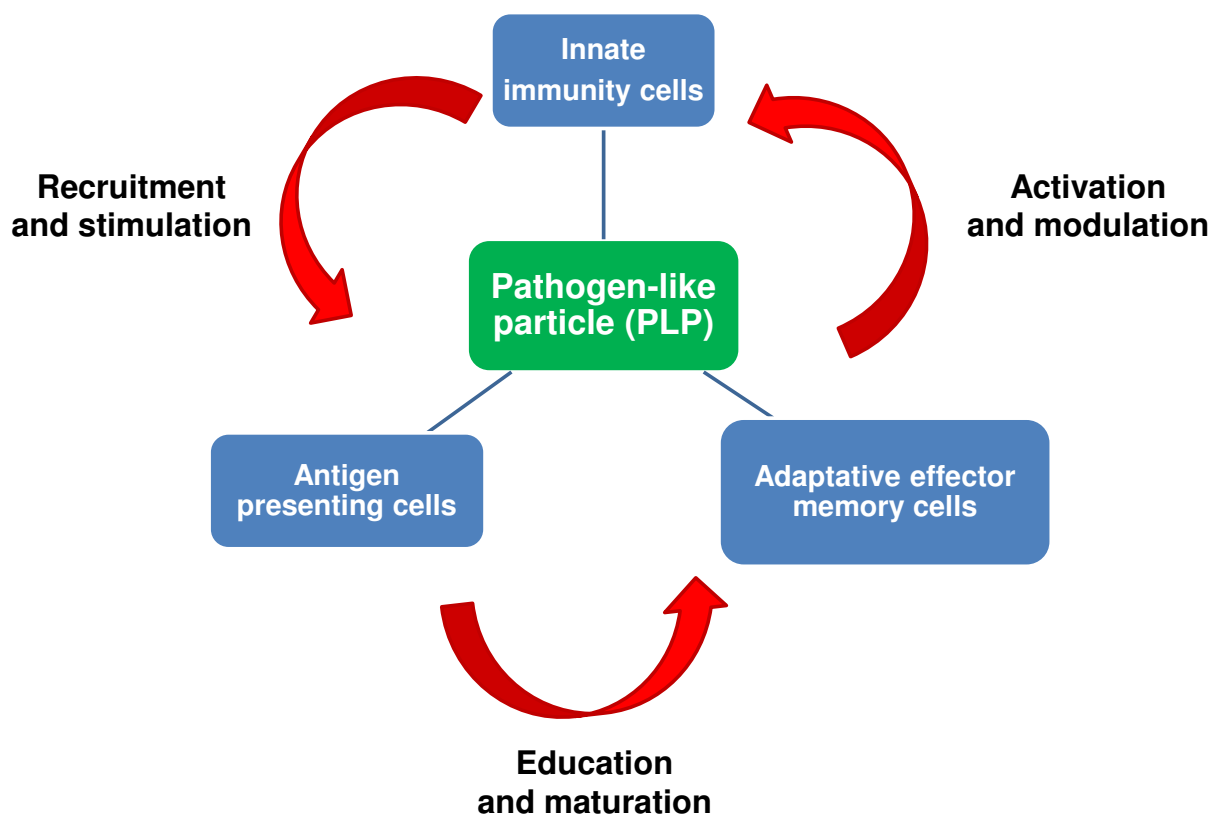


Figure 2. Immunostimulation routes of synthetic nanovaccine carriers.



Soluble antigens, independent of some larger delivery vector, suffer from reduced uptake by APCs and poor immunogenicity. These fundamental flaws have led to the development of particle-based vaccine carriers that can more closely mimic the physiochemical characteristics of natural pathogens, enhancing antigen delivery to the immune system<sup>9</sup>. PLP carriers can be formulated using nanoparticles created from biocompatible polymers, such as polylactic acid (PLA) and poly(lactic-co-glycolic) acid (PLGA), liposomes, and even simple lipid emulsions.<sup>8</sup> Antigens are then either encapsulated by, or integrated onto the surface of, these particles. Particle-based delivery is a promising technology due to its ability to target APCs such as dendritic cells (DCs) and stimulate antigen uptake, simultaneously deliver antigens and co-stimulatory signals, and generate strong and distinct immune responses (Figure 2). Furthermore, each of these characteristics may be finely tuned to the specific needs of the vaccine by varying the physiochemical attributes of the particle.

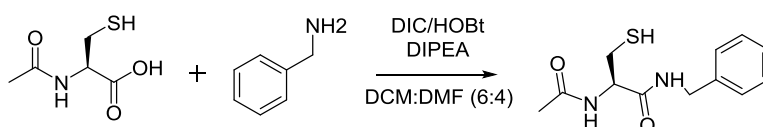
Nanovaccinology has applications in both prophylactic and therapeutic approaches and can be used to either increase antigen processing or presentation and/or as an immunostimulatory adjuvant.<sup>10,11</sup> This approach offers many advantages over traditional vaccine design; it has the potential to overcome the limitations associated with conventional vaccines (weak immunogenicity, intrinsic in vivo instability, toxicity and the requirement of multiple administrations).<sup>12</sup> The enhanced humoral and cellular immune response that is elicited by nano based vaccines is due to the smaller size – which increases uptake by phagocytic cells, the gut-associated lymphoid tissue, and the mucosa-associated lymphoid tissue. This subsequently leads to enhanced antigen recognition and presentation.<sup>12</sup> Surface modification of these nanocarriers with targeting moieties (peptides, carbohydrates, or antibodies) can facilitate specific and selective immune responses by targeting specific receptors on the surface of various immune cells.<sup>13,14</sup> An additional benefit of incorporating nanoparticles in vaccine formulations is accomplishing slow and sustained release of antigens or adjuvants.<sup>10,12</sup> Nanovaccines can also eliminate the requirement for cold-chain transport or storage as the formulation can be lyophilized, thereby prolonging shelf-life over an increased range of temperatures (from 0°C to 4°C). Another major advantage of using nanoparticles in vaccine delivery is that the sizes of these particles are approximately the same as viruses and bacteria, which the immune system readily identifies. Distinct populations of APCs may be targeted simply by modulating particle size. Smaller particles (20–200 nm) are able to more easily target DCs residing in lymph nodes by exploiting interstitial circulation to access the lymphatic system, whereas larger particles (0.5–2 mm) remain at the injection site and are taken up by peripheral DCs and tissue-resident macrophages.<sup>15</sup>

## **3.2 Experimental**

### **3.2.1 Covalent Immobilization of Glycopeptides and Proteins onto Carbon Nanonions (CNOs)**

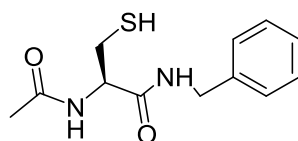
The functionalization of carbon-nanonions with biologically active peptide requires three consecutive steps: the synthesis of glycopeptide conjugated fluorophore, the surface functionalization of CNO and the conjugation of the fluorophore-glycopeptide on the activated CNO. Because the coupling reaction between the amino group of the fluorophore and the carboxylic group of the C-terminus cysteine residue of the glycopeptide is a crucial step in the chemical synthesis, a test reaction using N-acetyl L-cysteine and

benzylamine to mimic the larger substrate has been investigated (Scheme 1). It has been extremely useful to optimize the ligation chemistry before testing it on the final substrates. The DIC/HOBt coupling ligation has been performed and has been found to be very efficient with cysteine moieties. Indeed, reactions carried out on different scales have been tested giving an average isolated yield of 67%. The reaction consists of two consecutive steps. Firstly, the activation of the carboxylic acid moiety with diisopropylcarbodiimide (DIC) plays a key role. It gives the urea as byproduct which is water soluble and can be removed by aqueous extraction. Secondly, the formation of the amide bond occurs. Hydroxybenzotriazole (HOBt) that acts as the catalyst, forms an OBt esters which reacts with the primary amine giving the amide bond. Furthermore, an excess of N,N-Diisopropylethylamine (DIPEA) was added. This compound is a good base and a poor nucleophile and it is commonly used to improve the reaction yield.



Scheme 1. N-acetyl L-cysteine and benzylamine reaction.

### 3.2.2 Synthesis of Benzyl- N-acetyl L-cysteine

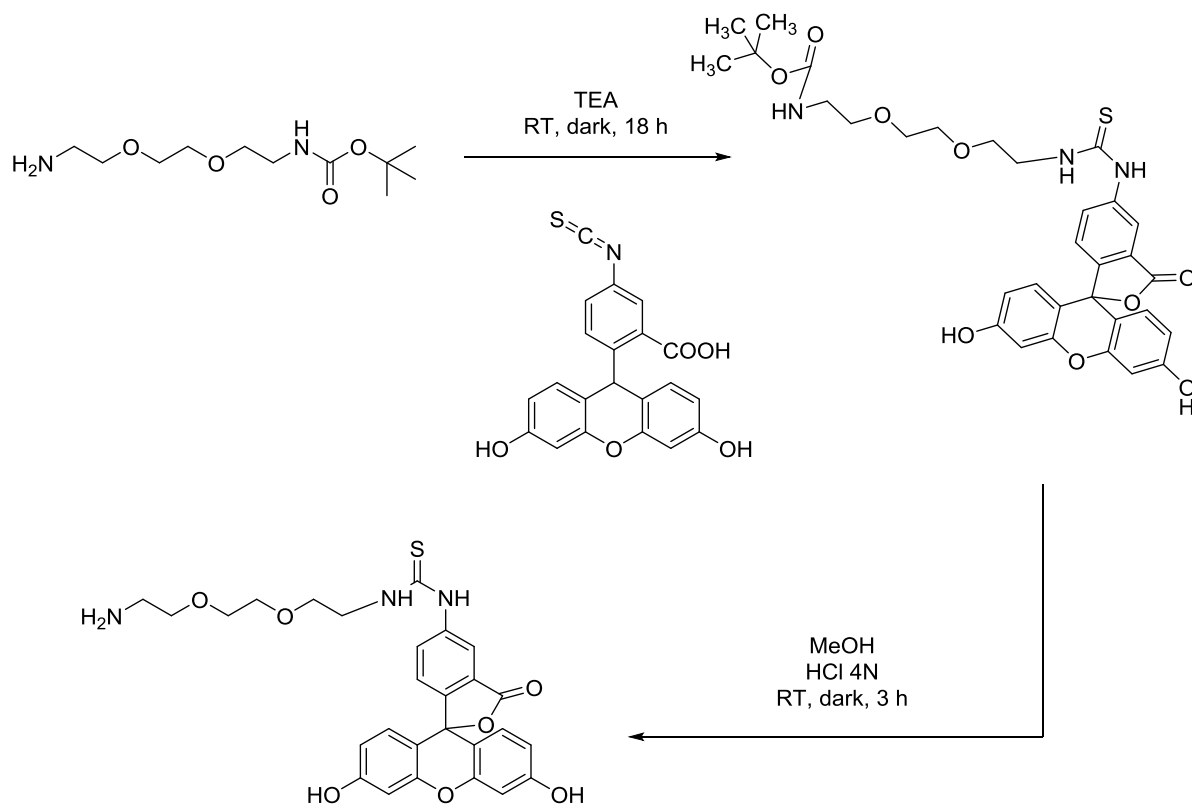


To N-Acetyl L-cysteine (50 mg, 0.31 mmol) in 60% dry DCM (30 mL), was added HOBt (45.9 mg, 0.34 mmol) and DIC (43.0 mg, 0.34 mmol) and the reaction was stirred at 0 °C for 1 h. The reaction was brought to rt and benzylamine (33.2 mg, 0.31 mmol) in 40% DMF (20 mL) and DIPEA (160.3 mg, 1.24 mmol) was added and stirred for 16 hours. The solvent was removed *in vacuo* and purification by flash chromatography (gradient elution from DCM to 3% methanol in DCM) afforded the final compound as a white solid in 68% yield.  $\delta$ H (400 MHz, MeOD) 7.29-7.23 (m, 5H, 5 x Ar-H), 4.48 (dd, 1H,  $J = 7.1$  and 5.8, H-3), 4.39 (s, 2H, Ar-CH<sub>2</sub>), 2.87 (dd, 1H,  $J = 13.9$  and 5.9, *HH*-10), 2.79 (dd, 1H,  $J = 13.9$  and 7.1, *HH*-10), 2.01 (s, 3H, CH<sub>3</sub>);  $\delta$ C (101 MHz, MeOD) 173.5 (C=O), 172.3 (C=O), 139.7 (C6), 129.5 (2 x Ar-H), 128.5 (2 x Ar-H), 128.2 (C9), 57.3 (C3), 44.1 (C5), 26.8 (C10), 22.5 (C1); HRMS (ES<sup>-</sup>)  $m/z$  calcd for C<sub>12</sub>H<sub>16</sub>N<sub>2</sub>O<sub>2</sub>S [M - H]<sup>-</sup> 252.0932, found 251.0862.

### 3.2.3 Synthesis of functionalized fluorescein

Once the peptide coupling reaction has been optimised on the model substrate, the ligation between the peptide and the fluorophore was carried out (Scheme 3). It is anticipated that the ligation reaction to form the target, fluorescently labelled glycopeptide has been carried out once the synthesis of the fluorophore linker has been performed. Following the Boc deprotection with HCl affording the fluorescein with the deprotected

linker containing a free amine (Scheme 2), the coupling between the fluorophore and the glycopeptide to furnish the target fluorescently labelled glycopeptide was investigated.

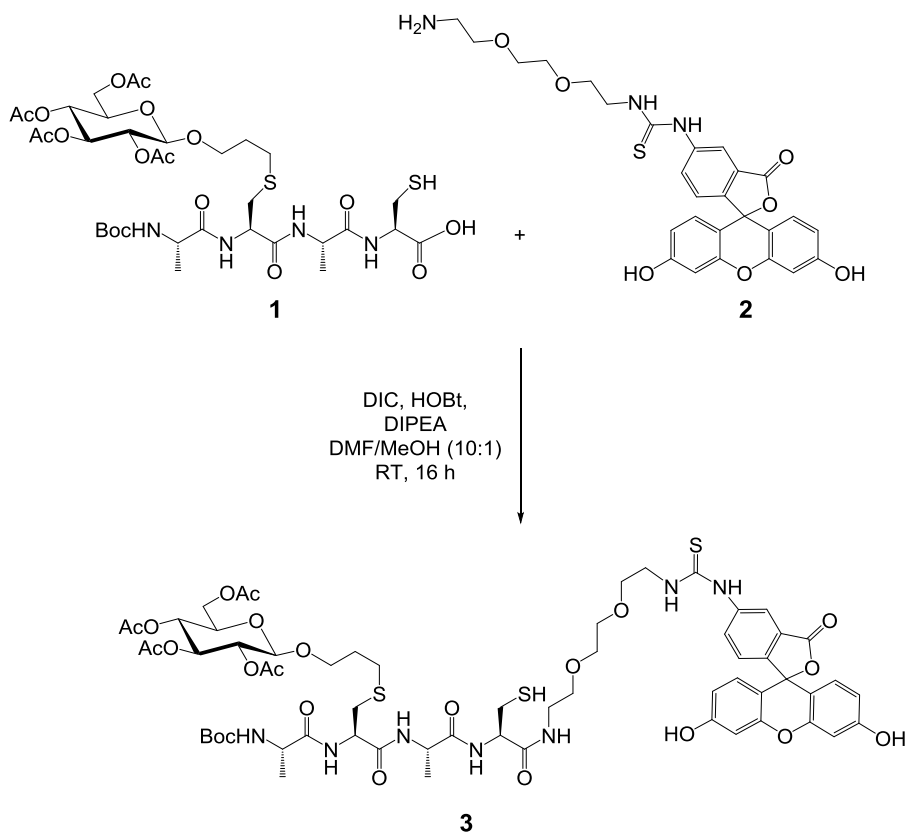


Scheme 2. Synthesis of functionalized fluorescein.

Synthesis of functionalized fluorescein. To a solution of Boc monoprotected 2,2'-(ethylenedioxy)bis(ethylamine) (166 mg, 0.67 mmol), in dry DCM (30 mL) was added FITC (200 mg, 0.51 mmol) in dry DMF (20 mL) and TEA (250  $\mu$ L, 1.53 mmol). The reaction mixture was stirred at room temperature, in the dark, for ca. 18 h. After reaction completion, the solvent was evaporated under reduced pressure and the crude product dissolved in MeOH (10 mL), and HCl 4 N in dioxane (5 mL) was added. The mixture was stirred at room temperature in the dark for 1 h, monitoring the reaction by TLC. The solvent was evaporated under reduced pressure and purification by flash chromatography (gradient elution in ethylacetate to methanol in ethylacetate) afforded the final product in 78% yield.<sup>1</sup> (orange solid). <sup>1</sup>H NMR (400 MHz, methanol-d<sub>4</sub>)  $\delta$  8.17 (s, 1H, Ar-H), 7.67 (d,  $J$  = 7.7 Hz, 1H, Ar-H), 7.01 (d,  $J$  = 8.2 Hz, 1H, Ar-H), 6.82 (d,  $J$  = 8.9 Hz, 2H, Ar-H), 6.70 (s, 2H, Ar-H), 6.58 (d,  $J$  = 8.8 Hz, 2H, Ar-H), 3.58 (s,  $J$  = 23.3 Hz, 2H, CH<sub>2</sub>NHCS), 3.53 – 3.43 (m, 8H, CH<sub>2</sub>O), 2.91 (s, 2H, CH<sub>2</sub>NH<sub>2</sub>). <sup>13</sup>C NMR (101 MHz, methanol-d<sub>4</sub>):  $\delta$  181.9 (C=S), 168.7 (C=O), 164.8, 155.7, 142.0 (C-Ar), 130.8, 129.2, 126.9, 115.6, 113.16, 102.4 (CH-Ar), 70.3, 69.1, 66.8 (CH<sub>2</sub>OCH<sub>2</sub>), 44.1 (CH<sub>2</sub>)NHSNH, 39.5 (CH<sub>2</sub>NH<sub>2</sub>); HRMS (ES<sup>-</sup>)  $m/z$  calcd for C<sub>27</sub>H<sub>27</sub>N<sub>3</sub>O<sub>7</sub>S [M - H]<sup>-</sup> 537.1570, found 536.1497.

### 3.2.4 Synthesis of fluorescein-functionalized glycopeptide

The ligation reaction between the glycopeptide and the functionalized-fluorescein was investigated using the reaction conditions optimized for the model system previously described (Scheme 1). DIC/HOBt mediated coupling conditions were employed for the reaction. The ligation reaction was successful and the target compound was isolated and fully characterized by  $^1\text{H-NMR}$  and  $^{13}\text{C-NMR}$ . The yield for the ligation reaction was 78%. The proposed synthetic route for the preparation of a fluorescently labelled glycopeptide, suitable for CNO conjugation is outlined in Scheme 3. The DIC coupling reaction was compatible with the cysteine moiety of the glycopeptide and formation of the desired amide conjugate proceed in high yield (74%).



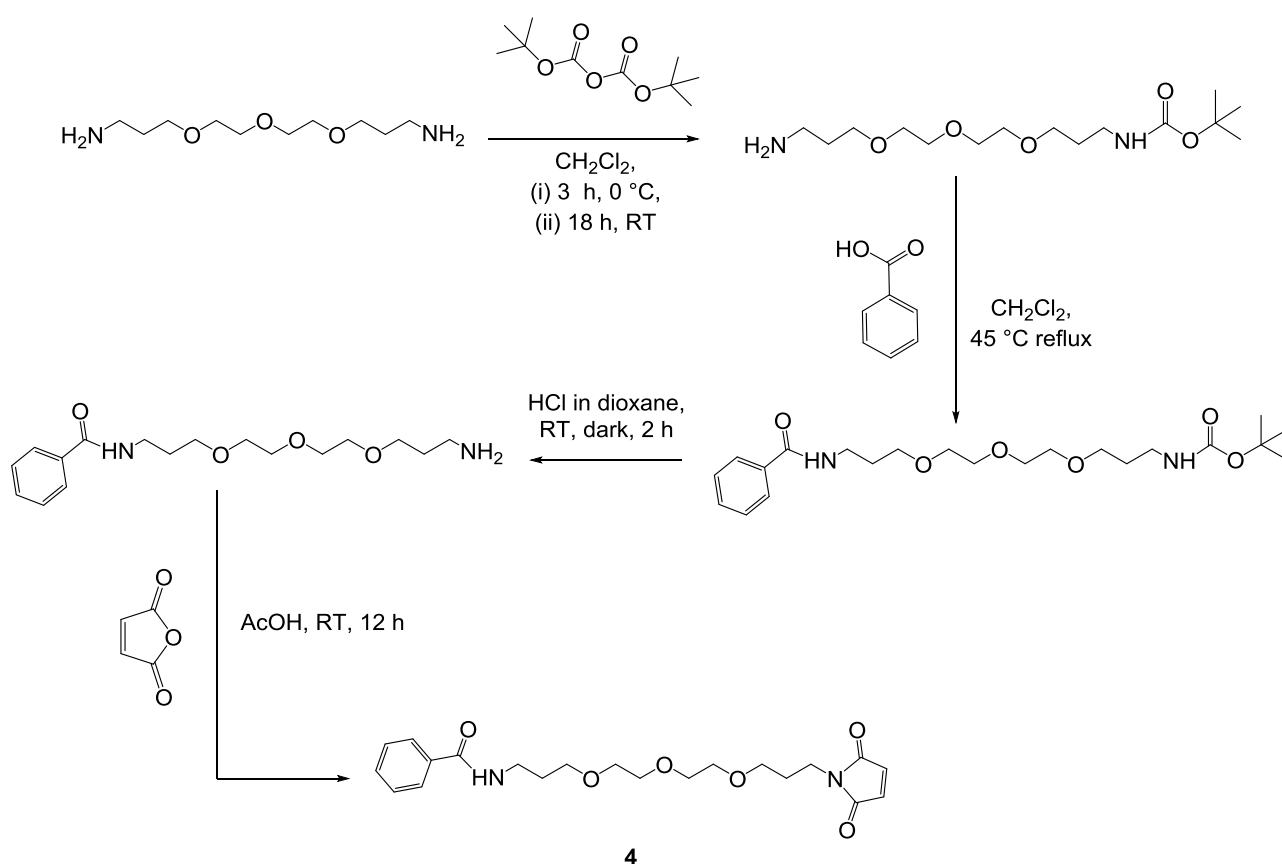
Scheme 3. Synthesis of fluorescein-functionalized glycopeptide.

Synthesis of fluorescein-functionalized glycopeptide. To a solution of **2** (50 mg, 0.06 mmol) in DMF (10 mL), was added HOBt (9.5 mg, 0.07 mmol) and DIC (7  $\mu\text{L}$ , 0.07 mmol) and the reaction was stirred at 0  $^{\circ}\text{C}$  for 1 h. The reaction was brought to room temperature and glycopeptide **1** (323 mg, 0.06 mmol) and DIPEA (160.3 mg, 1.24 mmol) in a mixture DMF:MeOH (10:1) was added and stirred for 16 h. The solvent was removed *in vacuo* and purification by flash chromatography (gradient elution in ethylacetate to methanol in dichloromethane) afforded the final compound as a yellow solid in 74% yield. IR 3305.44 (OH), 2925.25 (NH), 2853.96 (SH), 1747.76, 1658.09 (C=O), 1452.39 (SCH<sub>2</sub>), 1368.44 (C=S), 1225.24 (CH Alkyl), 1058.05 (COC), 900.01, 850.68 (CH-Ar).  $^1\text{H NMR}$  (400 MHz, MeOD)  $\delta$  8.13 (s, 1H, Ar-H), 7.76 (s, 1H, Ar-H), 7.13 (d,  $J = 8.2$  Hz, 1H, Ar-H), 6.66 (dd,  $J = 13.8, 5.3$  Hz, 4H, Ar-H), 6.52 (dd,  $J = 8.7, 2.3$  Hz, 2H, ArCH), 5.35 (s,  $J = 3.0$  Hz, 1H, H4), 5.17 – 4.98 (m, 4H, H-1,H-2,H-3,H-5), 4.60 (s, 2H, CH<sub>2</sub>OCH<sub>3</sub>), 4.09 (m,  $J = 7.2$  Hz, 4H, CHCH<sub>3</sub>, CHCH<sub>3</sub>, CH<sub>2</sub>NO), 3.84 (d,  $J = 27.4$  Hz, 2H, OCH<sub>2</sub>CH<sub>2</sub>), 3.75 – 3.60 (m, 8H, OCH<sub>2</sub>), 3.60 – 3.48 (m, 2H, CH<sub>2</sub>NS), 3.37 (s, 1H, CHCH<sub>2</sub>SH), 3.10 (s, 1H, CHCH<sub>2</sub>S), 2.90 (s, 2H, CHCH<sub>2</sub>SH), 2.86 – 2.72 (m, 2H,

CHCH<sub>2</sub>S), 2.58 (m, 2H, OCH<sub>2</sub>CH<sub>2</sub>), 2.11, 2.02, 1.99, 1.91 (s, 12H, COCH<sub>3</sub>), 1.42 (s, 12H, C(CH<sub>3</sub>)<sub>3</sub>, CHCH<sub>3</sub>), 1.31 (s, 3H, CHCH<sub>3</sub>). <sup>13</sup>C NMR (101 MHz, MeOD/CH<sub>3</sub>COOH-d) δ 179.67 (C=S), 173.1, 172.2, 170.3, 169.3, 168.92, 168.82, 168.33, 168.18, 167.98, 167.44 (C=O), 158.16, 150.94, 146.51, 139.11, 128.50, 127.12, 125.66, 122.59, 116.22, 110.41 (Ar-C), 108.23 (C1), 100.33, 99.06 (Ar-C), 77.55 (C(CH<sub>3</sub>)<sub>3</sub>), 69.12 (C3), 68.53 (C5), 68.29 (C2), 68.09, 67.35 (OCH<sub>2</sub>), 67.27 (OCH<sub>2</sub>), 66.02 (C4), 65.62 (CHCH<sub>2</sub>S), 64.45 (C6), 61.58 (CHCH<sub>2</sub>SH), 59.36 (CHCH<sub>3</sub>), 55.13 (CHCH<sub>3</sub>), 42.19 (CH<sub>2</sub>NS), 39.90 (CH<sub>2</sub>NO), 37.23 (SCH<sub>2</sub>CH), 29.92 (SCH<sub>2</sub>CH<sub>2</sub>), 27.41 (OCH<sub>2</sub>CH<sub>2</sub>), 26.18 (CHCH<sub>2</sub>SH), 25.41 (C(CH<sub>3</sub>)<sub>3</sub>), 22.03, 22.03, 22.03, 20.49 (C(O)CH<sub>3</sub>), 19.39, 17.77 (CHCH<sub>3</sub>). [α]<sub>D</sub><sup>26</sup> = (deg cm<sup>3</sup> g<sup>-1</sup> dm<sup>-1</sup>) = 117° (c = 0.000145, MeOH). HRMS (MALDI) m/z calcd for C<sub>61</sub>H<sub>79</sub>N<sub>7</sub>O<sub>23</sub>NaS<sub>3</sub> [M + Na]<sup>+</sup> 1396.4287, found 1396.4326.

### 3.2.5 Synthesis of Maleimido-PEG conjugate

Once the maleimide-PEG linker had been synthesized and fully characterized (Scheme 4), the conjugation with the fluorescent labelled glycopeptide was ready to be carried out. The maleimide group reacts specifically with sulfhydryl groups when the pH of the reaction mixture is between pH 6.5 and 7.5; the result is formation of a stable thioether linkage that is not reversible (i.e., the bond cannot be cleaved with reducing agents). Under more alkaline conditions (pH >8.5), the reaction favors primary amines and also increases the rate of hydrolysis of the maleimide group to a non-reactive maleamic acid. Maleimides do not react with tyrosines, histidines or methionines. Significantly, the synthetic methodology appeared to be highly reproducible.



Scheme 4. Synthesis of Maleimido-PEG conjugate.

Synthesis of maleimido-PEG conjugate. To a solution of 4,7,10-trioxa-1,13-tridecanediamine (10 g, 0.045 mol) in  $\text{CH}_2\text{Cl}_2$  (40 ml) in an ice bath, a solution of  $\text{Boc}_2\text{O}$  (5 g, 0.023 mol) in  $\text{CH}_2\text{Cl}_2$  (40 ml) was added dropwise over a period of 3 h. The reaction mixture was stirred overnight at room temperature. The solvent was removed under reduced pressure and after mixing the residue with  $\text{H}_2\text{O}$  (40 ml) the precipitate formed was filtered on celite. The filtrated  $\text{H}_2\text{O}$  was extracted with  $\text{CH}_2\text{Cl}_2$  (20 mL per 5), the organic phase was washed with  $\text{H}_2\text{O}$  (40 ml), brine (40 ml) and dried over  $\text{Na}_2\text{SO}_4$ . The evaporation of the solvent afforded the Boc-monoprotected compound as a colorless oil (83%). Benzoic acid (1.90 g, 0.016 mol) were dispersed in 200 ml  $\text{CH}_2\text{Cl}_2$  containing Boc-monoprotected PEG (5 g, 0.016 mol). After that, DMAP (1.95 g, 0.016 mol) and EDC HCl (3.07 g, 0.016 mol) were added and the reaction mixture was stirred under reflux at  $45^\circ\text{C}$  for 24 h. The solvent was evaporated under reduced pressure and once the residue was dispersed in  $\text{CH}_2\text{Cl}_2$ , it was washed with  $\text{Na}_2\text{HCO}_3$  (20 mL per 4), HCl 1M (20 mL per 4),  $\text{H}_2\text{O}$  (40 mL), brine (40 mL) and dried over  $\text{Na}_2\text{SO}_4$ . The evaporation of the solvent afforded the compound as a colorless oil (80%). The obtained compound was dissolved in 4M HCl in dioxane (5mL) and the mixture was stirred at room temperature in the dark for ca. 1 h monitoring by TLC. The solvent was evaporated under reduced pressure and the product was dried under vacuum overnight (100%). To that compound (4.66 g, 0.014 mol) a solution of maleic anhydride (1.41 g, 0.014 mol) in 15mL of glacial AcOH were added under vigorous stirring. The solution was stirred for 12h under nitrogen at R.T. The solvent was evaporated under reduced pressure and the product was dried under vacuum overnight. The crude was dispersed in 10 mL of  $\text{H}_2\text{O}$  and heated under reflux for 1 hour.<sup>2</sup> The evaporation of the solvent afforded the compound as a white oil (90%).  $^1\text{H}$  NMR (400 MHz, MeOD)  $\delta$  7.83 – 7.78 (d, 2H), 7.56 – 7.48 (t, 1H), 7.45 (t,  $J = 7.4$  Hz, 2H), 6.29 (s, 2H), 3.66 – 3.57 (m, 10H), 3.47 (t,  $J = 7.0$  Hz, 2H), 3.30 (t,  $J = 3.2, 1.5$  Hz, 2H), 3.14 – 3.02 (t, 2H), 1.96 – 1.83 (m, 4H).  $^{13}\text{C}$  NMR (101 MHz,  $\text{CDCl}_3$ )  $\delta$  168.45, 167.78 (C=O), 133.82, 132.72, 131.67, 128.54, 127.37 (C-Ar), 70.15, 69.93, 69.74, 69.65, 69.41, 39.84 ( $\text{OCH}_2$ ), 38.05, 29.09 ( $\text{CH}_2\text{N}$ ), 26.33, 26.33 ( $\text{OCH}_2\text{CH}_2$ ). HRMS (APCI<sup>+</sup>)  $m/z$  calcd for  $\text{C}_{21}\text{H}_{29}\text{N}_2\text{O}_6$  [M + H]<sup>+</sup> 405.201818, found 405.202013.

At this stage the Michael addition reaction involving the thiol as a nucleophile was ready to be performed. These steps are essential in order to improve and optimize the reaction conditions that will take place on the CNOs surface and also to furnish two different reference compound presenting a Cys moiety. According to this, a short polyethylene glycol (PEG) chain functioning as both a linker and a hydrophilic group bearing a maleimide functionality was synthesized and used as a thiol reacting unit (Scheme 4).

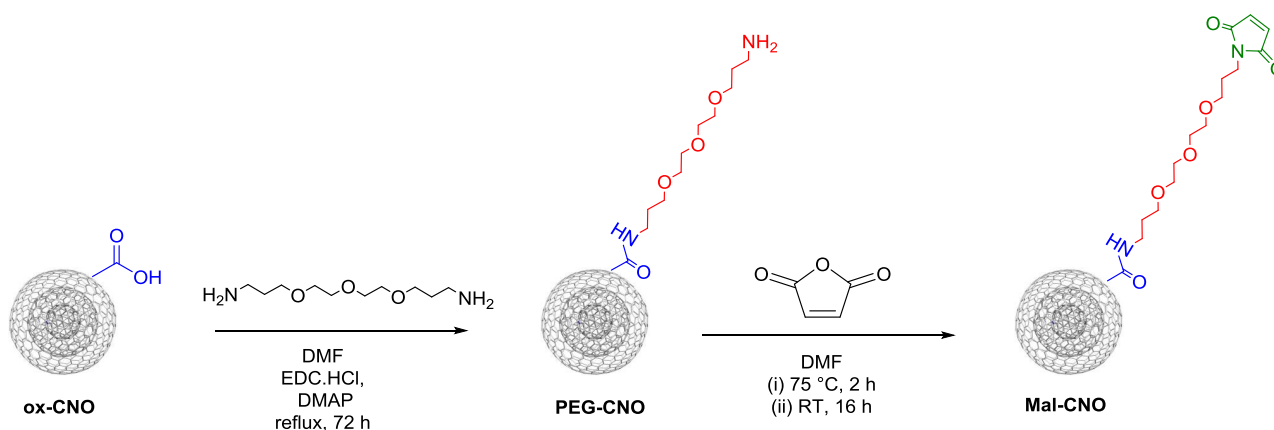
### 3.2.6 Reduction of organic disulfide bonds with TCEP

Thiols are prone to oxidative dimerization with the formation of disulfide bonds. Cysteine residues thus form cystine bridges, which stabilize protein tertiary structures. Disulfides do not react with maleimides. Therefore, it is necessary to reduce disulfides prior to the conjugation and exclude oxygen from the reaction. Tris(carboxyethyl)phosphine (TCEP) has been reported to be a very effective reagent for cleaving disulfide bonds in aqueous solution.<sup>17</sup> It is water-soluble and stable in both acidic and alkaline solutions and it has been applied to the cleavage of disulfide linkage patterns in peptides with tightly clustered cysteines.<sup>18,19</sup> TCEP is a potent, versatile, odorless, thiol-free reducing agent with broad application to protein and other research involving reduction of disulfide bonds. The compound is readily soluble and very stable in many aqueous solutions. It reduces disulfide bonds as effectively as dithiothreitol (DTT), but unlike DTT and other

thiol-containing reducing agents, TCEP does not have to be removed before certain sulfhydryl-reactive cross-linking reactions. The ability and virtues of trialkylphosphine compounds to reduce protein disulfide bonds have been known for many years.<sup>1,2</sup> Phosphines are stable in aqueous solution, selectively reduce disulfide bonds, and are essentially nonreactive toward other functional groups commonly found in proteins. TCEP selectively and completely reduces even the most stable water-soluble alkyl disulfides over a wide pH range. Reductions frequently require less than 5 minutes at room temperature. TCEP is non-volatile, odorless, and unlike most other reducing agents, is resistant to air oxidation. Compared to DTT, TCEP is more stable, more effective, and able to reduce disulfide bonds at lower pHs.<sup>5</sup> Once the synthetic glycopeptide has been prepared and fully characterised, it will be conjugated to CNOs suitably modified with reactive maleimide groups. The ligation reaction between the primary thiol and the maleimide Michael acceptor is extremely mild and can be carried out at room temperature and in buffered aqueous solution with sensitive substrates such as proteins and antibodies.

### 3.2.7 Mal-CNO synthesis

Once the main biologically active building blocks were synthesized and fully characterized, a chemoselective ligation methodology for covalent modification of CNOs with both synthetic and naturally occurring, cysteine containing biomolecules has been explored. The synthesis of the maleimido decorated CNOs is outlined in Scheme 5. Pristine CNOs (p-CNO) were prepared by annealing nanodiamonds of 5 nm average particle size in a tubular furnace at 1650 °C, according to the previously reported procedure.<sup>21</sup>



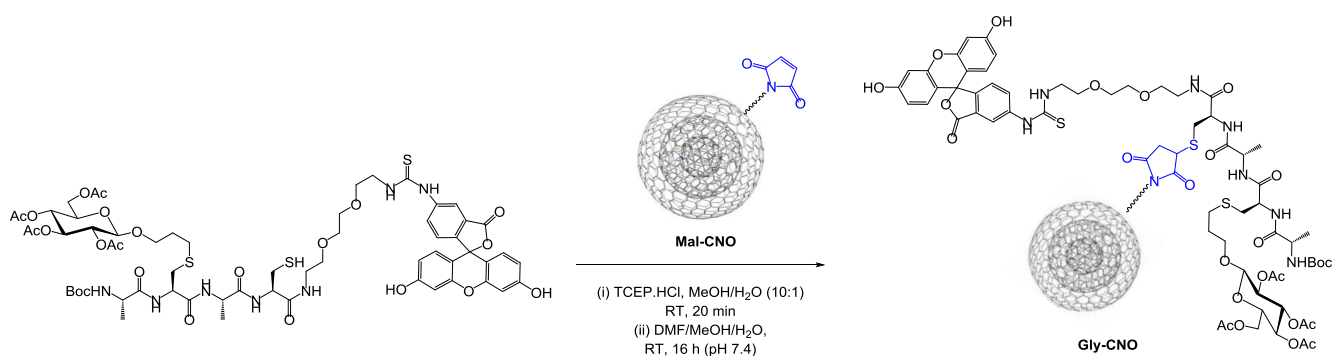
Scheme 5. Synthetic procedure for preparation of maleimido decorated CNOs.

Ox-CNOs were prepared from raw CNO material (p-CNO) through thermal annealing and subsequent oxidation by reflux heating in 3 N HNO<sub>3</sub>. The carboxylic groups of ox-CNOs (80 mg) were amidated with 4,7,10-Trioxa-1,13-tridecanediamine (15 mL) in dry DMF (15 mL) by water-soluble EDC HCl (152 mg, 0.79 mmol), NHS (50 mg, 0.43 mmol) and DMAP (50 mg, 0.41 mmol) stirring the ox-CNOs under reflux at 140°C for 4 days. After the complexation, the CNOs were filtered off on a nylon filter membrane (pore size 0.2 μm) and washed with water, methanol and acetone. 163 mg PEG-CNO were recovered as black powder after

drying over night at RT. 20 mg of PEG-CNOs were solubilized in dry DMF (5mL) and 120 mg of maleic anhydride were added. The solution was sonicated for 20 min, heated at 75 °C for 2 h and let it stirred at room temperature for 16 h. The reaction was filtered on nylon filter 0.2 μm and washed with DMF and THF to get rid of the unreacted compounds. The surface chemical composition at the different stages of the CNOs functionalization was probed by TGA analysis (Figure 8A). For each surface modification step, a variation in weight loss of combustible organics is clearly observed. Further confirmation of surface composition was achieved using ATR-FTIR analysis where clear evidence of COOH stretching was observed at 1750 cm<sup>-1</sup> for ox-CNO and at 1172 cm for CO stretch of the PEG groups. Evidence for the introduction of the maleimido moiety was provided by NMR analysis of the Mal-CNO that showed a strong signal for the maleimide C-H at 5.97 ppm.

### 3.2.8 Gly-CNO synthesis

With the Mal-CNO in hand, the ligation of a synthetic cysteine containing glycopeptide onto the CNOs has been investigated. The structure of the glycopeptide was based on our previously reported ala-cys-ala-cys tetrapeptide core.<sup>22</sup> The glycopeptide was prepared through a sequential native chemical ligation, thiol-ene click (NCL-TEC) approach. A protected galactose residue was S-linked onto the peptide backbone using a thiol-ene ligation reaction between a cysteine residue and a modified glycan displaying a terminal alkene residue at the anomeric position. A second cysteine residue was subsequently introduced through native chemical ligation to provide a reactive moiety for subsequent maleimido coupling. The glycopeptide was modified at the C-terminus with a short, fluorescein labelled PEG-group to furnish the fluorescently labelled glycopeptide. The coupling reaction was carried out using DIC/HOBt mediated conditions which are compatible with the sulfhydryl group. The glycopeptide was purified by column chromatography and fully characterized by NMR and mass spec analysis prior to maleimido coupling. With the fluorescent glycopeptide in hand, the Michael addition reaction between the CNOs bearing maleimido moieties and the fluorescent glycopeptide was investigated (Scheme 6). Importantly, the glycopeptide was first treated with a phosphine reducing agent to reduce unreactive disulfides.



Scheme 6. Ligation reaction between synthetic glycopeptide 3 and Mal-CNO.

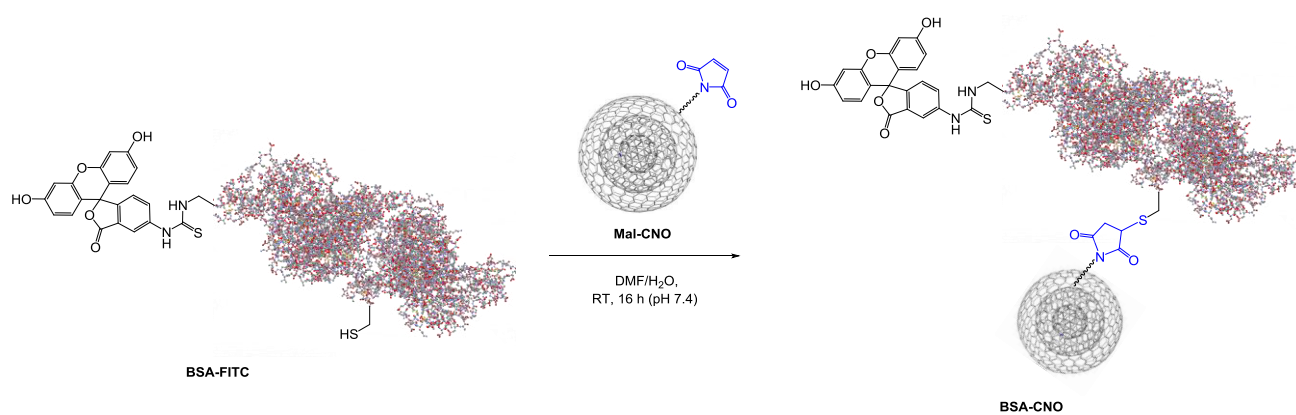
At this stage, Mal-CNO was treated at pH 7.4 with the fluorescent glycopeptide. 10 mg of Mal-CNO were dispersed in dry DMF (4mL) and 20 mg of fluorescently labelled glycopeptide were added. The reaction was stirred for 16 h at room temperature in the dark. The modified CNOs were filtered off on a nylon filter



membrane (pore size 0.2  $\mu\text{m}$ ) and washed with MeOH and Acetone. The resulting material was re-dispersed in MeOH, filtered again and centrifuged in MeOH to wash out any non-covalently bound species (Scheme 6).

### 3.2.9 BSA-CNO synthesis

As discussed in the introduction, covalent modification of nanomaterials with proteins represents an effective method for modifying biocompatibility. In order to investigate the maleimide mediated ligation methodology for covalent protein modification, we investigated the ligation reaction of Mal-CNO with the BSA-FITC. Mal-CNO was treated with BSA-FITC for 16 h at pH 7.4 in buffer. On completion of the ligation reaction, the solution was filtered on nylon and washed with MeOH and acetone. The BSA-CNO was re-dispersed in MeOH, filtered again and centrifuged three times in MeOH to wash out the unbound species (Scheme 7).



Scheme 7. Ligation reaction between BSA-FITC and Mal-CNO.

At this stage, Mal-CNO was treated at pH 7.4 with the fluorescent BSA. 10 mg of Mal-CNO were dispersed in dry DMF (4mL) and 20 mg of BSA were added. The reaction was stirred for 16 h at room temperature in the dark. The modified CNOs were filtered off on a nylon filter membrane (pore size 0.2  $\mu\text{m}$ ) and washed with MeOH and Acetone. The resulting material was re-dispersed in MeOH, filtered again and centrifuged in MeOH to wash out any non-covalently bound species (Scheme 7).

## 3.3 Results and Discussion

### 3.3.1 Absorption and Emission Spectroscopy

Once the fluorescent labelled glycopeptide 3 had been synthesized and fully characterized, emission and absorption studies have been performed and the molar extinction coefficient estimated. The fluorescent labelled glycopeptide 3 have been dissolved in DMSO at  $3.63 \times 10^{-4}$  M and diluted to a final concentration of  $3.63 \times 10^{-6}$  M,  $7.27 \times 10^{-6}$  M,  $7.27 \times 10^{-6}$  M,  $1.09 \times 10^{-5}$  M,  $1.45 \times 10^{-5}$  M and  $3.63 \times 10^{-5}$  M. Upon photoexcitation at 520 nm of a dispersion of fluorescent labelled glycopeptide 3 in DMSO, an intense emission band was observed with a maximum centered at 542 nm (Figure 3, top). Because the graph shows that the maximum of fluorescence above a concentration of  $10 \mu\text{g mL}^{-1}$  reaches a steady state probably due to intramolecular interactions and the tendency of aggregation of the glycopeptide, lower concentrations of the fluorescent labelled glycopeptide 3 have been prepared. According to this, the fluorescent labelled glycopeptide 3 have been dissolved in DMSO at  $3.63 \times 10^{-4}$  M and diluted to a final concentration of  $7.27 \times 10^{-7}$  M,  $1.45 \times 10^{-6}$  M,  $2.91 \times 10^{-6}$  M,  $3.63 \times 10^{-6}$  M,  $4.36 \times 10^{-6}$  M,  $5.81 \times 10^{-6}$  M,  $7.27 \times 10^{-6}$  M. Interestingly, the fluorescent labelled glycopeptide 3 shows a linear correlation for all the concentrations used for both absorption and emission studies (Figure 3, bottom). Furthermore, absorbance and fluorescence studies have been studied in DMEM white in order to evaluate the physio-chemical properties of the molecule in biological environment. Upon photoexcitation at 490 nm of the fluorescent labelled glycopeptide 3 in DMEM, an intense emission band was observed with a maximum at 516 nm and a linear correlation for all the concentrations used was still found.

### 3.3.2 Absorption studies of the fluorescent glycopeptide 3

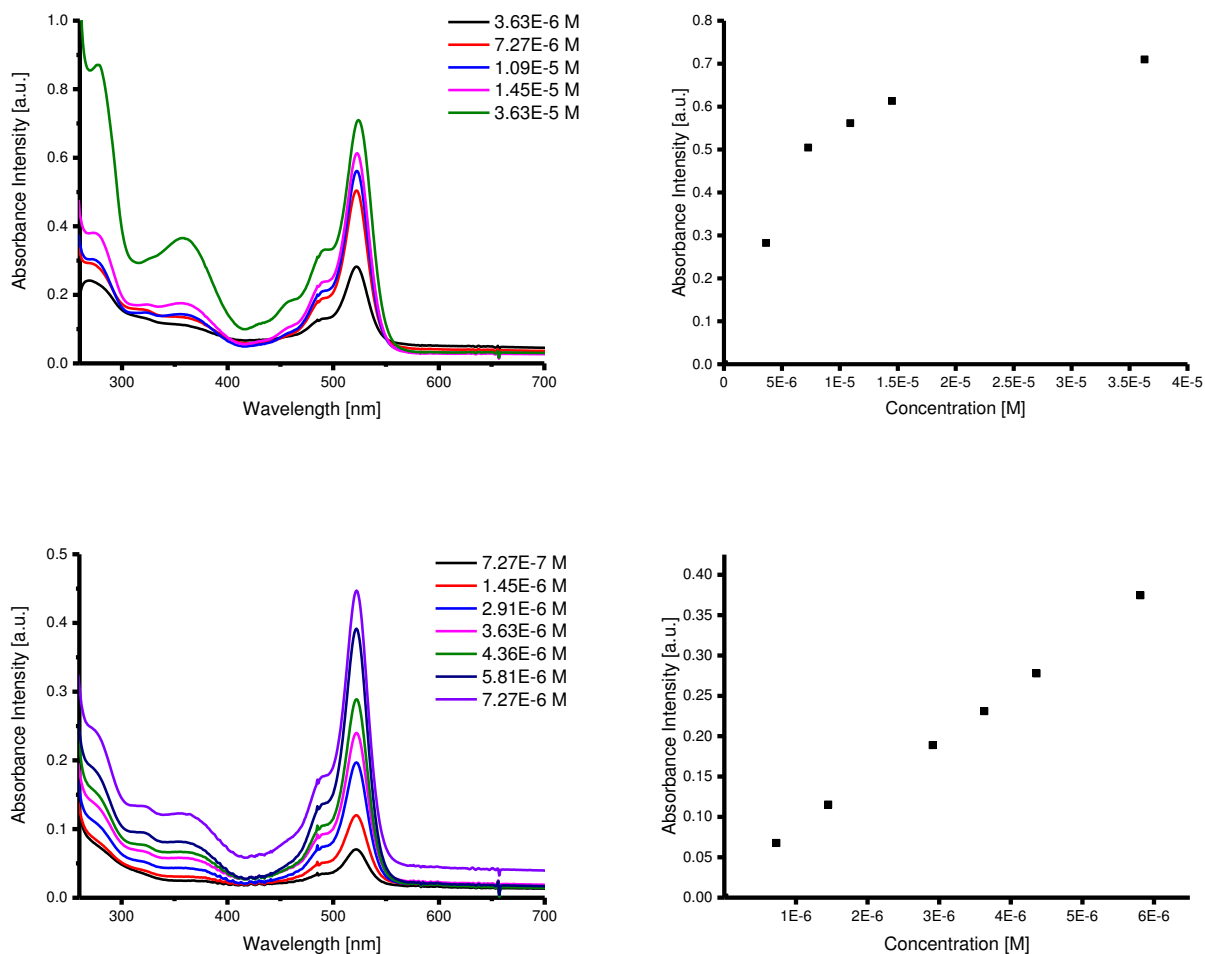


Figure 3. Absorption studies of fluorescent labelled glycopeptide 3 at a concentration of 5, 10, 15, 20 and 50  $\mu\text{g mL}^{-1}$  in DMSO (top) and 1,2,4,5,6,8 and 10  $\mu\text{g mL}^{-1}$  in DMSO (bottom).

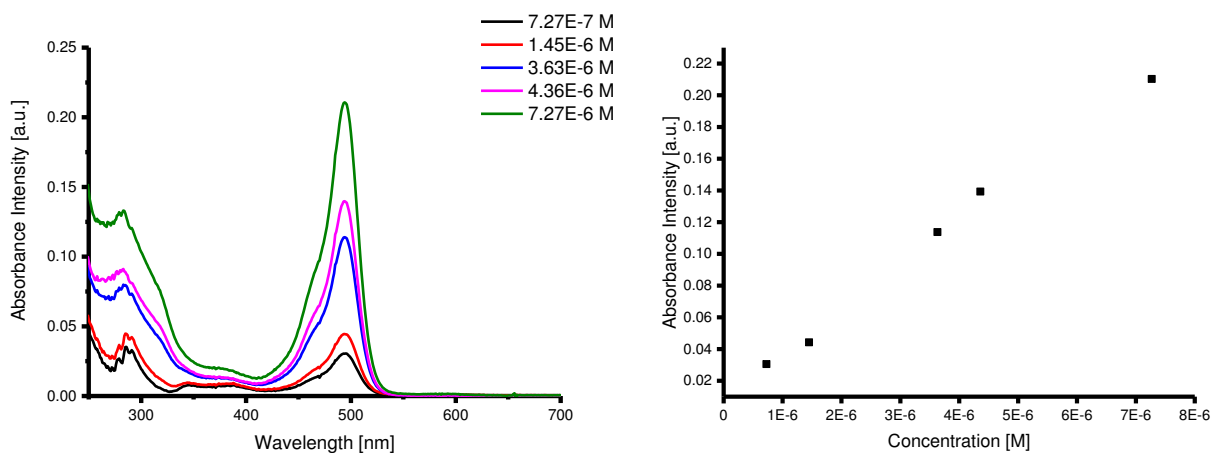


Figure 4. Absorption studies of fluorescent labelled glycopeptide 3 at a concentration of 1, 2, 5, 6 and 10  $\mu\text{g mL}^{-1}$  in DMEM phenol red free.

### 3.3.3 Emission studies of the fluorescent glycopeptide 3

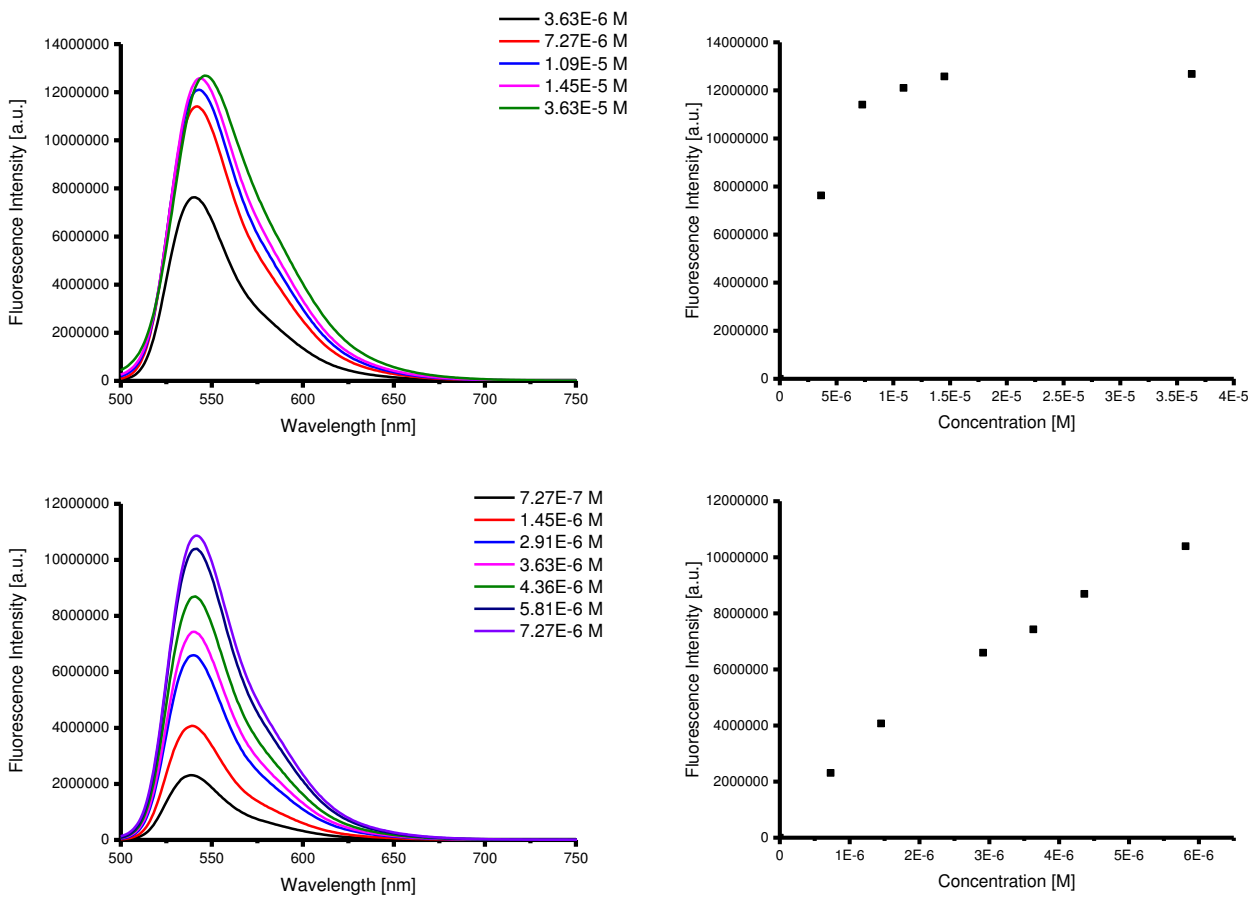


Figure 5. Emission studies of fluorescent labelled glycopeptide 3 at a concentration of 5, 10, 15, 20 and 50  $\mu\text{g mL}^{-1}$  in DMSO (top) and 1,2,4,5,6,8 and 10  $\mu\text{g mL}^{-1}$  in DMSO (bottom).

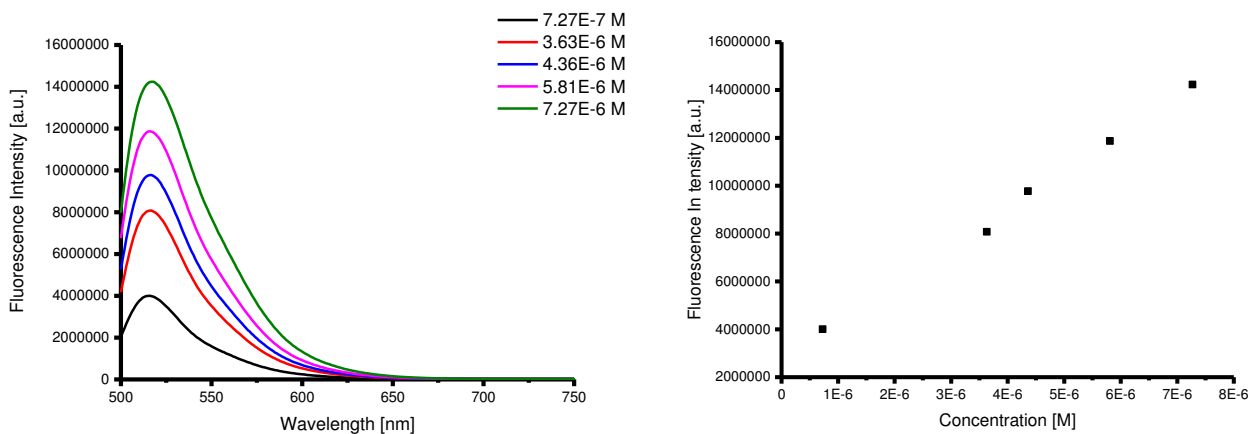


Figure 6. Emission studies of fluorescent labelled glycopeptide 3 at a concentration of 1, 5, 6, 8 and 10  $\mu\text{g mL}^{-1}$  in DMEM phenol red free.

### 3.3.4 (FT-IR)

FT-IR spectroscopy shows the characteristic stretching and vibration bands of the fluorescent labelled glycopeptide (Figure 7). In particular, the OH at  $3305\text{ cm}^{-1}$ , amide A (mainly  $\text{-NH}$  stretching vibrations) at  $2966\text{ cm}^{-1}$ , amide I (mainly  $\text{C=O}$  stretching vibrations) at  $1640\text{ cm}^{-1}$ , and amide II (the coupling of bending vibrates of N-H and stretching vibrates of C-N) bands at  $1559\text{ cm}^{-1}$ .

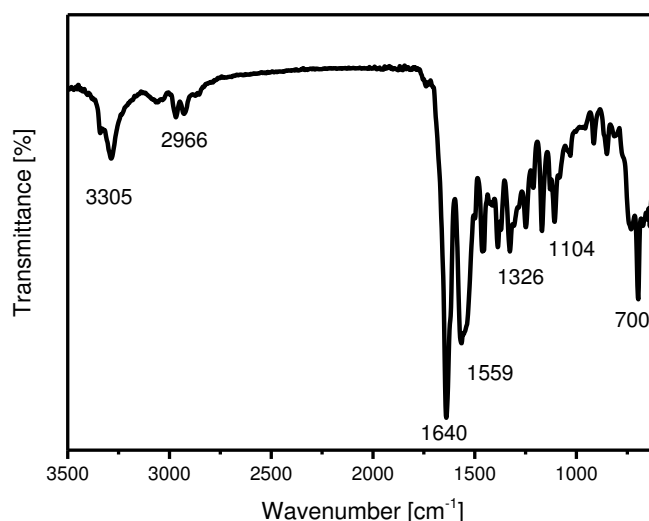


Figure 7. FTIR spectroscopy of synthetic glycopeptide 3.

### 3.3.5 Confocal Microscopy

A preliminary cell-uptake study was carried out using the MCF-7 cell line (human breast adenocarcinoma). In order to explore the ability of the synthetic glycopeptide to enter MCF-7 cells, confocal live cell imaging was carried on. MCF-7 cells grown in subconfluent monolayer on a glass slide were treated with a dispersion of fluorescently labelled glycopeptide in DMEM at concentrations  $20\text{ }\mu\text{g mL}^{-1}$ . After 24 h of incubation at  $37\text{ }^{\circ}\text{C}$ , the cells were carefully rinsed with fresh media to remove the excess of fluorescent glycopeptide and treated with Hoechst 33342, for live nuclear staining and WGA 594 for red plasma membrane labelling. The cellular uptake characteristics of the fluorescent glycopeptide are shown in Figure 8. Confocal imaging revealed that the synthetic glycopeptide was efficiently uptaken by MCF-7 cells with the distinct spot-like regions in the cytosol indicative of lysosomal localization following cellular uptake (Figure 8). Furthermore, sequential optical sections (Z-stacks),  $1\text{ }\mu\text{m}$  thickness, from the basal-to-apical surfaces of the cells were acquired to study the cellular internalization and distribution. Although the glycopeptide could undergo endocytosis in the absence of the nano-particle, the ability to deliver the covalently bound substrates into cancer cells offers fascinating prospects for controlled release and immunotherapy applications.

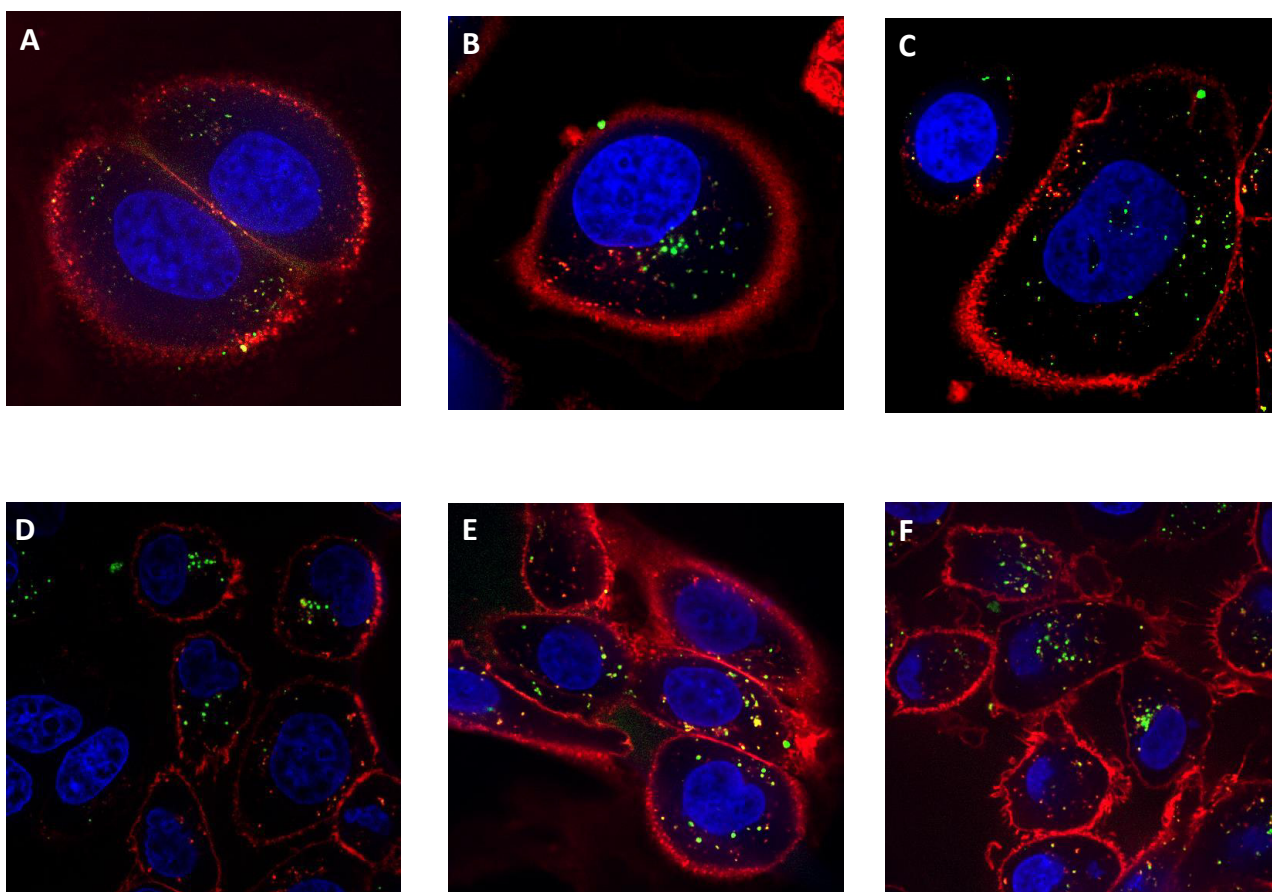


Figure 8. Confocal images of MCF-7 cells incubated with fluorescein-functionalized glycopeptide 3 at a mass concentration of  $20 \mu\text{g mL}^{-1}$  for 24 h. Nuclei are stained with Hoechst 33342 (blue), the presence of glycopeptide 3 is indicated by the green fluorescence signal. Hoechst 33342 (A), Green FITC signal (B), WGA 594 (C) merged images (D). Scale bars A-H=  $25 \mu\text{m}$ .

### 3.3.6 Glycopeptide-CNO conjugate characterization

Evidence for the successful covalent modification of Mal-CNO with the fluorescent glycopeptide was provided by NMR, ATR-FTIR, TGA, UV-spectroscopy and emission analysis. In the HR-MAS NMR spectrum of the conjugate, peaks corresponding to the methyl groups of the alanine residues, Boc protecting group, acetyl group, PEG and FITC moieties are clearly visible. FTIR analysis of the Gly-CNO sample shows the characteristic vibration bands of broad O-H centred at ( $3285 \text{ cm}^{-1}$ ), N-H ( $2940 \text{ cm}^{-1}$ ), S-H ( $2861 \text{ cm}^{-1}$ ), C=O and amides ( $1720, 1639, 1536 \text{ cm}^{-1}$ ), C=S ( $1368 \text{ cm}^{-1}$ ), COC ( $1056 \text{ cm}^{-1}$ ), (Figure 9,C). TGA performed in air shows thermal decomposition of surface organics at  $330^\circ\text{C}$  and at  $430^\circ\text{C}$  respectively, followed by the decomposition of the CNOs core at  $510^\circ\text{C}$  (Figure 9, A). The emission properties of the Gly-CNOs were investigated under physiological conditions. Upon photoexcitation at  $490 \text{ nm}$  in biological medium (DMEM) without phenol red, an intense emission band was observed with a maximum centered at  $518 \text{ nm}$  (Figure 9, D). The result is in comparison with the emission of the free glycopeptide ( $\lambda_{\text{em}} = 516 \text{ nm}$ ) suggesting a similar micro-environment surrounding the fluorophores once the biomolecules are anchored on the surface of the CNOs. The concentration of glycopeptide in a  $10 \mu\text{g mL}^{-1}$  dispersion of Gly-CNO was determined to be about  $4.6 \times 10^{-6} \text{ M}$  by absorption (Figure 9, B).

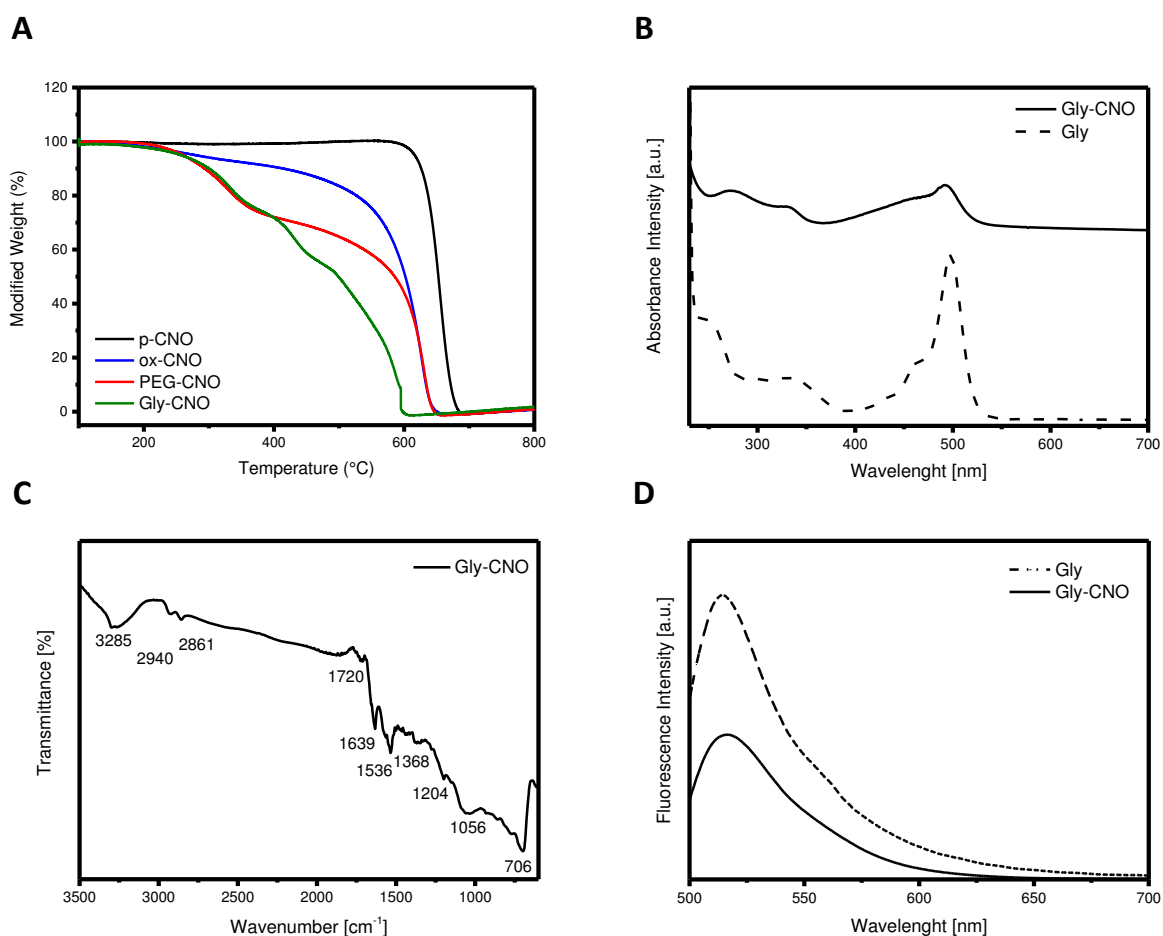


Figure 9. Characterization of the functionalized Gly-CNO. (A) Thermogravimetric analysis of p-CNO (black), ox-CNO (blue), PEG-CNO (red) and Gly-CNO (green). All experiments were run in air with a temperature rate of  $10\text{ }^{\circ}\text{C min}^{-1}$ . (B) Absorption spectra of Gly-CNO (solid line) and fluorescent labelled glycopeptide 3 (dotted line) in DMEM phenol red free at a concentration of  $10\text{ }\mu\text{g mL}^{-1}$ . (C) ATR-FTIR spectra of Gly-CNO using germanium crystals and 256 scans. (D) Emission spectra ( $\lambda_{\text{exc}} = 490\text{ nm}$ ) of fluorescent labelled glycopeptide 3 (dotted line) and Gly-CNO (solid line) in DMEM at a concentration of  $10\text{ }\mu\text{g mL}^{-1}$ .

The kinetic of aggregation and the size of the clusters formed were investigated by dynamic light scattering (DLS). DLS measurements were performed on the CNO samples dispersed in water. The hydrodynamic diameter was found to be  $236 \pm 4$  and  $325 \pm 6$  respectively for PEG-CNOs and Gly-CNOs at a concentration of  $5\text{ }\mu\text{g mL}^{-1}$  (Figure 10). Furthermore, Z-potential measurements of PEG-CNO and Gly-CNO samples were performed in phosphate buffer 0.01 M at pH 7.4. Under these conditions the zeta potentials for the PEG-CNO was found to be  $-28.1\text{ mV} \pm 1\text{ mV}$ , independently of the concentration used. Interestingly, after the glycopeptide ligation, the Z-potential has been found to be  $-36 \pm 1\text{ mV}$  for Gly-CNOs indicating that the biomolecules have a significant effect on the colloidal stability of the nanoparticles (Figure 10). Indeed, nanoparticles with Zeta Potential values above 25mV (either positive or negative) have high degrees of stability. The repulsion forces originating from the Gly-CNO surface charges prevent the particles from aggregations whereas nanoparticles with a low zeta potential value could aggregate due to Van Der Waal inter-particle attractions.<sup>23</sup>

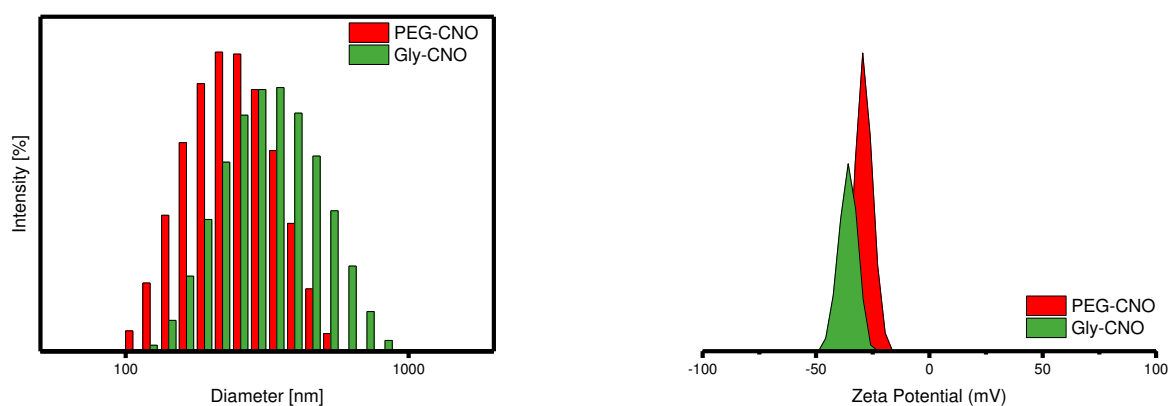


Figure 10. DLS of PEG-CNO (red) and Gly-CNO (green) at a concentration of  $5 \mu\text{g ml}^{-1}$  in water (left) and Z-potential measurement of PEG-CNO (red) and Gly-CNO (green) at a concentration of  $10 \mu\text{g ml}^{-1}$  in phosphate buffer 0.01 M at pH 7.4 (right).

### 3.3.7 BSA-CNO conjugate characterization

Evidence for the successful covalent modification of Mal-CNO with BSA-FITC was provided by ATR-FTIR, TGA, UV-spectroscopy and emission analysis. Strong stretching vibrations were recorded for BSA-CNO. The main peaks show the stretching vibration of OH at  $3293 \text{ cm}^{-1}$ , amide A (mainly  $\text{-NH}$  stretching vibrations) at  $2937 \text{ cm}^{-1}$ , amide I (mainly  $\text{C=O}$  stretching vibrations) at  $1636 \text{ cm}^{-1}$ , and amide II (the coupling of bending vibrates of N-H and stretching vibrates of C-N) bands at  $1573 \text{ cm}^{-1}$ . TGA performed in air displays the thermal decomposition of surface-bound organics at  $280 \text{ }^\circ\text{C}$  and at  $440 \text{ }^\circ\text{C}$ , followed by the decomposition of the CNOs core at  $720 \text{ }^\circ\text{C}$  (Figure 11, A). Furthermore, upon photoexcitation at  $490 \text{ nm}$  in biological medium (DMEM) without phenol red, an intense emission band was observed with a maximum at  $518 \text{ nm}$  (Figure 11, D). The result is in comparison with the emission of the free BSA-FITC ( $\lambda_{\text{em}} = 518 \text{ nm}$ ) suggesting a similar micro-environment surrounding the fluorophores once the biomolecules are anchored on the surface of the CNOs. The results are in close agreement with the Gly-CNO discussed above. The concentration of the BSA in a  $10 \mu\text{g mL}^{-1}$  dispersion of BSA-CNO was determined to be about  $1.7 \times 10^{-4} \text{ M}$ .



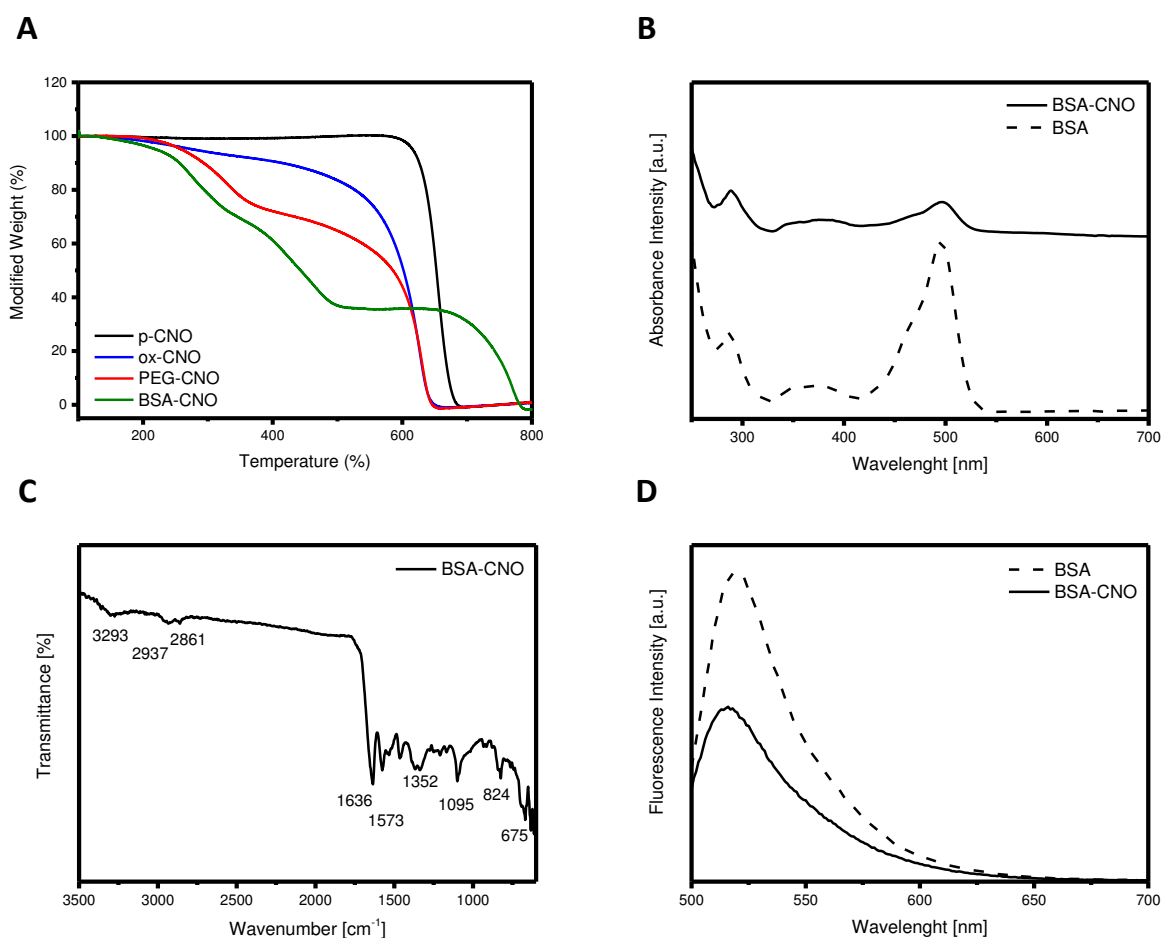


Figure 11. Characterization of the functionalized BSA-CNO. (A) Thermogravimetric analysis of p-CNO (black), ox-CNO (blue), PEG-CNO (red) and BSA-CNO (green). All experiments were run in air with a temperature rate of 10 °C min<sup>-1</sup>. (B) Absorption spectra of BSA-CNO (solid line) and BSA-FITC (dotted line) in DMEM phenol red free at a concentration of 10 µg mL<sup>-1</sup>. (C) ATR-FTIR spectra of BSA-CNO using germanium crystals and 256 scans. (D) Emission spectra ( $\lambda_{exc} = 490$  nm) of BSA-FITC (dotted line) and BSA-CNO (solid line) in DMEM at a concentration of 10 µg mL<sup>-1</sup>.

The hydrodynamic diameter was found to be  $236 \pm 4$  and  $705 \pm 70$  nm for PEG-CNOs and BSA-CNOs respectively at a concentration of 5 µg mL<sup>-1</sup> (Figure 12). Because the DLS measures the scattered intensity over a range of scattering angles for a given time, it is notable that when the density of the protein is high, the strong influence of bioconjugate interactions becomes important. Despite that, after the bioconjugation the Z-potential has been found to be  $-35 \pm 2$  (Figure 12). These observations are consistent with the results demonstrated for Gly-CNO.

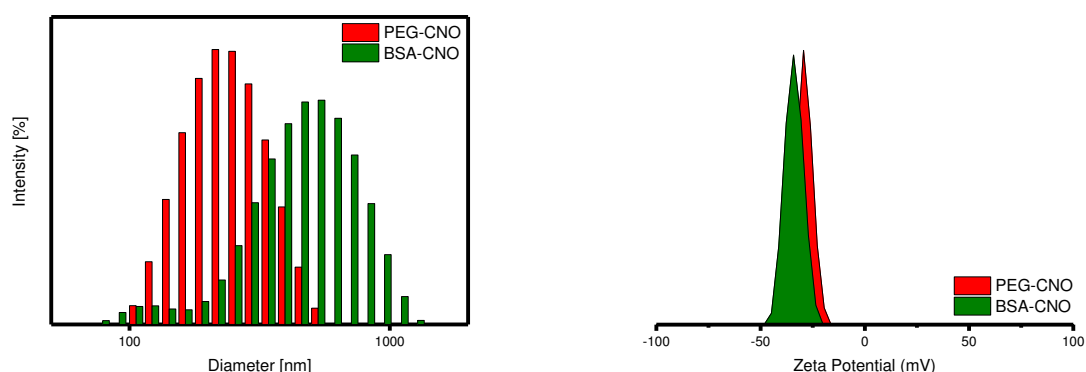


Figure 12. DLS of PEG-CNO (red) and BSA-CNO (green) at a concentration of  $5 \mu\text{g ml}^{-1}$  in water (left) and Z-potential measurement of PEG-CNO (red) and Gly-CNO (green) at a concentration of  $10 \mu\text{g ml}^{-1}$  in phosphate buffer 0.01 M at pH 7.4 (right).

### 3.3.8 Absorption and Emission Spectroscopy

Absorption and emission studies have been performed on both Gly-CNO and BSA-CNO in DMEM. CNO samples have been dissolved in DMEM at  $0.5 \text{ mg mL}^{-1}$  and diluted to a final concentration of 5, 10, 15, 20 and  $50 \mu\text{g mL}^{-1}$ . Upon a photoexcitation at 490 nm of a dispersion of Gly-CNO in DMEM, an intense emission band was observed with a maximum at 514 nm (Figure 14). Similarly, upon a photoexcitation at 490 nm of a dispersion of BSA-CNO in DMEM, an intense emission band was observed with a maximum at 516 nm (Figure 15). Interestingly, for both samples has been observed a linear correlation for all the concentrations used suggesting a good stability of the nano-carriers in biological media. Figure 13 shows a UV-visible spectrum for ox-CNO in DMEM-phenol red free as a comparison.

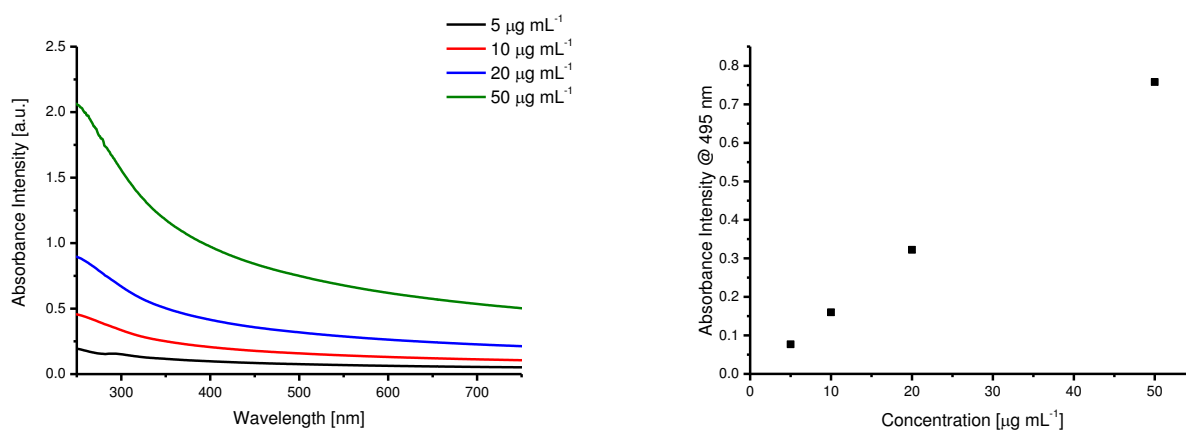


Figure 13. Absorption spectra of ox-CNO at 5, 10, 20 and  $50 \mu\text{g mL}^{-1}$  in DMEM-phenol red free.

### 3.3.9 Absorption and emission studies of Gly-CNO

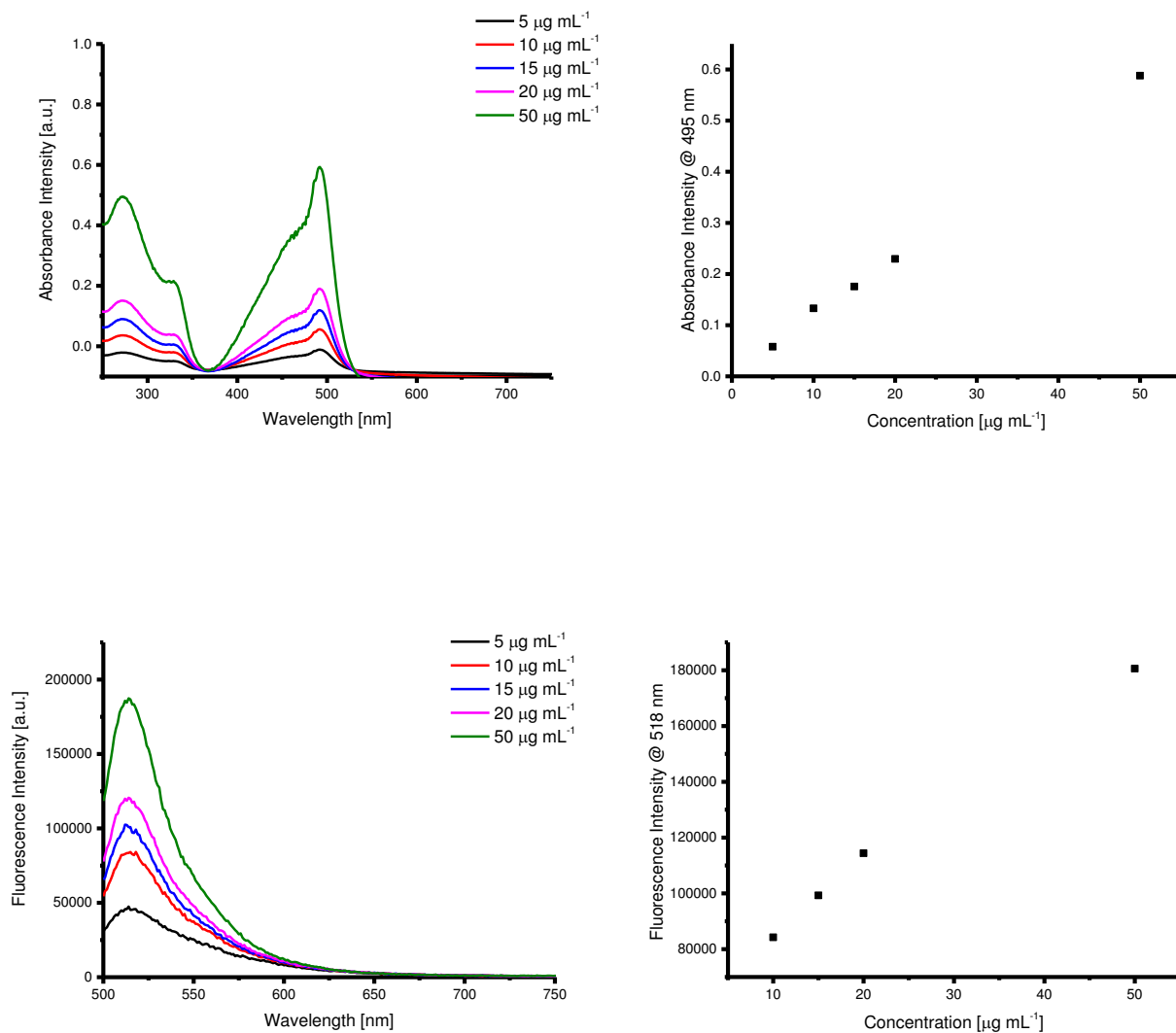
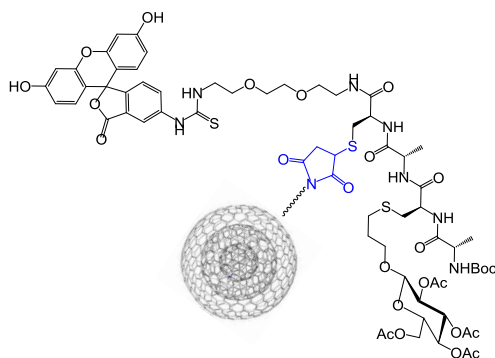


Figure 14. Absorption (top) and Emission spectra ( $\lambda_{\text{exc}} = 490 \text{ nm}$ ) of Gly-CNO at 5, 10, 15, 20 and 50  $\mu\text{g mL}^{-1}$  in DMEM-phenol red free.

### 3.3.10 Absorption and emission studies of BSA-CNO

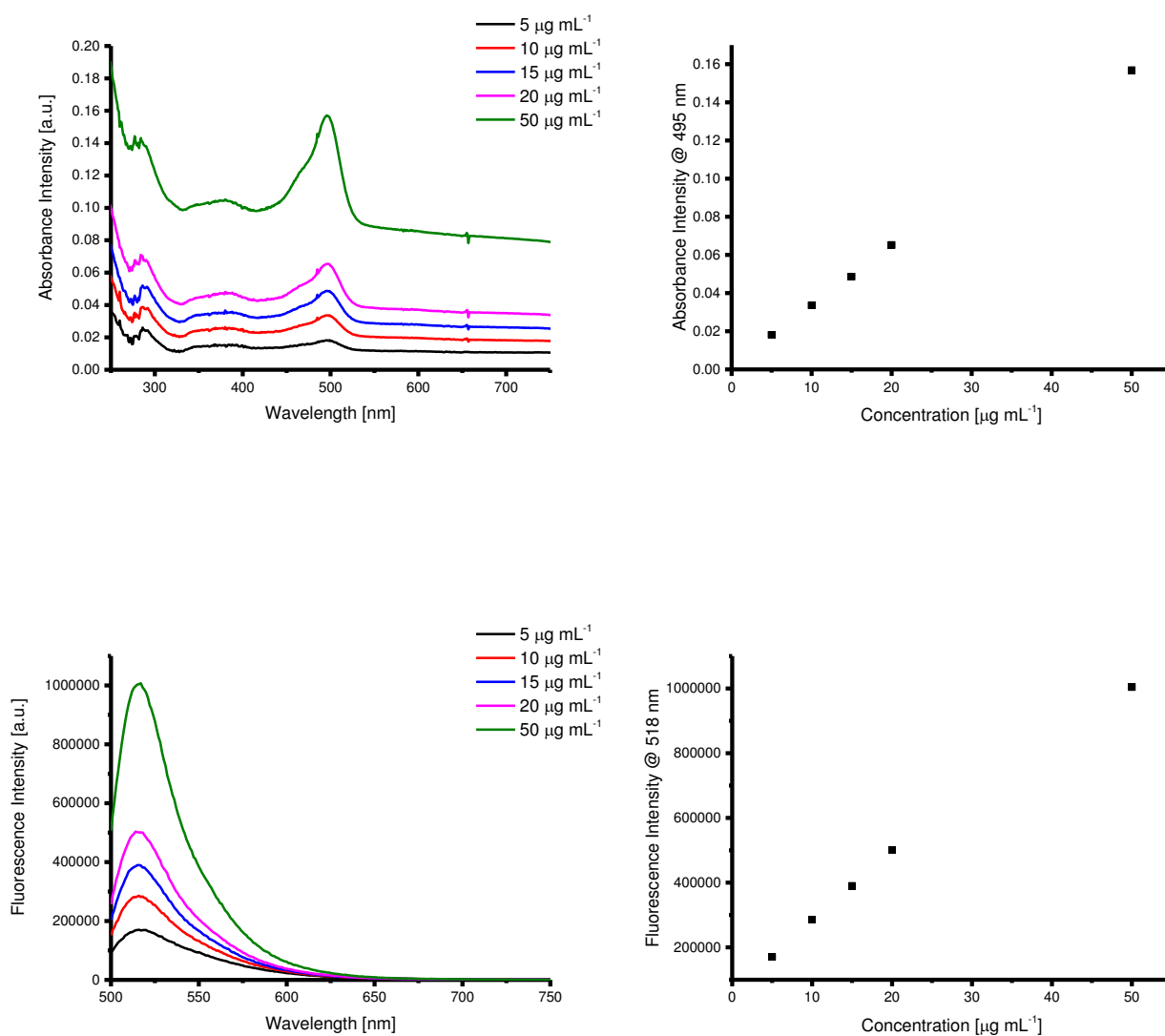
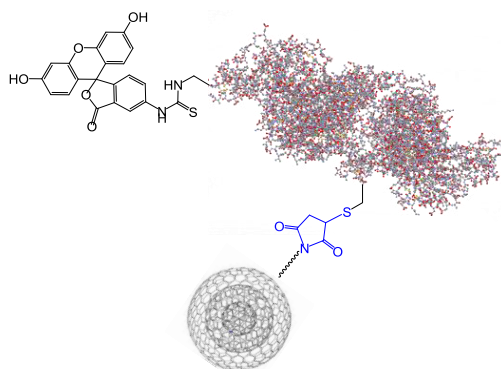


Figure 15. Absorption (top) and Emission spectra ( $\lambda_{\text{exc}} = 490 \text{ nm}$ ) of BSA-CNO at 5, 10, 15, 20 and 50  $\mu\text{g mL}^{-1}$  in DMEM-phenol red free.

### 3.3.11 Cell Studies: Toxicity

The cytocompatibility of the functionalized CNOs is a key consideration for their biomedical application. The cytotoxicity of the different CNO conjugates, ox-CNO, Gly-CNO and BSA-CNO, were tested on MCF-7 (human breast adenocarcinoma cell line) cells. The cells were treated with a suspension of the CNO at two different concentrations ( $10$  and  $20 \mu\text{g mL}^{-1}$ ) and the metabolic activity was assessed at three different incubation times ( $24$ ,  $48$  and  $72$  h), (Figure 16). The viability of the MCF-7 cells was evaluated by PrestoBlue<sup>TM</sup> Cell Viability Reagent. The data showed no significant differences in the cell metabolic activity between the ox-CNOs and those covalently modified with biomolecules. The viability of MCF-7 cells treated with Gly-CNO at both  $10$  and  $20 \mu\text{g mL}^{-1}$  was found to be more than  $80\%$  at all three timepoints. Data for the BSA-CNO conjugate presented very similar results, albeit with reduced viability observed at the lower concentration. It is well known that modification of nanomaterials with proteins can offer improved biocompatibility over the bare carbon nanomaterial. What is particularly noteworthy in our findings is that the small glycopeptide conjugate appears to offer an improved biocompatibility that is comparable to that of the larger BSA protein, suggesting a key role for small synthetic peptides and glycopetides in the development of nano-therapeutics. The results obtained are in good agreement with the previous biological studies made with other carbon nano-materials, in particular CNTs. Muzi and colleagues have demonstrated a high sensitivity to pristine SWCNTs in different cell lines and an attenuated behavior when the CNTs were coated with different types of blood protein, including BSA.<sup>24</sup> Holt and collaborators showed not only how BSA stabilized SWCNTs but also how it could be readily taken up by different cell lines without apparent acute lethal effects.<sup>25,26</sup>

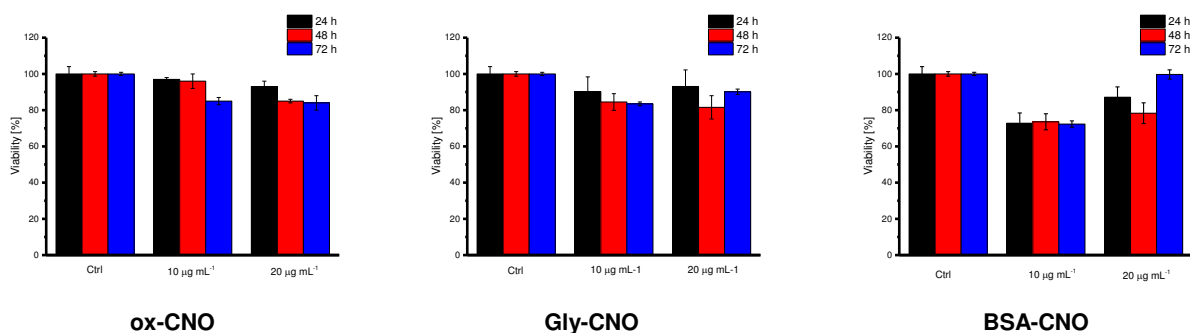


Figure 16. Cellular viability of MCF-7 cells after exposure to ox-CNO, Gly-CNO and BSA-CNO at a concentration of  $10 \mu\text{g mL}^{-1}$  and  $20 \mu\text{g mL}^{-1}$  for  $24$ ,  $48$  and  $72$  h. The viability was evaluated for the samples of CNOs against a non-treated control.

### 3.3.12 Cell Studies: Cellular Uptake

Uptake is an important consideration in the design of nanotherapeutics, because this will have a direct influence on the therapeutic load, and hence the appropriate dose, entering the cells. Variations in the physical properties of the nanoparticles, as well as differences in the cellular membrane characteristics, can affect the efficacy of the uptake process.<sup>27</sup> Accordingly, nanoparticle size is a major determinant of cellular uptake with approximately 50 nm in diameter being optimum for non-phagocytic cells.<sup>27</sup> Various ligands (proteins or peptides) can be used to enhance cellular uptake. For example, the HIV-derived TAT peptide is a well-recognized cell penetrating peptide, which can be used to facilitate cellular entry.<sup>28,29</sup> The surface charge of the nanoparticle has influence on whether or not it can cross the negatively charged cell membrane,<sup>9</sup> whereby increasing the overall surface charge of the nanoparticle can result in increased uptake across cellular membranes.<sup>27</sup> Mechanisms of cellular internalization of nanoparticles include phagocytosis, macropinocytosis, caveolar-mediated endocytosis, or clathrin-mediated endocytosis.<sup>8</sup> The size of the nanoparticle also determines the mechanism by which nanoparticles enter the cells and where it subsequently localizes intracellularly.<sup>3</sup> It has recently been demonstrated that the shape of nanoparticles is also a determining factor of the mechanism of uptake.<sup>30,31,32,33,34</sup> Therefore, knowledge of both of these aspects is invaluable in the engineering of nanoparticles targeted to specific microenvironments. Moreover, there is a strong relationship between the mode of particle uptake and the size of the particles themselves. Particles with small diameters (<200 nm) are taken up primarily via receptor-mediated endocytosis, while particles with larger diameters (>500 nm) are traditionally taken up by phagocytosis or micropinocytosis.

A preliminary cell-uptake study was carried out using the MCF-7 cell line. In order to explore the ability of the nano-conjugates to enter MCF-7 cells we performed confocal live cell imaging. MCF-7 cells were incubated for 24 h at 37 °C in the presence of 20 µg mL<sup>-1</sup> of fluorescently labelled glycopeptide 3 and Gly-CNO. Confocal imaging revealed that both Gly-CNO and compound 3 were efficiently uptaken by MCF-7 cells with the distinct spot-like regions in the cytosol indicative of lysosomal localization following cellular uptake (Figure 17). Although the glycopeptide could undergo endocytosis in the absence of the nano-particle, the ability to deliver the covalently bound substrates into cancer cells offers fascinating prospects for controlled release and immunotherapy applications. Given the numerous biological applications associated with synthetic glycopeptides, the ability to transfer these compounds into the cells using nano-platforms offers fascinating prospects for the development of these compounds as nanotherapeutics.

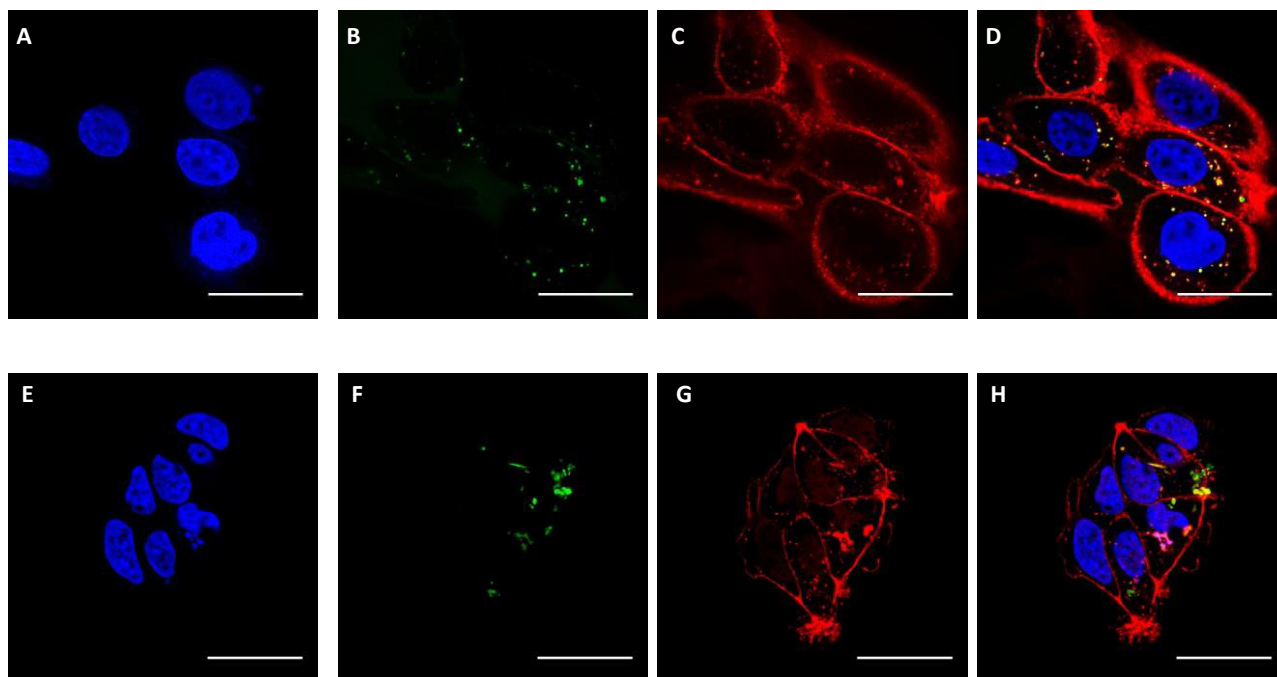


Figure 17: Confocal images of MCF-7 cells incubated with fluorescent labelled synthetic glycopeptide 3 (top panel) and Gly-CNO (bottom panel) at a concentration of  $20 \mu\text{g mL}^{-1}$  for 24 h. Nuclei are stained with Hoechst 33342 (blue), the presence of synthetic glycopeptide 3 and Gly-CNO is indicated by the green fluorescence signal. Hoechst 33342 (A), Green FITC signal (B), WGA 594 (C) merged images (D). Scale bars A-H=  $25 \mu\text{m}$ .

### 3.4 Conclusion

In summary, we have developed a versatile ligation approach for the covalent modification of CNOs employing chemoselective cysteine addition onto CNO bound maleimide residues. Both synthetic glycopeptides and native BSA protein were found to be compatible with these conditions. Covalently modified CNOs have been chemically and physically characterized by HR-MAS, infrared and fluorescence spectroscopy, FTIR, TGA, dynamic light scattering (DLS) and zeta potential measurements. The high biocompatibility and the efficient cellular uptake of these nanomaterials together with their high fluorescence reveal great promises for the development of new architectures for targeted imaging nanotherapeutics and antigen delivery devices. Of particular interest is the finding that a small glycopeptide conjugate appears to offer comparable biocompatibility to that of the larger BSA protein. This finding offers fascinating prospects for the development of biocompatible nano-materials, decorated with highly-defined synthetic peptides and glycopeptides as novel therapeutics. Furthermore, good functionalizations on the surface of CNOs could envisage the realization of multi stimuli-responsive and dynamic materials capable of changing their physicochemical behavior upon encountering specific micro-environmental signals becoming relevant for diagnosis, imaging and therapies of specific disease applications.

### 3.5 References

- (1) Wilson-welder, J. H.; Torres, M. P.; Kipper, M. J.; Mallapragada, S. K.; Wannemuehler, M. J.; Narasimhan, B. *J Pharm Sci* **2009**, 98:1278-1316.
- (2) Singh, M.; Chakrapani, A.; Hagan, D. O.; Hagan, O. *Expert Rev Vaccines* **2007**, 6:797-808.
- (3) Parboosing R, Maguire GE, Govender P, et al. *Viruses* **2012**; 4: 488–520.
- (4) Metcalfe, S. M.; Fahmy, T. M. *Trends Mol. Med.* **2012**, 18 (2), 72–80.
- (5) Yoo, J.; Irvine, D. J.; Discher, D. E.; Mitragotri, S. *Nat. Publ. Gr.* **2011**, 10 (7), 521–535.
- (6) Roldão A, Mellado MC, Castilho LR, Carrondo MJ, Alves PM: *Expert Rev Vaccines* **2010**, 9, 1149-1176.
- (7) Copland, M. J.; Rades, T.; Davies, N. M.; Baird, M. A. *Immunol Cell Biol* **2005**, 83, 97-105.
- (8) Petros, R. A.; Desimone, J. M. *Nat. Publ. Gr.* **2010**, 9 (8), 615–627.
- (9) Mcneela, E. A.; Mills, K. H. G. *Adv Drug Deliv Rev* **2001**, 51:43-54.
- (10) Zhao, L.; Seth, A.; Wibowo, N.; Zhao, C.; Mitter, N.; Yu, C.; Middelberg, A. P. J. *Vaccine* **2014**, 32 (3), 327–337.
- (11) Perrie, Y.; Mohammed, A. R.; Kirby, D. J.; Mcneil, S. E.; Bramwell, V. W. *Int J Pharm* **2008**, 364, 272-280.
- (12) Kim, M.; Yeon, J.; Shon, Y.; Kim, G. *Asian J. Pharm. Sci.* **2014**, 9 (5), 227–235.
- (13) Lepenies, B.; Lee, J.; Sonkaria, S. *Adv. Drug Deliv. Rev.* **2013**.
- (14) Misumi, S.; Masuyama, M.; Takamune, N.; Nakayama, D. *J Immunol* **2009**; 182, 6061–6070.
- (15) Manolova, V.; Flace, A.; Bauer, M.; Schwarz, K.; Saudan, P.; Bachmann, M. F. *Eur J Immunol* **2008**, 38, 1404-1413.
- (16) Chen, X.; Pradhan, T.; Wang, F.; Kim, J. S.; Yoon, J. *Chem. Rev.* **2012**, 112 (3), 1910–1956.
- (17) Burns, J. A.; Butler, J. C.; Moran, J.; Whitesides, G. M. *J. Org. Chem.* **1991**, 56, 2648-2650.
- (18) Gray, W. R. *Protein Science* **1993**, 2, 1749-1755.
- (19) Gray, W. R. *Protein Science* **1993**, 2, 1732-1748.
- (20) Frasconi, M.; Maffei, V.; Bartelmess, J.; Echevoyen, L.; Giordani, S. *Methods Appl. Fluoresc.* **2015**, 3 (4), 44005.
- (21) Kuznetsov, V. L.; Zilberberg, I. L.; Butenko, Y. V.; Chuvilin, A. L.; Segall, B. *J. Appl. Phys.* **1999**, 86 (2), 863–870.
- (22) Markey, L.; Giordani, S.; Scanlan, E. M. *J. Org. Chem.* **2013**, 78 (9), 4270–4277.
- (23) Hanaor, D.; Michelazzi, M.; Leonelli, C.; Sorrell, C. C. *J. Eur. Ceram. Soc.* **2012**, 32 (1), 235–244.
- (24) Muzi, L.; Tardani, F.; La Mesa, C.; Bonincontro, A.; Bianco, A.; Risuleo, G. *Nanotechnology* **2016**, 27 (15), 155704.
- (25) Holt, B. D.; Dahl, K. N.; Islam, M. F. *ACS Nano* **2012**, 6 (4), 3481–3490.
- (26) Holt, B. D.; Dahl, K. N.; Islam, M. F. *Small* **2011**, 7 (16), 2348–2355.
- (27) Kettler K, Veltman K, Van De Meent D, et al. *Environ Toxicol Chem* **2014**; 33, 481–492.
- (28) Vivès, E.; Richard, J.; Rispal, C.; Lebleu, B. *Curr Protein Pept Sci* **2003**; 4, 125–132.



- (29) Kaplan, I. M.; Wadia, J. S.; Dowdy, S. F. *J Control Release* **2005**; 102, 247–253.
- (30) Gratton, S. E. A.; Ropp, P. A.; Pohlhaus, P. D.; Luft, J. C.; Madden, V. J.; Napier, M. E.; Desimone, J. M. *Proc Natl Acad Sci U S A* **2008**; 105, 11613–11618.
- (31) Muro, S.; Garnacho, C.; Champion, J. A.; Leferovich, J.; Gajewski, C.; Schuchman, E. H.; Mitragotri, S.; Muzykantov, V. R. *Mol Ther* **2008**; 16, 1450–1458.
- (32) Champion, J. A.; Mitragotri, S. *Pharm Res* **2009**; 26, 244–249.
- (33) Decuzzi, P.; Pasqualini, R.; Arap, W.; Ferrari, M. *Pharm Res* **2009**; 26, 235–243.
- (34) Mitragotri, S.; Lahann, J. *Nat Mater* **2009**; 8, 15–23.

## 4. CNO for Photodynamic Therapy

### 4.1 Introduction

Photodynamic therapy (PDT) is a clinically approved therapeutic technique for the treatment of multiple diseases, mainly cancer.<sup>1</sup> It relies on the photoexcitation of an inactive photosensitizer (PS) at a wavelength that matches the absorption of the PS, leading to localized generation of cytotoxic reactive oxygen species (ROS). ROS cause oxidative damage to nearly all types of biomolecules (proteins, lipids and nucleic acids) and tumor cell death. PDT has remarkably improved selectivity and fewer side effects than traditional anticancer therapies. The photocytotoxic effects, which are utilized in PDT, are initiated by the absorption of light by a photosensitizer. A molecule that has absorbed a light quantum is excited to the first or higher excited states (Figure 1). The higher excited states are dissipated very rapidly (picoseconds) down to the first excited singlet state with a lifetime of the order of nanoseconds. This excited state can be deactivated by release of heat (non-radiative decay), emitted as fluorescence of a wavelength equal to or longer than that of the excitation light (utilized for cancer diagnosis) or undergo intersystem crossing (ISC). Photochemistry may occur from the first excited singlet state, but usually with low probability owing to the short life-time of this state. ISC is usually forbidden, but macrocyclic molecules with conjugated double bond systems ( $\pi$ -electron system) are exceptions and allow for ISC to long-lived (microseconds to milliseconds) triplet states. The triplet state may react in two ways, either by a type I mechanism involving electron or hydrogen atom transfer from one molecule to the other or by a type II mechanism involving energy transfer to molecular oxygen. Both mechanisms may occur simultaneously and their relative importance depends on the surroundings and the nature of the substrate molecules. Singlet oxygen causes mainly cell membrane damage by oxidizing amino acids (tryptophan, cysteine, histidine, methionine and phenylalanine), unsaturated fatty acids and cholesterol. Additionally, guanine may also be oxidized by singlet oxygen.

Once dioxygen is in its singlet excited state, it can be deactivated by other species to return to its ground state. This quenching can take place in two major ways:

- 1) Physical quenching: in which the interaction leads only to deactivation of singlet oxygen with no  $O_2$  consumption or product formation
- 2) Chemical quenching: where the quencher reacts with singlet oxygen to give a new product. This active species could oxidize substrates that were unaffected by oxygen in its normal energy state. Oxygen is ca. 1 V more oxidizing in its singlet excited state and is therefore significantly more electrophilic, reacting rapidly with unsaturated carbon/carbon bonds, neutral nucleophiles such as sulfides and amines, and as well as with anions. Each photosensitizer molecule can typically produce  $10^3/10^5$  molecules of  $^1O_2$  before being degraded through photobleaching by  $^1O_2$  or by some other process.

Singlet oxygen ( $^1O_2$ ), the lowest excited state of molecular oxygen, is a fascinating species in many ways. Its chemistry differs significantly from that of ground state triplet oxygen. Singlet oxygen readily reacts with a wide range of biological and organic materials which leads to their alteration and degradation. Arguably the most important way of singlet oxygen formation is the so-called photosensitizing process: A light excited molecule of an appropriate dye - so called photosensitizer (PS) - transfers energy to molecular oxygen giving rise to singlet oxygen. Singlet oxygen is involved in a rich variety of diverse biochemical processes, such as photosynthesis, cell signaling, immune responses or polymer degradation.

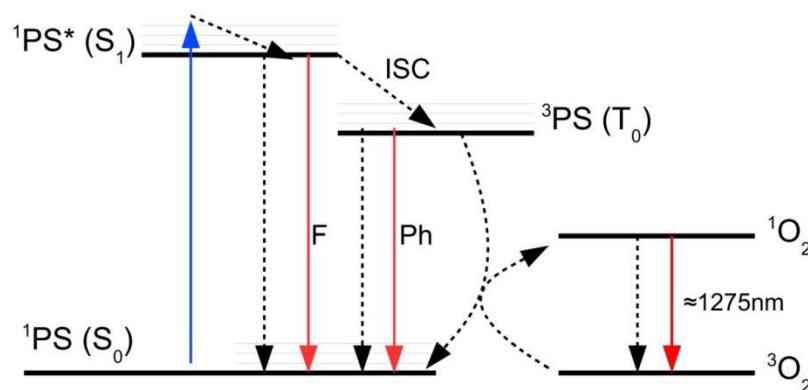


Figure 1. The diagram shows the electronic states following absorption of light by a photosensitizer. The blue arrow indicates the excitation of the photosensitizer to the excited singlet states ( $^1PS^*$ ). The other arrows indicate alternative pathways for dissipation of the energy in the excited state. ISC, intersystem crossing;  $^3PS$ , the sensitizer in the triplet state. F, fluorescence; Ph, phosphorescence.

#### 4.1.1 Carbon Nanomaterials for Photodynamic Therapy

Fullerenes such as  $C_{60}$  and  $C_{70}$  have been used as photosensitizers with a high efficiency of generating reactive oxygen species,<sup>2</sup> allowing for efficient photodynamic therapy using fullerenes without the need to load additional photosensitizing molecules. Ground state, singlet fullerene can be photoexcited to a short-lived triplet state, which transfers its energy to molecular oxygen in its triplet state, resulting in a series of reactive oxygen species including singlet oxygen and oxygen radicals. Hamblin et al. reported photodynamic therapy using N-methylpyrrolidinium-fullerene for the treatment of colon adenocarcinoma by intraperitoneal injection of the functionalized fullerene into the abdomen of the tumor-bearing mice, and found significantly slowed tumor growth compared to the control group.<sup>3</sup> Besides photodynamic treatment of tumor, the same group also reported the use of functionalized  $C_{60}$  fullerene as a broad-spectrum antimicrobial photosensitizer, which cures fatal wound infections under white light illumination in a mouse model.<sup>4</sup> Kim et al.<sup>5</sup> reported the synthesis of chitosan/fullerene nanogel for an efficient tumor therapy. At pH 7.4, electrostatic interactions between the pendant carboxylic acid groups of 2,3-dimethylmaleic acid (DMA) and the residual free amine groups of glycol chitosan (GC) resulted in the formation of multinanogel aggregates. Nevertheless, dissociation of the nanogel aggregates was observed at pH 5.0, resulting in improved singlet oxygen generation and elevated photodynamic tumor cell ablation.<sup>5</sup> The unique property of fullerenes in the efficient conversion from photons to reactive oxygen species has made fullerene derivatives competitive photosensitizers for PDT applications in vivo animal and even preclinical settings.<sup>6</sup> Lee et al. reported the synthesis of PEGylated SWCNTs loaded with a common photosensitizing drug, Chlorin e6 (Ce6), for PDT-based tumor treatment in mice.<sup>7</sup> It has also been reported by Tan et al. that the nanotube-photosensitizer complex can act as a “smart” PDT agent with molecular specificity. In this study, SWCNTs were used to quench singlet oxygen generation of the photosensitizer molecules, until the photosensitizer molecules were released from the backbone of SWCNTs in the presence of a specific molecular target.<sup>8</sup> Carbon nanotubes are known to strongly quench fluorescence of nearby molecular fluorophores and it was proposed that

photosensitizing molecules could be quenched in a similar fashion when in close proximity to the carbon nanotube surface. After conjugating an aptamer that recognized thrombin to the photosensitizer, Ce6, carbon nanotubes, and the aptamer-conjugated photosensitizer were mixed, leading to extremely high quenching of 98%. After the introduction of thrombin, a large increase in singlet oxygen generation was observed, indicating that the thrombin-recognizing aptamer– photosensitizer conjugate disassociated from the carbon nanotube and allowed recovery of photodynamic efficiency of Ce6. This approach has many significant benefits, namely that the generation of the cytotoxic reactive oxygen species is only produced after exposure to a particular target, resulting in a “smart” PDT agent that can be specifically turned on or off via selective molecular recognition and may have enhanced efficacy with mitigated toxicity to normal tissue.<sup>8</sup> By taking advantage of the ultrahigh loading of molecules through  $\pi$ - $\pi$  stacking, nanoGO has been used to deliver photosensitizers *in vitro* at high concentrations.<sup>9</sup> The same photosensitizer molecule as used in previous studies involving SWCNTs, Ce6 was used and loaded onto the PEGylated and well-dispersed nanoGO sheets through the supramolecular  $\pi$ - $\pi$  stacking. The GO-PEG-Ce6 conjugate demonstrated excellent serum stability and elevated cytotoxicity after irradiation. While the production of singlet oxygen species was slightly diminished by the presence of the quenching graphene surface (10–15% of free Ce6) in a similar fashion as reported in the previous study with carbon nanotubes,<sup>8</sup> many more surface defects are found in graphene oxide, which appears to be much less efficient at absorbing energy than carbon nanotubes. To this end, photodynamic therapy was still readily feasible utilizing nanoGO, evidenced by the large population of dead cells after incubation with GO-PEG-Ce6 conjugate and laser irradiation at 660 nm.

#### **4.1.2 Inhibited phototoxicity of a carbon nano-onion immobilized diiodo-BODIPY photosensitizer**

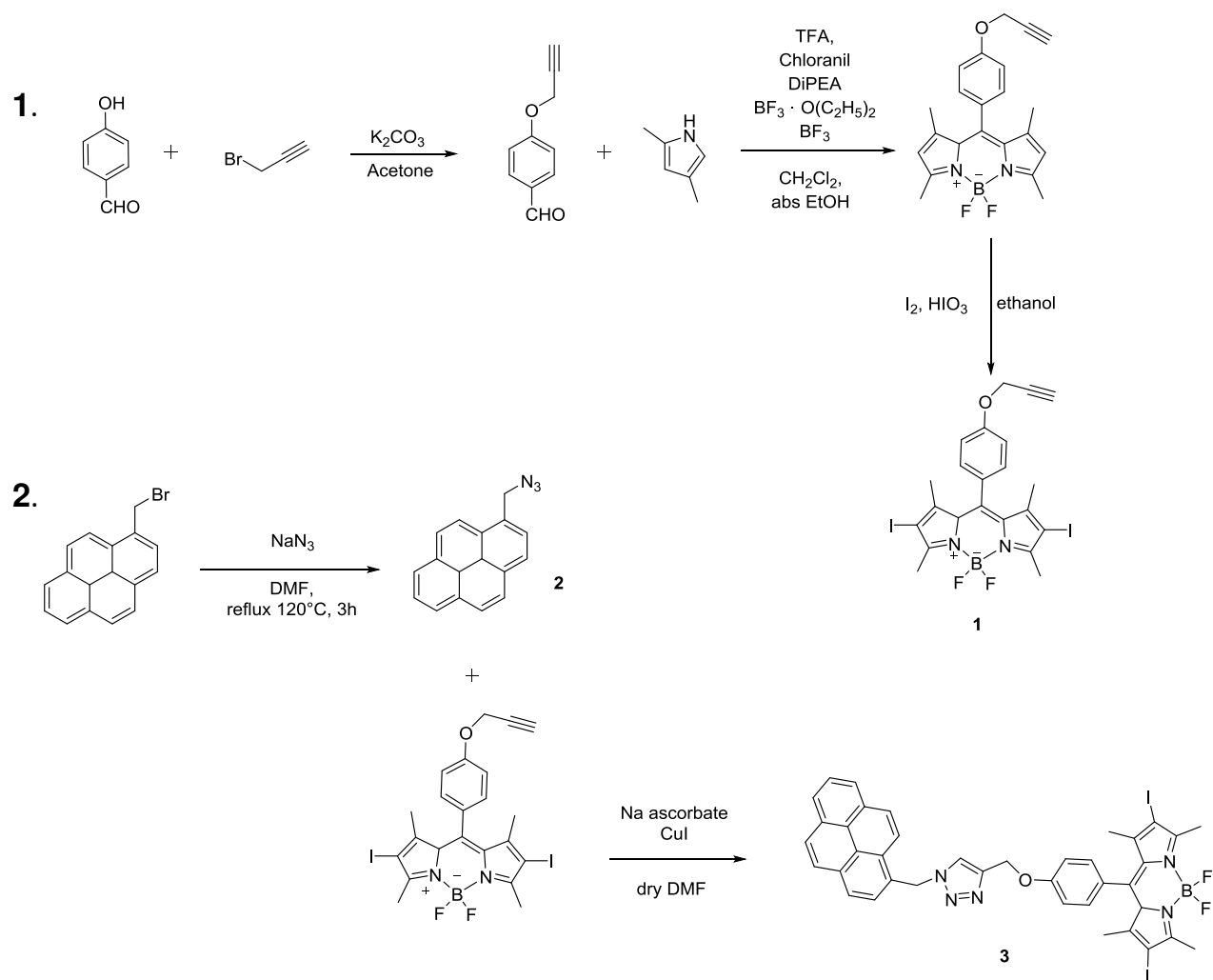
Photodynamic therapy is a non-invasive methodology for the treatment of malignant tumors and age related macular degeneration.<sup>10</sup> More recently, a significant cardiovascular potential for PDT was also demonstrated.<sup>11</sup> The treatment in general involves systemic administration of a photosensitizer. The sensitizer lingers longer in tumor tissues due to what is known as enhanced permeation and retention (EPR). Then, irradiation of the tumor tissues with preferably red light (due to its higher tissue permeability) excites the sensitizer, which should undergo an intersystem crossing before it excites dissolved ground state oxygen to generate highly reactive and (hence) cytotoxic singlet oxygen. While porphyrins are the most commonly used PDT sensitizers, there are many potential candidates for this role, most with impressive characteristics, such as strong absorption of red to near IR light, efficient generation of singlet oxygen, high chemical stability and availability in a pure, single isomeric state. Two classes of dyes recently added to the growing arsenal of potentially useful PDT sensitizers are Bodipy<sup>12</sup> derivatives and perylenediimides.<sup>13</sup> BODIPY dyes (Boron complexes of dipyrromethenes), have been established as suitable fluorophores for several applications due to their synthetic versatility, high photostability and bright fluorescence emission.<sup>14,15,16</sup> Based on the multiple possibilities to synthetically modify the BODIPY fluorophore, the tuning of the excited state properties of BODIPY dyes towards efficient triplet photosensitizers can be realized by the introduction of iodo-substituents on the BODIPY core.<sup>14,17</sup> In the biomedical field, the application of BODIPY dyes as singlet oxygen sensitizers for the photodynamic therapy (PDT) has emerged as one significant therapeutical approach for cancer treatment.<sup>18,19,20</sup> Furthermore, the photodynamic inactivation of microbes, fungi and viruses by iodo-substituted BODIPY derivatives was demonstrated and found to be dependent on the

photosensitizer dose and on the light source exposure, which can be specifically modulated to trigger the eradication of the bacterial strains.<sup>21</sup> Thus, Bodipy derivatives are especially interesting as these chromophores are easily derivatized to suit many applications.<sup>15,22</sup> Previously, it was shown that iodine or bromine substitution on the Bodipy nucleus enhanced intersystem crossing, and a few promising sensitizers for use in photodynamic therapy have been reported in the last few years.<sup>23</sup> An important issue with regard to photodynamic therapy agents is the delivery of these molecules into the organs/tumor tissues/tissues cells. There are many strategies for drug targeting, but a satisfactory multifunctional delivery agent is nevertheless needed. In this work, we report the synthesis of a novel pyrene-BODIPY dye acting as an efficient photosensitizer for photodynamic therapy and combine it with a CNO based delivery vector. The photosensitizer as well as the pyrene-iodo-BODIPY/CNO nanohybrids were characterized by optical spectroscopies. Moreover, the cellular uptake by HeLa cells and the photodynamic efficiency of the dye and the corresponding nanohybrids was investigated. The surprising finding of suppressed photodynamic efficiency of BODIPY/CNO nanohybrids is described and the recovery of the phototoxicity upon disruption of the nanohybrids is discussed. This report represents the first approach of CNM based molecular shuttles for a tunable delivery of hydrophobic BODIPY photosensitizer, including *in vitro* studies.

## 4.2 Experimental

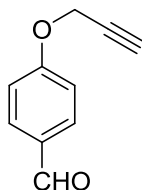
### 4.2.1 Synthesis of the pyrene-diiodoBODIPY dye

The synthesis of the pyrene-diiodoBODIPY dyad 3 was accomplished by a Huisgen type “click” reaction of a propargylated diiodo-BODIPY and 1-(azidomethyl)pyrene (Scheme 1). Despite previously reported non-iodated pyrene-BODIPY dyad,<sup>24</sup> the “click” reaction failed in the presence of catalytic amounts of CuI and sodium ascorbate. However, an excess of CuI and triethylamine, without ascorbate, led to the desired compound 3. Following this, 3 was immobilized on the surface of pristine CNOs by ultrasonication. The solution was filtered and the excess of dye was removed using our established protocol leading to 3/CNO. Additional experiments were carried out with benzoic acid functionalized CNOs (3/benz-CNO) in order to study the influence of different CNO surface modifications. Benz-CNOs were prepared based on our previous reports.<sup>24,25</sup>



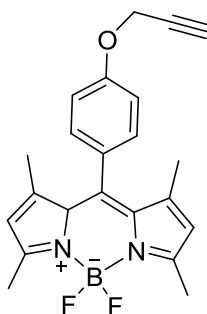
Scheme 1. Synthesis of diiodo-BODIPY photosensitizer 3.

## 4.2.2 Synthesis of 4-(prop-2-ynyloxy)benzaldehyde



4-Hydroxybenzaldehyde (2.44 g, 20 mmol) and K<sub>2</sub>CO<sub>3</sub> (3.88 g, 28 mmol) were dissolved in acetone (100mL). The reaction mixture was refluxed for 30 min at 76 C°, then propargyl bromide 80% in toluene solution (5.11 mL, 6.824 g, 57.4 mmol) was added and refluxed at 132°C. The reaction was refluxed until all 4-hydroxybenzaldehyde consumed (TLC 1:1 Hex/EtOAc). After 1 hour, the reaction mixture was filtered through a pad of silica and the solvent removed under reduced pressure to provide the desired compound as a light brown solid (96 % yield). <sup>1</sup>H NMR (400 MHz, CDCl<sub>3</sub>) δ 9.90 (s, 1H), 7.93 – 7.74 (m, 2H), 7.14 – 7.00 (m, 2H), 4.78 (d, J = 2.4 Hz, 2H), 2.59 (t, J = 2.4 Hz, 1H). <sup>13</sup>C NMR (101 MHz, CDCl<sub>3</sub>) δ 190.79 (s), 162.37 (s), 131.89 (s), 130.58 (s), 115.18 (s), 114.87 (s), 77.50 (d, J = 16.2 Hz), 77.10 (s), 76.78 (s), 76.42 (s), 55.95 (s) HRMS (ES+) m/z calcd for C<sub>10</sub>H<sub>8</sub>NaO<sub>2</sub> [M + Na]<sup>+</sup> 183.0422, found 183.0422

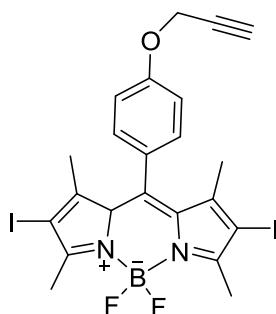
## 4.2.3 Synthesis of 1,3,5,7-Tetramethyl-8-(4-Propargyloxyphenyl)-4,4-difloroboradiaza-s-indacene



4-(prop-2-ynyloxy)benzaldehyde (752 mg, 4.7 mmol) and 2,4-dimethylpyrrole (900 mg, 9.6 mmol) were dissolved in a deoxygenated solution of dichloromethane (280mL) and absolute ethanol (20mL). After 15' the reaction was started by adding TFA (3 drops), and the reaction mixture was stirred at RT overnight, in the dark. Chloranil (1.144 g, 4.7 mmol) was added, and after stirring for 2h 30', the solvent was removed in reduced pressure, and the crude mixture was dissolved in dichloromethane (150mL). DiPEA (4.9 mL, 3.635 g - 28 mmol) was added, and 30' later, boron trifluoride diethyl etherate (5.2 mL, 5.98g, 28.8 mmol) was slowly added, and the reaction mixture was left stirring for 3 hours at RT. The reaction mixture was filtered through a pad of silica and the solvent removed under reduced pressure. The crude was purified by column chromatography. (SiO<sub>2</sub>, eluted with hexane:dichloromethane 1:1 (11% yield). <sup>1</sup>H NMR (400 MHz, CDCl<sub>3</sub>) δ 7.24 – 7.18 (m, 2H), 7.14 – 7.08 (m, 2H), 6.02 (d, J = 18.3 Hz, 2H), 4.84 – 4.73 (m, 2H), 2.62 – 2.54 (m, 6H), 1.59 (d, J = 15.8 Hz, 1H), 1.44 (s, 6H). <sup>13</sup>C NMR (101 MHz, CDCl<sub>3</sub>) δ 158.13 (s), 129.26 (s), 128.04 (s), 121.18 (s), 115.64 (s), 77.33 (s), 77.01 (s), 76.69 (s), 75.86 (s), 56.03 (s), 34.60 (d, J = 14.1 Hz), 31.60 (s),

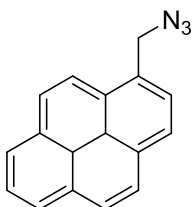
29.07 (s), 26.92 (s), 25.28 (s), 22.63 (d, J = 5.6 Hz), 20.68 (s), 18.75 (s), 14.53 (s), 14.10 (s), 11.42 (s). HRMS (ES+) m/z calcd for C<sub>22</sub>H<sub>22</sub>BF<sub>2</sub>N<sub>2</sub>NaO [M + Na]<sup>+</sup> 401.1617, found 401.1644

#### 4.2.4 Synthesis of 2,6-Diiodo-1,3,5,7-tetramethyl-8-(4-Propargyloxyphenyl)-4,4-difloroboradiaza-s-indacene



1,3,5,7-Tetramethyl-8-(4-Propargyloxyphenyl)-4,4-difloroboradiaza-s-indacene (50 mg, 0.13 mmol) and I<sub>2</sub> (83 mg, 0.33 mmol) were dissolved in deoxygenated absolute ethanol (100 ml). Iodic acid, HIO<sub>3</sub> (45.74 mg, 0.26 mmol) was dissolved in a few drops of water and added into previous solution. The reaction mixture was stirred at 80 °C for 3 hours till all reactant was consumed. Then, saturated sodium thiosulfate solution was added (50 ml) and it was stirred at room temperature for additional 30 min. Then, it was extracted with CHCl<sub>3</sub> and water. Organic layer was dried with MgSO<sub>4</sub> and evaporated under reduced pressure. The product was purified by silica gel column chromatography using CHCl<sub>3</sub>/DCM (50/50, v/v). Fraction containing the final compound was collected and the solvent was removed under reduced pressure (72% yield). <sup>1</sup>H NMR (400 MHz, CDCl<sub>3</sub>), 7.09 (d, J=8.8 Hz, 2H), 7.04 (d, J=8.8 Hz, 2H), 4.70 (s, 2H), 2.56 (s, 6H), 2.49 (s, 1H), 1.36 (s, 6H). <sup>13</sup>C NMR (101 MHz, CDCl<sub>3</sub>) 158.6, 156.7, 146.0, 141.4, 131.6, 129.1, 127.8, 116.0, 100.1, 85.8, 76.1, 56.1, 17.1, 16.0. HRMS (ES+) m/z calcd for C<sub>22</sub>H<sub>20</sub>BF<sub>2</sub>I<sub>2</sub>N<sub>2</sub>NaO [M + Na]<sup>+</sup> 652.9550, found 652.9515.

#### 4.2.5 Synthesis of 1-(azidomethyl)pyrene

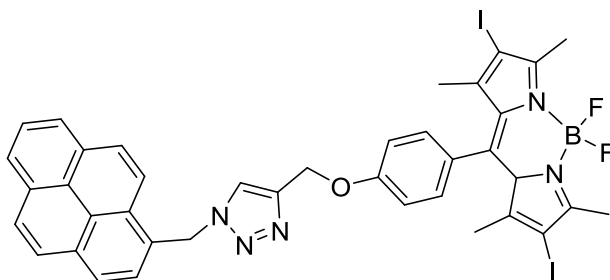


1-(azidomethyl)pyrene. 1-(bromomethyl)pyrene (537.9 mg, 1.83 mmol) and NaN<sub>3</sub> (616.3 mg, 9.48 mmol) were added to a flame dried round bottom flask under argon. 10 mL of DMF was added to the mixture. The reaction mixture was placed in an oil bath and heated at 120°C for 3 hours. The reaction was refluxed until all 1-(bromomethyl)pyrene was consumed. It was then poured into 100 mL water and extracted with CH<sub>2</sub>Cl<sub>2</sub> (3 x 25 mL). Combined organic extractions were dried (MgSO<sub>4</sub>) and concentrated to provide the desired compound as a light orange solid (87 % yield). <sup>1</sup>H NMR (400 MHz, CDCl<sub>3</sub>) δ 8.14 – 8.07 (m, 2H), 8.04 – 7.83 (m, 6H), 7.74 (d, J = 7.8 Hz, 1H), 4.78 (s, 2H). <sup>13</sup>C NMR (101 MHz, CDCl<sub>3</sub>) δ 131.56 (s), 131.15 (s), 130.63



(s), 129.40 (s), 128.94 (s), 128.59 (s), 128.15 (s), 127.70 (s), 127.19 (d,  $J = 14.3$  Hz), 126.10 (s), 125.53 (d,  $J = 4.8$  Hz), 124.78 (s), 124.52 (d,  $J = 6.6$  Hz), 122.43 (s), 77.88 (s), 77.56 (s), 77.24 (s), 52.95 (s). HRMS (FAB):  $m/z$  calculated for  $C_{17}H_{11}N_3$  257.0953, measured: 257.0955.

#### 4.2.6 Synthesis of photosensitizer 3

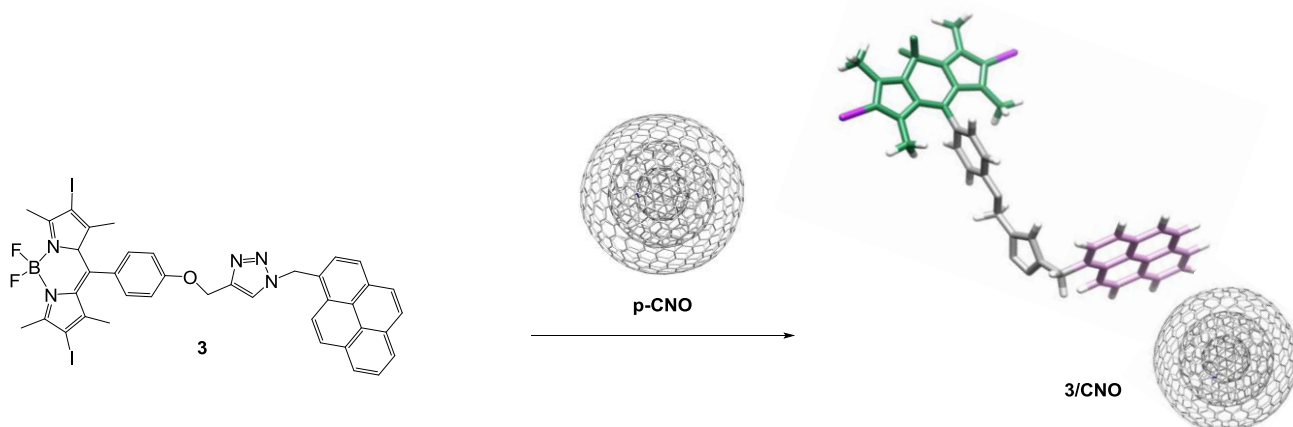


azidomethyl)pyrene (54.5 mg, 0.2 mmol), iodo-bodipy (75.6 mg, 0.2 mmol) and Na ascorbate (23.8 mg, 0.12 mmol) were dissolved in deoxygenated DMF (20 mL), and the reaction mixture was stirred for 20 minutes at RT. CuI (11.4 mg, 0.06 mmol) was added and the reaction mixture was stirred overnight at 40°, in the dark. Subsequently, the reaction mixture was extracted with dichloromethane and H<sub>2</sub>O, then the organic phase was dried with MgSO<sub>4</sub>, filtered, and the solvent removed under reduced pressure (82 % yield). The crude was purified by column chromatography (SiO<sub>2</sub>, eluted with hexane:dichloromethane 1:1). <sup>1</sup>H NMR (400 MHz, CDCl<sub>3</sub>)  $\delta$  8.32 – 7.98 (m, 9H), 7.46 – 7.33 (m, 1H), 7.11 – 6.93 (m, 4H), 6.33 (s, 2H), 5.32 (s, 2H), 5.16 (d,  $J = 11.7$  Hz, 2H), 2.62 (d,  $J = 23.9$  Hz, 6H), 1.35 (d,  $J = 6.8$  Hz, 6H). <sup>13</sup>C NMR (100 MHz, CDCl<sub>3</sub>) 14.4, 14.6, 52.7, 62.1, 115.4, 116.7, 121.1, 121.9, 122.7, 125.0, 125.9, 126.1, 126.4, 126.5, 127.2, 127.8, 128.5, 129.2, 129.4, 130.6, 131.2, 132.3, 141.5, 143.1, 155.3, 158.2, 158.7. HRMS (ESI)  $m/z$ : calcd. for  $C_{39}H_{31}BF_2N_5O^+$ : 636.2746 [M + H], found 636.2762.

#### 4.2.7 Synthesis of 3/CNO Nano-hybrid

While overall less research has been conducted on carbon nanomaterials for PDT, the synergistic effects of combining carbon nanotubes, graphene, and carbon dots with photosensitizers significantly boost the efficacy of treatment. Our group recently reported the non-covalent functionalization of carbon nano-onions (CNOs) with highly fluorescent pyrene-BODIPY dyads and their application for biomedical imaging, with promising results.<sup>24</sup> These findings were in line with other recent works, where CNOs exhibited a prompt and effective uptake by different cell lines, revealing high stability, low toxicity and high efficiency.<sup>25,26,27</sup> In a similar fashion to drug loading applications of carbon nanomaterials, photosensitizers could be non-covalently loaded onto the aromatic surface of carbon nanomaterials coated in biocompatible polymers through  $\pi$ - $\pi$  stacking for activation after laser excitation.

An important issue with regard to photodynamic therapy agents is the delivery of these molecules into the organs/tumor tissues/tissues cells. There are many strategies for drug targeting, but a satisfactory multifunctional delivery agent is nevertheless needed. To achieve this goal, we chose to use a strong pyrene-carbon nanoion  $\pi$ - $\pi$  interactions. Thus, our target molecule (Scheme 6) is composed of a red absorbing chromophore (Bodipy), intersystem crossing promoter heavy atoms (iodines at 2 and 6 positions of the Bodipy core), and a pyrene substituent on the branch of the chromophore for  $\pi$ -stacking interactions with the CNO (Scheme 2).

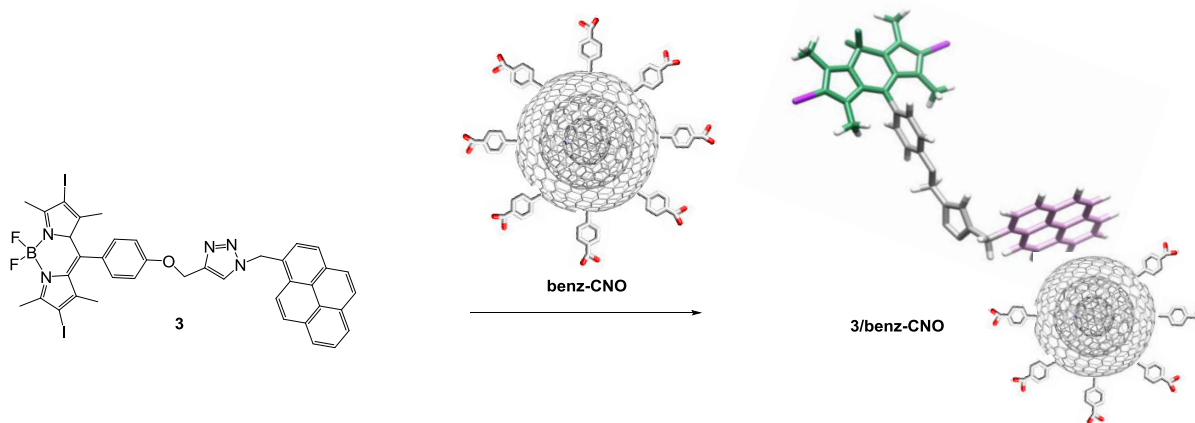


Scheme 2. Non covalent immobilization of diiodo-BODIPY photosensitizer 3 onto CNO.

3 (4 mg, 0.006 mmol) and 15 mg of pristine CNOs were dispersed in 15 mL of dry dimethylformamide (DMF) and sonicated in an ultrasonic bath for 30 minutes. Then, the CNOs were filtered through a nylon filter (0.2  $\mu$ m) and washed with THF until the THF appears colorless. Finally, the functionalized CNO nanomaterial was dried overnight at room temperature. 15 mg of 3/CNO hybrid were recovered from the filter as a black, fine powder.

## 4.2.8 Synthesis of 3/benz-CNO Nano-hybrid

Additional experiments were carried out with CNOs bearing benzoic acid functionalities on the surface (3/benz-CNO) in order to study the influence of different CNO surface modifications (Scheme 3). 3 (4 mg, 0.006 mmol) and pristine CNOs (12 mg) were dispersed in 15 mL of dry dimethylformamide (DMF) and sonicated in an ultrasonic bath for 60 minutes. Then, the CNOs were filtered through a nylon filter (0.2  $\mu\text{m}$ ) and washed with THF until the THF appears colorless (approx. 100 mL). Finally, the functionalized CNO nanomaterial was dried overnight at room temperature. 11 mg of 3/CNO hybrid was recovered from the filter as a black, fine powder.



Scheme 3. Non covalent immobilization of diiodo-BODIPY photosensitizer 3 onto benz-CNO.

## 4.3 Results and Discussion

### 4.3.1 Absorption and Emission spectroscopy of pyrene-diiodoBODIPY dye

The solubility of 3 in common polar organic solvents such as methanol, ethanol, isopropanol, but also in acetonitrile is negligible. Also in water, 3 is not soluble, while in non-polar organic solvents the solubility of 3 is excellent. 3 was characterized by absorption and fluorescence spectroscopy. The absorption maximum of 3 in DMSO is located at 536 nm with molar extinction coefficients of  $79.9 \times 10^3 \text{ M}^{-1} \text{ cm}^{-1}$ . Pyrene-centered absorption bands were observed at 268, 279, 316, 330 and 346 nm, with an additional broad, BODIPY-based absorption band located in the area around 400 nm in DMSO (Figure 2). The fluorescence quantum yield of 3 is very low, due to the heavy-atom effect of the iodo-substituents on the BODIPY core structure, with values between 1% and 3% and emission maxima between 552 and 555 nm. The singlet oxygen quantum yield of 3 upon irradiation, measured in relation to rose bengal in benzylalcohol, was found to be 0.37.<sup>28</sup>

### 4.3.2 Absorption and Emission spectroscopy of 3/CNO and 3/benz-CNO

The photophysical characterization of the two nano-hybrids clearly revealed the loading of the CNO nanoparticles with 3 (Figure 2). A dispersion of 3/CNO and 3/benz-CNO in DMSO showed the plasmonic

absorption and scattering of the CNO nanomaterial over the whole spectral area. Furthermore, distinct absorption peaks at 279, 329, 346 and 536 nm are related to the presence of 3 in an estimated concentration of  $2.3 \times 10^{-7}$  M for 3/CNO and  $7.7 \times 10^{-8}$  M for 3/benz-CNO at a mass concentration of  $10 \mu\text{g mL}^{-1}$  (Figure 2).

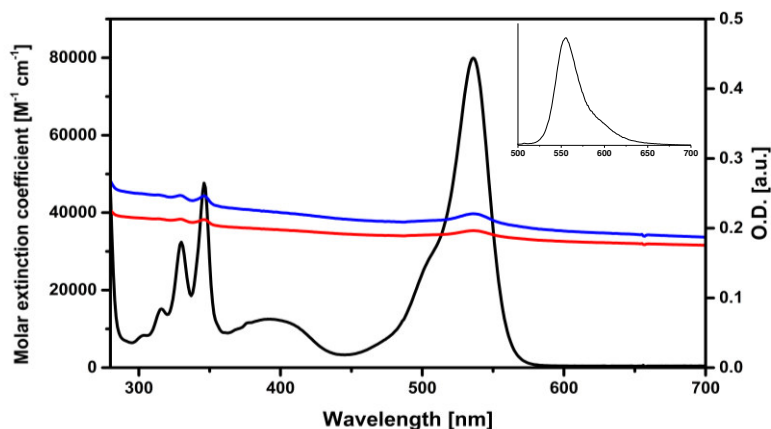


Figure 2. Absorption spectra of 3 (black) and of a dispersion of 3/CNO (blue,  $10 \mu\text{g mL}^{-1}$ ) and 3/benz-CNO (red,  $10 \mu\text{g mL}^{-1}$ ) in DMSO illustrating the molar extinction coefficient of 3 and the loading of the CNOs with dyad 3. Inset: Fluorescence spectrum of 3 upon excitation at 490 nm.

#### 4.3.3 Biological Studies of Nano-hybrid 3/CNO

In order to evaluate the suitability of these nano-hybrids as possible drug delivery system, the cellular uptake and cytotoxicity of 3/CNO *in vitro* on HeLa cells was investigated. For the uptake studies, HeLa cells were incubated with dispersion of 3/CNO at a mass concentration of  $10 \mu\text{g mL}^{-1}$ . An efficient uptake of 3/CNO into the cancer cells after 24 h of incubation (Figure 3) was confirmed by observing a green fluorescence signal of the BODIPY dye in the cytoplasm. The 3D combined rendering clearly showed a spot-like pattern inside the cells, suggesting an endocytosis pathway for the 3/CNO internalization.

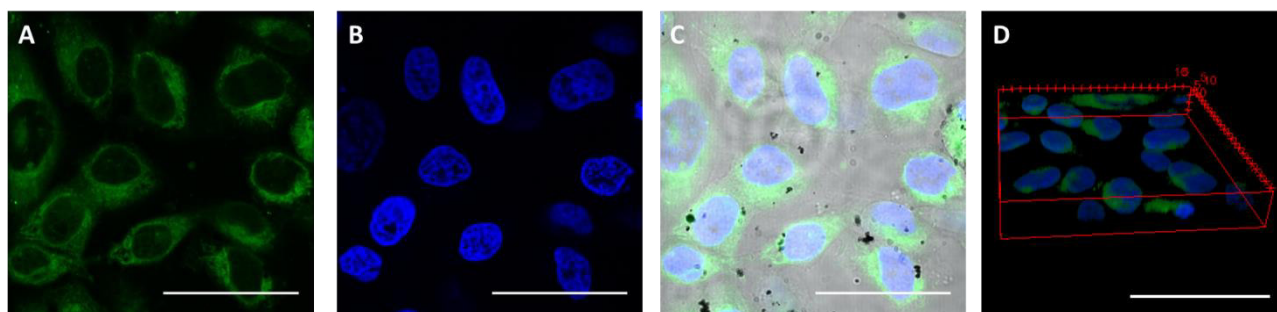


Figure 3. Confocal images of live HeLa cells incubated for 24h with 3/CNO at a mass concentration of  $10 \mu\text{g mL}^{-1}$ . Nuclei are stained with Hoechst 33342 (blue), the presence of 3/CNO is indicated by the green fluorescence signal. Green BODIPY signal (A), Hoechst 33342 (B) and combined images with bright field (C). (D) 3D combined rendering revealing the spotty pattern of the green BODIPY fluorescence. Scale bars A-D=  $50 \mu\text{m}$ .

For cytotoxicity studies, HeLa cells were incubated with dispersions of pristine CNO and 3/CNO at 10 and 20  $\mu\text{g mL}^{-1}$  in DMEM medium for 24h. Following the incubation, the cells were washed with PBS three times and illuminated with a white LED for different periods of time (5 and 15 minutes) in phenol red-free DMEM medium. Time-dependent phototoxicity of the treated cells was quantified by using the Presto Blue<sup>®</sup> assay. The cell's metabolic activity was not affected by CNOs at any mass concentrations and illumination time tested (Figure 4). Moreover, in control experiments BODIPY 3 demonstrates to be cytotoxic following irradiation, whereas the hybrid material 3/CNO did not impair the HeLa cell's metabolic activity.

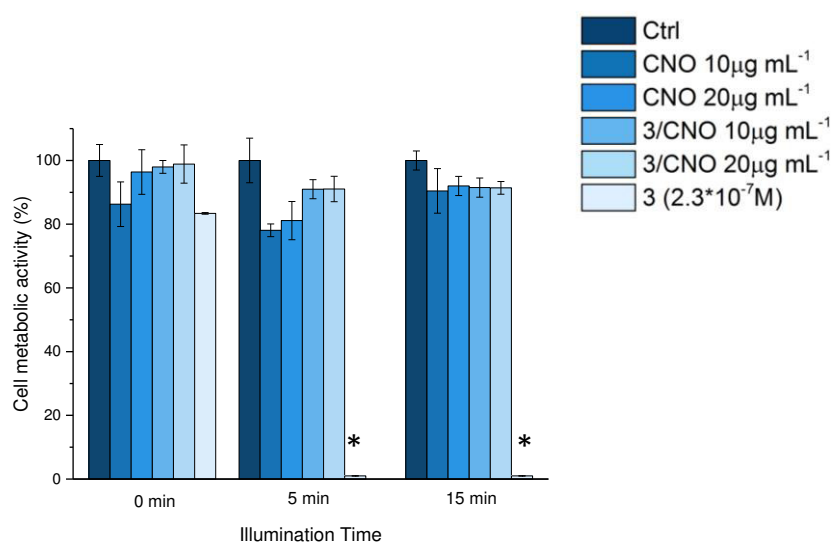


Figure 4. Cellular metabolic activity of HeLa cells incubated with different concentrations of CNO, 3/CNO and 3 following illumination at different time points. Please note: CNOs were dispersed in PBS buffer mother solutions.

Based on these preliminary observations, further modifications of the experimental procedure were instigated. The concentrations of 3/CNO were set to be 10 and 20  $\mu\text{g mL}^{-1}$ ; final working dilutions were obtained by dispersing CNOs from mother solutions in either PBS or DMSO in DMEM. Illumination exposure time points were set to 2, 5, 10, and 15 minutes. Non-irradiated experiments were conducted as well (dark control,  $t=0$ ). Furthermore, a  $2.3 \times 10^{-7}\text{M}$  solution of 3 (obtained by the dilution of a DMSO mother solution in DMEM, with a final DMSO concentration of 2 vol%) was used as reference, based on the estimated loading of 3 onto the nanohybrid. DMSO was added to all samples in order to obtain a final DMSO concentration of 2 vol%. As shown in Figure 6, photosensitizer 3 alone revealed an impressive cytotoxicity after illumination. After 2 minutes, no cellular metabolic activity can be detected, while in the dark control the cell's metabolic activity is not compromised by the exposure to the dye. The presence of 3/CNO, pre-dispersed in PBS, don't induce an illumination time or concentration dependent reduction of HeLa metabolic activity. On the other hand, by exposing cells to 3/CNO, pre-dispersed in DMSO – with increasing illumination time and CNO concentration, HeLa metabolic activity declined remarkably. The cytotoxicity assays clearly indicated that the

presence of CNOs prohibited the photodynamic efficiency of the BODIPY photosensitizer 3, as long as it is immobilized onto the CNO surface (Figure 5).

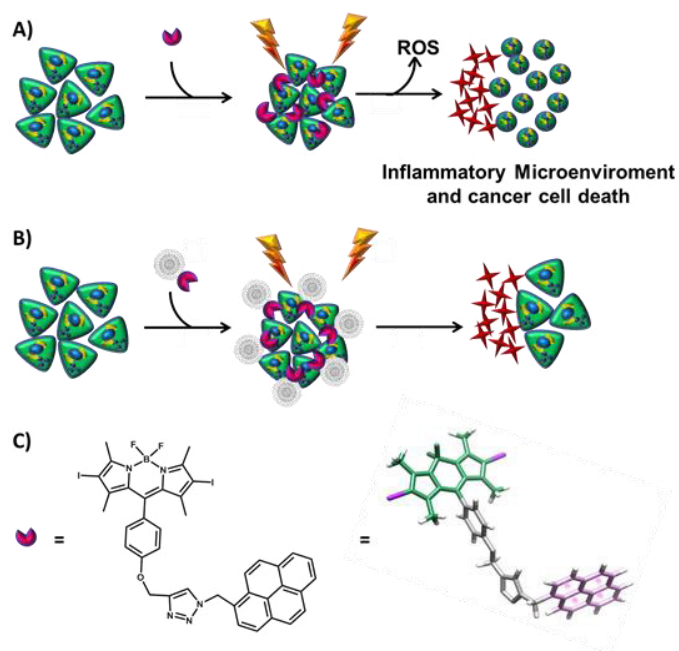


Figure 5. Schematic representation of the effect on the cells of the 3/CNO-nano hybrid.

When the photosensitizer was partially removed from the CNO surface, PDT efficiency was partially restored. To evaluate this conclusion, the following aspects need to be considered. Important for any drug delivery system is that the drug molecule does not detach from the surface of the molecular shuttle before being delivered intracellularly. Upon filtration of 3/CNO dispersed in DMSO by using a syringe filter with a 0.2  $\mu\text{m}$  nylon membrane, the BODIPY based absorption spectrum with the characteristic pyrene and BODIPY centered absorption bands, but no plasmonic CNO absorption, was observed. This clearly indicated that, when 3/CNO was dispersed in DMSO, 3 was removed from the CNO surface, thus released in solution. Similar treatment of a PBS dispersion of 3/CNO did not evidence any free BODIPY 3 after the filtration process. These findings strongly match with the *in vitro* results: when 3/CNO is dispersed in PBS, an intact nano hybrid delivery system where the active component is immobilized on the molecular shuttle is prepared. On the other hand, by initially dispersing 3/CNO in DMSO, BODIPY 3 is released in solution, and the drug delivery system is obviously disrupted and no longer comparable to the initial intact 3/CNO delivery system.

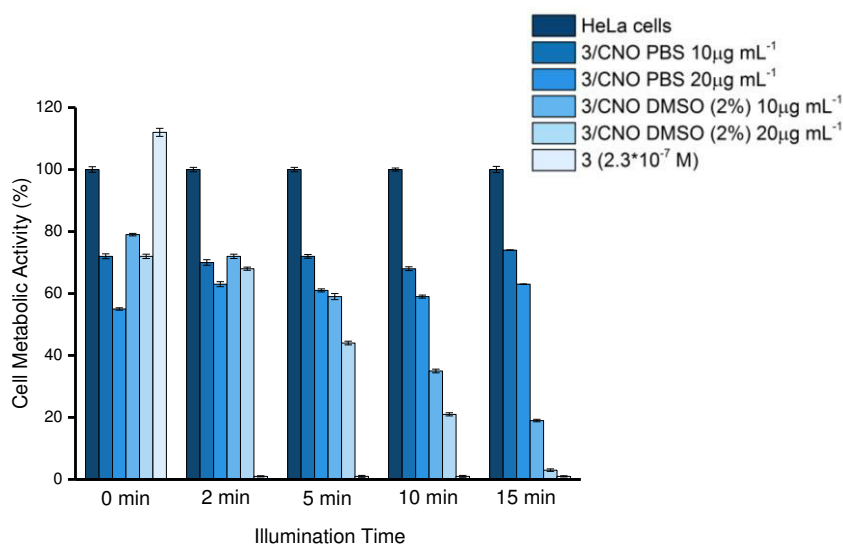


Figure 6. Cell metabolic activity of HeLa cells incubated with 3/CNO and 3 at different concentrations and illumination times, versus different dilution methods. Please note: Different CNO mother solutions (in PBS buffer or DMSO) were used as indicated.

#### 4.3.4 Biological Studies of Nano-hybrid 3/benz-CNO

The concentration of 3 in a 10 µg mL<sup>-1</sup> DMSO dispersion of 3/benz-CNO was determined to be about  $7.7 \times 10^{-8}$  M. This corresponds to 1/3 compared to the 3/CNO dispersion. Interestingly, also lower concentrations of 3 confirmed a strong photodynamic-triggered reduction of the cellular metabolic activity and again, in the PBS-based dispersions, 3 anchored at the whole nano-shuttle don't not reveal a significant cytotoxicity. On the other hand, by dispersing the 3/benz-CNO constructs in DMSO, the free photosensitizer 3 once being removed from the CNO surface, showed a clear efficiency in the photodynamic killing of HeLa cells (Figure 7A and 7B).

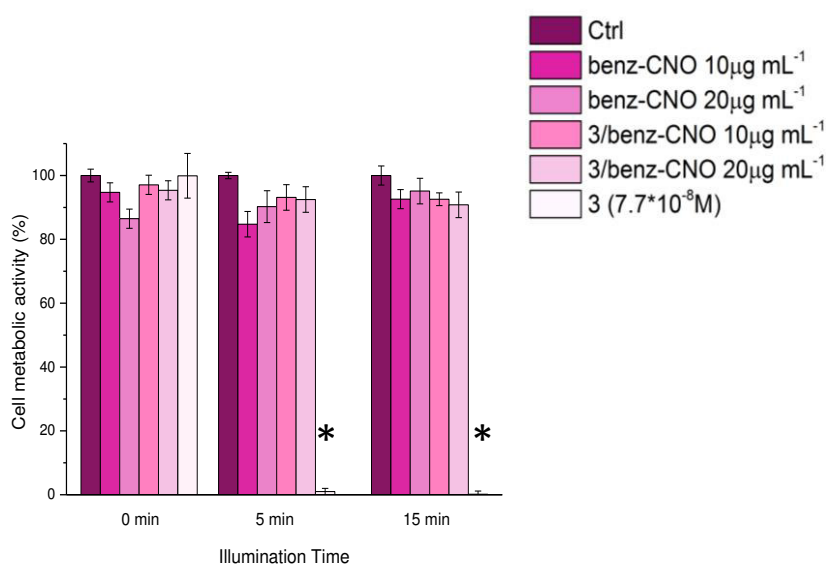


Figure 7A. Cellular metabolic activity of HeLa cells incubated with different concentrations of CNO, 3/CNO and 3 following illumination at different time points. Please note: CNOs were dispersed in PBS buffer mother solutions.

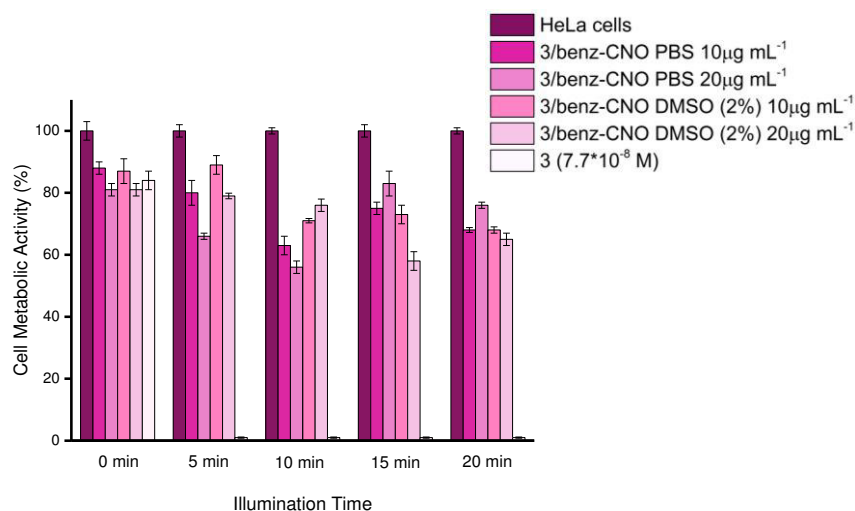


Figure 7B. Cell metabolic activity of HeLa cells incubated with 3/benz-CNO and 3 at different concentrations and illumination times, versus different dilution methods. Please note: Different CNO mother solutions (in PBS buffer or DMSO) were used as indicated (bottom graph).

#### 4.3.5 Photobleaching studies

1,3-diphenylisobenzofuran (DPBF) is a fluorescent molecule which possesses a highly specific reactivity towards singlet oxygen ( $^1\text{O}_2$ ) forming an endoperoxide which decomposes to give 1,2-dibenzoylbenzene (See Figure 8). In other words, DPBF is a singlet oxygen trap which reacts with  $^1\text{O}_2$  giving cis-dibenzoylbenzene. This reaction between DPBF and  $^1\text{O}_2$  can be followed by measuring the decrease in fluorescence intensity of DPBF. In 1993, Carloni et al.<sup>29</sup> in order to check the specificity of DPBF toward free radicals carried out a series of experiments. DPBF was reacted with hydroxy ( $\text{HO}\cdot$ ), alkyloxy ( $\text{RO}\cdot$ ), alkylperoxy ( $\text{ROO}\cdot$ ), and C-centered radicals (2-cyanoisopropyl radical) in Triton-X micelles and in natural systems (rat liver microsomes). In all cases, the DPBF is rapidly transformed to 1,2-dibenzoylbenzene in the case of O-centered radicals and to the corresponding adduct in the case of 2-cyanoisopropyl radical. The experiments in the model systems were also carried out from the chemical point of view and the reaction products were isolated and identified. From the results obtained, it should be stressed that DPBF must be used with caution in complex biological systems for the detection of  $^1\text{O}_2$ , as it also reacts with different radical species.<sup>29</sup>

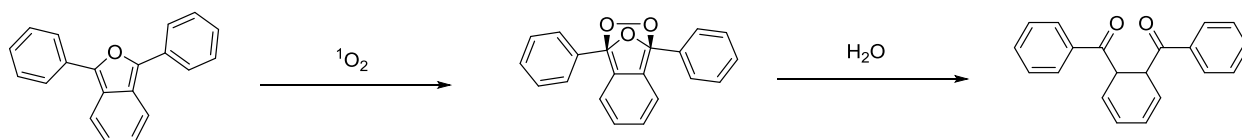


Figure 8. DPBF mechanism of action.

The use of DPBF is of particular interest, because when the molecule is incorporated in model biological membranes and excited at 410 nm, it shows a fluorescence emission spectrum with a maximum at 455 nm.<sup>30</sup> This allows the molecule to be used in biological membranes where the presence of proteins does not



interfere with the DPBF fluorescence. Hence, the monitoring of DPBF fluorescence would be a simple method which does not require particular techniques to detect  $^1\text{O}_2$  in natural systems.

Data derived from additional photobleaching experiments supported these results by describing the ability of BODIPY 3 to generate ROS and its release features from the CNO's surface. BODIPY dye 3 without CNOs showed a high efficiency in ROS generation, indicated by the rapid photobleaching of the ROS sensor molecule DPBF. When BODIPY loaded CNOs were used, the photobleaching of DPBF is slowed, but still progresses rapidly. This reflects the above-mentioned partial removal of the dye from the CNO surface in organic solvents such as benzylalcohol or DMSO (in the *in vitro* experiments) - a disruption of the delivery system - and thus a certain efficiency in singlet oxygen generation (See Figure 9). Also the lower loading of the benz-CNO/3, compared to the CNO/3 hybrids was confirmed by this set of data (See Figure 10).

### 4.3.6 Photobleaching studies for 3/CNO

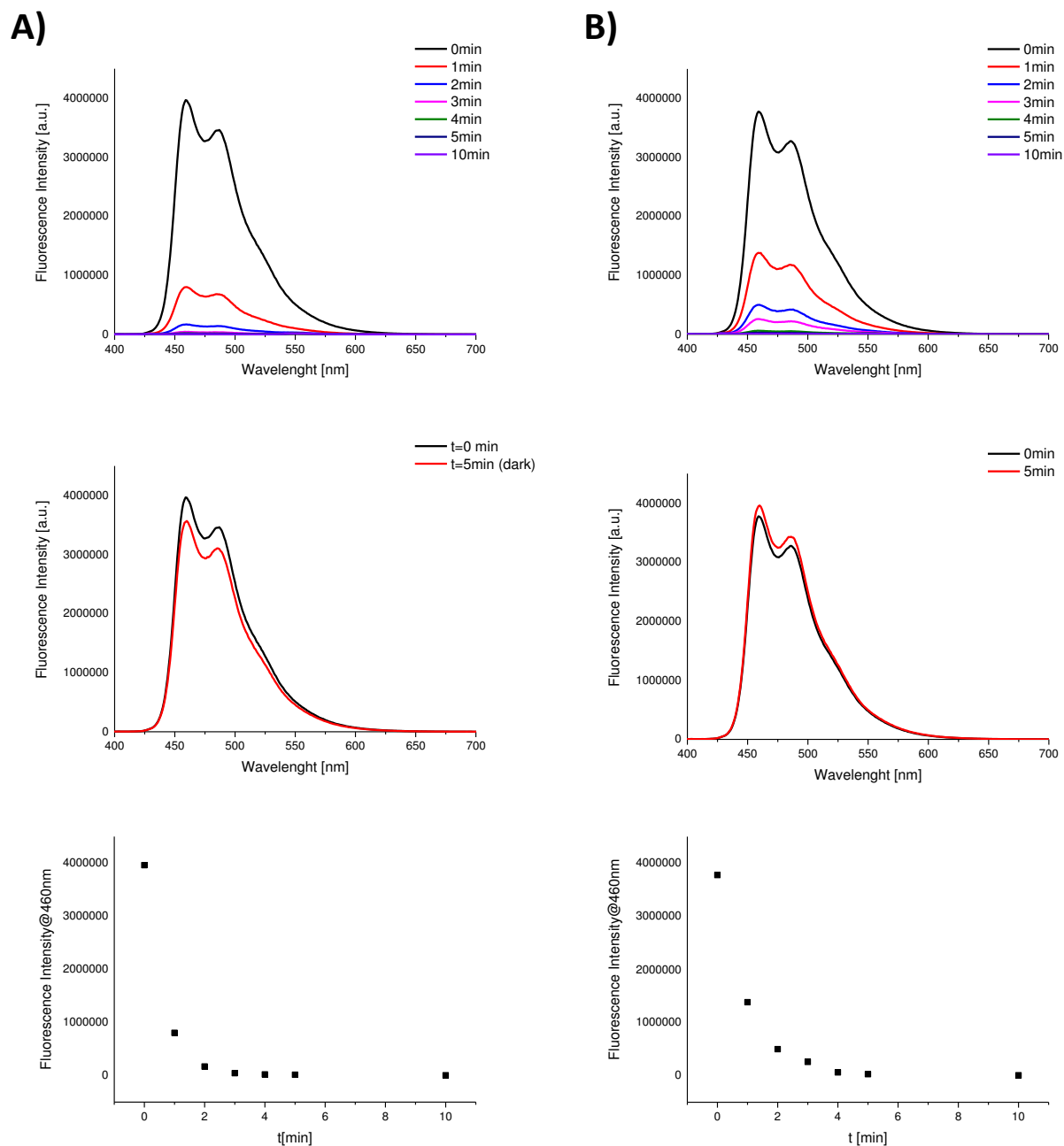


Figure 9. Fluorescence spectra of 1,3-diphenylisobenzofuran (DPBF) in the presence of 3 (A) and 3/CNO (B) upon 380 nm excitation in benzylalcohol. Concentration DPBF  $4.6 \times 10^{-6}$  M. Emission spectra recorded at different time intervals between 0 and 10 min (top row) of illumination. Control experiments in the dark after 0 and 5 min (center row), and maximum fluorescence intensities as function of illumination time (bottom row).

### 4.3.7 Photobleaching studies for 3/benz-CNO

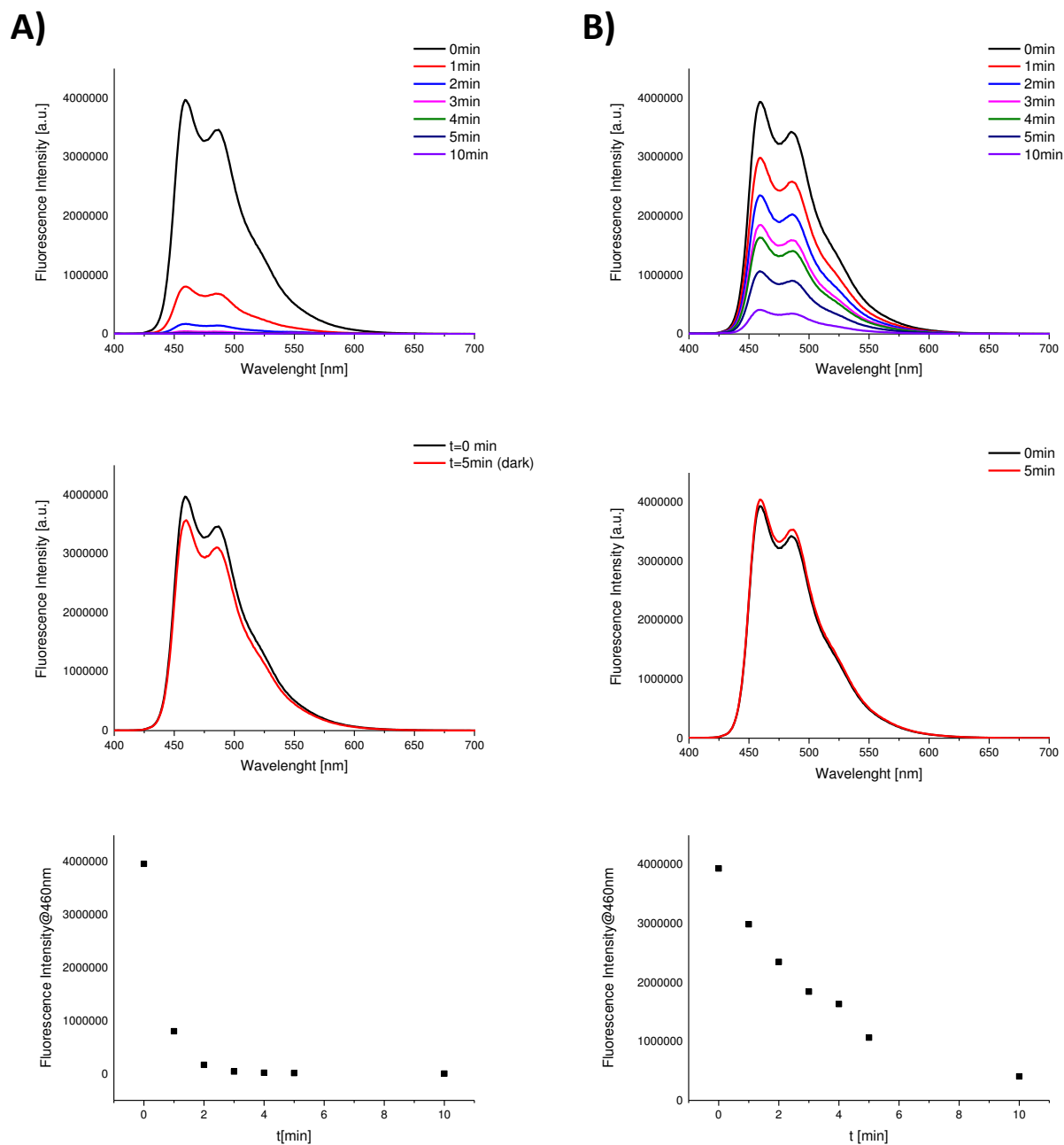


Figure 10. Fluorescence spectra of 1,3-diphenylisobenzofuran (DPBF) in the presence of 3 (A) and 3/benz-CNO (B) upon 380 nm excitation in benzylalcohol. Concentration DPBF  $4.6 \times 10^{-6}$  M. Emission spectra recorded at different time intervals between 0 and 10 min (top row) of illumination. Control experiments in the dark after 0 and 5 min (center row), and maximum fluorescence intensities as function of illumination time (bottom row).

## 4.4 Conclusion

In this study, a novel pyrene-BODIPY dyad was synthesized, isolated and characterized, revealing effective features for the application in photodynamic therapy. *In vitro* tests on HeLa demonstrated a ROS-triggered phototoxicity of the photosensitizer 3. The pyrene-diiodo-BODIPY dyad 3 was then successfully immobilized onto the surface of carbon nano-onions, with the CNOs acting as molecular shuttle for the hydrophobic photosensitizer. Live-cell confocal imaging revealed that the pyrene-diiodo-BODIPY dyad 3 was effectively internalized by the cells, monitoring the residual fluorescence of the BODIPY chromophore. Illumination of the BODIPY/CNO treated cells, however, revealed no significant, illumination time or CNO mass concentration dependent, reduction in cell metabolic activity. The phototoxicity of the pyrene-BODIPY dyad could be restored by disrupting the nanohybrids in a DMSO solution. When the nanohybrids were disrupted, e.g. the photosensitizer was detached from the CNO surface before exposing the cells to the nanomaterial, a clear photo-triggered cytotoxic effect was observed, comparable to the results for the free BODIPY photosensitizer 3. This indicated that the BODIPY photosensitizer 3 is deactivated by the presence of the CNOs, while being attached to the CNO surface. The non-covalent approach presented here paves the way to a systematic study of intact and disassembled non-covalent delivery systems, which is not readily feasible in covalent bonding approaches. It is, to our best knowledge, the first systematic approach, including *in vitro* studies, where a non-covalent BODIPY PDT photosensitizer-CNM system is evaluated. Future research efforts will involve a thorough photophysical elucidation of the observations herein reported, including in-depth studies of the ongoing cellular metabolic pathways as well as of possible CNO-promoted quenching effects of the photoexcited BODIPY moiety.

## 4.5 References

- (1) Gross, S.; Gilead, A.; Scherz, A.; Neeman, M.; Salomon, Y. *Nat. Medicine* **2003**, *9* (10), 1327–1331.
- (2) Yamakoshi, Y.; Umezawa, N.; Ryu, A.; Arakane, K.; Miyata, N.; Goda, Y.; Masumizu, T.; Nagano, T. *J. Am. Chem. Soc.*, **2003**, *125*, 12803–12809.
- (3) Mroz, P.; Xia, Y.; Asanuma, D.; Konopko, A.; Zhiyentayev, T.; Huang, Y.; Sharma, S. K.; Dai, T.; Khan, U. J.; Wharton, T.; Hamblin, M. R. *Nanomedicine Nanotechnology, Biol. Med.* **2011**, *7* (6), 965–974.
- (4) Lu, Z.; Huang, L.; Kurup, D. B.; Wharton, T.; Hamblin, M. R. *Nanomedicine* **2010**, *5* (10), 1525–1533.
- (5) Kim, S.; Jin, D.; Sup, D.; Yeol, U.; Seok, Y.; Seong, E. *Carbohydr. Polym.* **2014**, *101*, 692–698.
- (6) Sharma, S. K.; Chiang, L. Y.; Hamblin, M. R. *Nanomedicine* **2011**, *6*(10), 1813–1825
- (7) Lee, D. J.; Park, S. Y.; Oh, Y. T.; Oh, N. M.; Oh, K. T. *Macromolecular Research* **2011**, *19* (8), 848–852.
- (8) Zhu, Z.; Tang, Z.; Phillips, J. A.; Yang, R.; Wang, H.; Tan, W. J. *Am. Chem. Soc.* **2008**, *130*, 10856–10857.
- (9) Tian, B.; Wang, C.; Zhang, S.; Feng, L.; Liu, Z. *ACS Nano* **2011**, *9*, 7000–7009.
- (10) Bonnett, R.; Martinez, G.; *Tetrahedron*, **2001**, *57*, 9513–9547.
- (11) Waksman, R.; Mcewan, P. E.; Moore, T. I.; Pakala, R.; Kolodgie, F. D.; Hellinga, D. G.; Ms, C.; Seabron, R. C.; Rychnovsky, S. J.; Vasek, J.; Ng, B. E.; Scott, R. W.; Virmani, R. *J. Am. Coll. Cardiol.*, **2008**, *52*, 1024–1032.
- (12) Ozlem, S., Akkaya, E.U. *J. Am. Chem. Soc.*, **2009**, *131*, 48–49.
- (13) Yukruk, F.; Dogan, A. L.; Canpınar, H.; Guc, D.; Akkaya, E. U. *Org. Lett.* **2005**, *7*, 2885–2887.
- (14) Loudet, A.; Burgess, K. *Chem. Rev.*, **2007**, *107*, 4891–4932.
- (15) Ulrich, G.; Ziesel, R.; Harriman, A. *Angew. Chem., Int. Ed.*, **2008**, *47*, 1184–1201.
- (16) Hinkeldey, B.; Schmitt, A.; Jung, G. *ChemPhysChem*, **2008**, *9*, 2019–2027.
- (17) Yogo, T.; Urano, Y.; Ishitsuka, Y.; Maniwa, F.; Nagano, T.; V, D. V. Di. *J. Am. Chem. Soc.*, **2005**, *127*, 12162–12163.
- (18) Awuah, S. G.; You, Y.; *RSC Adv.*, **2012**, *2*, 11169.
- (19) Kamkaew, A.; Lim, H.; Lee, B.; Kiew, V. et al. *Chem. Soc. Rev.*, **2013**, *42*, 77.
- (20) Kamkaew, A.; Burgess, K. *J. Med. Chem.*, **2013**, *56*, 7608.
- (21) Carpenter, B. L.; Situ, X.; Scholle, F.; Bartelmess, J.; Weare, W. W.; Ghiladi, R. A. *Molecules*, **2015**, *20*, 10604–10621.
- (22) Rousseau, T.; Cravino, A.; Bura, T.; Ulrich, G.; Roncali, J. *Chem. Commun.*, **2009**, 1673–1675.
- (23) Gorman, A.; Killoran, J.; Shea, C. O.; Kenna, T.; Gallagher, W. M.; Shea, D. F. O. *J. Am. Chem. Soc.*, **2004**, *126*, 10619–10631.
- (24) Bartelmess, J.; Frasconi, M.; Balakrishnan, P. B.; Signorelli, A.; Echegoyen, L.; Pellegrino, T.; Giordani, S. *RSC Adv.* **2015**, *5* (62), 50253–50258.
- (25) Yang, M.; Flavin, K.; Kopf, I.; Radics, G.; Hearnden, C. H. A.; Mcmanus, G. J.; Moran, B.; Villalta-cerdas, A.; Echegoyen, L. A.; Giordani, S.; Lavelle, E. C. *Small*, **2013**, *9*, 4194.4206.
- (26) Frasconi, M.; Maffei, V.; Bartelmess, J.; Echegoyen, L.; Giordani, S. *Methods Appl. Fluoresc.* **2015**, *3* (4), 44005.
- (27) Giordani, S.; Bartelmess, J.; Frasconi, M.; Biondi, I.; Cheung, S.; Grossi, M.; Wu, D.; Echegoyen, L.;

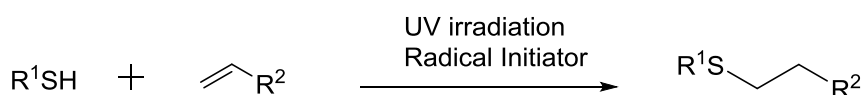
- O'Shea, D. F. *J. Mater. Chem. B* **2014**, *2* (42), 7459–7463.
- (28) Redmond, R. W.; Gamlin, J. N. *Photochemistry and Photobiology* **1999**, *70* (4), 391–475.
- (29) Greci, L. *Res. Chem. Intermed.* **1993**, *19* (5), 395–405.
- (30) Ohyashiki, T.; Nunomura, M.; Katoh, T. *Biochimica et Biophysica Acta* **1999**, *1421*, 131–139.

## 5. CNOs for Photocatalysis

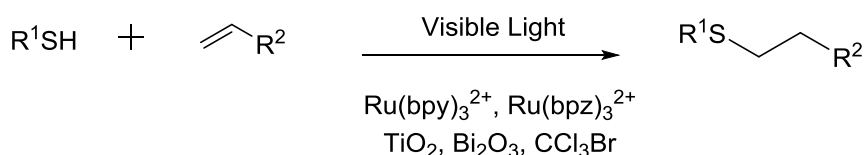
### 5.1 Introduction

Organosulfur compounds are widely present in nature and play important roles in many biological structures and functions.<sup>1,2</sup> Sulfur containing functional groups such as thioether, thioester, and disulfide are found in a number of natural products, for example the disulfide depsipeptide FK228 (romidepsin, anticancer);<sup>3</sup> the thioester depsipeptide largazole (anticancer);<sup>4</sup> and pharmaceutical agents such as ranitidine (Zantac, antiulcer), NCH-31 (antitumor),<sup>5</sup> and the cyclic tetrapeptide disulfide SCOP (HDAC inhibitor).<sup>6</sup> Disulfide-containing linkers are now used in antibody–drug conjugates (ADCs), which are used as targeted cell-based immunotherapeutics.<sup>7</sup> Lastly, organosulfur compounds commonly serve as useful synthetic intermediates, with applications in chemical biology, medicinal, and polymer chemistry. A common method to construct carbon–sulfur bonds is via the thiol–ene reaction, a prototypical “click reaction” that effects the anti-Markovnikov radical addition of thiol across nonactivated carbon–carbon double bonds.<sup>8</sup> The high efficiency and orthogonality of thiol–ene chemistry has led to increased utility in polymer functionalization, macromolecular synthesis, biological applications, and functionalization of biomaterials.<sup>9</sup> Growing concerns about the environment and energy use have spurred extensive efforts to make chemical processes more sustainable and “green”. Examples include employing sunlight or low energy visible light to promote reactivity and performing synthetic transformations without the use of rare, expensive, and potentially toxic elements, especially in the pharmaceutical industry.<sup>10</sup> Pioneering work by Yoon<sup>11</sup> and Stephenson<sup>12</sup> on radical thiol–ene coupling of alkenes and thiols using visible-light-absorbing ruthenium polypyridyl complex ( $\text{Ru}(\text{bpz})_3^{2+}$  and  $\text{Ru}(\text{bpy})_3\text{Cl}_2$ ) photocatalysts constitutes a striking development of chemical transformations promoted by low cost energy.<sup>13</sup> However, both methodologies require the use of rare, expensive, and toxic metals (See Figure 1). More recently, Greaney and co-workers reported the use of the naturally abundant and nontoxic metal oxide  $\text{TiO}_2$  for thiol–ene coupling, but the protocol requires a nanoparticulate form of  $\text{TiO}_2$  and the substrate scope was limited.<sup>14</sup> It is well established that highly efficient photocatalysts can be prepared as composite semi-conducting materials composed of metal oxides displayed on the surface of carbon nanomaterials.<sup>15,16</sup> These low-cost photocatalysts have been widely investigated for environmental applications including water purification.<sup>17</sup> Carbon nanomaterial metal oxide composites (NMMO composites) are readily prepared through a number of methods including the simple stirring of the two materials.<sup>18</sup> The carbon NMMO composite offers a synergic effect induced by the presence of carbon materials in the hybrid photocatalyst.<sup>19</sup> This is mainly attributed to the decrease of electron/hole recombination, bandgap tuning and increase in the adsorptive active sites.<sup>20</sup> In this chapter, an application of Carbon NMMO composites as highly-efficient photocatalysts for light-mediated thiol-ene ligation reactions has been investigated. Characterisation of the composite materials is presented and a putative mechanism for the catalytic cycle is depicted. Substrate scope is explored across inter and intramolecular thiol-ene ligation and intermolecular thiol-yne reactions. The simple catalyst preparation, high-yields, ease of purification and biocompatibility render this a highly attractive option for cytocompatible thiol-ene ligation reactions.

### A. Traditional Condition for TEC



### B. Visible-light mediated thiol-ene reaction



### C. This work: Carbon/Bi<sub>2</sub>O<sub>3</sub> nanocomposite

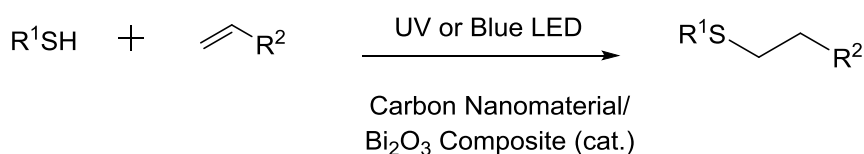


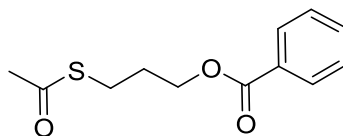
Figure 1. Pathway for photocatalysed thiol-ene ligation reactions, common reagents used and overview of catalyst described herein.

## 5.2 Experimental

### 5.2.1 General Procedure for Radical Thiol-Ene Reaction

To a solution of an alkene (1 eq) and a thiol (1.5 eq) or thioacetic acid (4 eq) in ethylacetate (700  $\mu\text{L}$ ) was added 56  $\mu\text{L}$  of GO/Bi<sub>2</sub>O<sub>3</sub> nanocomposite. The vial was sealed with a Teflon cap and left at room temperature under irradiation with UV lamp for 1 h. Upon completion of the reaction, the solution was concentrated *in vacuo*, and the residue was purified by flash column chromatograph ( gradient elution in Hexane to ethylacetate 7:3) to afford the final thiol-ene adducts.

### 5.2.2 Synthesis of compound 1

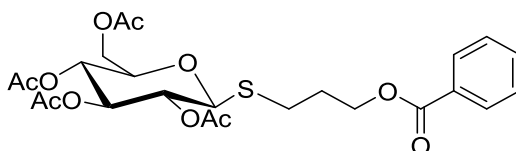


**3-(acetylthio)propyl benzoate:** To a solution of allyl benzoate (81.03 mg, 0.5 mmol) and thioacetic acid (142.71  $\mu\text{L}$ , 2mmol) in ethylacetate (700  $\mu\text{L}$ ) was added 56  $\mu\text{L}$  of GO/Bi<sub>2</sub>O<sub>3</sub> nanocomposite. The vial was sealed with a Teflon cap and left at room temperature under irradiation with UV lamp for 1 h. Upon completion of the reaction, the solution was concentrated *in vacuo*, and the residue was purified by flash column chromatograph ( gradient elution in Hexane to ethylacetate 7:3) to afford the final thiol-ene adduct. 90% yield. <sup>1</sup>H NMR (400 MHz, CDCl<sub>3</sub>)  $\delta$  8.10 – 8.01 (m, 2H), 7.60 – 7.52 (m, 1H), 7.45 (ddt, *J* = 8.0, 6.9, 1.2



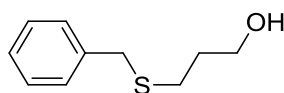
Hz, 2H), 4.48 – 4.27 (m, 2H), 3.04 (t,  $J = 7.2$  Hz, 2H), 2.35 (s, 3H), 2.16 – 1.97 (m, 2H).  $^{13}\text{C}$  NMR (101 MHz,  $\text{CDCl}_3$ )  $\delta$  196.08, 167.04, 133.55, 130.16, 128.94, 63.89, 31.18, 29.40, 26.36. IR 3064, 2956, 1717, 1692, 1453, 1270, 1114, 958, 713, 617. HRMS ( $\text{ES}^+$ )  $m/z$  calcd for  $\text{C}_{12}\text{H}_{14}\text{NaO}_3\text{S}$  [ $\text{M} + \text{Na}$ ] $^+$  261.055404, found 261.055586.

### 5.2.3 Synthesis of compound 2



**(2R,3R,4S,5R,6S)-2-(acetoxymethyl)-6-((3-(benzoyloxy)propyl)thio)tetrahydro-2H-pyran-3,4,5-triacetate:** To a solution of allyl benzoate (81.0 mg, 0.5 mmol) and 1-Thio- $\beta$ -D-glucose tetraacetate (273 mg, 0.75mmol) in ethylacetate (700  $\mu\text{L}$ ) was added 56  $\mu\text{L}$  of  $\text{GO}/\text{Bi}_2\text{O}_3$  nanocomposite. The vial was sealed with a Teflon cap and left at room temperature under irradiation with UV lamp for 1 h. Upon completion of the reaction, the solution was concentrated *in vacuo*, and the residue was purified by flash column chromatograph ( gradient elution in Hexane to ethylacetate 7:3) to afford the final thiol-ene adduct. 72% yield.  $^1\text{H}$  NMR (400 MHz,  $\text{CDCl}_3$ )  $\delta$  8.13 – 7.97 (m, 2H), 7.57 (t,  $J = 7.4$  Hz, 1H), 7.44 (dd,  $J = 16.0, 8.5$  Hz, 2H), 5.23 (dd,  $J = 17.5, 8.1$  Hz, 1H), 5.06 (dd,  $J = 19.5, 9.7$  Hz, 2H), 4.51 (d,  $J = 10.0$  Hz, 1H), 4.41 (t,  $J = 6.2$  Hz, 2H), 4.21 (dt,  $J = 18.6, 9.3$  Hz, 1H), 4.17 – 4.04 (m, 1H), 3.76 – 3.62 (m, 1H), 2.85 (dtd,  $J = 20.3, 13.1, 7.3$  Hz, 2H), 2.14 – 2.07 (m, 2H), 2.05 (d,  $J = 3.0$  Hz, 6H), 2.01 (d,  $J = 7.3$  Hz, 6H).  $^{13}\text{C}$  NMR (101 MHz,  $\text{CDCl}_3$ )  $\delta$  170.63, 170.18, 169.41, 133.05, 129.59, 128.42, 83.65, 75.98, 73.83, 69.75, 68.28, 63.29, 62.11, 29.09, 26.70, 20.70, 20.62, 20.59. IR 2954, 1752, 1454, 1369, 1224, 1119, 1037, 908, 713, 601. HRMS ( $\text{ES}^+$ )  $m/z$  calcd for  $\text{C}_{24}\text{H}_{30}\text{NaO}_{11}\text{S}$  [ $\text{M} + \text{Na}$ ] $^+$  549.140020, found 549.140103.

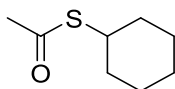
### 5.2.4 Synthesis of compound 3



**3-(benzylthio)propan-1-ol:** To a solution of allyl alcohol (80.0 mg, 1.40 mmol) and benzyl mercaptan (0.16 mL, 2.06 mmol) in ethylacetate (700  $\mu\text{L}$ ) was added 56  $\mu\text{L}$  of  $\text{GO}/\text{Bi}_2\text{O}_3$  nanocomposite. The vial was sealed with a Teflon cap and left at room temperature under irradiation with UV lamp for 1 h. Upon completion of the reaction, the solution was concentrated *in vacuo*, and the residue was purified by flash column chromatograph ( gradient elution in Hexane to ethylacetate 7:3) to afford the final thiol-ene adduct. 84% yield.  $^1\text{H}$  NMR (400 MHz,  $\text{CDCl}_3$ )  $\delta$  7.33 (dd,  $J = 10.3, 2.8$  Hz, 4H), 7.26 (ddd,  $J = 11.8, 5.4, 2.0$  Hz, 1H), 3.73 (dd,  $J = 11.4, 5.3$  Hz, 4H), 2.56 (t,  $J = 6.5$  Hz, 2H), 1.83 (dq,  $J = 13.1, 6.5$  Hz, 2H), 1.77 (s, 1H).  $^{13}\text{C}$  NMR (101 MHz,  $\text{CDCl}_3$ )  $\delta$  138.35, 128.87, 128.54, 127.04, 61.74, 36.29, 31.59, 28.00. IR 3408, 2921, 1705, 1597,

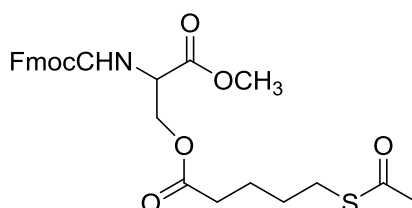
1500, 1453, 1353, 1226, 1053, 912, 708, 560. TOF MS (EI<sup>+</sup>) m/z calcd for C<sub>10</sub>H<sub>14</sub>OS [M<sup>+</sup>] 182.0765, found 182.0768.

### 5.2.5 Synthesis of compound 4



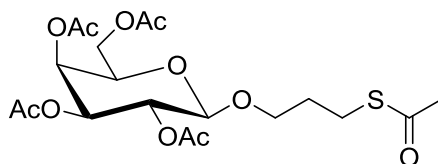
**S-cyclohexyl ethanethioate:** To a solution of cyclohexene (81.0 mg, 1 mmol) and thioacetic acid (0.28 mL, 4 mmol) in ethylacetate (700  $\mu$ L) was added 56  $\mu$ L of GO/Bi<sub>2</sub>O<sub>3</sub> nanocomposite. The vial was sealed with a Teflon cap and left at room temperature under irradiation with UV lamp for 1 h. Upon completion of the reaction, the solution was concentrated *in vacuo*, and the residue was purified by flash column chromatograph (gradient elution in Hexane to ethylacetate 7:3) to afford the final thiol-ene adduct. 85% yield. <sup>1</sup>H NMR (400 MHz, CDCl<sub>3</sub>)  $\delta$  3.57 – 3.41 (m, 1H), 2.28 (s, 3H), 1.90 (dt, *J* = 9.2, 4.5 Hz, 2H), 1.67 (td, *J* = 10.2, 5.0 Hz, 2H), 1.57 (ddd, *J* = 12.7, 7.7, 4.9 Hz, 1H), 1.50 – 1.33 (m, 4H), 1.31 – 1.19 (m, 1H). <sup>13</sup>C NMR (101 MHz, CDCl<sub>3</sub>)  $\delta$  195.81, 42.43, 42.43, 32.99, 30.77, 25.91, 25.53. IR 2932, 2855, 1730, 1686, 1434, 1357, 1221, 1105, 1002, 946, 590. TOF MS (EI<sup>+</sup>) m/z calcd for C<sub>8</sub>H<sub>14</sub>OS [M<sup>+</sup>] 158.0765, found 158.0771.

### 5.2.6 Synthesis of compound 5



**(E)-2-((2-((9H-fluoren-9-yl)methoxy)-2-oxoethylidene)amino)-3-methoxy-3-oxopropyl 5-(acetylthio)pentanoate:** To a solution of (E)-2-((2-((9H-fluoren-9-yl)methoxy)-2-oxoethylidene)amino)-3-methoxy-3-oxopropyl pent-4-enoate (81.0 mg, 0.19 mmol) and thioacetic acid (54  $\mu$ L, 4 mmol) in ethylacetate (700  $\mu$ L) was added 56  $\mu$ L of GO/Bi<sub>2</sub>O<sub>3</sub> nanocomposite. The vial was sealed with a Teflon cap and left at room temperature under irradiation with UV lamp for 1 h. Upon completion of the reaction, the solution was concentrated *in vacuo*, and the residue was purified by flash column chromatograph (gradient elution in Hexane to ethylacetate 7:3) to afford the final thiol-ene adduct. 82% yield. <sup>1</sup>H NMR (600 MHz, CDCl<sub>3</sub>)  $\delta$  7.79 (d, *J* = 7.6 Hz, 2H), 7.66 – 7.60 (m, 2H), 7.43 (t, *J* = 7.5 Hz, 2H), 7.34 (tt, *J* = 7.4, 1.2 Hz, 2H), 5.70 (d, *J* = 8.2 Hz, 1H), 4.70 – 4.63 (m, 1H), 4.51 (dd, *J* = 11.4, 3.9 Hz, 1H), 4.48 – 4.38 (m, 3H), 4.26 (t, *J* = 7.1 Hz, 1H), 3.78 (d, *J* = 34.9 Hz, 3H), 2.88 (t, *J* = 7.2 Hz, 2H), 2.38 (h, *J* = 7.1 Hz, 2H), 2.33 (s, 3H), 1.74 – 1.57 (m, 4H). <sup>13</sup>C NMR (151 MHz, CDCl<sub>3</sub>)  $\delta$  195.88 (s), 172.77 (s), 169.95 (s), 143.76 (d, *J* = 12.7 Hz), 141.33 (s), 127.78 (s), 127.11 (s), 125.11 (s), 120.04 (s), 77.27 (s), 77.06 (s), 76.85 (s), 67.30 (s), 63.91 (s), 53.44 (s), 52.92 (s), 47.13 (s), 33.30 (s), 30.63 (s), 28.94 (s), 28.52 (s), 23.79 (s), 21.06 (s), 14.22 (s). IR 3356, 2947, 1738, 1680, 1532, 1444, 1353, 1216, 1136, 1052, 957, 736, 618.

## 5.2.7 Synthesis of compound 6



### (2R,3S,4S,5R,6R)-2-(acetoxymethyl)-6-(3-(acetylthio)propoxy)tetrahydro-2H-pyran-3,4,5-triyl

**triacetate:** To a solution of allyl 2,3,4,6-Tetra-O-acetyl- $\beta$ -D-galactopyranoside (80.0 mg, 0.21 mmol) and thioacetic acid (58  $\mu$ L, 4 mmol) in ethylacetate (700  $\mu$ L) was added 56  $\mu$ L of GO/Bi<sub>2</sub>O<sub>3</sub> nanocomposite. The vial was sealed with a Teflon cap and left at room temperature under irradiation with UV lamp for 1 h. Upon completion of the reaction, the solution was concentrated *in vacuo*, and the residue was purified by flash column chromatograph (gradient elution in Hexane to ethylacetate 7:3) to afford the final thiol-ene adduct. 82% yield. <sup>1</sup>H NMR (400 MHz, CDCl<sub>3</sub>)  $\delta$  5.39 – 5.33 (m, 1H), 5.22 – 5.12 (m, 1H), 5.03 – 4.95 (m, 1H), 4.44 (t, *J* = 6.5 Hz, 1H), 4.21 – 4.05 (m, 2H), 3.97 – 3.85 (m, 2H), 3.58 – 3.48 (m, 1H), 2.96 – 2.81 (m, 2H), 2.34 – 2.25 (m, 3H), 2.11 (d, *J* = 7.1 Hz, 3H), 2.08 – 2.04 (m, 3H), 2.03 – 2.00 (m, 3H), 1.97 (d, *J* = 10.3 Hz, 3H), 1.27 – 1.16 (m, 1H). <sup>13</sup>C NMR (101 MHz, CDCl<sub>3</sub>)  $\delta$  195.65 (s), 170.49 – 170.02 (m), 169.45 (s), 101.30 (s), 70.89 (s), 70.63 (s), 68.81 (s), 68.22 (s), 67.03 (s), 61.26 (s), 30.61 (s), 29.36 (s), 25.60 (s), 20.87 – 20.45 (m), 14.03 (m). IR 2959, 1750, 1686, 1437, 1375, 1215, 1133, 1040, 952, 902, 738, 626. HRMS (ES<sup>+</sup>) *m/z* calcd for C<sub>19</sub>H<sub>29</sub>O<sub>11</sub>S [M + H]<sup>+</sup> 465.142660, found 465.142509.

## 5.3 Results and discussion

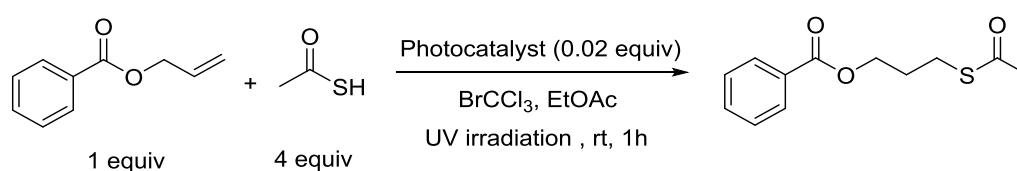
### 5.3.1 Bismuth Oxide and Tungsten Oxide

#### Photocatalytic Initiation of Radical Thiol–Ene Reaction

We were interested in finding alternative photoredox catalytic initiation conditions to promote hydrothiolation with carbon nanomaterials, possibly mild, cheap, and nontoxic beside being more efficient and suitable for late-stage functionalization of biologically relevant molecules. Upon review of the literature, we were inspired by the work of Pericàs and co-workers in which inexpensive and nontoxic bismuth-based materials were used as photocatalysts for the direct asymmetric alkylation of aldehydes.<sup>21</sup> Based on this precedent, at the first stage, a mild photocatalytic method for alkene hydrothiolation utilizing UV light activation and two inorganic photocatalyst such as bismuth oxide and tungsten oxide has been investigated. Recently, Pericàs reported the use of the bismuth oxide photocatalysts for the atom transfer radical addition (ATRA) reaction of organobromides to alkenes.<sup>22</sup> We first set out to determine if bismuth oxide (Bi<sub>2</sub>O<sub>3</sub>) and tungsten oxide (WO<sub>3</sub>) would catalyze the UV light initiated radical thiol–ene reaction and optimize the reaction conditions (Table 1). Initial investigation into the proposed Bi<sub>2</sub>O<sub>3</sub> catalyzed thiol–ene reaction focused on the reaction of allyl benzoate and thioacetic acid in ethylacetate (Table 1). Irradiation of the alkene and thiol in the presence of photocatalyst Bi<sub>2</sub>O<sub>3</sub> (0.02 equiv.) produced only poor conversion to the addition product after 1 h (Table 1, entry 2). However, the addition of 0.1 equiv. of a single electron acceptor bromotrichloromethane (BrCCl<sub>3</sub>) provided the desired thioether in higher conversion (Table 1, entry 1) after 1 h. Utilization of BrCCl<sub>3</sub> to promote the generation of the thiyl radical was previously reported by Stephenson and co-workers.<sup>12</sup> It is

presumed that the trichloromethyl radical generated from the photocatalyst abstracts the hydrogen atom of the mercaptan to give the electrophilic thiyl radical intermediates that undergo addition reaction with the alkene to give the desired thioether. Similarly, irradiation of the thiol and the alkene in the presence of  $\text{WO}_3$  (0.02 equiv.) gives a final product with an isolated yield of 14% (Table 1, entry 7). Just the utilization of  $\text{BrCCl}_3$  helps to improve the conversion (Table 1, entry 6) highlighting the essential roles of the photocatalyst,  $\text{BrCCl}_3$ , and light in this transformation. The background reaction was observed in the absence of the bismuth photocatalyst and  $\text{BrCCl}_3$  (entries 3, 4 and 5). Interestingly, the thiol-ene reaction proceeded highly efficiently under sunlight (entry 10). Importantly, increasing of the catalyst loading to 0.04 equiv. had no impact on the overall performance of this protocol (entry 5), so due to reaction operational simplicity, 0.02 equiv. was utilized as the optimal catalyst loading for the next photocatalytic studies.

Table 1. Preliminary optimization studies for the Thiol-Ene Reaction of allyl benzoate with thioacetic acid<sup>a</sup>



Entry	$\text{BrCCl}_3$	Photocatalyst	Yield (%) <sup>b</sup>
1	0.1 equiv	$\text{Bi}_2\text{O}_3$	84
2	-	$\text{Bi}_2\text{O}_3$	27
3	0.1 equiv	-	33
4	-	-	22
5	-	$\text{Bi}_2\text{O}_3$ (0.04 equiv)	16
6	0.1 equiv	$\text{WO}_3$	40
7	-	$\text{WO}_3$	14

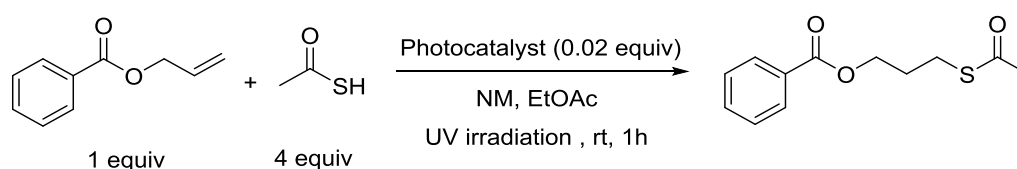
<sup>a</sup>Reactions were conducted by irradiating allyl benzoate (0.5 mmol), thioacetic acid (2.0 mmol), and the photocatalyst (0.02 equiv) in EtOAc (0.7 mL) with 365 nm lamps for 1 h. <sup>b</sup>Isolated yields.

### 5.3.2 Nanomaterials screened for the thiol-ene ligation reaction

Previous studies have found that carbon quantum dots (C QDs) can enhance the photocatalytic activity under visible light irradiation.<sup>23</sup> Zhuo et al have prepared Graphene QDs/ $\text{TiO}_2$  nanoparticles,<sup>24</sup> Ming et al have prepared C QDs/ $\text{TiO}_2$  nanoparticles,<sup>25</sup> Liu et al have prepared C QDs/ $\text{TiO}_2$  nanosheet, Xu et al have prepared Graphene/ $\text{TiO}_2$  composite to improve the visible light photocatalytic activity.<sup>26</sup> Compared with traditional nanostructure, porous  $\text{TiO}_2$  nanotubes are recognized as a high-efficiency photocatalyst due to the novel 3-D nanostructure. Titanium dioxide ( $\text{TiO}_2$ ) is the most widely used semiconductor in photocatalytic applications. Nevertheless, due to its relatively high bandgap (3.2eV corresponding to a wavelength of 388 nm),  $\text{TiO}_2$  is marginally activated under solar irradiation, since UV light represents less than 5% of the overall solar energy reaching Earth's surface. Carbon materials are widely employed to couple with conventional semiconductors due to properties such as large specific surface area, stability in both acid and basic media, and tunable surface chemistry. They have demonstrated to induce some beneficial effects on the photocatalytic performance of semiconductor metal oxides by creating synergies between both metal oxide

and carbon phases. Generally, this effect is attributed to the decrease of the bandgap energy of the composite catalysts, to an enhancement of the adsorptive properties as well as charge separation and transportation properties. In porous nanotubes, the double-walled structure possessing high specific surface area and porosity, could improve the photon application efficiency, the adsorption of dye and convection of solution, which would introduce remarkable photocatalytic abilities. In the second stage of my research, I studied the Thiol-Ene reaction utilizing different carbon nanomaterials. Nanodiamonds (ND), pristine-carbon nanooxide (p-CNO), oxidized-carbon nanooxide (ox-CNO), pegylated carbon nanooxide (PEG-CNO) and graphene oxide (GO) have been tested in this reaction. Initially, carbon nanomaterials have been tested in the presence of the photocatalyst ( $\text{Bi}_2\text{O}_3$ ) yielding a final product with an excellent NMR conversion (Table 2, entries 1-5). Similarly, utilizing  $\text{WO}_3$  as photocatalyst in addition to the carbon nanomaterials an NMR conversion of >99% has been observed (Table 2, entries 6-10). Interestingly, the nanomaterials by itself in the absence of the photocatalyst (both  $\text{Bi}_2\text{O}_3$  and  $\text{WO}_3$ ) have been found to complete the reaction in high conversion (Table 2, entries 11-15).

Table 2. Nanomaterials Screening for the Thiol-Ene Reaction of allyl benzoate with thioacetic acid<sup>a</sup> (Note: nanomaterial instead of  $\text{BrCCl}_3$ )



Entry	NM	Photocatalyst	Yield (%) <sup>b</sup>
1	ND	$\text{Bi}_2\text{O}_3$	>99
2	p-CNO	$\text{Bi}_2\text{O}_3$	>99
3	Ox-CNO	$\text{Bi}_2\text{O}_3$	>99
4	PEG-CNO	$\text{Bi}_2\text{O}_3$	>99
5	GO	$\text{Bi}_2\text{O}_3$	>99
6	ND	$\text{WO}_3$	>99
7	p-CNO	$\text{WO}_3$	>99
8	Ox-CNO	$\text{WO}_3$	>99
9	PEG-CNO	$\text{WO}_3$	>99
10	GO	$\text{WO}_3$	>99
11	ND	-	89
12	p-CNO	-	65
13	Ox-CNO	-	70
14	PEG-CNO	-	94
15	GO	-	84

NM = nanomaterial; ND = nanodiamonds; CNO = carbonanooxide; GO = graphene oxide; <sup>a</sup>Reactions were conducted by irradiating allyl benzoate (0.5 mmol), thioacetic acid (2.0 mmol), the NM (10  $\mu\text{g}/\text{mL}$ ), the photocatalyst (0.02 equiv) in EtOAc (0.7 mL) with 365 nm lamps for 1 h.  
<sup>b</sup><sup>1</sup>H-NMR conversion.

### 5.3.3 Carbon NM-MO composites investigation

In order to achieve full conversion using the great potential of the carbon nanomaterials, an optimization study with ox-CNO and GO has been carried on. The graphene oxide powder used, (15-20 sheets, 4-10%

edge-oxidized) was purchased from Sigma. I first set out to determine if ox-CNO/Bi<sub>2</sub>O<sub>3</sub> nanocomposite and GO/Bi<sub>2</sub>O<sub>3</sub> nanocomposite would catalyze the UV light initiated radical thiol-ene reaction and optimize the reaction conditions (Table 3). The initial investigation into the nanocomposite catalyzed thiol-ene reaction focused on the reaction of allyl benzoate and thioacetic acid in ethylacetate (Table 3). Initially, ox-CNO/Bi<sub>2</sub>O<sub>3</sub> nanocomposite was synthesized by a two-step process. Firstly, 1 mg of oxidized-carbon nanoion (ox-CNO) and 4.6 mg Bi<sub>2</sub>O<sub>3</sub> were dissolved in 1 mL EtOAc. This mixed dispersion was ultrasonicated for 5 min at 37 kHz and let it stirring for 16 h at room temperature. Subsequently, the mixture was filtered off on a nylon syringe filter (pore size 1 μm) in order to remove the excess of Bi<sub>2</sub>O<sub>3</sub> and maintain the synthesized product. The final product was a transparent and clear solution of oxidized-carbon nanoion-bismuth oxide composite (See figure 2). In the same way, GO/Bi<sub>2</sub>O<sub>3</sub> nanocomposite was synthesized. 1 mg of graphene oxide (GO) and 4.6 mg Bi<sub>2</sub>O<sub>3</sub> were dissolved in 1 mL EtOAc. This mixed dispersion was ultrasonicated for 5 min at 37 kHz and let it stirring for 16 h at room temperature. Subsequently, the mixture was filtered off on a nylon syringe filter (pore size 1 μm) in order to remove the excess of Bi<sub>2</sub>O<sub>3</sub> and maintain the synthesized product. As previously stated, also for GO/Bi<sub>2</sub>O<sub>3</sub> nanocomposite the final product was a transparent and optically clear solution.

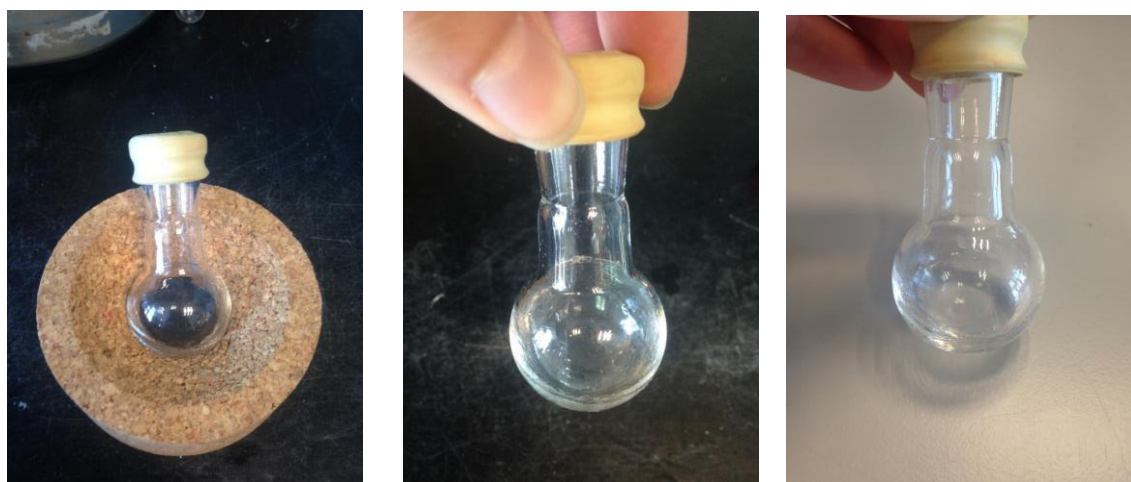
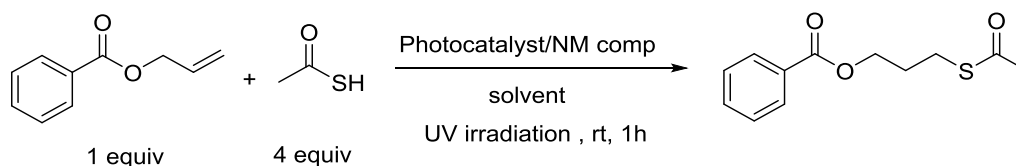


Figure 2. Transparent solution of filtered ox-CNO/Bi<sub>2</sub>O<sub>3</sub> nanocomposite.

The photocatalytic initiation of the radical Thiol-Ene Reaction was tested under different concentration of this clear solution and the optimized conditions were identified and investigated with a range of different substrates (Table 3). Four different concentrations in ethylacetate were tested for the thiol-ene reaction (Table 3, entries 1-4). A stock solution of 1 mg mL<sup>-1</sup> was prepared and consequent dilutions to 10, 20, 40, 80 μg mL<sup>-1</sup> were made. If the lowest concentration of ox-CNO/Bi<sub>2</sub>O<sub>3</sub> nanocomposite corresponding to 10 μg mL<sup>-1</sup> (7 μL) gives an NMR conversion of 90% (Table 3, entry 1), the highest concentration corresponding to 80 μg mL<sup>-1</sup> (56 μL) gives an NMR conversion >99% (Table 3, entry 4). The same behavior is notable also with GO/Bi<sub>2</sub>O<sub>3</sub> nanocomposite suggesting a reproducible mechanism (Table 3, entries 7-8). Irradiation of the alkene and thiol in the presence of the nanocomposite produced excellent conversion to the addition product after 1 h (Table 3). Finally, an evaluation of solvents has been carried on. The reaction tested in dry ethylacetate revealed high NMR conversion (Table 3, entry 5). On the other hand the reaction tested using

EtOAc : water (6:1) reveals just a 39% of conversion (Table 3, entry 6). On the basis of these observation I selected EtOAc (non-anhydrous) as the solvent for the next reactions.

Table 3. Optimization study with ox-CNO for the Thiol–Ene Reaction<sup>a</sup>



Entry	NM	Bi <sub>2</sub> O <sub>3</sub> /NM composite	solvent	Yield (%) <sup>b</sup>
1	Ox-CNO	10 µg/mL	EtOAc	90
2	Ox-CNO	20 µg/mL	EtOAc	91
3	Ox-CNO	40 µg/mL	EtOAc	92
4	Ox-CNO	80 µg/mL	EtOAc	>99
5	Ox-CNO	10 µg/mL	dry EtOAc	>99
6	Ox-CNO	80 µg/mL	EtOAc + H <sub>2</sub> O	39
7	GO	10 µg/mL	EtOAc	90
8	GO	80 µg/mL	EtOAc	>99

NM = nanomaterial; CNO = carbonnanooxions; <sup>a</sup>Reactions were conducted by irradiating allyl benzoate (0.5 mmol), thioacetic acid (2.0 mmol) and the NM (at indicated concentration) in EtOAc (0.7 mL) with 365 nm lamps for 1 h; <sup>b</sup><sup>1</sup>H-NMR conversion.

### 5.3.4 Carbon NM-MO composites characterization

The morphologies and crystallography of the samples were characterized by transmission electron microscopy (TEM). Bright-field TEM imaging of Bi<sub>2</sub>O<sub>3</sub>/ox-CNO composite and Bi<sub>2</sub>O<sub>3</sub>/GO composite was performed on a Jeol JEM-1011 instrument equipped with a thermo ionic tungsten source operated at 100 kV. Samples were prepared by spreading a droplet of the dispersed composite material in ethanol on a copper grid coated with a lacey carbon film. Figure 3, A shows TEM image of Bi<sub>2</sub>O<sub>3</sub> nanoparticles, which display mainly a spherical shape with a size ranging from 10 to 20 nm. Figure 3, B shows TEM image of GO, which display the typical transparent paper-like structure of GO with a lateral size of about 1 µm and around 15-18 layers, which is in agreement with the Sigma-Aldrich specifications. Interestingly, in comparison with the TEM image of graphene nanosheets, the TEM image of the Bi<sub>2</sub>O<sub>3</sub>/GO composites (Figure 3, D) show that the surface of the graphene–bismuth oxide composite is much rougher than that of graphene nanosheets. This might be attributed to the growth of bismuth oxide nanoparticles on graphene sheets. Moreover, as clearly suggested by the TEM images the bismuth oxide nanoparticles (about 10 nm in size) are uniformly distributed on 2D graphene nanosheets (Figure 3, D). Similarly, TEM image of ox-CNO composite show homogenous black spots onto ox-CNO surfaces in respect to the smooth ox-CNO with size ranging from 20 to 40 nm (Figure 3, C). For both composites, TEM images indicate that the catalyst is well dispersed and attached to the graphene oxide and the oxidized carbon nanooxion surfaces. The structures of the composites exhibit porous morphologies, with many projections and outcroppings indicating that the nanocomposite exhibit a larger total surface area and a more porous structure than those modified by non-

modified CNO or GO. This should enable an increase of the effective surface area and facilitate the electron transfer during the Thiol-Ene Reaction.

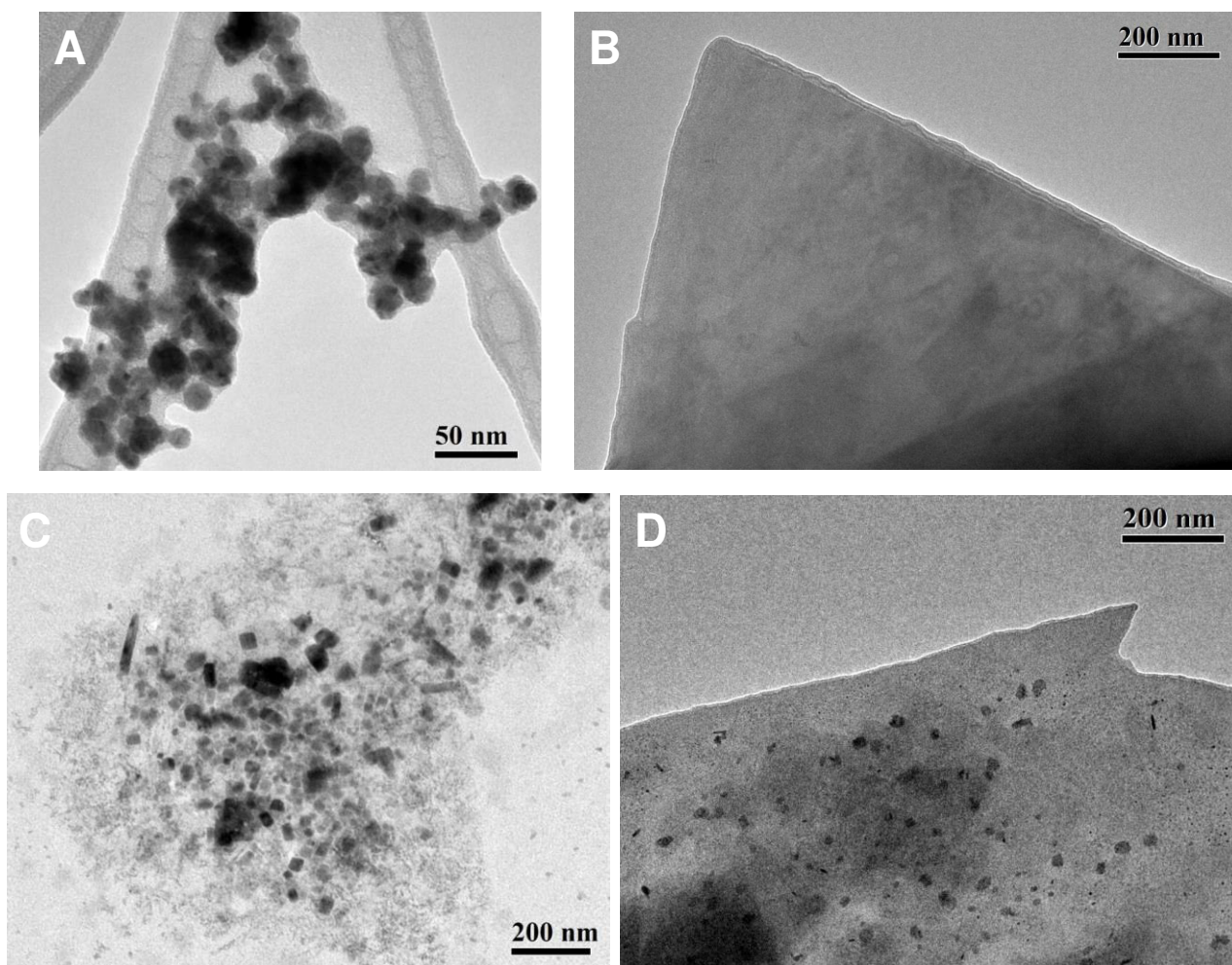


Figure 3. TEM images of (A)  $\text{Bi}_2\text{O}_3$  nanoparticles, (B) GO nanosheets, (C)  $\text{Bi}_2\text{O}_3$ /ox-CNO composite and (D)  $\text{Bi}_2\text{O}_3$ /GO nanocomposite.

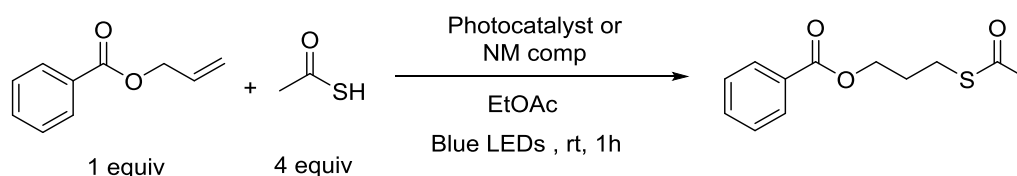
### 5.3.5 Carbon NM-MO composites screened for the thiolene-ligation under visible light

This photoredox process driven by an organic photocatalyst is synthetically complementary to both traditional (using UV irradiation or thermolysis) methods of radical initiator and transition-metal-mediated approaches. In particular, a metal-free process could potentially benefit peptide and glycoprotein chemistry, since certain polypeptide sequences and proteins have been shown to interfere with transition-metal mediated processes.<sup>27</sup> To test the theory, LED mediated thiol-ene reaction between allyl benzoate and thioacetic acid in the presence of ox-CNO and GO by themselves (Table 4, entries 6-10) and the nanocomposite ox-CNO/ $\text{Bi}_2\text{O}_3$  and GO/ $\text{Bi}_2\text{O}_3$  (Table 4, entries 11-13) has been explored. Surprisingly, ox-CNO and GO successfully initiated the photocatalytic thiol-ene reaction under blue light-emitting diode (LED) irradiation, providing the thiol-ene adduct in 70% and 71% isolated yield respectively, upon 1 hour



irradiation (Table 4, entries 8 and 10). An higher NMR conversion has been obtained by using ox-CNO/Bi<sub>2</sub>O<sub>3</sub> nanocomposite and GO/Bi<sub>2</sub>O<sub>3</sub> nanocomposite giving a final conversion of 79% and 78% respectively (Table 4, entries 11 and 12). The time extension to 3 hours reaction did not improve the conversion to the final adduct (Table 4, entry 13).

Table 4. LEDs mediated Thiol–Ene Reaction of allyl benzoate with thioacetic acid<sup>a</sup>



Entry	Photocatalyst	NM	Yield (%) <sup>b</sup>
1	Bi <sub>2</sub> O <sub>3</sub> , BrCCl <sub>3</sub>	-	>99
2	Bi <sub>2</sub> O <sub>3</sub>	-	51
3	-	-	40
4	WO <sub>3</sub> , BrCCl <sub>3</sub>	-	80
5	WO <sub>3</sub>	-	
6	-	ND (10 µg/mL)	90
7	-	p-CNO (10 µg/mL)	79
8	-	Ox-CNO (10 µg/mL)	70
9	-	PEG-CNO (10 µg/mL)	78
10	-	GO (10 µg/mL)	71
11	-	Bi <sub>2</sub> O <sub>3</sub> /Ox-CNO (80 µg/mL)	79
12	-	Bi <sub>2</sub> O <sub>3</sub> /GO (80 µg/mL)	78
13	-	Bi <sub>2</sub> O <sub>3</sub> /GO (80 µg/mL), 3h	80

NM = nanomaterial; CNO = carbonanionions; <sup>a</sup>Reactions were conducted by irradiating allyl benzoate (0.5 mmol), thioacetic acid (2.0 mmol), the NM (composite with photocatalyst) in EtOAc (0.7 mL) with 405 nm lamps for 1 h; <sup>b</sup><sup>1</sup>H-NMR conversion.

### 5.3.6 Scope Expantion

With the optimized ligation conditions in hand, the general applicability of the composite nanomaterials for photocatalysed TEC across a broad variety of structurally varying thioacids/thiols and alkenes has been demonstrated. As depicted in Figure 4, all the desired thioesters/thioethers were obtained in high isolated yields. Alkyl thiols showed a good reactivity in the thiol-ene reactions and the use of the protected cysteines and the paracetylated thiosugars demonstrate the synthetic potential of our catalytic approach for the preparation of bioconjugates. Of particular importance in these synthetic studies was the ease of purification of the products, with no purification step required for removal of the catalyst. This offers significant advantage over the traditional DPAP/MAP initiated processes where extensive column chromatography is required in order to isolate the product from the degraded initiator and photosensitizer. In addition, no discoloration of the reaction mixture was observed during UV or visible-light-mediated photolysis, ensuring that the photoinitiation was not compromised at any point. This is a major advantage over processes where

milligram quantities of metal oxide are utilized and strong discoloration and precipitation of metal oxides is observed. (See the experimental paragraph to see the yields for the reactions in Figure 4 and Figure 8).

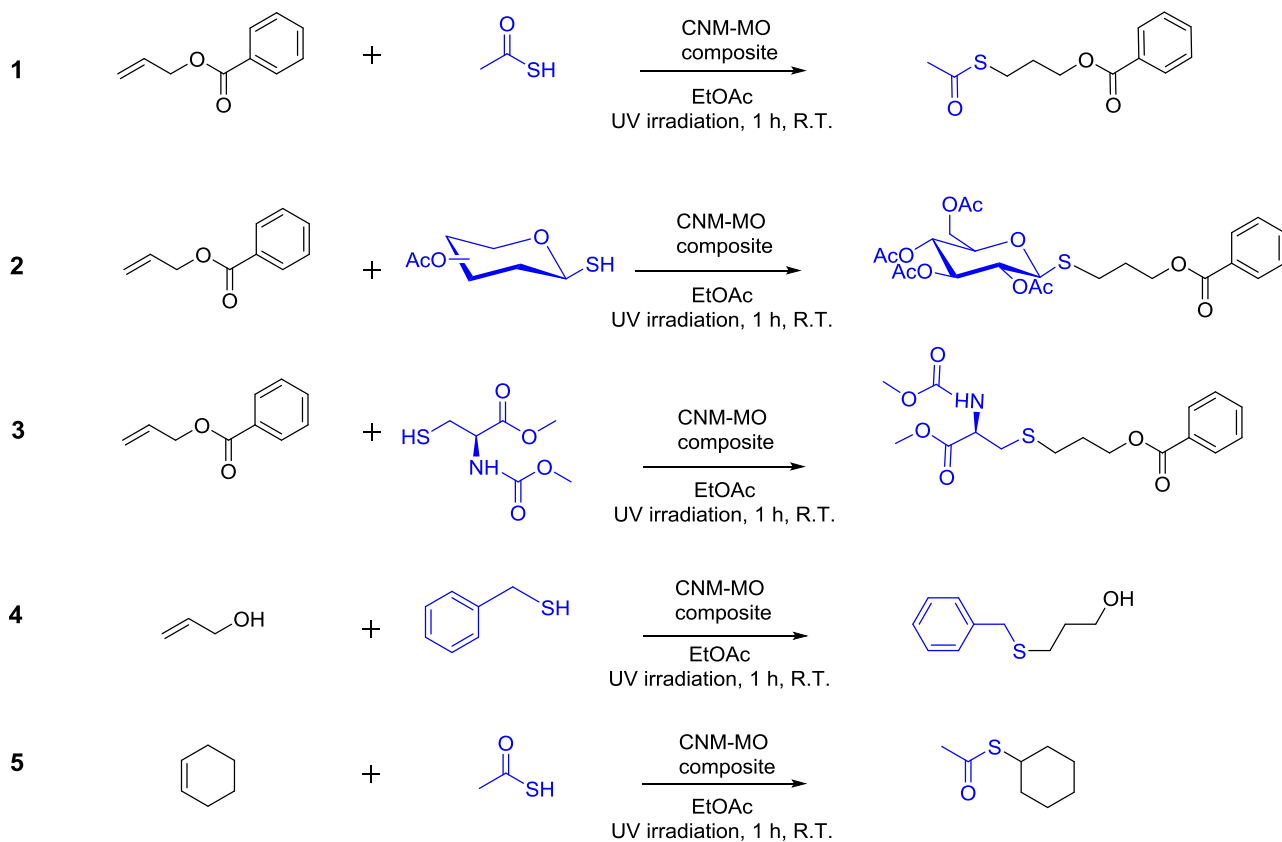


Figure 4. Carbon NM-MO catalysed thiolene ligation: expansion of the scope with simple substrate.

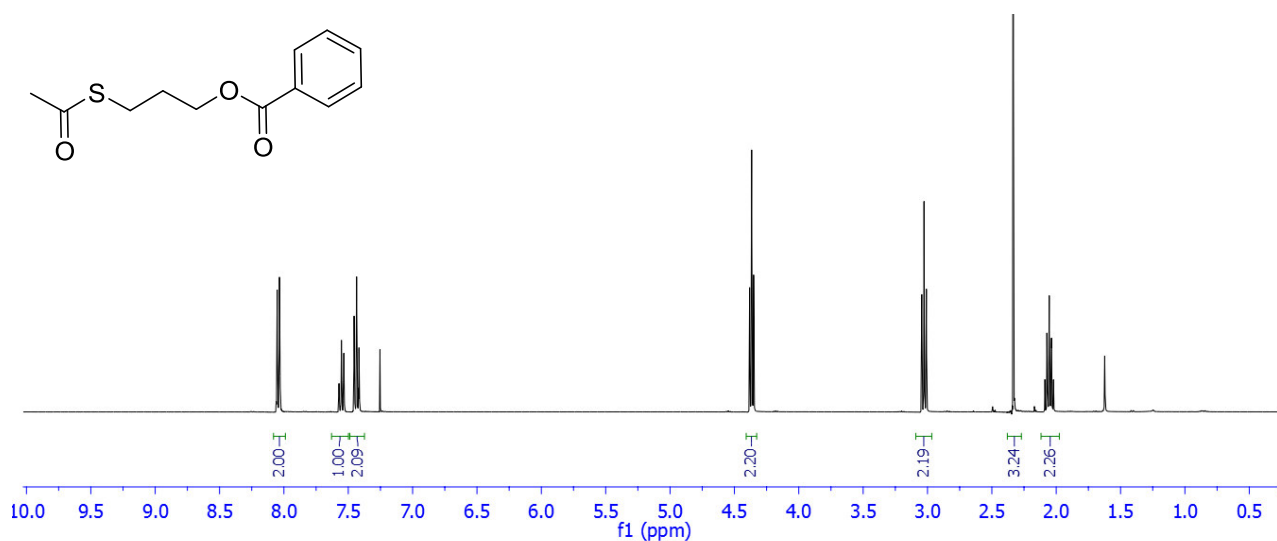


Figure 5: NMR spectrum of crude ligation product 1 after photolysis in EtOAc for 1 h in the presence of GO/Bi<sub>2</sub>O<sub>3</sub> nanocomposite (Figure 4, Entry 1).

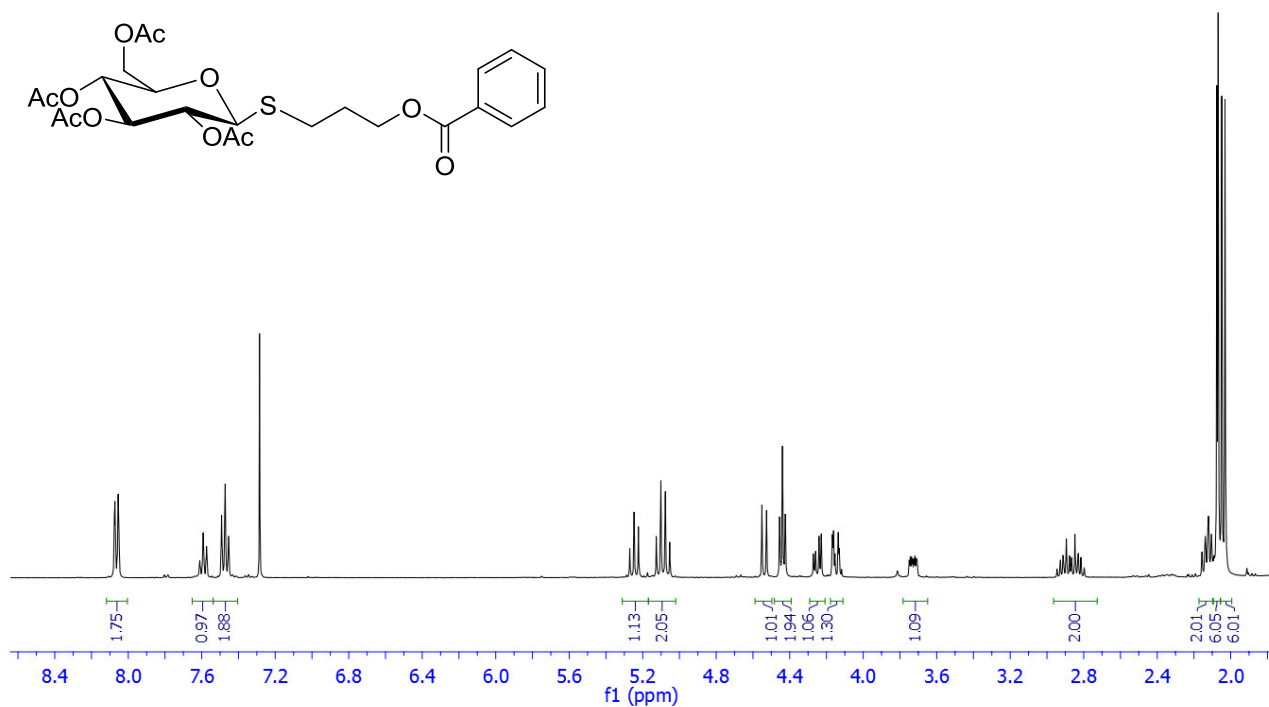


Figure 6: NMR spectrum of crude ligation product 2 after photolysis in EtOAc for 1 h in the presence of GO/Bi<sub>2</sub>O<sub>3</sub> nanocomposite (Figure 4, Entry 2).

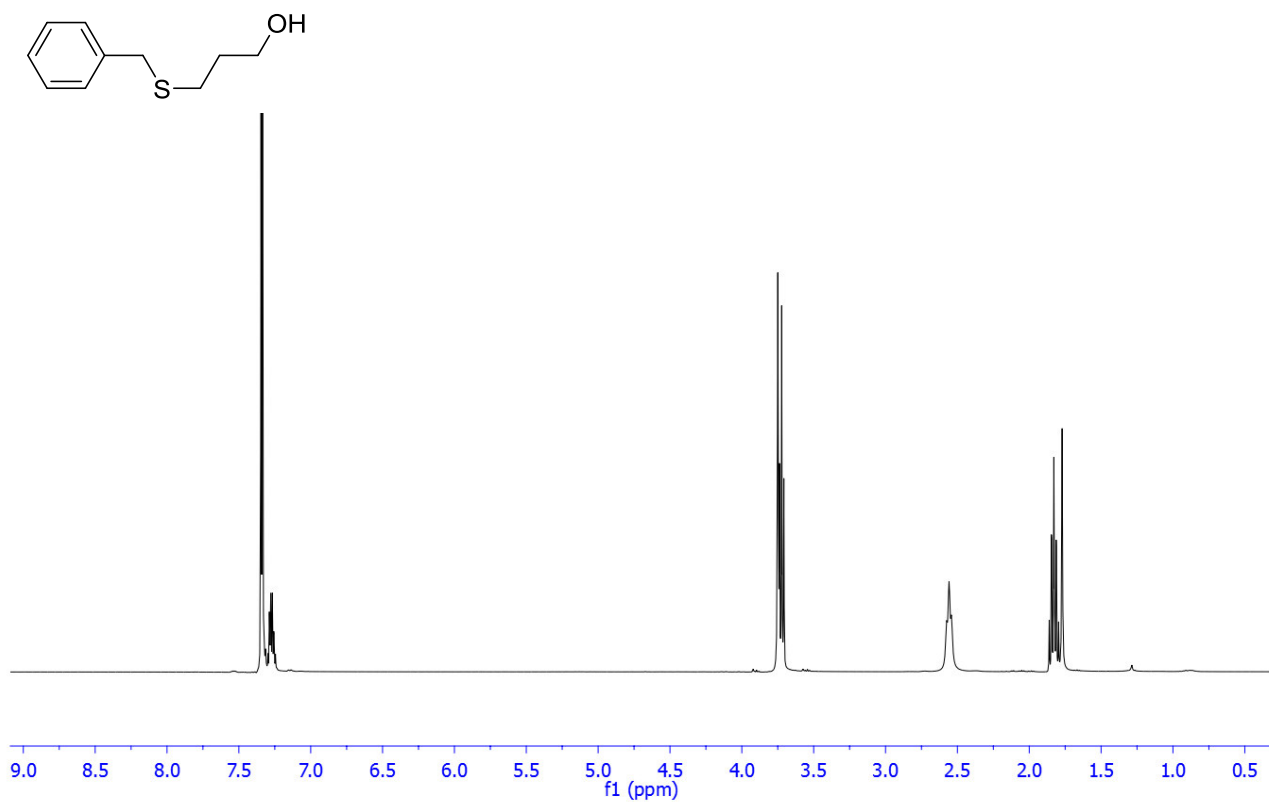


Figure 7: NMR spectrum of crude ligation product 4 after photolysis in EtOAc for 1 h in the presence of GO/Bi<sub>2</sub>O<sub>3</sub> nanocomposite (Figure 4, Entry 4).

Having demonstrated the high efficiency of the visible-light-mediated thiol-ene reaction, I have also investigated the applicability of this chemistry to enable the synthesis of glycoconjugates between glycosyl thiols and amino acid derivatives (See Figure 8). Glycoconjugates have become important tools for the exploration of many biological processes,<sup>28, 29</sup> and more recently, S-linked glycoconjugates have become promising analogues of glycopeptides and glycoproteins because of their enhanced chemical stability and enzymatic resistance.<sup>30</sup> Happily, the thiol-ene reaction between a Fmoc protected peptide derivative with thioacetic acid (Figure 8, 6) and a galactopyranoside with thioacetic acid (Figure 8, 8) occurred smoothly, giving the corresponding S-linked coconjugates in good yields. Other complex examples serve to demonstrate the potential utility of this method for bioconjugation. Notably, the reaction is compatible with N-Fmoc protected amino acid and sugars, with no effect on the rate or overall performance of the protocol. This demonstrated that a variety of complex drug-like molecules could be accessed via late-stage functionalization by employing this mild technology.

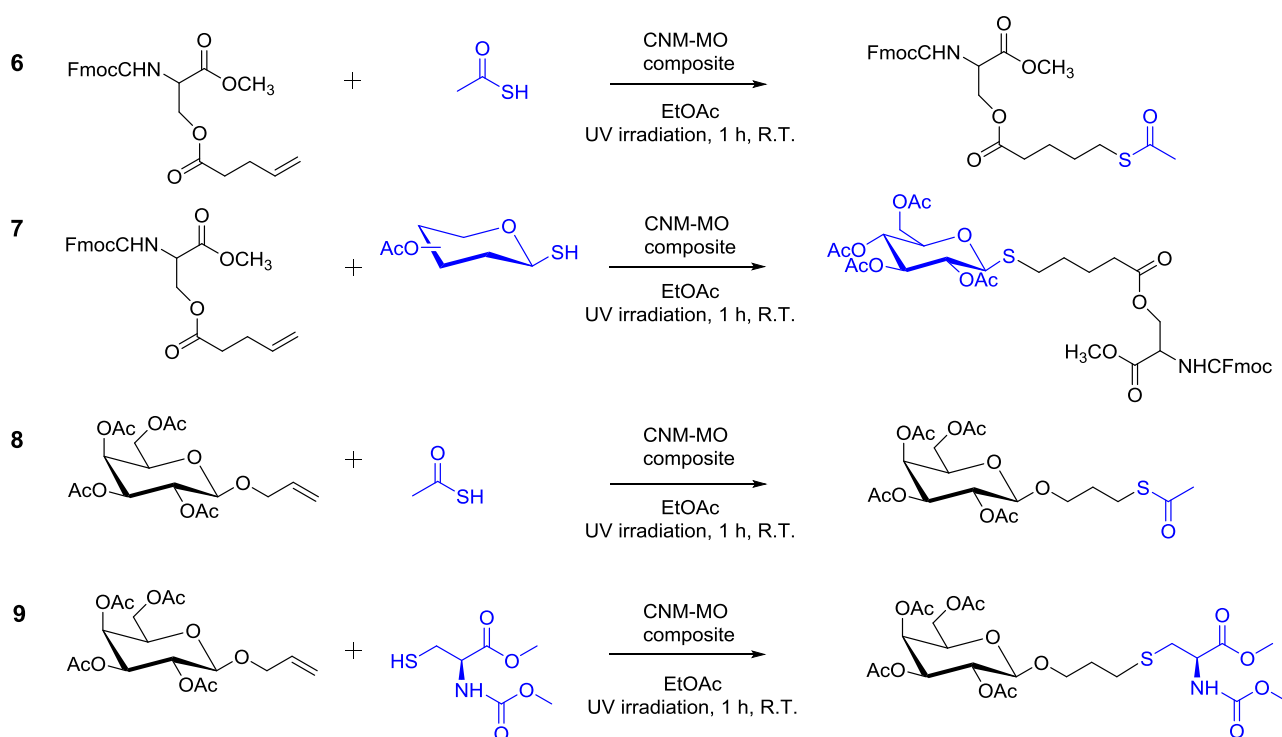


Figure 8. Carbon NM-MO catalysed thiolene ligation: expansion of the scope with relevant biological substrate.

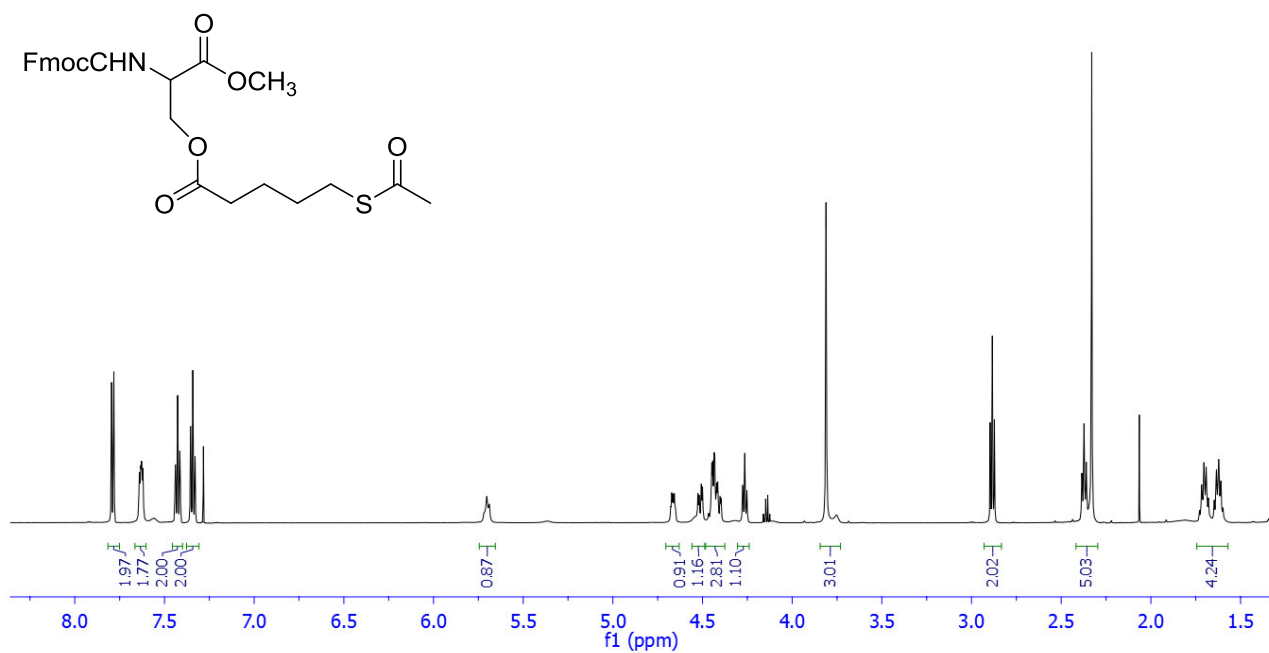


Figure 9. NMR spectrum of crude ligation product 6 after photolysis in EtOAc for 1 h in the presence of GO/Bi<sub>2</sub>O<sub>3</sub> nanocomposite (Figure 8, Entry 6).

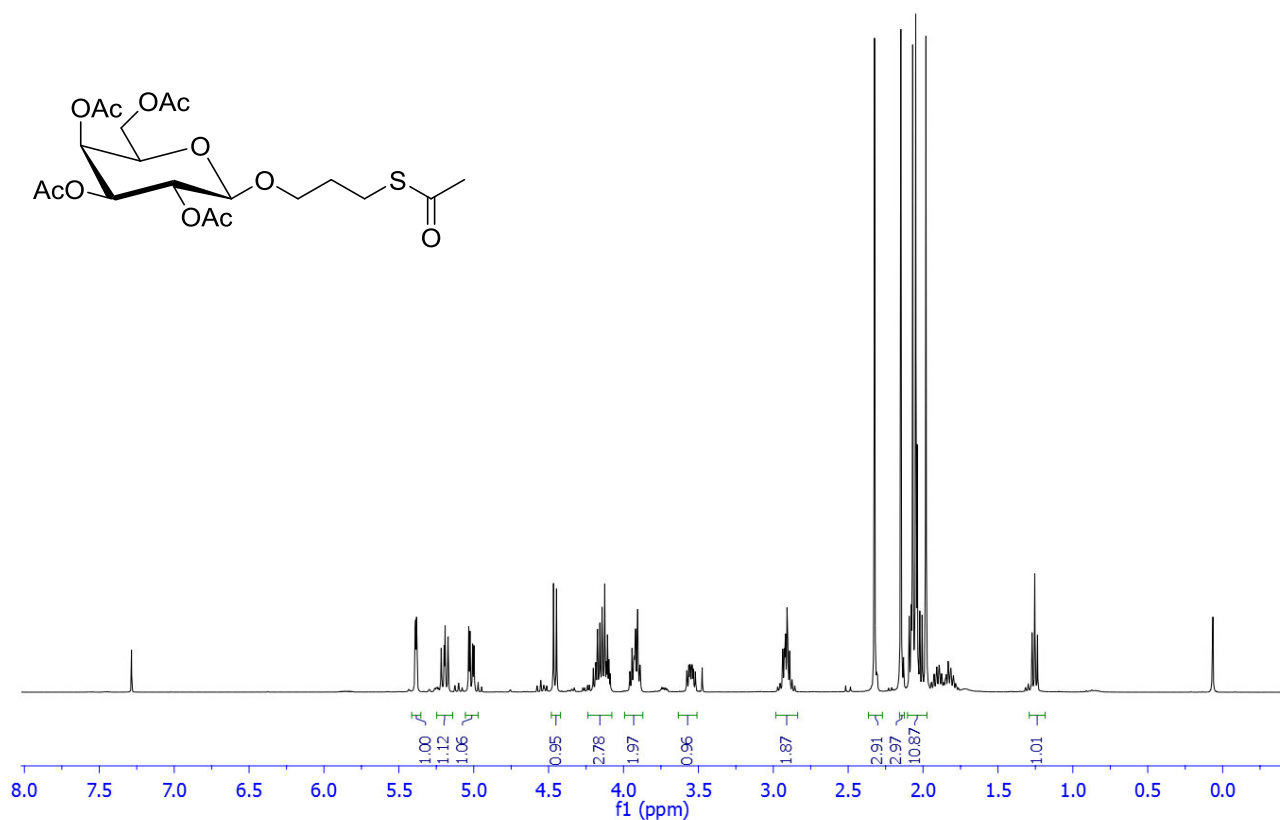
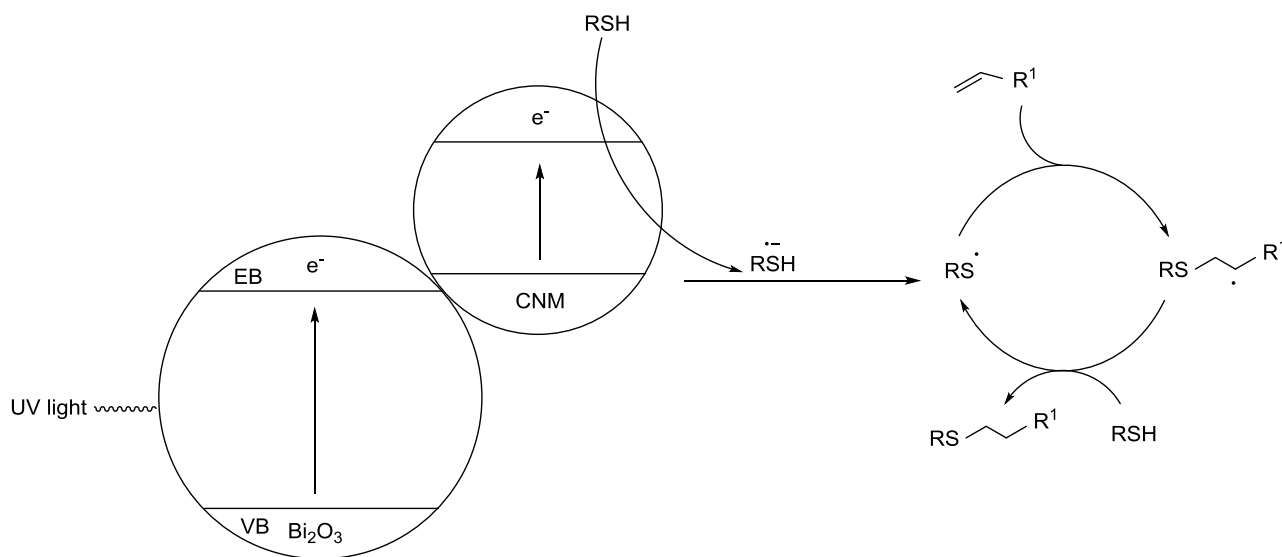


Figure 10. NMR spectrum of crude ligation product 8 after photolysis in EtOAc for 1 h in the presence of GO/Bi<sub>2</sub>O<sub>3</sub> nanocomposite (Figure 8, Entry 8).

### 5.3.7 Mechanism

A proposed mechanism for the overall photocatalytic process is outlined in Scheme 1. Initiation relies on the photo-excitation of electrons to the conduction band of the  $\text{Bi}_2\text{O}_3$  catalyst. The resultant holes in the carbon nanomaterial are reductively quenched by the thiol, resulting in formation of a thiyl radical anion, which can spontaneously lose a proton to furnish a thiyl radical. Oxygen may function as a sacrificial electron acceptor, enhancing reaction efficiency by reducing hole-electron recombination in the nanocomposite. The thiyl radical initiates the TEC process through anti-Markovnikov addition onto an alkene and generation of an alkyl radical, which propagates the reaction by abstracting a hydrogen atom from the starting thiol.



Scheme 1. Proposed mechanism for nanocomposite catalysed thiol-ene reaction.

## 5.4 Conclusion

We have developed an efficient, robust and readily accessible photocatalytic process for the thiol-ene 'click' reaction. Full conversion to the corresponding thioester or thioether product is observed for a range of carbon nanomaterial/metal oxide nanocomposites. The process appears to be general for a wide range of ligation reaction including, inter- and intramolecular thiol-ene, and thiol-yne ligation. The process is efficient with commercially available carbon nanomaterials rendering it easy to use. The nanomaterials were fully characterized as bismuth oxide nanoparticles adhered to the surface of the carbon nanomaterials, and a putative reaction mechanism for the catalytic cycle is presented. We believe these studies set the stage for future development in the area of nanocomposite thiol-ene ligation reactions and may have broader implications in photocatalysis of thiyl-radical mediated processes. This highly efficient reaction shows scope generality, as demonstrated by the use of a variety of thiols and alkenes to provide thioethers in excellent yields. Moreover, this method demonstrates promise for future glycoprotein studies through the successful generation of model glycoconjugates and synthesis of relevant pharmaceutical agents.

## 5.5 References

- (1) Kadereit, D.; Kuhlmann, J.; Waldmann, H. *ChemBioChem* **2000**, (1) 144–169.
- (2) Hoyle, C. E.; Bowman, C. N. *Angew. Chem., Int. Ed.* **2010**, 49, 1540-1573.
- (3) Grant, C.; Rahman, F.; Piekarz, R.; Peer, C.; Frye, R.; Robey, R. W.; Gardner, E. R.; Figg, W. D.; Bates, S. E. *Expert Rev. Anticancer Ther.* **2010**, 10, 997-1008.
- (4) Cole, K. E.; Dowling, D. P.; Boone, M. A.; Phillips, A. J.; Christianson, D. W. *J. Am. Chem. Soc.* **2011**, 133, 12474-12477.
- (5) Suzuki, T.; Nagano, Y.; Kouketsu, A.; Matsuura, A.; Maruyama, S.; Kurotaki, M.; Nakagawa, H.; Miyata, N. *J. Med. Chem.* **2005**, 48, 1019-1032.
- (6) Nishino, N.; Jose, B.; Okamura, S.; Ebisusaki, S.; Kato, T.; Sumida, Y.; Yoshida, M. *Org. Lett.* **2003**, 5, 5079.
- (7) Badescu, G.; Bryant, P.; Bird, M.; Henseleit, K.; Swierkosz, J.; Parekh, V.; Tommasi, R.; Pawlisch, E.; Jurlewicz, K.; Farys, M.; Camper, N.; Sheng, X.; Fisher, M.; Grygorash, R.; Kyle, A.; Abhilash, A.; Frigerio, M.; Edwards, J.; Godwin, A. *Bioconjugate Chem.* **2014**, 25, 1124.
- (8) Finn, M. G.; Fokin, V. V. *Chem. Soc. Rev.* **2010**, 39, 1231.
- (9) Sletten, E. M.; Bertozzi, C. R. *Angew. Chem. Int. Ed.* **2009**, 48, 6974-6998.
- (10) Yoon, T. P.; Ischay, M. A.; Du, J. *Nat. Publ. Gr.* **2010**, 2 (7), 527–532.
- (11) Tyson, E. L.; Niemeyer, Z. L.; Yoon, T. P. *J. Org. Chem.* **2014**, 79, 1427.
- (12) Keylor, M. H.; Park, J. E.; Wallentin, C.; Stephenson, C. R. J. *Tetrahedron* **2014**, 70,4264.
- (13) Xu, J.; Boyer, C. *Macromolecules* **2015**, 48, 520.
- (14) Bhat, V. T.; Duspara, P. A.; Seo, S.; Abu Bakar, N. S. B.; Greaney, M. F. *Chem. Commun.* **2015**, 51, 4383.
- (15) Zhang, H.; Lv, X.; Li, Y.; Wang, Y.; Li, J.. *ACS Nano*, **2010**, 4, 380-386.
- (16) Xiang, Q.; Yu, J.; Jaroniec, M. *J Am Chem Soc*, **2012**, 134, 6575-6578.
- (17) Ye, A.; Fan, W.; Zhang, Q.; Deng, W.; Wang, Y. *Catalysis Science & Technology*, **2012**, 2, 969-978.
- (18) Frederick, R. T.; Novotny, Z.; Netzer, F. P.; Herman, G. S.; Dohnalek, Z. *Journal of Physical Chemistry B*, **2017**, DOI: 10.1021/acs.jpcc.7b05518, Ahead of Print.
- (19) Bell, N. J.; Ng, Y. H.; Du, A.; Coster, H.; Smith, S. C.; Amal, R. *Journal of Physical Chemistry C*, **2011**, 115, 6004-6009.
- (20) Geng, W.; Liu, H.; Yao, X. *Physical Chemistry Chemical Physics*, **2013**, 15, 6025-6033.
- (21) Riente, P.; Adams, A. M.; Albero, J.; Palomares, E.; Pericàs, M. A. *Angew. Chem., Int. Ed.* **2014**, 53, 9613.
- (22) Riente, P.; Pericàs, M. A. *ChemSusChem* **2015**, 8, 1841.
- (23) Li, H.; He, X.; Kang, Z.; Huang, H.; Liu, Y.; Liu, J.; Lian, S.; Tsang, C. H. A.; Yang, X.; Lee, S. *Angew. Chem. Int. Ed.*, **2010**, 49, 4430–4434.
- (24) Zhuo, S.; Shao, M.; Lee, S. *ACS Nano*, **2012**, 6, 1059–1064.
- (25) Ming, H.; Ma, Z.; Liu, Y.; Pan, K.; Yu, H.; Wang, F.; Kang, Z. *Dalton T.*, **2012**, 41, 9526–31,
- (26) Zhang, Y.; Tang, Z.; Fu, X.; Xu, Y. *ACS Nano*, **2010**, 4, 7303-7314.
- (27) Takashima, H.; Shinkai, S.; Hamachi, I. *Chem. Commun.* **1999**, 2345-2346.
- (28) Davis, B. G. *Chem. Rev.* **2002**, 102, 579.
- (29) Helenium, A.; Aebi, M. *Science* **2001**, 291, 2364.

(30) Dere, R. T.; Zhu, X. *Org. Lett.* 2008, 10, 4641.



## 6. Materials and Methods

### 6.1 Materials

Analytical thin-layer chromatography was performed using silica gel (precoated sheets, 0.2 mm thick, 20 cm × 20 cm) and visualized by UV irradiation or molybdenum staining (heating with a phosphomolybdic acid reagent). DCM, MeOH, THF and toluene were dried over flame-dried 3 or 4 Å sieves. Dimethylformamide (DMF), triethylamine (Et<sub>3</sub>N), and trifluoroacetic acid (TFA) were used dry from Sure/Seal bottles. Other reagents were purchased from industrial suppliers. All commercially available chemicals were used without further purification unless otherwise stated. All UV reactions were carried out in a Luzchem photoreactor, LZC-EDU (110 V/60 Hz), containing 10 UVA lamps centered at 350 nm. Yields refer to chromatographically and spectroscopically purified compounds.

### 6.2 Instrumentation

#### 6.2.1 Thermogravymetric analysis (TGA)

TGA was conducted on a TA Q500 analyser, using a Pt pan as sample holder. After equilibrating the sample at 30 °C for 5 min and then at 100 °C for additional 20 min, the measurement was performed in air using a heating rate of 10 °C/min. The sample weight was monitored until 900 °C.

#### 6.2.2 Attenuated total reflectance Fourier transformed infrared (ATR FTIR) spectroscopy

The FTIR spectra were recorded with a Bruker Vertex 70v FTIR spectrometer equipped with a Platinum ATR accessory on solid samples.

#### 6.2.3 Raman spectroscopy

Raman spectra were measured on a Horiba Jobin Yvon HR 800 UV LabRam Raman microscope. For the Raman measurements, the samples were excited with a built-in 632 nm laser. The samples were deposited by adding the dry compound to a drop of methanol on the glass slide. The slides were dried in air for 2 h.

#### 6.2.4 Absorption and fluorescence spectroscopy

Absorption spectra were recorded on an Agilent Cary 8454 UV–vis diode array spectrophotometer. Fluorescence spectra were taken on a Horiba Jobin Yvon Fluoromax-4 spectrofluorometer in 1.00 cm × 1.00 cm quartz glass cells. The CNO samples were dispersed in DMSO, PBS 0.01M or cell medium to a final concentration of 500 μg ml<sup>-1</sup>. The dispersion of CNO was sonicated for 15 min at 37 kHz and then diluted respectively in DMSO, PBS 0.01M or cell medium to achieve final concentrations of 50, 20, 10, 5 and 1 μg ml<sup>-1</sup>.

### 6.2.5 Fluorescence quantum yields

The fluorescence quantum yield ( $\Phi_F$ ) is determined by the comparative method of Williams *et al.*<sup>1</sup> and is calculated using the following equation,

$$\Phi_x = (\Phi_{st}) (Grad_x / Grad_{st}) (\eta_{st}^2 / \eta_x^2)$$

where *st* and *x* denotes the standard and test respectively,  $\Phi$  is the fluorescence quantum yield, *Grad* is the gradient obtained from the plot of integrated fluorescence intensity vs. absorbance of the dye at the excitation wavelength and  $\eta$  represents the refractive index of the used solvents.

### 6.2.6 Dynamic light scattering (DLS) and zeta-potential measurements

DLS Measurements were performed on the Malvern Nano-ZS instrument operating in backscattering (173°) mode and analysed with the software Zetasizer, with automatic selection of the optimal detector position and number of independent measurements. The CNO samples were dispersed in DMSO, PBS 0.01M or cell medium to a final concentration of 500  $\mu\text{g ml}^{-1}$ . The samples were sonicated for 30 min at 37 kHz and then diluted respectively in DMSO, PBS 0.01M or cell medium to achieve final concentrations of 50, 20, 10, 5 and 1  $\mu\text{g ml}^{-1}$ . The CNOs samples were sonicated for additional 15 min and the size of the particle was measured. Z-potential measurements were performed on the same apparatus using the disposable Z-potential cuvettes.

### 6.2.7 Transmission electron microscopy (TEM)

Bright-field TEM imaging was performed on a Jeol JEM-1011 instrument equipped with a thermoionic tungsten source operated at 100 kV. Samples were prepared by spreading a droplet of the dispersed material in ethanol on a copper grid coated with a lacey carbon film.

### 6.2.8 High-resolution mass spectrometry (HRMS)

The Accurate Mass measurements (HRMS) were performed on a Waters SYNAPT G2 High Resolution Mass Spectrometry instrument equipped with an Electrospray Ionization interface and coupled to a Waters ACQUITY UPLC. Electrospray ionization in positive mode was applied in the mass scan range 50-1200 Da. The analysis were performed on a Waters ACQUITY UPLC BEH C18 column 100 x 2.1 mm ID (particle size 1.7  $\mu\text{m}$ ) with an in-line filter. The mobile phase was 0.1% formic acid in H<sub>2</sub>O and 0.1% formic acid in acetonitrile.

### 6.2.9 Nuclear Magnetic Resonance Spectroscopy (NMR)

For NMR spectra, a 400 MHz spectrometer was employed for <sup>1</sup>H (400.13 MHz) and <sup>13</sup>C (100.61 MHz) spectra, a 600 MHz spectrometer was employed for <sup>1</sup>H (600.13 MHz) and <sup>13</sup>C (150.90 MHz) spectra. Resonances  $\delta$ , are in ppm units downfield from an internal reference in CDCl<sub>3</sub> ( $\delta\text{H} = 7.26$  ppm,  $\delta\text{C} = 77.0$  ppm), or MeOH ( $\delta\text{H} = 3.31$  ppm,  $\delta\text{C} = 49.0$  ppm).

### 6.2.10 Confocal microscopy

Confocal imaging was performed with a laser scanning confocal microscope equipped with a resonant scanner (Nikon A1R) using a 20 × objective.

## 6.3 Biological methods

### 6.3.1 Cell Culture

HeLa cells (human epithelial cervix adenocarcinoma cell line ATCC CCL2) and MCF-7 cells (human mammary gland adenocarcinoma cell line ATCC HTB-22) were cultured on 75 cm<sup>2</sup> culture flasks in Dulbecco's modified Eagle medium (DMEM) supplemented with 10% FBS, 2% Penstrep and 1% glutamine. Cells were grown in a humidified incubator at 37°C with 5% CO<sub>2</sub> and 95% air.

### 6.3.2 Sample preparation for cell study

The samples of functionalized-CNO were prepared by suspending 1 mg of CNOs in 1 mL sterile phosphate buffered saline (PBS) solution followed by sonication for 30 min at 37 kHz. The samples were then dispersed in the cell culture media (DMEM) at final concentrations of 1, 2, 5, 10, 20 μg mL<sup>-1</sup>.

### 6.3.3 Cell viability

Cells were seeded in 24 well chamber slides at a density of 5 × 10<sup>4</sup> cells/well and incubated in a 500 μl cell culture medium to obtain a subconfluent monolayer after 48 h in a humidified atmosphere at 37 °C and 5% CO<sub>2</sub>. The cell culture medium was removed and replaced with 500 μl of medium with dispersions of functionalized-CNO at the final concentrations. The viability of the cells was measured after 12, 24, 48 and 72 h of exposure to the samples of CNO, utilizing the PrestoBlue™ cell viability assay (Life Technologies). Prestoblue™ is a blue non-fluorescent, cell permeable compound (resazurin-based solution), that is reduced by living cells into a fluorescent compound (resorufin). Assays were performed by measuring the absorbance on a microplate reader at a wavelength of 570 nm (experimental wavelength) and 600 nm (normalization wavelength). The percent viability was determined by normalizing absorbance values to non-treated cells and calculated as:

$$\frac{\text{Absorbance Intensity of Experiment Sample}}{\text{Average (n = 8) Absorbance intensity of Untreated Sample}} * 100 = \text{Percent Viability (\%)}$$

following a procedure previously described<sup>2</sup>. Each measurement was normalized with the average signal of untreated wells to determine the percent cell viability expressed as the mean ± SD.

### 6.3.4 Cellular imaging

Cells were grown in subconfluent monolayer (50–60 % confluent) on 25 mm glass bottom dishes at 37 °C under a 5% CO<sub>2</sub> atmosphere in a humidified environment. The culture medium was removed and replaced with 1, 5 and 10, 20 μg ml<sup>-1</sup> suspension of functionalized-CNO and incubated for 24 h. After the incubation

time, the cells were washed with PBS three times to remove any remaining media and the cells were incubated for 7 min at 37 °C with a solution of Hoechst 33342, for live nuclear staining. Excitation of the fluorescein on the CNO samples was performed at 488 nm and the emission was acquired in the spectral window between 500–560 nm. The Hoechst 33342 was excited at 405 nm and the images were acquired in the emission range of 415–480 nm. In the same way, in order to see the plasma membrane, after the washinf with PBS, WGA 594 (Life Technologies, 5 µg/mL) was added to the cells and the cells were incubated for 10 min at 37°C. Then, the cells were washed again with PBS before imaging. Sequential optical sections (Z-stacks), 1 µm thickness, from the basal-to-apical surfaces of the cells were acquired to study the cellular internalization and distribution. Excitation of the fluorescein on the CNO samples was performed at 488 nm and the emission was acquired in the spectral window between 500–560 nm. The Hoechst 33342 was excited at 405 nm, while the WGA 594 was excited at 577 nm and the images were acquired in the emission range of 415–480 nm and 600-680 respectively.

## 6.4 References

- 1) A. T. R. Williams, S. A. Winfield, J. N. Miller, *Analyst* **1983**, *108*, 1067.
- 2) J V Jokerst, A J Cole, D Van de Sompel, S S Gambhir, *ACS Nano* **2012**, *6*, 10366–77.

## Conclusion and Outlook

The expansion of carbon materials, as demonstrated in the chapters of this thesis, is multidisciplinary and is related to physics, chemistry, biology, applied sciences and engineering. With the emergence of biopharmaceuticals and immunotherapies at the forefront of modern medicine, there is a particular interest in the controlled chemical derivatization of carbon nanomaterials with fluorophores, photosensitizers and biomolecules to fully realize the potential of nanomedicine in the treatment of disease. Recently, nanotechnology has been applied to address the clear biomimicry challenge inherent to the next generation of more potent and sophisticated adjuvants. Although early adjuvants, such as aluminum hydroxide, have been successful in stimulating the immune response, the advent of nanoscale antigen delivery platforms has catalyzed the transition from these simple immunoactive chemical agents to adjuvants that can engage and direct immune responses more akin to the methods employed by pathogens themselves. Furthermore, since photocatalytic technologies have been gaining increasing commercial interest worldwide with applications in chemical biology, medicinal, and polymer chemistry, a photocatalytic technology using carbon nanomaterials has been explored. A mild, inexpensive and general initiation protocol for thiol-ene ligation reactions using carbon nanomaterial/metal oxide (Carbon NM-MO) composites have been described. Graphene oxide (GO), nanodiamonds (ND) and carbon nano-onions (CNO) displaying bismuth oxide nanoparticles adhered to the surface, were found to be efficient photocatalysts for this process. The straightforward and cheap catalyst preparation, excellent overall yields, ease of purification and broad substrate scope render this a highly versatile process for biorthogonal thiol-ene ligation. The high efficiency of the visible-light mediated thiol-ene reaction, enable the applicability of this chemistry to the synthesis of glycoconjugates, pharmaceutical agents and antibody-drug conjugates (ADCs). The simple catalyst preparation, high-yields, ease of purification and biocompatibility render this a highly attractive option for cytocompatible thiol-ene ligation reactions. These are key relevant topics for the future of our society. In this thesis, it has been highlighted how carbon nano-onions, due to their low toxicities and powerful characteristics, can be extremely useful not only in various biology-related applications such as nanomedicine, drug delivery, bio-labeling but also in important photocatalytic applications especially for the synthesis of organosulfur compounds, which play fundamental roles in many biological structures and functions. As described in the previous chapters, carbon nano-onions have emerged as a novel platform for drug delivery, imaging and sensing, showing enhanced therapeutic efficacy, photostable fluorescence and high biocompatibility. This opens new doors in using carbon nano-materials to probe, adjust and control biological processes at the cellular and subcellular level and points toward the possible application of carbon nano-onions as novel agents for gene therapy. The topics treated defines some of the trends and outlooks in this exciting area, with the effort of evidencing some of the possibilities offered from the growing level of knowledge and providing bases for a more rational design of carbon nanomaterial based therapeutics. The aim is to stimulate ideas and research on a field that is strongly believed and will represent one of the key areas for the future of the new generations.